DOE/ER-0046/18

Damage Analysis and Fundamental Studies

Quarterly Progess Report
April-June 1984

August 1984

U.S. Department of Energy
Office of Energy Research
Office of Fusion Energy
Washington, DC 20545

NOTICE

Printed in the United States of America
Available from
National Technical Information Service
U.S. Department of Commerce
5285 Port Royal Road
Springfield, VA 22161

NTIS price codes
Printed copy: A08
Microfiche copy: A01

DOE/ER-0046/18
UC-20,20c

Damage Analysis and Fundamental Studies

Quarterly Progress Report
April-June 1984

August 1984

U.S. Department of Energy
Office of Energy Research
Office of Fusion Energy
Washington, DC 20545

FOREWORD

This report is the twenty-sixth in a series of Quarterly Technical Progress Reports on ***Damage Analysis and Fundamental Studies*** **(DAFS),** which is one element of the Fusion Reactor Materials Program, conducted in support of the Magnetic Fusion Energy Program of the U.S. Department of Energy (DOE). The first eight reports in this series were numbered DOE/ET-0065/1 through 8. Other elements of the Fusion Materials Program are:

- Alloy Development for Irradiation Performance (ADIP)
- Plasma-Materials Interaction (PMI)
- Special Purpose Materials (SPM).

The OAFS program element is a national effort composed of contributions from a number of National Laboratories and other government laboratories, universities, and industrial laboratories. **It** was organized by the Materials and Radiation Effects Branch, DOE/Office of Fusion Energy, and a Task Group on ***Damage Analysis and Fundamental Studies,*** which operates under the auspices of that branch. The purpose of this series of reports is to provide a working technical record of that effort for the use of the program participants, the fusion energy program in general, and the DOE.

This report is organized along topical lines in parallel to a Program Plan of the same title so that activities and accomplishments may be followed readily, relative to that Program Plan. Thus, the work of a given laboratory may appear throughout the report. Note that a new chapter has been added on Reduced Activation Materials to accommodate work on a topic not included in the early program plan. The Contents is annotated for the convenience of the reader.

This report has been compiled and edited under the guidance of the Chairman of the Task Group on *Damage* ***Analysis and*** *Fundamental* ***Studies,*** D. G. Doran, Hanford Engineering Development Laboratory (HEDL). His efforts, those of the supporting staff of HEDL, and the many persons who made technical contributions are gratefully acknowledged. T. C. Reuther, Materials and Radiation Effects Branch, is the DOE counterpart to the Task Group Chairman and has responsibility for the DAFS program within DOE.

G. M. Haas, Chief
Fusion Technologies Branch
Office of Fusion Energy

CONTENTS

CONTENTS (Cont'd)

CONTENTS (Cont'd)

CHAPTER 1

IRRADIATION TEST FACILITIES

C.M. Logan and D. W. Heikkinen (Lawrence Livermore National Laboratory)

1.0 Objective

The objectives of this work are operation of RTNS-II (a 14-MeV neutron source facility), machine development, and support of the experimental program that utilizes this facility. Experimenter services include dosimetry, handling, scheduling, coordination, and reporting. RTNS-II is supported jointly by the U.S. and Japan and is dedicated to materials research for the fusion power program. Its primary use is to aid in the development of models of high-energy neutron effects. Such models are needed in interpreting and projecting to the fusion environment, engineering data obtained in other spectra.

2.0 Summary

Irradiations were performed on 10 different experiments during this quarter. Ion source developnent continues. A redesigned ground electrode assembly was installed. Target cooling water leaks were encountered and repaired.

3.0 Program

Title: RTNS-II Operations (WZJ-16)
Principal Investigator: C. M. Logan
Affiliation: Lawrence Livermore National Laboratory

4.0 *Relevant DAFs Program Plan Task/Subtask*

TASK II,A,2,3,4,
TASK II,B,3,4
TASK II,C,1,2,6,11,18,

5.0 Irradiation - M. Logan, D. W. Heikkinen and M. W. Guinan

During this quarter, irradiations (both dedicated and add-on) were done for the following people.

Experimenter	P or A*	Sample Irradiated
R. Smither (ANL)	A	Al - the $^{27}Al(n,2n)^{26}Al$ cross section near threshold
K. Saneyoshi (TIT)	A	LiF - determine the feasibility of TLD self irradiation as a tritium production monitor
D. Heikkinen (LLNL)	A	Nb - dosimetry calibration
K. Abe (Tohoku) H. Matsui (Tohoku) H. Kayano (Tohoku) M. Kiritani (Hokkaido)	P	Metals -mechanical properties room temperature

Experimenter	P or A*	Sample Irradiated
H. Takahashi (Hokkaido) K. Shinohara (Kyushu) E. Kuramoto (Kyushu) N. Yoshida (Kyushu) T. Kinoshita (Kyushu) N. Igata (Tokyo) A. Kohyama (Tokyo) K. Mihayara (Tokyo) H. Kawanishi (Tokyo) K. Kamada (Nagoya) M. Iseki (Nagoya) K. Sata (Nagoya)		
Y. Shimomura (Hiroshima)	A	Au - room temperature experiment cascade and microsctructural damage
K. Sumita (Osaka)	A	Insulators - electrical and mechanical properties
P. Hahn (Vienna)	A	Nb-Ti - measure fluxoid pinning strength of superconductors
K. Okamura (Tohoku)	A	Silicon carbide fibers - mechanical properties
L. Lucht (LLNL)	A	Oil shale tracer transport in fluidized bed
P. Pawlikowski (LLNL) G. Coleman (LLNL)	P	(n,2n) cross section

*P - primary, A = Add-on

5.1 RTNS-II Status - C. M. Logan and D. W. Heikkinen

The ion source system development continues on the right mchine.

General cleanup was performed in June on all areas of the facility.

Left mchine target hub and water lines developed leaks. Hoses were replaced and the hub was repaired.

A new ground electrode assembly was installed on the right machine in order to improve vacuum conductance and allow for ground electrode biasing.

6.0 Future Work

Irradiations will be continued for H. Heinisch (HEDL) et al., K. Saneyoshi (TiT), R. Smither (ANL), L. Lucht (LLNL), P. Pawlikowski/G. Coleman (LLNL), D. Heikkinen (LLNL). Also during this period, irradiations for N. Yoshida (Kyushu), H. Matsui (Tohoku), K. Kawamura (TIT) and D. Nethaway (LLNL) will be initiated.

A new bypass and filtering system will be installed on the target cooling water system.

CHAPTER 2

DOSIMETRY AND DAMAGE PARAMETERS

DOSIMETRY MEASUREMENTS AND DAMAGE CALCULATIONS FOR THE ORR-MFE4B EXPERIMENT

L. R. Greenwood and R. K. Smither (Argonne National Laboratory)

1.0 Objective

To measure the neutron fluence and calculate the resultant damage in irradiated specimens during the MFE4B spectral-tailoring experiment in ORR.

2.0 Sumnary

Dosimetry measurements and damage calculations are reported for the MFE4B spectral-tailoring experiment in the ORR. With an expsoure of 424 full power days the maximum fluence was 1.9 $\times 10^{22}$ n/cm^2 producing about 64 appm helium and 5.1 dpa in 316 stainless steel. The status of all other experiments is summarized in Table I.

TABLE I

STATUS OF DOSIMETRY EXPERIMENTS

	Facility/Experiment	Status/Comments
ORR	- MFE 1	Completed 12/79
	- MFE 2	Completed 06/81
	- MFE 4A1	Completed 12/81
	- MFE 4A2	Completed 11/82
	- MFE 48	Completed 04/84
	- TBC 07	Completed 07/80
	- TRIO-Test	Completed 07/82
	- TRIO-1	Completed 12/83
	- Hf Test	Completed 03/84
	- JP Test	Samples Sent 06/84
HFIR	- CTR 32	Completed 04/82
	- CTR 31, 34, 35	Completed 04/83
	- CTR 30	Samples Received 07/84
	- T2, RB1	Completed 09/83
	- T1, CTR 39	Completed 01/84
	- RB2, R83, T3	Irradiations in Progress
	- CTR 40-52	Irradiations in Progress
	- JP 1-8	Irradiations in Progress
Omega West	- Spectral Analysis	Completed 10/80
	- HEDL1	Completed 05/81
	- HEDL2	Samples Sent 05/83
	- LANL 1	Samples Sent 06/84
EBR II	- X287	Completed 09/81
IPNS	- Spectral Analysis	Completed 01/82
	- LANL1 (Hurley)	Completed 06/82
	- Hurley	Completed 02/83
	- Coltman	Completed 08/83

3.0 Program

Title: Dosimetry and Damage Analysis
Principal Investigator: L. R. Greenwood
Affiliation: Argonne National Laboratory

4.0 Relevant DAFS Program Plan Task/Subtask

Task II.A.l Fission Reactor Dosimetry

5.0 Accomplishments and Status

The MFE4B experiment in the Oak Ridge Research Reactor (ORR) is a spectral-tailoring irradiation designed to achieve fusion-like helium-to-dpa ratios in stainless steel.[1] The experiment is nearly identical to the MFE4A irradiation reported earlier.[2] The irradiation took place in core position E7 from April 22, 1981 to October 20, 1982 for a total exposure of 424 full power days. The present analysis is based on four dosimetry tubes removed from the assembly when it was repackaged. New replacement dosimetry tubes were inserted at that time and the experiment is now undergoing further exposure in ORR. The present interim measurements are thus designed to check on the progress of the experiment, especially regarding the critical helium-to-dpa ratio and the subsequent insertion of the hafnium core piece to reduce the helium accumulation.[1]

The four stainless steel dosimetry tubes measured 1/16" O.D. x 2-3/4" long and contained small specimens of Fe, Ni, Co, Ti, Nb, Cu, 80% Mn-Cu, and helium accumulation monitors supplied by Rockwell International. All of the samples were gama counted by Ge(Li) spectroscopy and the measured activation rates are listed in Table II. One dosimetry tube apparently burst during the irradiation and some of the dosimeters could not be removed from the tube for gama analysis. Two of the tubes were located on the upper level and two on the lower level of the MFE4B assembly. In each case, one tube was outside and one inside of a stainless steel annulus surrounding the NaK and experimental samples. The top tubes were at 600°C while the lower tubes were in the 500°C temperature region.

TABLE II

ACTIVATION RATES MEASURED FOR ORR-MFE4B
Dosimeters removed 10/82 at 424 FPD; normalized to 30 MW
Burnup corrections included; accuracy ±2% unless noted

Reaction	Height, in.	Activity (atom/atom-s) Inside		Outside	
$^{58}Fe(n,\gamma)^{59}Fe$ (±4%)	-0.84	1.60	E-10	1.69	E-10
	-2.41	1.68	E-10	1.78	E-10
	-3.91			1.70	E-10
	-4.03	1.73	E-10		
	-5.72	1.49	E-10	1.54	E-10
$^{59}Co(n,\gamma)^{60}Co$	-1.02			5.52	E-9
	-4.08			5.46	E-9
	-4.20	5.10	E-9		
$^{93}Nb(n,\gamma)^{94}Nb$	-1.56	2.72	E-10	2.89	E-10
	-4.88	2.72	E-10	2.77	E-10
$^{54}Fe(n,p)^{54}Mn$	-0.84	9.80	E-12	9.89	E-12
	-2.41	10.48	E-12	10.22	E-12
	-3.91			10.47	E-12
	-4.03	10.76	E-12		
	-5.72	10.22	E-12	10.03	E-12
$^{46}Ti(n,p)^{46}Sc$	-1.31			1.40	E-12
	-4.37	1.37	E-12	1.45	E-12
	-4.62	1.42	E-12	1.43	E-12
$^{55}Mn(n,2n)^{54}Mn$	-1.81	3.71	E-14	3.96	E-14
	-5.12	3.71	E-14	3.33	E-14
$^{63}Cu(n,\alpha)^{60}Co$	-2.06			6.94	E-14
	-5.37	7.19	E-14	6.83	E-14
$^{58}Ni(n,p)^{58}Co$*	-2.25	3.96	E-12	4.29	E-12
	-4.37			4.46	E-12
	-5.56	4.76	E-12	5.00	E-12
$^{60}Ni(n,p)^{60}Co$*	-2.25	1.29	E-12	1.58	E-12
	-4.37			1.57	E-12
	-5.56	1.26	E-12	1.30	E-12

* Burnup corrections not included but estimated to be 50% of more for both nickel reactions.

The activities listed in Table II can all be fit to a simple polynomial of form:

$$f(h) = fmax\ [1 + c\ (x-x_0)^2] \quad (1)$$

where fmax = highest value and x_0 = center of flux gradient. The thermal and fast reactions were fit separately and the resultant parameters are listed in Table III. As can be seen, the vertical gradient is only about 15% over the sample region while the inner-to-outer gradient is quite small, with a thermal difference of about 5% and no apparent fast gradient.

TABLE III

MAXIMUM ACTIVITIES FOR ORR-MFE4B
(Values Determined from Polynomial Fit)

Reaction	Activation Rate (atom/atom-s) Inside	Outside	Ratio ($\frac{Out}{In}$)
$^{58}Fe(n,\gamma)^{59}Fe$	1.72 E-10	1.77 E-10	1.03
$^{59}Co(n,\gamma)^{60}Co$	5.25 E-9	5.70 E-9	1.08
$^{93}Nb(n,\gamma)^{94}Nb$	2.85 E-10	2.96 E-10	1.04
$^{54}Fe(n,p)^{54}Mn$	1.07 E-11	1.06 E-11	0.99
$^{46}Ti(n,p)^{46}Sc$	1.42 E-12	1.43 E-12	1.01
$^{55}Mn(n,2n)^{54}Mn$	3.85 E-14	3.85 E-14	1.00
$^{63}Cu(n,\alpha)^{60}Co$	7.20 E-14	7.20 E-14	1.00

Gradient Polynomial Function

$F(x) = Fmax\ [1 + c\ (x-x_0)^2]$
where Fmax = maximum value
x_0 = center of activity (inches)

	c	x_0
Fast	-1.269 E-2	-3.35"
Thermal	-1.521 E-2	-2.81"
Global	-1.395 E-2	-3.06

The maximum activity values were used as input to the STAYSL computer code to adjust the neutron spectrum calculated by R. A. Lillie.[1] The adjusted flux and fluence values are listed in Table IV and the spectrum is shown in Fig. 1. These values are quite similar to those reported previously for the MFE4A experiment after a similar exposure.[2] The thermal flux was calculated assuming a temperature distribution centered at 95°C, the temperature of the surrounding moderator. The derived 2200 m/s flux is also listed for comparison.

TABLE IV

MAXIMUM FLUX AND FLUENCE VALUES FOR ORR-MFE4B
(Values at 30 MW after 424 FPD at -3" below midplane)

Energy	Error, %	Flux, x 10^{14} n/cm^2-s Inside	Outside	Fluence, x 10^{21} n/cm^2 Inside	Outside
Total	6	5.19	5.36	19.0	19.6
Thermal (<.5 eV) (2200 m/s)	6	1.70	1.83	6.24	6.72
Fast, >.11 MeV	10	1.76	1.70	6.43	6.43
0.5 eV - 0.11 MeV	12	1.73	1.77	6.33	6.48

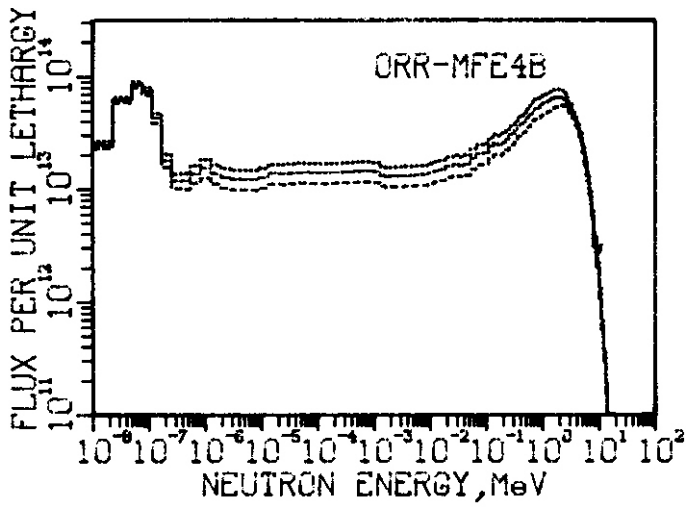

Fig. 1. Adjusted flux spectrum for the ORR-MFE4B experiment normalized to 30 MW after 424 full power days. The dotted and dashed lines indicate one standard deviation; however, the flux groups are highly correlated.

Displacement damage and helium calculations were performed using the SPECTER computer code. Values are listed for a number of elements at the maximum flux position in Table V. The He and dpa values at other heights in the assembly can be determined using Eq. (1) and the maximum values in Table V.

TABLE V

DAMAGE PARAMETERS FOR ORR-MFE4B (424 FPD)

Element		He (appm)		OPA	
		Inside	Outside	Inside	Outside
Al		3.91	3.92	8.65	8.65
Ti		2.96	2.96	5.51	5.51
V		0.14	0.14	6.12	6.12
Cr		0.97	0.97	5.48	5.48
Mn[a]		0.81	0.81	5.86	5.87
Fe		1.68	1.68	4.87	4.87
Co[a]		0.81	0.81	5.61	5.66
Nib	Thermal	457.0	517.8	0.81	0.91
	Fast	23.9	23.8	5.13	5.14
	Total	480.9	541.6	5.94	6.05
cu		1.45	1.46	4.70	4.70
Zr		0.15	0.15	5.08	5.08
Nb		0.31	0.31	4.68	4.68
Mo		--	--	3.44	3.44
Ta		--	--	2.36	2.36
316 ss[c]		63.8	71.7	5.10	5.12

[a] Self-shielding corrections may be needed for the (n,γ) damage in Mn (5%) and Co (17%).

[b] See references 3 and 4 for nickel calculations.

[c] 316 ss: Cr (.18), Mn (.019), Fe (.645), Ni (.13), Mo (0.026)

Helium and damage rates for nickel and 316 ss were computed separately and are listed in Table VI and shown in Fig. 2. The procedure used in these calculations was described in detail in a recent publication.3 The extra d a from the ^{56}Fe recoils is also included using the formula of one displacement for every 567 appm helium.! As shown in reference 3, we expect the helium calculations to be quite accurate (±5-10%). Of course, samples from this experiment will also be analyzed by Rockwell International and measurements will then become available for a number of elements. These data will be used to refine our helium production cross sections and to improve our dosimetry technique.

TABLE VI

KLIUM AND DPA GRADIENTS FOR ORR-MFE4B (424 FPD)
(Values are listed for the inner position)

Height, in.	Fluence	Helium, appm		DPA	
	(x 1022 n/cm2)	Ni	316 ss	Ni	316 ss
0	1.67	381.	50.7	5.18	4.48
-1	1.81	441.	58.5	5.61	4.85
-2	1.88	472.	62.6	5.87	5.04
-3	1.90	481.	63.8	5.94	5.10
-4	1.86	463.	61.4	5.80	4.99
-5	1.76	419.	55.7	5.46	4.72
-6	1.61	357.	47.5	4.93	4.30

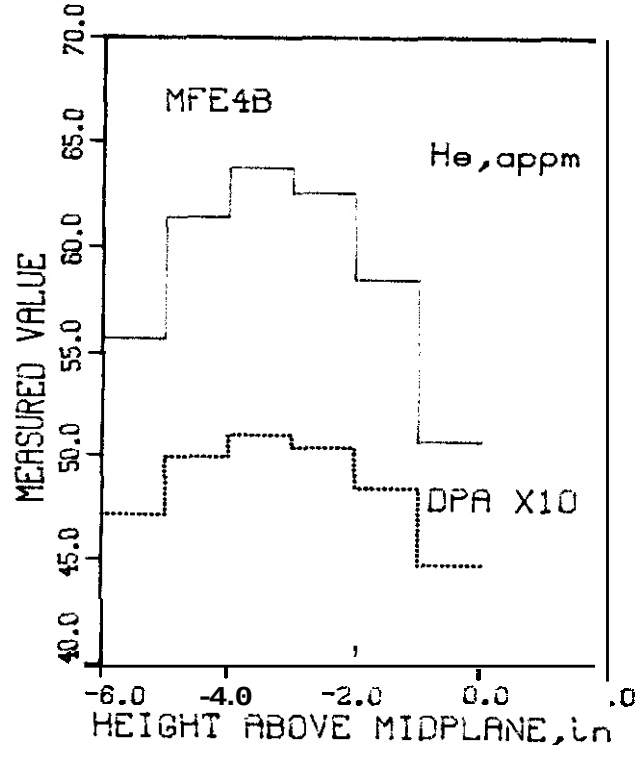

Fig. 2. Helium (appm) and dpa (x 10) values are shown for 316 stainless steel as a function of the height above midplane.

6.0 References

1. R. A. Lillie, Neutronics Calculations in Support of the ORR-MFE4A and 4B Spectral-Tailoring Experiments, Alloy Development for Irradiation Performance, Semiannual Progress Report, pp. 38-39, DOE/ER/0045/11, September 1983.

2. L. R. Greenwood, Dosimetry and Damage Analysis for the MFE4A Spectral Tailoring Experiment in ORR, Damage Analysis and Fundamental Studies Quarterly Progress Report, DOE/ER-0046/12, pp. 14-23, 1983.

3. L. R. Greenwood, D. W. Kneff, R. P. Skowronski, and F. M. Mann, A Comparison of Measured and Calculated Helium Production in Nickel Using Newly Evaluated Neutron Cross Sections for ^{59}Ni, to be published in the Journal of Nucl. Mater., 1984.

4. L. R. Greenwood, A New Calculation of Thermal Neutron Damage and Helium Production in Nickel, Journal of Nucl. Mater. 115, 137-142 (1983).

7.0 Future Work

We will continue to monitor the progress of the MFE4 spectral-tailoring experiment in ORR. Samples were also prepared for further experiments in HFIR and the Omega West Reactor.

MEASUREMENT OF Cu SPALLATION CROSS SECTIONS AT IPNS

L. R. Greenwood and R. K. Smither (Argonne National Laboratory)

1.0 Objective

To develop new cross sections and techniques for dosimetry and damage analysis at accelerator-based neutron sources.

2.0 Sumnary

Spallation cross sections for Cu have been measured at the IPNS at Argonne National Laboratory. Results are reported for the production of 21 different radioisotopes at 13 dfferent energies between 25 and 450 MeV. These data are now being tested for spectral adjustments at IPNS and LAMPF and some preliminary results are reported.

3.0 Program

Title: Dosimetry and Damage Analysis
Principal Investigator: L. R. Greenwood
Affiliation: Argonne National Laboratory

4.0 Relevant DAFS Program Plan Task/Subtask

Task II.A.2 High-Energy Neutron Dosimetry

5.0 Accomplishments and Status

Spallation cross sections are being developed in order to extend our dosimetry and damage techniques to higher energies for accelerator-based neutron sources. especially spallation sources such as the Intense Pulsed Neutron Source (IPNS) at ANL and the Los Alamos Meson Physics Facility (LAMPF) at LANL. Results were reported previously[1] for the production of ^{7}Be, ^{22}Na, and ^{24}Na from Al. In the present report results are listed for 21 different radioisotopes from Cu.

A stack of three copper foils, each measuring 4" x 4" x 5 mils, was directly irradiated in the proton beam of the IPNS. The large size of the foils guarantees interception of the entire proton beam which is subsequently stopped in a beam dump Faraday cup and integrated to determine the total number of protons. The center foil was gama counted while the front and back foils were used to correct for recoil losses. Each irradiation required about 1 hour to obtain a proton fluence of about 10^{17}. The foils were autoradiographed prior to cutting and gama counting to determine the beam profile. Absorbers were used to reduce the proton energy below 50 MeV.

The cross section results are listed in Tables I-III. Tables 1-11 list true spallation products which presumably are identical for either neutron or proton irradiation. Table III lists specific proton-induced reactions which are produced from peripheral reactions on individual copper isotopes. Most of the values are accurate to ±5%. It is important to note that each foil had to be counted at least four times at different decay times, in order to correctly identify and separate all of the different isotopes. For example, ^{60}Co can not be accurately counted until about 30 days after the irradiation due to interference from ^{52}Mn (1333.6 keV, 5.6 days), ^{62}Zn (1173.0 keV, 9.3 hours), and ^{56}Co (1175.1 keV, 78.8 days).

TABLE I

SPALLATION PRODUCT CROSS SECTIONS FOR Cu

Energy, MeV	Cross Section, mb					
	^{60}Co	^{59}Fe	^{58}Co	^{57}Ni	^{57}Co	^{56}Mn
26	--	--	3.92	--	--	--
32	6.04	--	69.2	--	0.52	--
40	10.8	0.08	81.3	0.33	20.2	--
50	13.2	0.20	57.8	1.87	62.8	--
80	10.1	0.77	49.8	1.20	34.7	--
100	9.90	0.84	47.2	1.74	41.2	--
150	9.35	1.02	42.6	1.80	39.0	--
200	9.10	1.12	38.6	1.65	36.6	2.37
250	9.61	1.25	37.5	1.58	34.2	2.89
300	9.54	1.33	36.3	1.46	32.4	2.80
350	9.61	1.39	34.9	1.39	33.4	2.94
400	8.93	1.38	32.3	--	33.4	--
450	8.71	1.38	30.7	1.21	28.6	2.92

TABLE II

ADDITIONAL SPALLATION PROOUCT CROSS SECTIONS FOR Cu

Energy, MeV	Cross Section, mb					
	^{56}Co	^{55}Co	^{54}Mn	^{52}Fe	^{52}Mn	^{51}Cr
40	0.028	--	0.056	--	--	--
50	0.25	--	1.61	--	--	--
80	13.2	0.96	3.62	--	0.56	0.31
100	10.4	1.44	8.40	0.030	1.84	2.55
150	12.0	1.70	13.4	0.083	3.87	7.29
200	11.6	1.86	15.7	0.131	5.21	11.1
250	11.7	1.83	18.0	0.153	6.50	14.7
300	11.4	1.92	19.1	0.178	7.15	17.3
350	11.1	1.76	19.9	0.181	7.88	19.6
400	10.2	--	20.2	--	--	20.2
450	9.67	1.67	19.6	0.209	8.18	21.0

	^{48}V	^{48}Sc	^{47}Sc	^{46}Sc	^{44}Sc
100	0.129	--	--	0.02	--
150	0.976	0.027	0.184	0.188	0.060
200	2.26	0.090	0.350	0.542	0.251
250	3.80	0.116	0.554	1.07	0.572
300	5.16	0.321	0.821	1.64	0.914
350	6.27	0.381	0.991	2.24	1.41
400	7.43	--	--	3.02	--
450	7.87	0.318	1.48	3.28	2.17

TABLE III

PERIPHERAL PROTON REACTIONS WITH Cu

Energy, MeV	Cross Section, mb			
	$^{65}Cu(p,n)^{65}Zn$	$^{65}Cu(p,np)^{64}Cu$	$^{63}Cu(n,2n)^{62}Zn$	$^{63}Cu(p,2np)^{61}Cu$
26	44.0	436.	102.	89.7
32	32.6	306.	33.0	354.
40	26.3	269.	25.1	282.
50	22.4	241.	24.9	194.
80	8.56	133.	8.07	105.
100	6.24	103.	5.50	66.2
150	3.85	75.3	3.28	49.6
200	3.09	64.5	2.41	30.7
250	2.44	55.6	1.85	30.4
300	2.15	52.8	1.46	29.0
350	2.04	54.0	1.19	25.6
400	1.88	--	--	--
450	1.64	51.4	0.95	21.7

Since Spallation produces all masses lower than the target mass, most of our cross sections should be considered as chain yields, comparable to the fission case. For example, our cross section for ^{48}V includes contributions from ^{48}Cr (21.6 hour), ^{56}Mn includes ^{56}Cr (5.9 m), and so on. ^{52}Fe and ^{57}Ni are listed separately since they could be easily identified. However, the cross sections for ^{52}Mn and ^{57}Co also include these contributions. Such effects should be carefully considered in the application of the cross sections in Tables I-II.

The peripheral reaction data in Table III is compared to previous measurements[2,3] at lower energy in Figure 1. The excellent agreement with previous data helps to confirm the accuracy of our proton beam current integration and energy calibration.

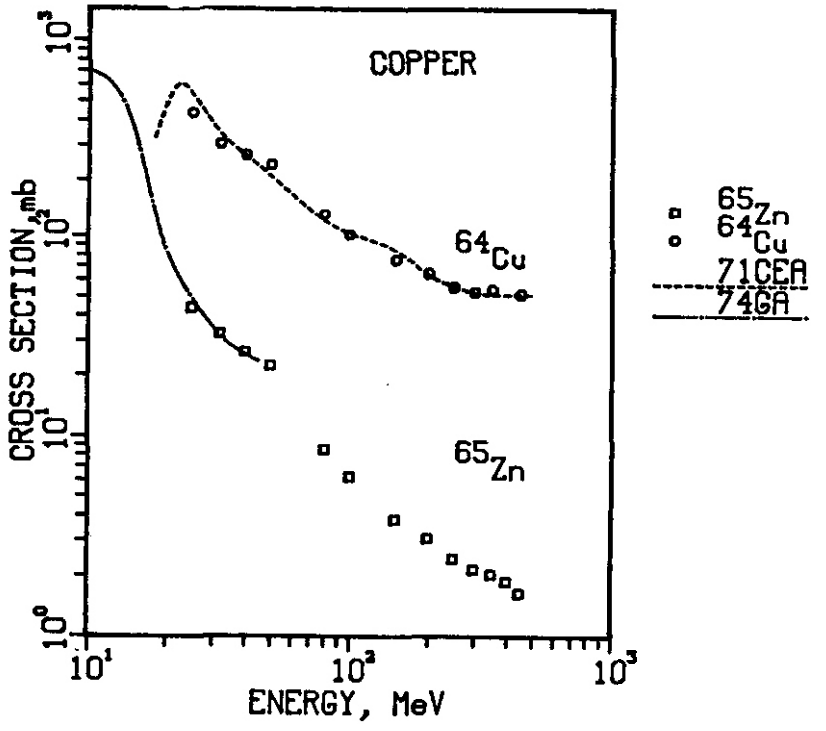

Fig. 1. Comparison of measured cross sections for peripheral reactions on Cu with previous measurements.

Some of the spallation cross sections are shown in Figures 2-4. The overall spallation yield mass dependence is shown in Figure 5 and compared to semi-empirical theories.[4,5] As can be seen, the semi-empirical equations incorrectly predict the mass dependence of the spallation yield. These theories also do not predict the energy dependence of the cross sections, as demonstrated in Figure 4. At present the models only appear to be accurate to within about a factor of 2. Clearly, the present data could be used to readjust these semi-empirical models, although this has not yet been done.

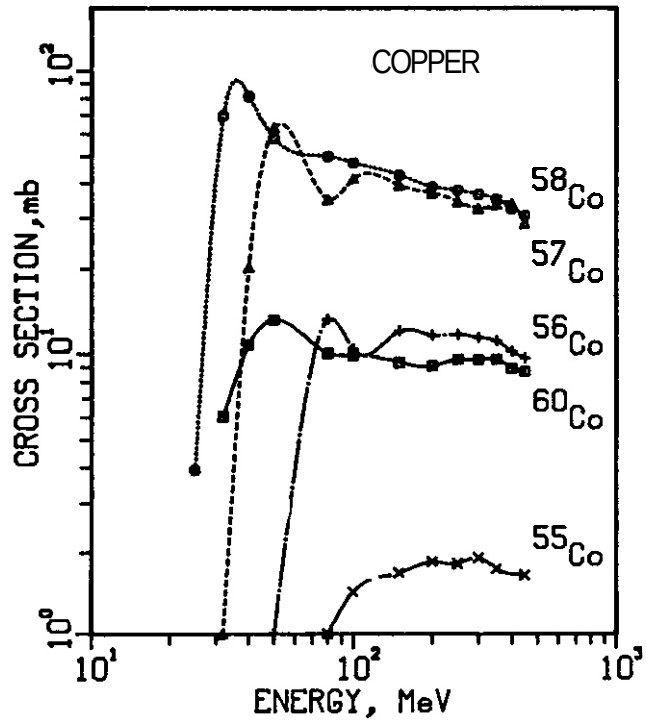

Fig. 2. Spallation cross sections are shown from Cu to various Co radioisotopes.

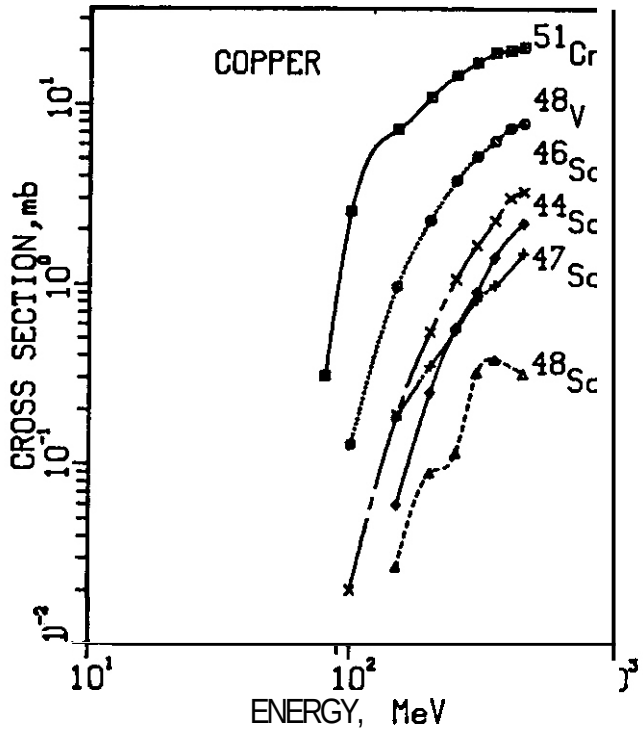

Fig. 3. Spallation cross sections are shown from Cu to Sc, V, and Cr radioisotopes.

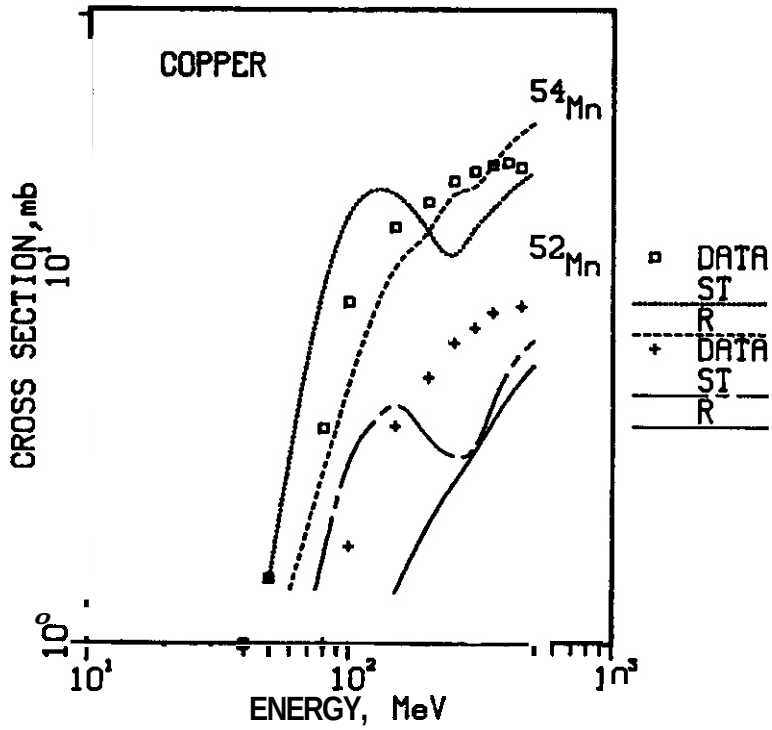

Fig. 4. Spallation cross sections are shown from Cu to ^{52}Mn to ^{54}Mn. The curves are calculated using the model of Rudstam (Ref. 4) and the model of Silberberg and Tsao (Ref. 5). Neither model adequately predicts the cross section.

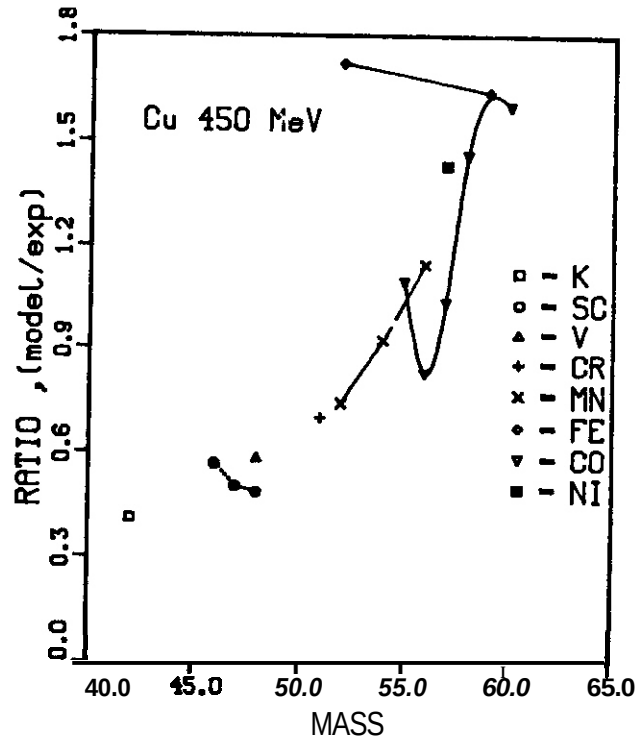

Fig. 5. The ratio of the predicted spallation cross-sections at 450 MeV to our measured values is shown as a function of mass. Ideally, this ratio should be equal to 1. Clearly, the model of Silberberg and Tsao (Ref. 5) does not predict this dependence correctly. The Rudstam model (Ref. 4) also shows a similar behavior.

Sone preliminary testing of spallation cross sections for spectral adjustment has already been done at IPNS and LPMPF. The Al data reported previously[1] and some Fe data [6] has been used to extend several cross sections to 800 MeV. In particular, measurements of the Al reactions to ^{7}Be and ^{22}Na and the Fe reactions to ^{51}Cr and ^{54}Mn appear to agree reasonably well with neutronics calculations at both facilities. An adjusted spectrum at LPMPF is shown in Figure 6. This data is now being written up for publication (see section 8.0) and presentation at the Williamsburg conference in June.

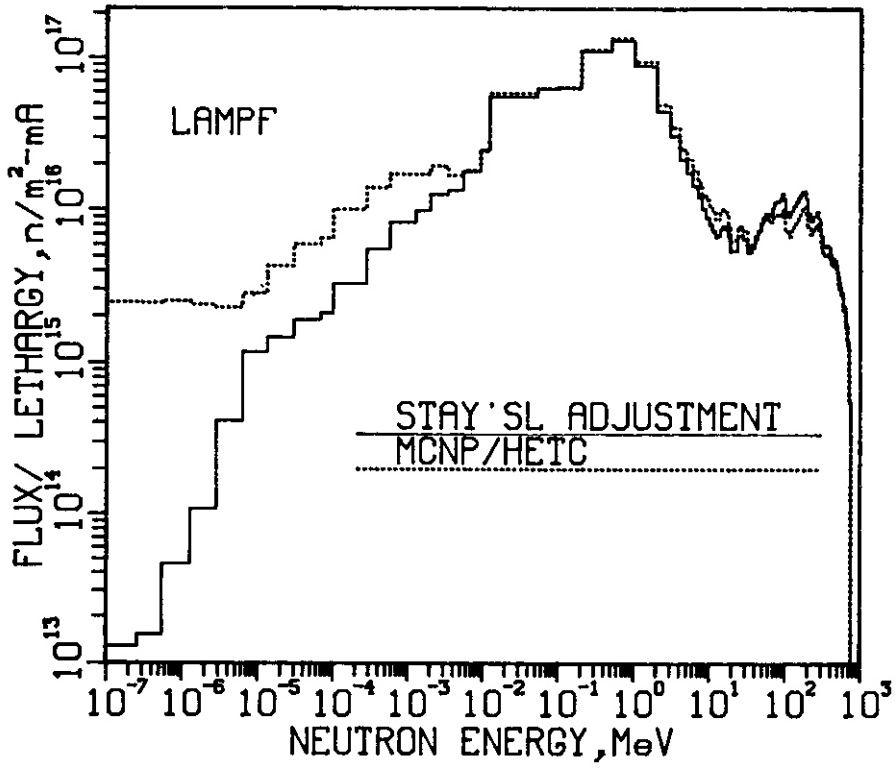

Fig. 6. The adjusted neutron spectrum from STAY'SL for the LPMPF radiation effects facility is compared with neutronics calculations using the MCNP and HETC computer codes. Note that adjustments are now being made up to 800 MeV using our new spallation cross sections.

6.0 References

1. L. R. Greenwood and R. K. Smither, Measurement of Spallation Cross Sections at IPNS, Oamage Analysis and Fundamental Studies Quarterly Progress Report, DOE/ER-0046/14, pp. 19-24, 1983.

2. J. Tobailern, et al., Cross Sections of the Nuclear Reactions Induced by Protons, Deuterons, and Alpha Particles, CEA-N1466 (1971).

3. E. Gadioli, Nuovo Cim. 22A, pp. 547-558S (1974).

4. G. Rudstam, Z. Naturforsch., 21A, 1027 (1966).

5. R. Silberberg and C. H. Tsao, Astrophysical Journal Suppl. 25, pp. 315-367, (1973). (Parameters updated in succeeding International Cosmic Ray Conference Proceedings).

6. R. Michel and R. Stuck, Proceedings of the Fourteenth Lunar and Planetary Science Conference, Part 2, Jour. Geophysical Research 89, B673-B684, (1984).

7.0 Future Work

These spallation cross sections are now being tested for application at IPNS and LRMPF. They will also be evaluated for application at FMIT for measuring the weak neutron flux between 30-55 MeV.

8.0 Publications

Two papers have been submitted for publication in the Proceedings of the 12th International Symposium on the Effects of Radiation on Materials, Williamsburg, VA, 18-20 June 1984.

1. Measured Radiation Environment at the LRMPF Irradiation Facility, O. R. Davidson, R. C. Reedy, W. F. Sommer, and L. R. Greenwood.

2. The Calculation of Radiation Damage Parameters for the LAMPF Irradiation Facility, D. R. Davidson, W. F. Sommer, M. S. Wechsler, and L. R. Greenwood.

HELIUM GENERATION MEASUREMENTS FOR Ti AND Cu FROM ORR

B. M. Oliver, D. W. Kneff, and R. P. Skowronski (Rockwell International)

1.0 Objective

The objectives of this work are to apply helium accumulation neutron dosimetry to the measurement of neutron fluences and energy spectra in mixed-spectrum fission reactors utilized for fusion materials testing, and to measure helium generation rates of materials in these irradiation environments.

2.0 Summary

Helium generation measurements have been made for Ti and Cu samples irradiated in the Oak Ridge Research Reactor (ORR) experiment MFE4A2. The results are significantly different from helium generation predictions based on ENDF/B-V cross section evaluations, providing evidence that the ENDF/B-V files for helium generation in Ti and Cu require revision for fission reactor neutron spectra. Similar discrepancies have previously been observed in analyses of samples irradiated in the Experimental Breeder Reactor-II (EBR-II). Measurements were also made using platinum-encapsulated samples to test helium retention in Ti, Cu, and Fe in the severe ORR irradiation environment. Preliminary results show less than 1% loss from iron, but losses of ~3.5% and ~6% from Ti and Cu, respectively.

3.0 *Program*

Title: Helium Generation in Fusion Reactor Materials
Principal Investigators: D. W. Kneff and H. Farrar IV
Affiliation: Rockwell International

4.0 Relevant DAFS Program Plan Task/Subtask

Task II.A.1	Fission Reactor Dosimetry
Task II.A.4	Gas Generation Rates
Subtask II.A.5.1	Helium Accumulation Monitor Development

5.0 Accomplishments and Status

Helium generation measurements have been performed for Ti and Cu samples irradiated in ORR as part of experiment MFE4A2, and helium-retention measurements have been made for a set of platinum-encapsulated Fe, Ti, and Cu samples also irradiated in this experiment. These measurements are part of a joint Rockwell-Argonne National Laboratory (ANL) program to measure total helium production rates over the range of fission reactor neutron spectra and fluences used for fusion materials testing, and to use the results to integrally test helium production cross section evaluations used in damage calculations. The present results extend the measurements recently reported for nickel samples from nine different materials irradiations,[1] iron samples from ORR-MFE4A2 and EBR-II,[2] and Ti and Cu samples from EBR-II.[2]

The analyzed Ti and Cu samples from ORR experiment MFE4A2 (MFE4A, over the irradiation period June 12, 1580 to April 26, 1982) were incorporated in that experiment as bare wire segments for both helium accumulation and radiometric dosimetry measurements. These samples are listed in Column 1 of Table 1. The sample number designates the ANL dosimetry tube in which each sample was placed. After irradiation, the activated samples were radiometrically counted at ANL and then returned to Rockwell. At Rockwell they were etched,

TABLE 1

HELIUM PRODUCTION MEASUREMENTS FOR TITANIUM AND COPPER IRRADIATED IN ORR-MFE4A2

Sample	Irradiation Location		^{4}He Concentration		
	z[a] (cm)	Radius	Measured[b] (appm)[c]	Calculated[d] (appm)[c]	Calculated / Measured
Ti-5	-4.22	inner	1.20	2.75	2.29
Ti-8	-4.22	outer	1.27	2.94	2.31
Ti-4	-12.62	outer	1.23	2.90	2.36
Ti-1	-12.78	inner	1.17	2.71	2.32
Cu-5	-5.40	inner	2.14	1.31	0.61
Cu-8	-5.41	outer	2.29	1.38	0.60
Cu-4	-13.82	outer	2.15	1.30	0.60
Cu-1	-13.97	inner	1.99	1.22	0.61

(a) Distance above core midplane
(b) Preliminary values, based on preliminary corrections for helium loss during irradiation (see text). Concentration uncertainties are ~±5%
(c) Atomic parts per million (10^{-6} atom fraction)
(d) Based on calculations by L. R. Greenwood (Ref. 4; see text) using ENDF/B-V

to remove all possible surface effects of helium recoil, and then segmented and analyzed by high-sensitivity gas mass spectrometry[3] for their irradiation-generated helium concentrations. Multiple specimens were analyzed for each sample location, with good reproducibility. The absolute uncertainty in each helium analysis was ±1-2%.

One sample of each material was also analyzed for ^{3}He, which can be formed from the decay of tritium often found in reactor environments. The 3He concentration in each case was measured to be about 1 appb (10^{-9} atom fraction).

The MFE4A2 experiment also included a set of Fe, Ti, and Cu samples vacuum-encapsulated within miniature platinum capsules. Analysis of these samples was initiated to test helium retention within the samples themselves under the high-temperature irradiation conditions in ORR. Five capsules were sheared within the mass spectrometer system and the helium release from the samples into the capsule void was measured. The capsule helium release was then compared with the helium release from the other bare wire samples to get a preliminary estimate of the fractional helium loss. The results indicate that the iron released less than 1% of its helium during irradiation, but that the Ti and Cu samples released ~3.5% and ~6%, respectively. The fractional helium release is variable, introducing an estimated ±5% uncertainty in the final measured sample helium concentrations. These results compared the helium release from unetched, encapsulated wire samples with the helium remaining in etched samples from nearby locations. Further measurements will be made for the helium remaining in the unetched samples themselves, to determine whether the etching removes some of the effect. If so, the actual helium loss from the measured samples will be less than quoted, and the final 4He concentrations will be adjusted accordingly.

The measured helium concentrations for the ORR-irradiated Ti and Cu samples are given in Column 4 of Table 1. They have been corrected for helium loss during irradiation, and have estimated uncertainties of about 25%. We consider these results to be preliminary, because further analyses are in progress to refine the helium loss measurements.

Column 5 of Table 1 gives the predicted helium concentrations in the analyzed samples, based on helium production cross section evaluations from the ENDF/B-V General Purpose File. These predictions were derived from L. R. Greenwood's calculations for the maximum-exposure core-height location (-5.84 cm) for MFE4A2.[4] Those calculations were used as an estimate for the Ti-5 and Cu-5 irradiation positions. This estimate introduces negligible uncertainty, because of the small neutron fluence gradients.[4] Predictions for the other sample locations were calculated from the maximum-exposure values using the ratios of the ^{46}Ti(n,p) and ^{63}Cu(n,α) reaction rates in the different Ti and Cu samples, respectively, as measured by Greenwood.[4]

Comparisons between the measured and calculated helium concentrations in the Ti and Cu samples show large discrepancies. The titanium predictions are about 230% high, while the copper predictions are about 40% low. These comparisons are similar to the results obtained previously for Ti and Cu samples from EBR-II

experiment X287, for which the Ti and Cu predictions were -270% high and -40% low, respectively.[2] The present comparisons provide further evidence that the ENDF/B-V files for helium generation in Ti and Cu need significant revision for fission reactor neutron spectra.

6.0 References

1. D. W. Kneff, R. P. Skowronski, B. M. Oliver, and L. R. Greenwood, "A Comparison of Measured and Calculated Helium Production in Nickel for Fission Reactor Irradiations," in Damage Analysis and Fundamental Studies, Quarterly Progress Report July-September 1983, DOE/ER-0046/15, U.S. Department of Energy, 12 (1983).

2. B. M. Oliver, D. W. Kneff, and R. P. Skowronski, "Helium Generation Measurements for EBR-II and ORR," in Damage Analysis and Fundamental Studies, Quarterly Progress Report January-March 1984, DOE/ER-0046/17, U.S. Department of Energy (1984).

3. H. Farrar IV, W. N. McElroy, and E. P. Lippincott, "Helium Production Cross Section of Boron for Fast-Reactor Neutron Spectra," Nucl. Technol., 25, 305 (1975).

4. L. R. Greenwood, "Dosimetry and Damage Analysis for the MFE4A Spectral Tailoring Experiment in ORR," in Damage Analysis and Fundamental Studies, Quarterly Progress Report October-December 1982, DOE/ER-0046/12, U.S. Department of Energy, 14 (1983).

7.0 Future Work

Helium measurements and integral cross section testing are continuing, in a joint effort with ANL. This work includes the analysis of several materials that have been, and will be, incorporated in a number of different experiments in ORR and HFIR (High Flux Isotopes Reactor). The goals of this work are the accurate prediction of helium generation in materials irradiation experiments and the further development of helium accumulation fluence monitors for stable-product neutron dosimetry.

8.0 Publications

None.

CHAPTER 3

REDUCED ACTIVATION MATERIALS

ACTIVATION OF SEVERAL OXIDES

D. G. Doran, F. M. Mann, and H. L. Heinisch (Hanford Engineering Development Laboratory)

1.0 Objective

Oxides are used as dispersion hardening agents in alloys. The purpose of this work was to examine several candidate oxides for compatibility with the goal of reducing the activation of fusion reactor materials to meet shallow burial criteria.

2.0 *Summary*

The activation of MgO, BeO, Y_2O_3, Al_2O_3, and CaO was estimated for a 10 MW-y/m^2 irradiation at a STARFIRE first wall position. At the concentrations used for dispersion hardening, none of the oxides would, in themselves, cause an alloy to exceed shallow burial limits.

3.0 Program

Title: Irradiation Effects Analysis
Principal Investigator: D. G. Doran
Affiliation: Hanford Engineering Development Laboratory

4.0 Relevant Program Plan Task/Subtask

No tasks on reduced activation were identified in the original OAFS program plan.

5.0 Accomplishments and Status

5.1 Introduction

Estimates have been made of the activation of the five oxides listed in Table 1. Following Mann[1], the reference irradiation condition was 10 MW-y/m^2 at a STARFIRE first wall position, i.e., 2.8 years at 3.6 MW/m^2. Mann has calculated activities for all the elements of interest except Ca and Y, using the code REAC[2]. For the present work, the necessary cross sections for Ca and Y were estimated using the code THRESH[3] and BNL 325[4].

It is assumed that the relevant regulat'on governing near-surface land disposal of low level radioactive waste is 10CFR61, issued early in 1983.' This regulation defines classes of wastes in terms of stability and half-life. Class C is the most active waste that meets the criteria for shallow land burial. A period of 500 years is permitted for Class C waste to decay to a level that is not an unacceptable hazard to an intruder. This regulation permits activities higher by a factor of 10 for certain radionuclides if they are in the form of an activated metal. We have assumed that this credit is applicable also to the oxides. Estimated Class C limits are given in Table 2.

5.2 Oxygen

^{14}C is produced by two reactions,

$$^{17}O(n,\alpha)^{14}C \qquad 83\% \qquad \text{and}$$

$$^{18}O(n,n\alpha)^{14}C \qquad 17\%,$$

resulting in the reported 26 Ci/m^3 for oxygen (at liquid density]. There are also several multi-step reactions that produce ^{14}C; the most important are

$$^{16}O(n,\alpha)^{13}C(n,\gamma)^{14}C, \quad \text{and}$$

$$^{16}O(n,d)^{15}N(n,d)^{14}C.$$

At 10 MW-y/m^2, they contribute about 10 % of the total activity of 29 Ci/m^3. Since the production rate for these two-stage reactions increases as the square of the fluence, their proportionate contribution will increase at higher doses.

The 10CFR61 Class C limit for ^{14}C contained in an activated metal is 80 Ci/m^3.

5.3 Beryllium

Mann found that the reaction $^{9}Be(n,\gamma)^{10}Be$ produced 1.5 Ci/m^3 (metal). Kennedy[6] has estimated the Class C limit for ^{10}Be to be 7000 Ci/m^3 for an activated metal.

5.4 Magnesium

^{22}Na is produced by the $^{24}Mg(n,t)$ reaction, but because its halflife is only 2.6 years it is not of concern for waste management.

5.5 Aluminum

Long-term activity from Al, due to ^{26}Al, is 56 Ci/m^3(metal) according to Mann. (Preliminary analysis of a new measurement of the $^{27}Al(n,2n)^{26}Al$ cross section suggests that the currently used cross section, hence the calculated activity, is too high.) Kennedy's[6] estimated Class C limit for ^{26}Al as an activated metal is 20 Ci/m^3.

5.6 Calcium

Two long-lived isotopes are produced by the irradiation of Ca:

$$^{42}Ca(n,\alpha)^{39}Ar$$

$$^{40}Ca(n,p)^{40}K.$$

The activity of ^{39}Ar is estimated to be about 800 Ci/m^3 and that of ^{40}K about 0.05 Ci/m^3. The latter value is about 40 times the activity of natural potassium. No limit is given in 10CFR61 for either of these isotopes. We suggest that the limit for K, which is readily ingested into the body, would be equivalent to that for ^{137}Cs and ^{90}Sr. The limits for both the latter are such that the activity after 500 years would be 0.05 Ci/m^3. Since the half-life of ^{40}K is essentially infinite, we have assumed a limit of 0.05 Ci/m^3. We find no convincing rationale for setting a limit for ^{39}Ar, but estimate a value of the order of 1000 Ci/m^3 by comparison with other values in 10CFR61. The values in Table 2 reflect a factor of 10 credit for the waste form as an activated metal.

5.7 Yttrium

This work was stimulated initially by a concern that an excessive amount of ^{90}Sr would be produced in yttrium through the two-stage reactions:

$^{89}Y(n,p)^{89}Sr(n,\gamma)^{90}Sr$ and

$^{89}Y(n,\gamma)^{90}Y(n,p)^{90}Sr.$

Estimated upper limits on the activities are about 300 Ci/m^3 from the first reaction and about 4 Ci/m^3 from the second. The Class C limit for ^{90}Sr is 7000 Ci/m^3.

5.8 Conclusions

The results of this exercise are summarized in Tables 1 and 2. Only the aluminum and calcium oxides exceed the assumed Class C limits at 10 MW-y/m^2; all the oxides would at 40 MW-y/m^2. At the Concentrations used for dispersion hardening, none of the oxides would, in themselves, cause an alloy to exceed the limit. They must be included, however, along with all the radioisotopes in an alloy, in a "sum of fractions rule" to determine if the alloy meets Class C limits.

These results are of course applicable to any application of an oxide in or near a reactor first wall. The production of ^{14}C from oxygen is sufficiently high at 10 MW-y/m^2 to limit the permissible activation of any component that might contain or be associated with an oxide in a reactor component, if that component is to meet Class C waste criteria.

6.0 References

1. F. M. Mann, "Reduced Activation Calculations for the STARFIRE First Wall," Hanford Engineering Development Laboratory Report HEDL-TME 83-27, Oct., 1983. (An abbreviated version has been accepted for publication in Fusion Technology.)

2. F. M. Mann, "Transmutation of Alloys in MFE Facilities as Calculated by REAC," Hanford Engineering Development Laboratory Report HEDL-TME 81-31, Aug. 1982.

3. S. Pearlstein, "Nuclear Cross Sections and Their Uncertainties Obtained from Nuclear Systematics," Proceedings of a Conf. on Nuclear Cross Sections and Technology, CONF-75-11469, Wash. D.C., Mar. 1915.

4. D. I. Garber and R. R. Kinsey, "Neutron Cross Sections", BNL-325, Third Edition, Jan. 1976.

5. Code of Federal Regulations, "Licensing Requirements for Land Disposal of Radioactive Waste," Title 10, Part 61, Nucl. Reg. Comm., Wash. D.C., Jan. 10, 1983.

6. W. E. Kennedy, Jr. and R. A. Peloquin, "Potential Low-Level Waste Disposal Limits for Activation Products from Fusion," Battelle-Pacific Northwest Laboratory Report PNL-4844, Sept. 1983.

7. R. K. Smither and L. R. Greenwood, "Measurement of the $^{27}Al(n,2n)^{26}Al$ Cross Section Near Threshold," Damage Analysis and Fundamental Studies Quarterly Progress Report DOE/ER-0046/13, Vol. 1, May 1983.

7.0 Future Work

Further work specifically on the activation of oxides is not planned, but work on evaluating limits is included in an ongoing program on reduced activation.

8.0 Publications

None planned.

TABLE 1

ESTIMATED ACTIVATION OF SEVERAL OXIDES AFTER 10 MW-Y/M^2 AT A STARFIRE FIRST WALL LOCATION

MATERIAL	DENSITY g/cm^3	ACTIVATION Ci/m3 Oxide		CLASS C LIMIT Ci/m^3	
		O	M	O	M
MgO	3.7	40	-	80	-
BeO	3	50	1	80	7000
Y_2O_3	5	30	300	EO	70000
Al_2O_3	4	50	45	EO	20
CaO	3.4	25		80	
^{39}Ar		1300		10000	
^{40}K		0.05		0.5	

TABLE 2

PRINCIPAL ISOTOPES

ISOTOPE	HALF-LIFE (YEARS)	GAMNA EMITTER?	EST. CLASS C LIMIT (Ci/m^3) VALUE	SOURCE
^{14}C	5700	no	EO	10CFR61
^{10}Be	1.6(6)*	no	7000	Ref. 6
^{90}Sr	29	no	70000**	10CFR61
^{26}Al	7.3(5)	yes	20	Ref. 6
^{39}Ar	269	no	10000	Authors' est.
^{40}K	1.3(9)	yes	0.5	Authors' est.

* 1.6 x 10^6

** Assumes a factor of 10 credit above 10CFR61 value because waste form is an "activated metal".

THE EFFECTS OF SUBSTITUTIONAL ALLOYING ELEMENTS IN AN Fe-10Cr FERRITIC ALLOY

D. S. Gelles and W. L. Beem (Hanford Engineering Development Laboratory)

1.0 Objective

The object of this effort is to determine the effects of substitutional alloying elements in an Fe-10Cr base composition on microstructural development due to neutron irradiation. The alloying elements selected are of interest in reduced activation applications and include a wide range of atom sizes.

2.0

In order to determine the effect of minor element additions on microstructural development due to fast neutron irradiation, a series of 12 alloys has been prepared for irradiation in MOTA 1C. The alloy series involves additions of Si, Mn, V, W, Ta, and Zr to form alloys of Fe-10Cr-0.1M and Fe-10Cr-1M (where M designates the alloying addition).

3.0 Program

Title: Irradiation Effects Analysis (AKJ)
Principal Investigator: D. A. Doran
Affiliation: Westinghouse Hanford Company

4.0 Relevant OAFS Program Plan Task/Subtask

Task II.C.1 Effects of Material Parameters on Microstructure

5.0 Accomplishments and Status

5.1 Introduction

Martensitic stainless steels have been identified as a potential alloy class for low activation alloy development[1]. A martensitic stainless steel satisfying a low activation requirement[2] would differ from comnercially available steels because additions of niobium, molybdenum and nickel must be limited. The major consequence to alloy design is the removal of molybdenum, a universally used solid solution hardening element. Possible alloying substitutes are vanadium, tantalum and tungsten[1]. The present effort is intended to provide a fundamental series of alloys which can be used to investigate effects of solid solution hardening elements in a base composition, Fe-10Cr, similar to that of commercial martensitic stainless steels.

In addition to vanadium, tantalum and tungsten, silicon and zirconium were included in order to determine effects of atom misfit on behavior and manganese was included because it can be used as an alloying element in substitution for nickel to control phase stability in martensitic stainless steels[3]. The atomic sizes of these elements in comparison with iron and chromium are given in Table 1. (The misfit for molybdenum is 0.0968.)

The purpose of this investigation is to determine if these substitutional alloying additions have major consequences on microstructure and properties following fast neutron irradiation. Such a determination will provide not only fundamental information on solute segregation and phase stability in a ferritic base

TABLE 1

ATOMIC SIZE COMPARISON OF ALLOYING ELEMENTS USED IN THIS INVESTIGATION[4]

Element	Atomic Number	Atomic Weight	Atomic Radius	Misfit $\left(\frac{r_M - r_{Fe}}{r_{Fe}}\right)$
Fe	26	55.8	1.24	---
Cr	24	52.0	1.25	0.0081
Si	14	28.1	1.17	-0.0565
Mn	25	54.9	1.23 - 1.48	-0.0081 - 0.1935
V	23	50.9	1.31	0.0565
W	74	183.9	1.37	0.1048
Ta	73	180.9	1.43	0.1532
Zr	40	91.2	1.58 - 1.61	0.2742 - 0.2984

alloy,, but also will generate fundamental alloying information of use in the design of low activation martensitic stainless steels. Two levels of alloy additions have been prepared, 0.1 wt.% and 1.0 wt.%, in order to study effects both in dilute and moderately concentrated alloys.

5.2 Experimental Procedure

175 gram buttons of each of the twelve alloys listed in Table 2 were made by standard arc melting techniques using commercially pure starting materials (Fe-99.95%, Cr-99.5% with Fe-0.35% max, Mn-99.7%, Si-98.0%, V-99.85%, W-99%, Ta-99.9% and Zr-98%. The buttons were rod shaped, ~1 cm in diameter by ~5 cm in length. All buttons were homogenized at 1250°C for 2 hours and then were cold rolled. Rolliny was accomplished in two steps (to 0.25 cm and to 0.03 cm) with one intermediate anneal (700°C for 0.5 hours). Following specimen fabrication the final heat treatment given was 1040°C for one hour, air cooled plus 760°C for 2 hours, air cooled (which duplicates procedures used in a related alloy series[5]).

TABLE 2

ALLOY COMPOSITIONS (wt%)

Alloy	Composition	Engraving Code
R117	Fe-10Cr-0.1Si	R9
R118	Fe-10Cr-1.0Si	AH
R119	Fe-10Cr-0.1Mn	AU
R120	Fe-10Cr-1.0Mn	AX
R121	Fe-10Cr-0.1V	AZ
R122	Fe-10Cr-1.0V	A1
R123	Fe-10Cr-0.1W	A3
R124	Fe-10Cr-1.0W	A4
R125	Fe-10Cr-0.1 Ta	A5
R126	Fe-10Cr-1.0Ta	A6
R127	Fe-10Cr-0.1Zr	A7
R128	Fe-10Cr-1.0Zr	A9

5.3 Results

Alloys were successfully manufactured and fabricated into 0.03 cm thick sheet for each of the compositions listed in Table 2. Specimen disks 0.3 cm in diameter were punched from the sheet, engraved with a four digit composition and irradiation history code and given a final heat treatment. Five specimens of each of the alloys were then loaded into identical packets for irradiation in MOTA 1C at four irradiation temperatures. Irradiation conditions are summarized in Table 3.

TABLE 3

PLANNED MOTA IRRADIATIONS OF THE SUBSTITUTIONAL FERRITIC ALLOY SERIES

Packet Code	Temperature (°C)	Dose (dpa)
KX	370	6
K2	370	18
K1	420	30
K3	420	90
K4	500	30
K5	500	60
K9	500	90
K6	600	30
K7	600	90

5.4 Discussion

It is anticipated that the substitutional alloying elements selected for investigation will provide an optimum series to determine solute behavior in an irradiation environment with regard to low activation alloy development. The phenomena of concern are solute segregation and irradiation induced or enhanced precipitation and their consequences on void and dislocation evolution. Each of the elements selected is expected to have negligible radioactivity 100 years after irradiation in a fusion reactor and each is expected to remain in solid solution (at least at levels of 1% or below) during long term thermal aging. Three of the six, Mn, V, and W, are commonly used as alloying elements in commercial martensitic stainless steels, one is a common impurity, Si, and the remaining two are infrequently added. As noted in Table 1, a wide range of atom misfits is covered by the alloy series and therefore it should be possible to generalize the results to a wide range of solute additions.

5.5 Conclusions

A series of 12 alloys of the type Fe-10Cr-0.1 or 1.0M have been prepared having substitutional alloying elements (M) Si, Mn, V, W, Ta and Zr. Those alloys are now being irradiated in FFTF MOTA IC at 370, 420, 500 and 600°C.

5.6 Expected Accomplishments in the Next Reporting Period

Irradiated specimens will not be available before June 1985, at which time this effort will be continued.

6.0 References

1. D.S. Gelles, H.R. Brager and F.A. Garner, "Reduced Activation Activities," Damage Analysis and Fundamental Studies Quarterly Progress Report, DOE/ER-0046/16, October-December 1984, p. 17.

2. F.M. Mann, "Activation of Components of a Fusion Alloy," ibid, DOE/ER-0046/13, January-March 1983, p. 63.

3. F.B. Pickering, Physical Metallurgy and the Design of Steels, (Applied Science Publishers Ltd., London, 1978), p. 166.

4. L.V. Azaroff, Introduction to Solids, (McGraw-Hill Book Co., Inc., N.Y., 1960), p. 441.

5. D.S. Gelles, "Microstructural Examination of Neutron Irradiation Simple Ferritic Alloys," J. Nucl. Mater. 108 & 109, (1983), p. 515.

CHAPTER 4

FUNDAMENTAL MECHANICAL BEHAVIOR

RELATING BUBBLE SIZE TO THE FAILURE MODE OF NEUTRON- AND HELIUM-IRRADIATED AUSTENITIC STAINLESS STEEL

R. D. Gerke and W. A. Jesser (University of Virginia)

1.0 Objective

The objective of this effort is to investigate the effect of small helium bubbles in causing intergrarular failure in austenitic stainless steel.

2.0 *Summary*

Helium irradiated type *316* microtensile specimens containing tiny bubbles were tensile tested at 250°C and 450°C under rapid and slow strain rates. Mixed mode failure occurred under all conditions suggesting strain rate insensitive microstructures are possible. These results support previous work suggesting that dynamic interaction between clusters of helium and dislocations occur at high temperatures to finely distribute helium-vacancy clusters at the grain boundary and initiate intergranular failure. These results show that it is also possible to establish a fine distribution of tiny bubbles by cold injection of helium and thereby cause intergranular failure at low temperatures (<450°C).

3.0 Program

Title: Simulating the CTR Environment in the HVEM
Principal Investigators: W. A. Jesser and R. A. Johnson
Affiliation: University of Virginia

4.0 Relevant DAFS Program Plan Task/subtask

Subtask II.C.13 Effects of Helium and Displacements on Crack Initiation and Propagation.

5.0 Accomplishments and Status

A unified helium embrittlement mechanism has not emerged due to discrepancies between experiment ard theory. It seems likely that the embrittlement is associated with helium accumulation along grain boundaries under the influence of applied stress. Many helium embrittlement theories treat the number density of helium filled cavities on the grain boundaries as a criterion for brittle failure. The presence of large grain boundary bubbles has been suggested as the cause for high temperature embrittlement through grain boundary weakening [1]. The character of grain boundary bubbles has been investigated in an attempt to characterize certain microstructural aspects of the helium bubbles with temperature and their relationship to intergranular failure. Microstructural parameters which have been of primary interest are grain boundary area fractional coverage by helium bubbles, α_R, [2,3,4] and pressure in grain boundary bubbles, p. [2,3-5]. Bennetch and Jesser showed strong evidence that α_R and p are not critical parameters for the onset of brittle fracture in neutron irradiated and helium ion irradiated austenitic stainless steel [3]. Specimens fracturing intergranularly could exhibit a range of α_R and p values thus indicating that the parameters do not adequately describe the conditions for embrittlement. In certain cases, helium filled cavities have served to increase specimen ductility. Grain boundary bubble spacing versus tensile test temperature has been shown to be an important parameter. This graph has shown helium embrittlement to be a thermally activated process in austenitic stainless steels [3]. A graph of edge to edge (grain boundary) bubble spacing, L, plctted against tensile test temperature reveals a fracture 'map' indicating regions of transgranular and intergranular failure separated by a J-shaped boundary of mixed mode failure, as schematically shown in figure 1. There are two distinctly different fracture behaviors represented in the L versus T graph, one temperature independent (T<550°C) for small bubble spacings and one temperature dependent (T>550°C) for. large bubble spacing, which define the onset of intergranular failure. It should be noted that a plot of d versus T closely parallels the 'J' shape of figure 1 since d is probably not independent of L. There are

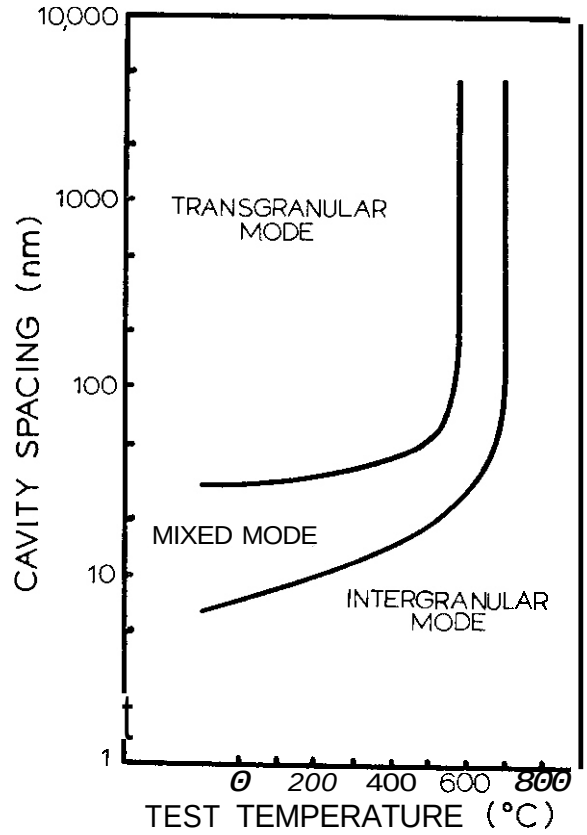

Figure 1 - Schematic Plot of Cavity Spacing versus Tensile Test Temperature for Neutron and Helium Irradiated Austenitic Stainless Steel (after Bennetch and Jesser [3]).

critical values of $L \leq 30$ nm and correspondingly $d \leq 4$ nm for which the onset of brittle fracture occurs. At temperatures below 550°C cleavage cracks dominated the transgranular failure mode which suggested that extremely close packed small bubbles can embrittle solids by acting as effective dislocation obstacles [3]. In the temperature dependent region of the 'J' curve helium embrittlement was shown to be a function of only temperature for cavity spacings ranging over two orders of magnitude (~30 nm to >3000 nm). Temperatures below 550°C resulted in transgranular failure, mixed mode failure occurred between 550°C and 700°C while an intergranular mode of failure occurred for all test temperatures above 700°C. Another important variable which assists in the promotion of intergranular fracture in irradiated specimens is strain rate. At intermediate strain rates, tensile tests reveal fracture behavior depicted by the 'J' curve. However, austenitic stainless steels containing as little as 20 appm helium tested at slow strain rates and high temperatures ($T \geq 700$°C) failed intergranularly while similar specimens tested at fast strain rates failed transgranularly [2,8]. Bubble dragging by dislocations has been invoked to explain these results. In a recent DAFS report [6] and elsewhere [7] attempts to relate the two fracture behaviors in the 'J' curve have been reported. The temperature dependent region may be related to the temperature independent region through a dynamic process requiring a sufficiently high temperature for high helium mobility and a sufficiently low strain rate (i.e, dislocation velocity) for dislocation dragging of very small helium-vacancy clusters. When these conditions are not met helium may aggregate in bubbles or may not be properly distributed at the grain boundary. In order to study the helium embrittlement phenomenon, Type 316 austenitic stainless steel foil specimens were helium ion irradiated and tensile tested in-situ in a high voltage electron microscope (HVEM). Failure mode was investigated with particular reference to its dependence on strain rate and temperature.

5.1 Experimental Results and Discussion

5.1.1 Experimental Procedure

As received type 316 Stainless Steel foil, 40 μm thick, was punched into rectangular microtensile specimens 12.5 mm X 2.5 mm in size. Next the central portion of each specimen was electropolished to perforation in a 90% acetic - 10% perchloric acid solution at room temperature. Specimens were they ion irradiated in an HVEM-ion accelerator facility [9]. Fluences of 9.4×10^{20} ions m^{-2} (flux = 3.9×10^{18} ions $m^{-2} s^{-1}$) were

produced using 80 keV helium ions and irradiation temperatures were estimated to be ~300°C. Because the helium deposition range is calculated to be 281.6 nm (assumed gaussion distribution with standard deviation of 77.9 nm) for 80 keV helium [10], irradiations were conducted on both sides of the foil microspecimens to increase the effect of helium on the fracture process. These irradiation conditions produced a microstructure in the temperature independent region of the mixed mode region of the 'J' curve (figure 1) just below the critical values for L and d ('30 nm and '4 nm respectively). Tensile testing in the HVEM was performed in a hydraulically operated single tilt quantitative lead-elongation tensile stage [11]. Specimens were tensile tested to failure at 250°C and 450°C at strain rates of ~10^{-4} S^{-1} and ~1 S^{-1}. During tensile testing HVEM observations (in the 10^{-4} S^{-1} tests) were recorded on still micrographs in order to obtain the type of failure. Ductility was determined primarily by the nature of the crack propagation through the specimen (in the slow strain rate experiments). If most of the cracks propagated transgranularly the specimen was said to fail in a ductile (T) mode. When grain boundary failure was observed the specimen was said to fail in a brittle intergranular (I) mode. Mixed mode failure (I and T) was observed in the HVEM observations. Fracture surfaces observed in a SEM were used to determine mode of failure in fast strain rate tensile tests where HVEM observations were not practical. In all experiments HVEM and SEM observations agreed with one another with respect to fracture mode.

5.1.2 Strain Rate Effects

Specimens containing bubbles and tensile tested at rapid strain rates have been shown to fail in a ductile transgranular mode for both bulk like [8] and thin foil type specimens [6,7]; while similar specimens tensile tested under slow strain rates yield primarily intergranular failure. Bubble dragging by dislocations has been used to explain this phenomenon [8,12]. However, brittle failure occurs in the temperature independent region of the 'J' curve where no visible bubbles exist. It seems that dislocations are active in the fracture process; however, the primary cause of embrittlement is felt to be the small clusters or atomistic helium [6,7]. The temperature dependent region (large bubbles) may be related to the temperature independent region by a dynamic condition set up by dislocations which actively bring small helium-vacancy clusters in solution to the grain boundary. In order to test this hypothesis under conditions of pre-existing small bubbles of very high number density, the fracture mode was observed for specimens, microstructurally in the temperature independent region of the 'J' curve, tested at rapid and slow strain rates. The result? at 250°C appear to be that strain rate has no effect on fracture mode (in the range $\dot{\varepsilon}$ = 10^{-4} S^{-1} - ~1 S^{-1}). At the slightly higher temperature of 450°C rapid straining also has minimal effect. There is no noticeable effect of strain rate in the temperature independent region of the 'J' where small bubbles and clusters of helium dominate the irradiation produced microstructure. These results are very different from results of tensile tests performed on specimens containing large bubbles. This obvious difference in the sensitivity of fracture behavior to strain rate tends to support the idea suggested earlier that dislocations dynamically set up the condition at the grain boundary that is present in the bottom of the 'J' curve in specimens containing large bubbles at high temperatures [6,7]. Specimens exhibiting this fine microstructure due to irradiation would be insensitive to strain rate because the proper conditions for intergranular failure already exist.

5.1.3 Mixed Mode Failure and Critical Strain Rate

The sweeping of helium to grain boundaries by dislocations is considered to be dominant in causing high temperature helium embrittlement. Strain rate (and dislocation velocity) as a function of temperature can be used to predict the onset of brittle behavior (i.e. mixed mode) by calculating critical conditions for which the helium (in bubble or atomistic form) may be transported by dislocations. A model for dislocations sweeping helium bubbles to grain boundaries as a function of temperature and strain rate has been proposed by Motsumoto et al. [8]. In this model a bubble velocity v is calculated from the relationship

$$v = D_B \mu b^2 \cos\phi / kT \qquad (1)$$

here μ is the average shear modulus, b the Burgers vector, ϕ the half angle subtended by the dislocation at the bubble ($\mu b^2 \cos\phi$ represents the bubble dragging force), k the Boltzmann constant, T the absolute temperature and D_B the diffusivity of the bubble.
The strain rate of a specimen in which helium bubbles are swept along by dislocations is then determine? by

$$\dot{\varepsilon} = \rho b v \qquad (2)$$

where ρ is the density of active dislocations. When ρ is considered to be on the order of ~10^{10}-10^{11} cm^{-2} (typical for a deformed crystal), $\dot{\varepsilon}$ is calculated to be in agreement with experimental results. This model would seem to explain high temperature helium embrittlement in specimens with bubbles visible by TEM but does not attempt to explain embrittlement of specimens without bubbles. This latter case corresponds to brittle behavior depicted by the region at the bottom of the 'J' curve in figure 1.
There are numerous examples of helium embrittlement occurring in austenitic stainless steel without the presence of visible bubbles (less than ~2 nm) [2,13-16]. The above observations tend to strongly suggest

that small clusters or atomistic helium play an important role in the promotion of intergranular failure in austenitic steels.

Reduction of ductility caused by atomistic hydrogen has been extensively studied for years. A kinetic model has been developed to explain the transport of hydrogen as Cottrell atmospheres on dislocations [17-19]. The model is developed in a similar manner to the one developed by Matsumoto et al. [8] for dislocations sweeping helium bubbles to grain boundaries. In this model atoms are bound to dislocations and considered to move with them as a cloud or atmosphere. The atmospheres can then be deposited at various interfaces (primarily grain boundaries). When a critical dislocation velocity, v_c, is exceeded the dislocation can break away from the atmosphere. For the atmosphere transport to occur $\dot{\varepsilon} < \dot{\varepsilon}_c$ where $\dot{\varepsilon}_c$ is a critical strain rate. The critical velocity is estimated by

$$v_c = \frac{D \quad E_B}{kT \quad 30b} \tag{3}$$

where D is the diffusivity, k the Boltzmann constant, T the absolute temperature, E_B the binding energy of the gas atom to a dislocation and b the burgers vector (30 b is the interaction distance). The value for v_c is then used to determined $\dot{\varepsilon}_c$ by substituting v_c from equation 3 for v in equation 2. The result is

$$\dot{\varepsilon}_c = \frac{\rho D E_B}{30kT} \tag{4}$$

which was derived earlier [17]. Equation 4 may be evaluated for atomistic helium to predict intergranular failure behavior as a function of tensile test temperature and strain rate. When a critical strain rate at or near $\dot{\varepsilon}_c$ is selected, inhomogeneities in the localized dislocation density likely establish regions where the active dislocations exceed the critical velocity v while other regions exhibit dislocation velocities below v_c. This condition corresponds to a mixed mode Failure behavior. If the test conditions are not near $\dot{\varepsilon}_c$, such variations in dislocation density and correspondingly dislocation velocity do not attain the critical velocity v and no mixed mode failure is observed.
No attempt is made here to evaluate equation 4 because of the lack of reliable data for some of the necessary parameters. However, it is possible to select reasonable values of the parameters to yield the experimentally observed $\dot{\varepsilon}_c$.

5.1.4 Uislocation - Helium Interactions

It is anticipated that dislocations can accumulate atomistic helium atmospheres by two mechanisms: 1) interaction with overpressurized bubbles and 2) by cutting through existing helium bubbles. Dislocations may strip helium atoms from overpressurized bubbles due to the effectively negative binding energy the bubble may have for (excess) helium atoms. This event is thought to occur even though the binding energy of a helium atom to a dislocation is quoted by Trinkhaus to be only a few tenths of an eV and is thought not to be significant at high temperatures [20]. A high density of dislocations intersecting and cutting a helium bubble in three dimensions i.e. though multiple slip systems being active is thought to produce helium clusters and possibly atomistic helium which in turn may become an atmosphere around the dislocation. The result of this 'chopping' of bubbles is observed in the pulled out ligaments in a fracture surface where the ligaments accommodating a localized high density of dislocations are free of bubbles [21]. When dislocations bring large numbers of helium atoms to the grain boundaries it is not likely that de-cohesion is acting as the mechanism for the embrittlement because specimens tensile tested at this facility irradiated to over 10,000 appm helium (and fractured below 550°C) failed transgranularly [10]. In such high helium experiments, one might expect to exceed any critical concentration of lattice helium for intergranular failure unless large, benign bubbles contained almost all of the helium.

5.2 Conclusions

High temperature helium embrittlement seems to require a set of kinetic conditions. It is consequently proposed that helium embrittlement is largely the result of a dynamic condition set up as a consequence of competition between strain rate (dislocation velocity) and test temperature (helium mobility). Moving dislocations may drag or 'sweep' atomistic helium in solution or small helium-vacancy clusters to such sinks as (large) helium bubbles and grain boundaries. Helium in solution may interact with dislocations as atmospheres and can move with the dislocation and contribute to intergranular failure as long as a critical dislocation velocity, v_c, (i.e. a critical strain rate, $\dot{\varepsilon}_c$) for a particular temperature is not exceeded. Mixed mode failure is tfierefore expected when the critical conditions for v_c and $\dot{\varepsilon}_c$ are established at test temperature T due to the fact that these conditions correspond to the intergranular-transgranular transition. Equations which relate strain rate and dislocation velocity to describe intergranular failure at a particular test temperature should focus attention on this critical condition. Intergranular failure may

also be initiated by the presence of a fine distribution of helium without the dynamic assistance from dislocations when the irradiated microstructure corresponds to that of the temperature independent region of the 'J' curve. Microstructures such as these already contain the necessary fine distribution of helium necessary for embrittlement. Under these conditions intergranular failure is possible at low temperatures (below about 550°C) and is strain rate insensitive.

6.0 References

1. R. S. Barnes, Nature, 206, 1965, 1307.

2. A. A. Sagues, H. Schroeder, W. Kesternich, and H. Ullmaier, Journal of Nuclear Materials, 78, 1978, 289.

3. J. I. Bennetch and W. A. Jesser, Journal of Nuclear Materials, 103 and 104, 1981, 809.

4. H. Trinkhaus and H. Ullmaier, Journal of Nuclear Materials, 85 and 86, 1979, 823.

5. D. Hull and D. E. Rimmer, Philosophical Magazine, 4, 1969, 673.

6. R. D. Gerke and W. A. Jesser, "Relations Among Tensile Test Temperature and Strain Rate in the Fracture of He-Irradiated Type 316 Stainless Steel," DAFS Quarterly Report DOE/ER-0046/17, May 1984.

7. R. D. Gerke and W. A. Jesser, "Fracture in Helium-Irradiated Type 316 Stainless Steel Micro-Tensile Specimens," presented at the 12th International Symposium on the Effects of Radiation on Materials, Williamsburg, VA, 1984. To be published in ASTM.

8. K. Matsumoto, T. Katooka, M. Terasawa, M. Shinada, S. Nakahigashi, H. Sakairi and E. Yagi, Journal of Nuclear Materials, 67, 1977, 97.

9. W. A. Jesser, J. A. Horton, and L. L. Scribner, Radiation Effects, 29, 1976, 79.

10. J. I. Bennetch, "Microstructural Aspects of Helium Embrittlement in Stainless Steel," Doctoral Dissertation, University of Virginia, Charlottesville, VA, 1981.

11. R. D. Gerke and W. A. Jesser, Journal of Nuclear Materials, 117, 1983, 320.

12. J. O. Smith and B. Russell, Journal of Nuclear Materials, 37, 1970, 96.

13. D. E. Rawl, Jr., G. R. Caskey, Jr., and J. A. Donavan, Journal of Metals, 31, 1979, 124.

14. R. E. Clausing, E. E. Bloom, "Grain Boundaries in Engineering Materials," Claitor's Publishing Division, 1975, 491.

15. J. I. Bennetch and W. A. Jesser, "Microstructural Aspects of Helium Embrittlement," DAFS Quarterly Report DOE/ER-0046/4, Jan. 1981.

16. J. I. Bennetch and W. A. Jesser, "Room Temperature Helium Embrittlement in 316 Type Stainless Steel," DAFS Quarterly Report DOE/ER-0046/3, Oct. 1980.

17. J. K. Tien, A. W. Thompson, I. M. Bernstein and R. J. Richards, Metallurgical Transactions A, 7A, 1976, 821.

18. S. V. Nair, R. R. Jensen, and J. K. Tien, Metallurgical Transactions A, 14A, 1983, 385.

19. J. K. Tien, and R. J. Richards, Scripta Metallurgica, 9, 1975, 1097.

20. H. Trinkhaus, Journal of Nuclear Materials, 118, 198, 39.

21. J. A. Horton, "HVEM Studies of Helium Embrittlement in Stainless Steel," Doctoral Dissertation, University of Virginia, Charlottesville, VA, 1980.

FUNDAMENTAL FLOW AND FRACTURE STUDIES OF HT-9

G.R. Odette, G.E. Lucas, R. Maiti and J.W. Sheckherd (University of California, Santa Barbara)

1.0 Objectives

The objectives of this effort are to investigate the microstructure-property-property relationships dictating lower shelf fracture toughness of HT-9 and to determine the appropriate procedures for estimating fracture loads in martensitic stainless steel structures containing pre-existing flaws.

2.0 *Summary*

Results of electron microscopy studies of cleavage crack formation and propagation in HT-9 are consistent with a model for stress-controlled cleavage in which the critical stress σ_f^* is related to the lath packet size. Moreover, σ_f^* appears to undergo a sharp transition at low temperaturef and high strain rates; this is probably a result of a change in mechanism from slip- to twinning-nucleated cleavage. This change in σ_f^* effects corresponding changes in lower shelf fracture toughness. A simple two-parameter approach is shown to be a reasonable basis for predicting fracture loads for various size and crack-geometry bend specimens. These results indicated that cleavage fracture will occur near plastic collapse loads for thin wall structures containing shallow surface cracks. Further, results of an initial study of ductility in the cleavage regime indicate deflectional displacements on the order of 1-2 cm/m will be the limit for such shallow surface cracks in thin walls. Finally, the effects of dissolved hydrogen and stress state variations induced by side grooving were investigated. Hydrogen charges resulted in an average reduction in measured K_Q values of about 17% and 5% in the ratio of maximum load fracture-to-collapse stress ratios. No significant effect of hydrogen on ductility was observed. Side grooving resulted in increases in both apparent K_Q toughness levels and fracture-to-collapse stress ratios. Side grooving decreased ductility for shallow cracks and increased it for deep cracks. However, in general these effects are judged to be relatively modest compared to uncertainties in the measurements and the effects of significant variations in size and strength levels.

3.0 Program

Title: Damage Analysis and Fundamental Studies for Fusion Reactor Materials Development

Principle Investigators: G.R. Odette and G.E. Lucas

Affiliation: University of California, Santa Barbara

4.0 Relevant OAFS Program Plan Task/Subtask

Subtask B Mechanical Properties

5.0 Accomplishments and Status

5.1 Introduction

The martensitic/ferritic stainless steel alloy class has many attractive features as a candidate fusion structural alloy. However, the potential for increased temperature delineating the ductile-brittle fracture mode transition induced by irradiation has been identified as a major problem to be resolved for this alloy

class. In a previous analysis' it was suggested that the increase in transition temperature would be largely irrelevant if it could be demonstrated that actual fusion structures can be reliably operated in the lower shelf toughness, cleavage fracture regime. Such demonstration requires that: 1) irradiation and other environmental factors do not significantly degrade lower shelf toughness; and 2) fracture occurs at loads beyond those associated with large-scale plastic deformation -- i.e., general yield. The response of lower shelf toughness to service conditions depends on both the effects of the environment on the alloys' microstructure and microchemistry and the basic mechanism of cleavage fracture. The critical load at initiation of cleavage fracture depends on not only the microscopically-dictated material state (e.g., toughness and strength) but also on the macroscopic mechanisms as controlled by size and flaw-structure-loading geometry.

Experience with low alloy pressure vessel steels, in which cleavage is stress controlled, shows that irradiation at typical light water reactor end-of-life conditions (about 0.1 dpa at 300°C) has little or no effect on lower shelf toughness. This is consistent with the fine-scale damage (~ 1 nm) induced by such irradiation conditions; this microstructure does not perturb the pre-existing microstructural features on the size scale 1-100 μm which control cleavage fracture. It has also be shown[2] that cleavage fracture in HT-9 is stress controlled and can be modeled by the Ritchie, Knott and Rice (RKR) critical stress-critical distance criteria.[3] Further, it was found that the critical microcleavage fracture stress (σ_f^*) and critical distance (l^*) parameters for HT-9 were consistent with behavior observed in other tempered bainitic/martensitic steels. This suggests that there may be ways to optimize the microstructure of fusion alloys to increase values of lower shelf toughness.

There are, however, a number of remaining problems and questions relating to the micromechanics of cleavage fracture in HT-9. These include:

1) The effect of irradiation microstructure characteristic of fusion service conditions on the fracture parameters.

2) The effect of hydrogen on the fracture parameters

3) The effect of thermal segregation and precipitation, as perturbed by irradiation, on the fracture parameters.

4) The combined (synergistic) effects of items 1 to 3 above

5) A rigorous mechanistic model of the relation of microstructure to basic fracture parameters. The models developed to date have been only semiquantitative and largely phenomenological. Improved models would assist in both analysis of irradiation and other environmental effects data and in developing optimized alloy microstructures.

Based on information in the fracture mechanics literature and estimates of in-service properties, it was also previously shown[4] that thin fusion structures would probably fail by plastic collapse following general yield, rather than brittle fracture at loads below yield. This was postulated to be true even at lower shelt temperatures and conditions of large amounts of irradiation strengthening. Indeed, it was shown that under such conditions thin fusion structures would experience increased failure loads due to irradiation. This is, of course. in direct contrast to the behavior of thick-walled vessels which would manifest decreasing fracture loads for these circumstances.

The mechanics analysis described above was based largely on a simplified interpolation procedure for predicting the fracture loads for the range of conditions from fully-elastic to fully-plastic behavior. This so-called two-parameter procedure (TPP), which derives from a plane stress Bilby-Cottrell-Swinden crack field', requires only geometry, strength, and fully-elastic fracture toughness data to estimate fracture loads. The TPP specifically avoids the complications of elastic-plastic fracture mechanics (EPFM); however, EPFM may still be required to obtain valid fracture toughness data from small specimens.

This progress report describes work addressing a number of these issues. Specifically, transmission and scanning electron microscopy studies of crack formation and propagation mechanisms have been carried out in support of developing improved micromechanical cleavage fracture models. Further, the effect of loading (strain) rate on fracture parameters has been investigated along with a preliminary evaluation of the effect uf dissolved hydrogen. Applicability of the TPP was investigated using a range of specimen sizes and crack deptn to ligament ratios for sample three-point bend loading geometries. Further, the effect of stress-srate variations using side grooving was investigated. Finally, the effect of loading rate and hydrogen on the applicability of the TPP was evaluated along with their implications to micromechanical fracture mechanisms. All of these studies are for the MFE program heat of ESR HT-9 supplied by T. Lechtenberg of G A Technologies.

5.2 Macromechanics

5.2.1 The Applicability of the Two-Parameter Procedure to Predicting Fracture Loads of HT-9 Structures

In the initial study of the applicability of the TPP to fusion alloys and structures, a simple three-point bend geometry was chosen. In addition to the convenience of bend bars as standard test specimens and the ability to link the results to other studies in the literature, this geometry should provide the most conservative basis for estimating cleavage fracture loads.

The standard bend bar geometry is illustrated schematically in Figure 1a. Sizes range from B = .25 to 1 cm with nominal crack depth (a) to width (w) ratios a/w of about .05 to 0.9; the range of specimen dimensions is illustrated in Fig. 1b. The specimens were precracked from notches machined to various depths at a maximum ΔK from crack notch of 21 MPa$\sqrt{m}$. For both very deep (> .75 a/w) and shallow (< .25 a/w) cracks, the nearest surface was machined away after precracking to give the final nominal a/w ratio. The actual crack length was established subsequent to the testing using a 9-point averaging procedure on an optical microscope; in general, the actual crack lengths were within twenty percent of nominal specifications.

Tests were conducted at temperatures of -73 and -101°C (-100 to -150°F) and at nominal static displacement rates of .025 mm/s with equivalent nominal notch tip strain rates of 10 to 10^3 s[†] for 2.54 cm thick bend bars. For other sizes, the strain rate can be estimated by dividing these values by the specimen thickness in inches†. This range of strain rates is expected to account for uncertainties in converting data from displacement rates to appropriately averaged crack tip deformation rates. At these strain rates and temperatures, the yield stress increment above room temperature is about 75 to 175 MPa, and is about 175 to 275 MPa above the yield strength at 100°C. Hence, the conditions approximately represent a corresponding level of irradiation strengthening. In addition, tests of B ~ .5 cm specimens with a/w from .05 to 0.75 were conducted at similar displacement rates at room temperature. In this temperature regime, the fracture mode is ductile microvoid coalescence following gross plastic deformation. Therefore, these data were used to evaluate the collapse loads in a region of large-scale yielding.

The fracture stress was calculated from the maximum load determined from load displacement curves. Limited interrupted tests indicate that at temperatures in the cleavage regime there is relatively little stable crack growth; hence, the assumption of fracture initiation coincidence with maximum load seems justified. However, this assumption may not be valid in the room temperature ductile fracture regime.

In general, however, the maximum load collapse (= fracture) stress from room temperature tests approximately equaled a calculated collapse stress σ_c^c determined from the following equation given by Chell[8]

$$\sigma_c^c = 2.18\,\sigma_u\,(1 - a/w)^2 \qquad (1)$$

A comparison is given in Table 1. Values of the ultimate tensile strength used in eqn. (1) were measured in tensile tests, and were found to be σ_u(-101°C) = 918±20 MPa and σ_u(-73°C) = 862 ± 20 MPa. The largest deviation at low values of a/w (a/w ≤ .2) is about 10 percent. Indeed, as shown in Fig. 2, there appears to be a systematic reduction in the ratio of calculated to measured collapse load σ_c^c/σ_c^m with increasing a/w. As mentioned previously, this may be due to some stable crack growth at low a/w. However, the absolute amounts of crack growth would be small (< .05 mm); considering the difficulty in establishing crack lengths and other experimental uncertainties, these differences are not considered to be significant.

The data taken at lower temperatures are summarized in Table 2. All the specimens tested at low temperatures (less than about -50°C) showed a predominantly cleavage fracture morphology independent of the specific geometry temperature and strain rate. These data were analyzed quantitatively by comparing the ratio of experimental fracture to collapse stress to calculated stress ratios using the TPP as formulated by Chell.[6] Chell's expression is given by

$$\frac{\sigma_f}{\sigma_c} = \frac{2}{\pi}\cos^{-1}\left(\exp\left[-\frac{\pi K_{1c}^2}{8aY^2\,\sigma_c^2}\right]\right) \qquad (2)$$

† Notch tip strain rates reported here were determined by using the analysis of Server[19] as a lower limit and a simple crack opening model for an upper limit. These limits differ by an order of magnitude. and hence all strain rates are reported here as a range.

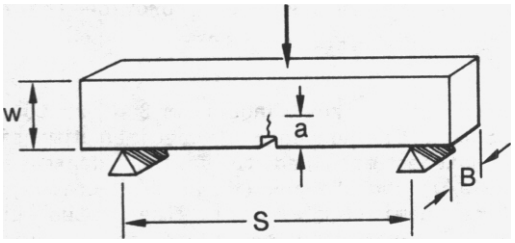

S = 4w
w = 2B

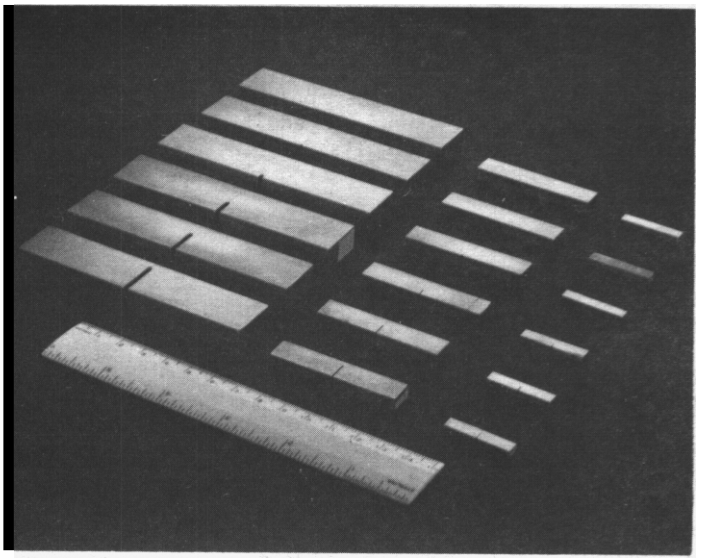

(a) (b)

Fig. 1. a) Schematic of bend bar geometry; and b) photograph illustrating the range of sizes.

Table 1

Collapse Stresses for E = .5 cm Bend Bar[a]

a/w	Collapse Stress (MPa) [b] Experimental ($6P_{max}/BW$)	Calculated $2.18\ \sigma_u(1-a/w)^2$
.054	1206	1360
,113	1048	1195
.247	766	862
.545	302	315
,740	103	103

(a) T = 25°C; $\dot{\varepsilon} \sim 5x10^{-3}/5x10^{-2}s^{-1}$; σ_u = 697 MPa

(b) By definition, the collapse stress is the elastic outer fiber stress in a bend bar which results in plastic collapse. The elastic fiber stress of a rectangular bar in a 3-point bend is given by Timoshenko[20] as 6P/BW. The predicted collapse stress is given by eqn. (1).

Here, K_{Ic} is the plane strain fracture toughness and Y is the bend bar compliance factor which is a function of a/w. The values of the fracture toughness were taken from previously-reported results[2] and were K_{Ic} (-101°C) of about 57 to 63 MPa$\sqrt{m}$ and K_{Ic} (-73°C) of about 65 to 68 MPa$\sqrt{m}$. The experimental ratio was defined as the measured maximum load fracture stress given in Table 2 divided by the calculated collapse stress using σ_u(-73°C) of 862 MPa and σ_u (-101°C) of 918 MPa.

Results of the comparison are shown in Figure 3. The cross-hatched regions represent the sensitivity of the calculated ratios to uncertainties in the input toughness parameter, K_{Ic}, and ultimate tensile strength. The experimental ratio due to uncertainties in crack length and ultimate tensile stress and variability in the maximum load are estimated to be of the order ± .1. Uncertainties at the smallest (< .1) and largest (> .9) a/w ratios are somewhat larger.

Overall, the agreement between the TPP predictions and experimental values is reasonably good. At a test temperature of -73°C (Figure 3a), agreement is somewhat better; experimental ratios falling both slightly above (B = 1 cm) and below (B = .5 and .25 cm) the calculated values at low a/w values (a/w ≤ .1 for B = .25 and .5; a/w ≤ .25 for B = 1.0). Clearly, the trends predicted by the TPP are observed in the experimental data and deviations are generally within the combined uncertainties in the calculated and experimental ratios. Note that the toughness values are not adjusted for the variations in strain rate at different sizes. This is consistent with constant value of lower shelf toughness independent of temperature and strain rate. However, as shown below at low temperatures and high rates, reductions in toughness occur. This would not affect the -73°C calculations. However, at -101°C, the calculated fracture-to-collapse loads would be somewhat reduced for the .25 cm and .5 cm bend bars, particularly the former (K_Q ~ 42 to 50 MPa$\sqrt{m}$ versus K_{Ic} = 57 MPa$\sqrt{m}$). This would result in somewhat better agreement at low a/w values and conservative predictions of fracture loads at higher values. These effects will be discussed explicitly in Section 5.3.3.

The possible design implications of the broad confirmation of the TPP results will be considered in detail elsewhere, but presentation of one example is useful. Consider a .25 cm thick wall containing a .05 cm crack which, due to irradiation, has manifested a large yield stress increase of about 300 MPa above the unirradiated value of 600 MPa; further, assume the alloy has also experienced a reduction in its lower shelf toughness from 50 MPa$\sqrt{m}$ to 35 MPa$\sqrt{m}$. Eased on TPP estimate, which appears to be slightly conservative, the load bearing capacity at fracture will increase by about 25% due to irradiation.

5.2.2 Stress State and Side Grooving Effects

For the standard bend bar geometry, the thickness B varies along with the width w (w = 2B). For small thicknesses, increasing loss of lateral (thickness) constraint corresponds to a transition from plane strain to plane stress state conditions. This transition normally results in increasing fracture loads and may, indeed, result in a fracture mode transition, viz. cleavage to microvoid coalescence. This is due to a reduction in the maximum (principal) tensile stress σ_{max}; for elastic-perfectly-plastic behavior, the reduction is about a factor of 3, i.e., from $\sigma_{max} \simeq 3\sigma_Y$ to $\sigma_{max} = \sigma_Y$. Standard testing requirements suggest that minimum size requirements for plane strain conditions are $B_{min} \simeq 2.5\ (K_{Ic}/a_Y)^2$; for the -73°C and -101°C testing conditions, this suggests B_{min} of about 2.5 cm and 1.5 cm, respectively. In practice, it is known that these size requirements are highly conservative. However, since the specimen thicknesses used in this study were in the range of only .25 to 1 cm, thickness effects may be significant.

In order to evaluate this possibility, a series of side-grooved $B_o \simeq 0.4$ cm bend bars with a/w ratios of about .05 to .9 were tested at a temperature of -101°C and at approximate notch tip strain rates of 6×10^{-2} to 6×10^{-2} s^{-1}. In addition, the effect of side grooving on ductile collapse stresses at a test temperature of 25°C was investigated.

Side grooves increase the lateral constraint and hence principle stress as a function of specimen-loading geometry, size, a/w, notch depth, flank angle and root radius, and the material properties. Unfortunately, there is no simple procedure available to quantify the overall effect. In general, in addition to increasing the triaxiality (plane strain character) of the stress state, side grooving enhances flat fracture, promotes fracture initiation and unstable crack growth at maximum load, and reduced shear lips. A variety of approaches could be used to study these effects. For example, a constant ligament thichness B and sample width could be maintained, with varying notch depth $(B_o - B)/2$. Alternately, the side groove flank angle could be varied.

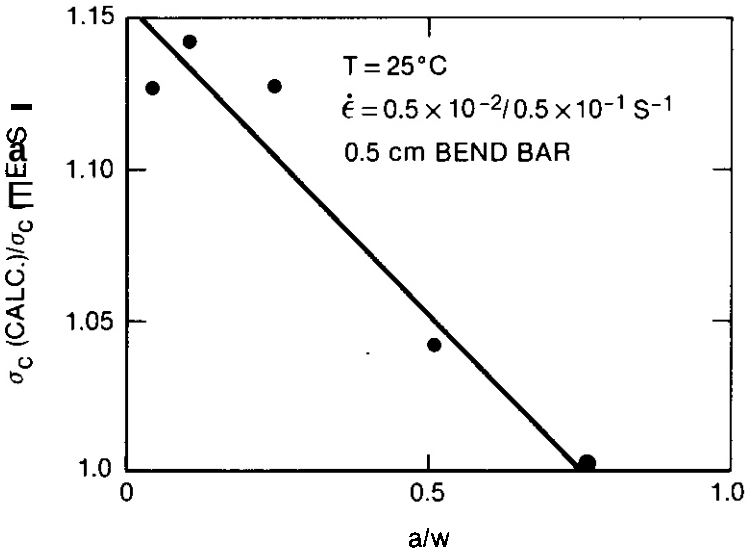

Fig. 2. Comparison of calculated to measured collapse stress with increasing a/w.

Table 2

Measured Maximum Load Bend Bar Fracture Stresses

B	Temperature -73°C -73°C		Temperature -101C	
(cm)	(a/w)	σ_f	(a/w)	σ_f
.25	,046	1570	,068	1329
.25	.106	1583	.089	1488
.25	,231	1852	.272	1418
.25	.532	1679	.958	1849
.25	.742	1776	--	--
.25	.725	1758	--	--
.25	.893	1751	--	--
.50	,061	1290	,068	1027
.50	.110	1319	.093	1007
.50	,274	1266	,249	1079
.50	.519	1428	.536	1228
.50	,553	1269	,506	1252
.50	,732	1618	,752	1636
50	,872	1956	.930	2079
1.00	,084	1172	,095	1060
1.00	.107	1114	.119	1059
1.00	.234	1026	,235	884
1.00	.530	1145	--	--
1.00	.775	1436	.759	1303
1.00	.913	1611	.936	1962

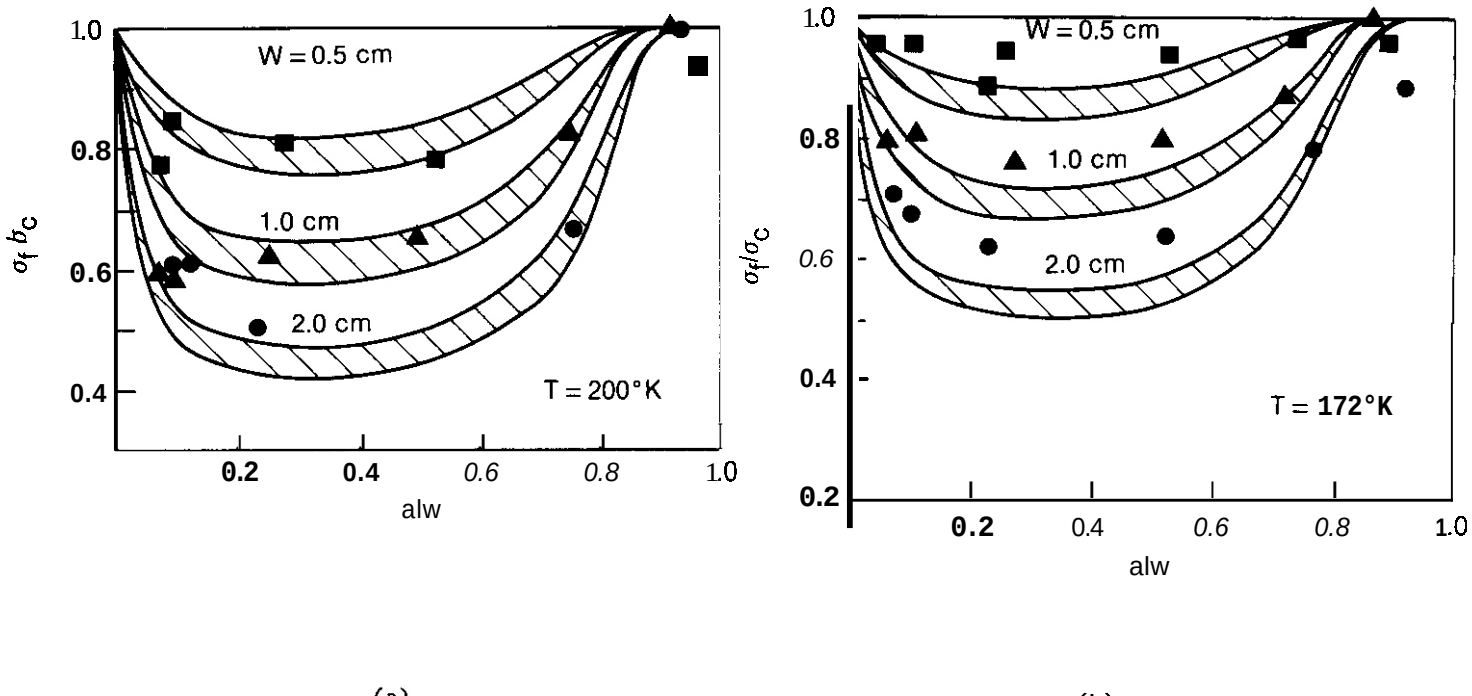

(a) (b)

Fig. 3. Comparison of measured values of σ_f/σ_c to values calculated with the TPP for a) -73°C and b) -101°C

Table 3

Collapse Stresses for Side-Grooved B = .4 cm Bend Bars(c)

a/w	% Side Groove	Collapse Stress (MPa)	
		Experimental	Calculated
.047	0.0	1255	1380
.100	0.0	1096	1232
,125	13.18	1124	1166
.128	15.81	1034	1159
.128	31.00	1145	1159
.227	0.0	807	910
.504	0.0	345	374
.528	9.80	323	338
.519	21.31	348	352
,532	37.37	328	324
.751	0.0	91	94
.767	11.37	81	83
.756	22.50	87	90
.763	36.81	88	85
,881	0.0	28	22

(c) Test temperature = 25°C;
Strain rate $\dot{\varepsilon}$ - $6x10^{-3}/6x10$-2s-1.

In this study, the side grooves were cut at a constant 45° flank angle with a root radius of .025 cm. The outside bar thickness B_o was kept constant at 0.4 cm while the actual ligament thickness B varied from 0.4 to 0.25 cm in three increments of .05 cm; viz. notching of 0%, 12.5%, 25% and 37.5%. The width of the specimens was kept at 0.8 cm. Other specimen fabrication and precracking procedures were constant with those discussed previously.

Table 3 summarizes the collapse test results for tests at 25°C. For specimens without side grooves, the results are consistent with the B = .5 cm data given in Table 2. The predicted collapse stresses agree with calculated values within about 10 to 15% with decreasing deviation with increasing a/w. Similar trends are observed in the side-grooved specimens but the deviations are somewhat smaller. These results are shown in Fig. 4. One explanation far these slight differences is that side grooving reduces stable crack growth at low a/w. Overall, the measured to calculated deviations are smaller in side-notched specimens and hence even less significant than for standard bend bars.

Values of toughness from the low temperature (-101°C) tests of the a/w ~ .5 bend bars are summarized in Table 4. The K_Q toughness is found to increase with increasing notch depth with minimum value for the normal bend bar geometry with no side notch. While the variations are not large, ranging from 41 to 52 MPaJm, they are systematic and go in the opposite direction anticipated. This may be due to a predominance of the effect of reduced ligament thickness over the influence of the notch itself. Alternatively, this may be related to effects on the specimen compliance coupled with the Secant procedure used to establish K_Q. Specifically, small specimens showing larger elastic-plastic compliance prior to cleavage initiation near maximum load would yield artificially low values of K_Q. Hence, additional tests with constant ligament thickness and with and without notches will be conducted in the future and on larger specimens.

Table 5 summarizes the experimental fracture-to-collapse load results for the side grooved specimens tested at -101°C for a/w ~ .1 to .9. Figure 5 compares the predictions of the TPP for nominal properties and a w = 0.8 cm bend bar with the experimental fracture-to-collapse stress ratios. The specimens without side grooves are systematically low by about 0.1. This is in contrast to the data for the w = 1 cm bars which are in good agreement with the TPP predictions except at low a/w ratios (~.1), where they are also low. Hence, these deviations are probably not significant, except for small crack depths where some systematic error in the TPP procedure may be indicated. As noted above, agreement would be better if possible effects of notch tip strain rate in reducing the lower shelf toughness were considered.

Figure 6 shows the fracture-to-collapse stress ratio plotted against percent side groove for nominal values of a/w of .l, .5 and .75. The indicated rate of increase is most rapid with the initial side grooving leveling off thereafter; the maximum increase is similar for various a/w values and is about 0.1 to 0.15. Indeed, this increase is relatively small. The B = .4 cm results can be compared to data from the larger B = 0.5 cm bend bar tests for similar conditions. For the smaller a/w, the B = 0.5 cm data is reasonably Consistent with the B = .4 cm data. However, if the B = .5 cm data are adjusted for the difference in size by an amount predicted by the TPP, they fall above the B = .4 cm data. The size corrected B = 5 cm data is also shown in Fig. 6. This would suggest a smaller effect of side grooving. For the high a/w ratio the B = .5 cm data indicate little or no effect of side grooving with or without size adjustment.

In summary, while there appears to be some systematic effects of side grooving, they are relatively small; if they are significant, it is primarily at small a/w ratios. Indeed, the apparently anomalous behavior of increasing toughness and fracture loads with increased side grooving may be a consequence of material variability and uncertainties and the effect of factors such as effective strain rate, or effects on specimen compliance factors. In this regard, we note that similar anomalous behavior in static toughness values measured with B = 2.5 cm bend bars in the temperature range of -60 to -90°C; these data fall significantly above (by ~ 7-20 MPaJm) a value measured with a smaller B = 1 cm specimen at -70°C. As noted above, stress state effects will be studied further with different specimen configurations and sizes.

5.2.3 Strain Rate Effects

Low strain rate, quasi static results may not apply to high strain rate loading conditions. Indeed, both strength increases and possible toughness reductions would result in more brittle behavior. Such dynamic rates might occur, for example, if someone were to drop a reactor component during a maintenance operation during cold shutdown. Therefore, fracture toughness tests on B = .5 cm thick bend bars were conducted from near static ($5x10^{-3}/10^{-2} s^{-1}$) to dynamic (above $10^2 s^{-1}$) strain rates at -101°C. Additional testing involved the following: a B = 1.0 cm bend bar was conducted at a strain rate of $3x10^{-3}/10^{-2} s^{-1}$ at -130°C; both Charpy-V-notch (CVN) and pre-cracked Charpy-V-notch (PCCV) specimens tested at -101°C at strain rates of 100 to $200 s^{-1}$ and 250 to $350 s^{-1}$, respectively; B = .4 cm at $6x10^{-3}/10^{-2}$; a B = 2.5 cm bend bar tested at liquid nitrogen temperature (T = -195°C) and static ($10^{-3}/10^{-2} s^{-1}$) strain rates. The latter was carried out to achieve cleavage fracture at very high values of yield strength. A strain rate temperature parameter $T \ln 10^{-8}/\dot{\varepsilon}$ parameter can be crudely used to estimate a strength equivalent strain rate for a temperature of

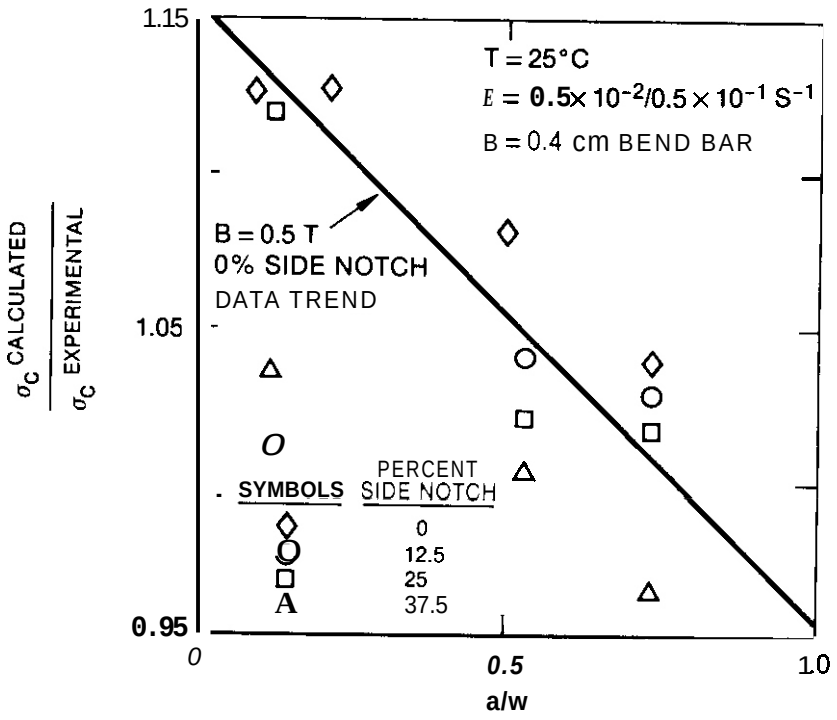

Fig. 4. Comparison of calculated to measured collapse stresses for side-grooved specimens.

% Side Groove	B (cm)	KQ (MPa√m)	P_M/P_Q	$2.5(K_Q/\sigma_y)^2$ (cm)
0	.41	**41**	**1.23**	**.79**
14.7	.35	**47**	**1.19**	1.02
26.6	**.30**	**44**	1.38	**.90**
37.6	.25	52	**1.19**	1.28

(d) Test temperature = -101°C;
Strain rate = $6x10^{-3}/6x10$-2s-1

Table 5

Measured Values of Fracture-to-Collapse Stress Ratios and Bend Ductilities for Side-Grooved Bend Bars[e]

a/w	% Side Groove	σ_f/σ_c	ε_B
,092	0.0	0.610	.0047
.100	0.0	0.636	.0040
,118	11.52	0. 718	.0020
.109	25.06	0.766	.0022
,136	37.31	0.774	.0010
.194	0.0	0.560	.0043
.529	0.0	0.683	.0030
.532	14.68	0.742	,0029
.527	26.62	0.806	,0031
.546	37.56	0.838	.0029
.749	0.0	0.748	,0028
.780	14.68	0.873	,0065
.759	26.18	0.881	.0043
.755	38.87	0.819	.0039
.907	0.0	0.878	,0022

(e) Test temperature T = -101°C;

Strain rate $\dot{\varepsilon} = 6\text{x}10^{-3}/6\text{x}10^{-2}\text{s}^{-1}$

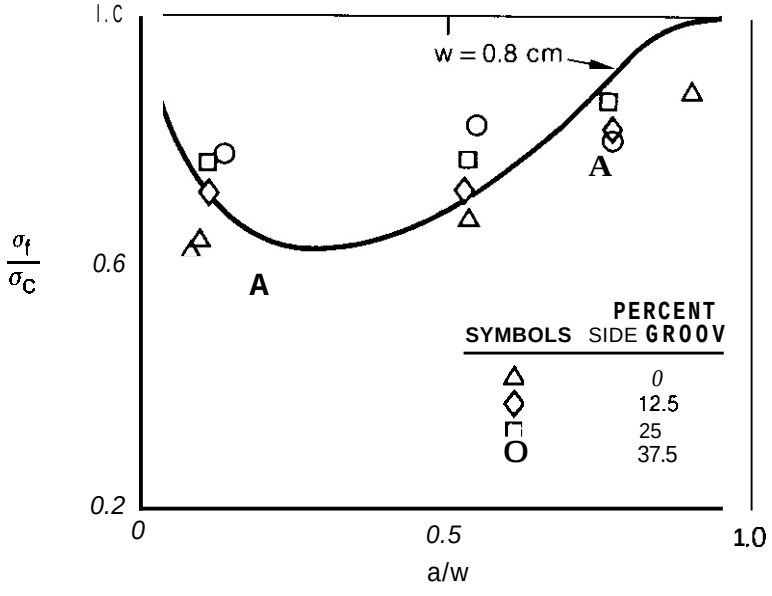

Fig. 5. Comparison of measured values of σ_f/σ_c to values calculated with the TPP for side-grooved specimens

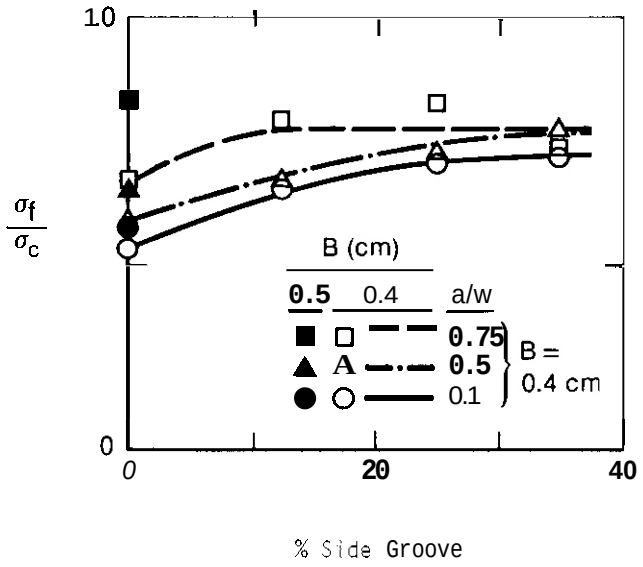

Fig. 6. Variation of σ_f/σ_c with percent side grooving and a/w

Table 6

Dynamic Toughness Data

Specimen Type	Specimen Thickness (cm)	Test Temperature (°C)	Strain Rate (s^{-1})	K_{1c}/K_{1d} (MPa$\sqrt{m}$
Bend bar	2.54	-101	$10^{-3}/10^{-2}$	57
Bend bar	.51	-101	$.5x10^{-2}/.5x10^{-1}$	44/50(h)
Bend bar	.51	-101	$10^{-1}/10^{0}$	34/44(h)
Bend bar	.51	-101	$10^{1}/10^{2}$	33
Bend bar	1.02	-130	$2.5x10^{-3}/2.5x10^{-2}$(g)	57(h)
Bend bar	1.02	-195	$2.5x10^{-3}/2.5x10^{-2}$(g)	30(h)
CVN	1.0	-150	100/200	38(i)
PCCV	1.0	-150	250/350	43

(g) Strength equivalent rate at -101°C is $.2/1.2s^{-1}$ for the -130°C test and $1900/5300s^{-1}$ for the -195°C test.

(h) K_Q

(i) Extrapolated, assuming ρ_o = .05 mm.

-73°C; the strength equivalent rate is about $130/350 s^{-1}$. The results are summarized in Table 6. It should be noted that because of measurement uncertainties in the PCCV results and the need to extrapolate the CVN point to a sharp crack geometry, these data points must be viewed as subject to considerable error.

Figure 7 plots toughness as a function of strain rates (including equivalent rates at -101°C), including data for B = .46 cm side-grooved specimens. The results suggest that there is a transition in toughness at a strain rate of about 10^{1} to $10^{0} s^{-1}$ from about 65 ± 5 to about 35 ± 8 MPaJm. The micromechanical implications of these results will be discussed below. With respect to assessing the influence of fusion structures, this suggests that strain rate effects on **both** strength and toughness must be considered in estimating fracture loads. Indeed, high rate loading conditions may result in a transition from irradiation-induced increases to decreases in fracture load.

This behavior is illustrated in Fig. 8 where the TPP predictions are compared to experimental measures of the fracture to collapse stresses for B = .5 cm bend bars with a/w = .5 and tested at -101°C at static to dynamic strain rates. Here both ultimate tensile stress and toughness values were taken for appropriate strain rates. The results indicate that the TPP is applicable at dynamic strain rates. orovided relevant dynamic material parameters are used. Further, Fig. 8 illustrates the substantial effect of strain rate in reducing fracture loads by about a factor of 2.

However, it should be noted that Eq. (2) shows that even for low toughness and high yield/ ultimate stress values, plastic collapse will occur at very small crack lengths. By eauating predicted failure loads this size is approximately given as

$$a_{min} \sim .5 \frac{K_{1c}^2}{\sigma_u^2} \qquad (3)$$

Hence, an irradiated steel with a high strength level of 1000 MPa and low toughness of 35 MPaJm containing shallow cracks of $\leq$ .06 cm would still fail only when loads in excess of those required for collapse occurred even in the "brittle" bend geometry.

5.2.4 Cleavage Fracture Ductility

In the lower shelf cleavage fracture regime, ductility is limited. Hence, this parameter, as well as maximum tolerable load, is an important factor in structural design. The most appropriate measure of ductility for the bend geometry is the plastic deflection at maximum load, d_p, divided by the half span length, S/2, i.e., $\varepsilon_B \sim \tan \theta = d_p/S/2$. This geometry is illustrated in Fig. 9. The static bend bar ε_B data are presented in Fig. 10 for temperatures of -73°C, -101°C and 25°C. Clearly, there is a specimen size and a/w effect as well as an effect of temperature. Increasing size leads to lower ductility; and ductility is minimum at intermediate ratios of a/w. Indeed, the overall pattern is similar to the fracture to collapse stress ratio. However, the sensitivity of the bend ductility parameter is much greater; indeed, the variation between B = .25 and 1 cm is a factor of 10; and the minimum ductility at intermediate a/w ratios is a factor of 5 to 10 below that for very short or long cracks, In general, the cleavage fracture ductilities are about a factor of 5 to 20 below ductile fracture limits.

For crack length to width ratios $\leq$ .5, we have found that the data can be crudely correlated by plotting the measured ductility times thickness $B\varepsilon_B$ versus the actual crack length, a. This is shown in Fig. 11. Here we have normalized the data at the two temperatures, by decreasing the ductility at -73°C by a factor of 3. The $B\varepsilon_B$ parameter decreases rapidly at low values of a leveling off at a ~ .15 to .25 cm. At -101°C the minimum bend ductility is $B\varepsilon_B \sim .0005/B$ (cm). At small crack sizes, (a < .3 cm) the bend ductility parameter can be represented approximately by the function

$$\varepsilon_B \sim .005 \exp(a/.32)/B \qquad (4)$$

For example, at -101°C for the w = 0.25 cm specimen and a 0.1 cm deep crack, a net bend ductility of .008 would be anticipated, while for a .025 cm :rack a ductility of about .018 would be predicted. These compare to eiastic strain limits of about .006 for these geometries. At -73°C the ductilities increase by a factur of about 2 to 4 (with an average of ~ 3). In contrast, the ductilities in the microvoid coalescence ductile fracture regime are about .04-.09 as determined from the room temperature tests on B = .5 cm bend bars described earlier.

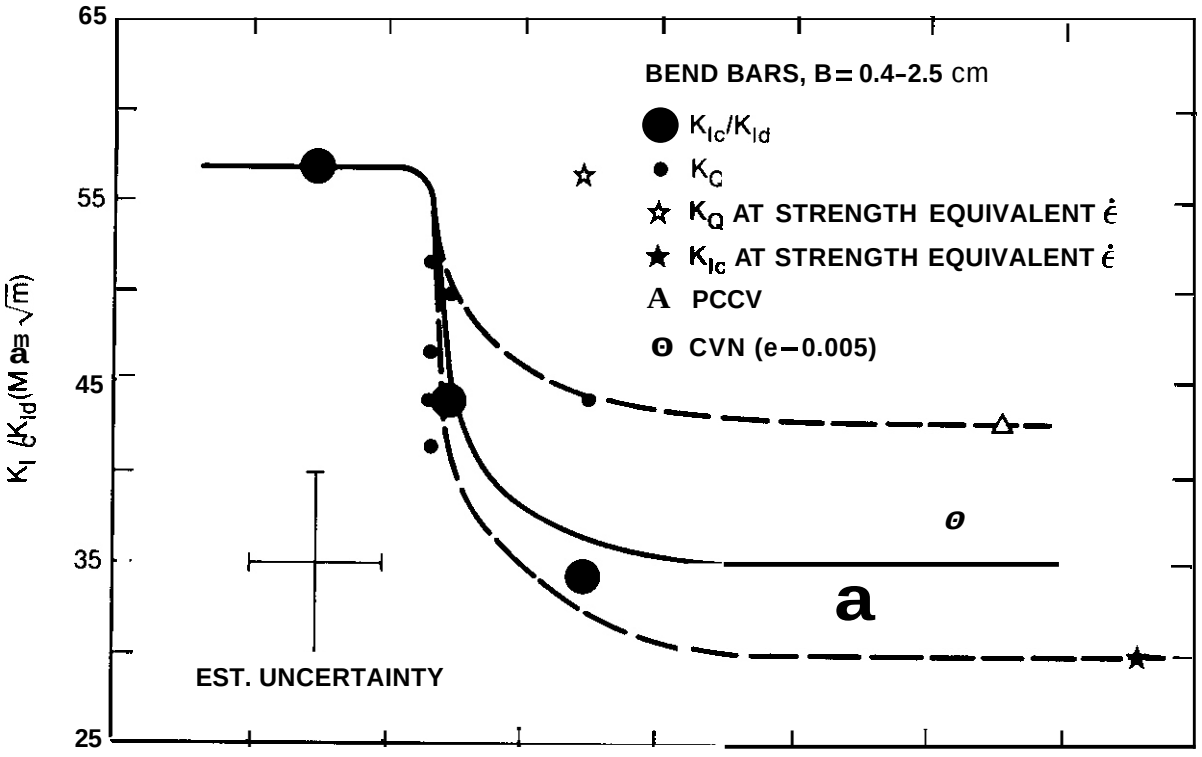
65
55
45
35
25
K_I (K_{Id}) (MPa$\sqrt{m}$)
BEND BARS, B = 0.4–2.5 cm
K_{Ic}/K_{Id}
K_C
K_Q AT STRENGTH EQUIVALENT $\dot{\epsilon}$
K_{Ic} AT STRENGTH EQUIVALENT $\dot{\epsilon}$
A PCCV
Θ CVN (e=0.005)
EST. UNCERTAINTY
a

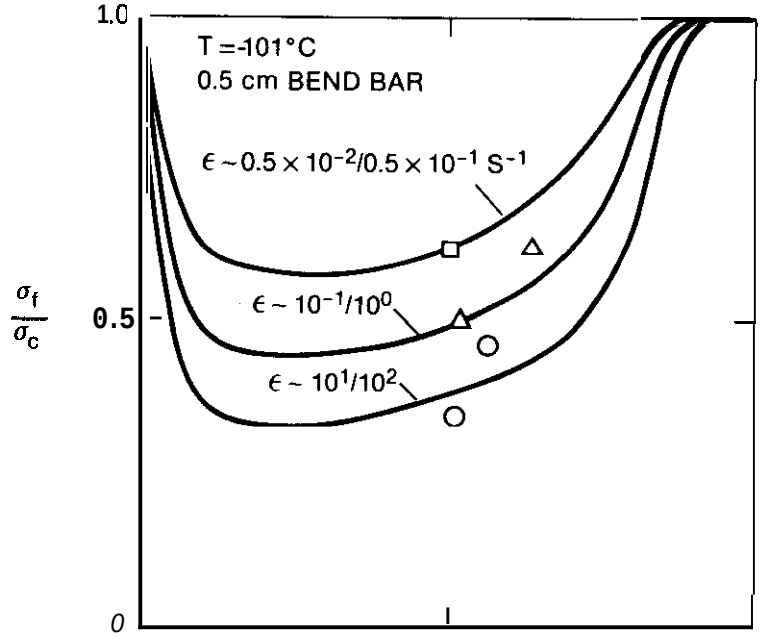
1.0
0.5
0
$\frac{\sigma_f}{\sigma_c}$
T = -101°C
0.5 cm BEND BAR
$\epsilon \sim 0.5 \times 10^{-2}/0.5 \times 10^{-1}$ S^{-1}
$\epsilon \sim 10^{-1}/10^{0}$
$\epsilon \sim 10^{1}/10^{2}$

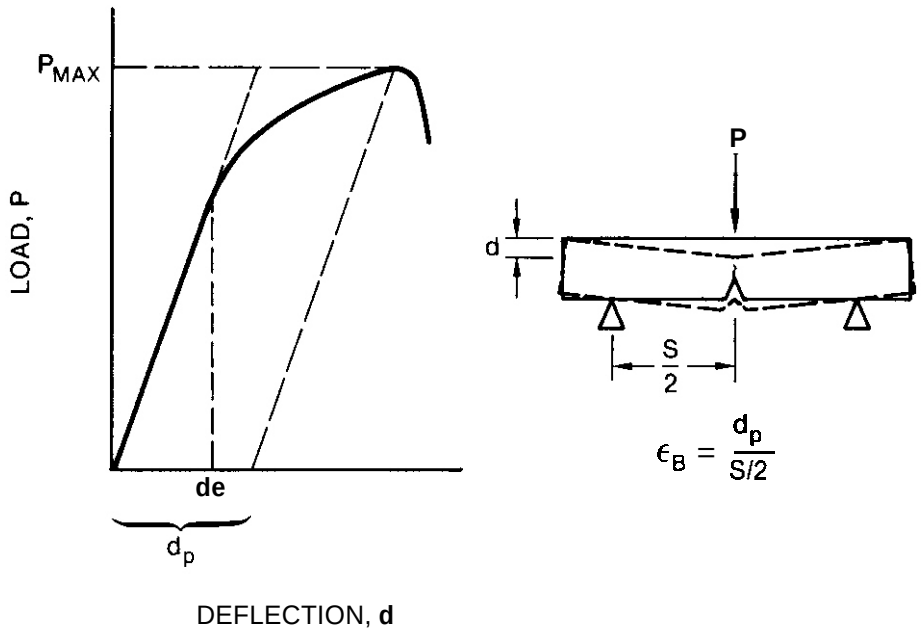

Fig. 9. Schematic illustration of the definition of bend ductility ε_B.

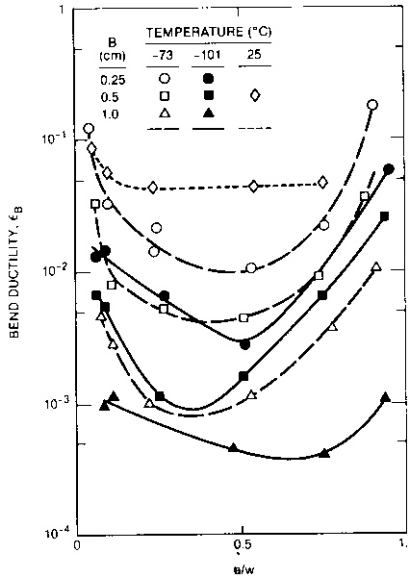

Fig. 10. Variation of ductility with a/w for three different temperatures and bend bars

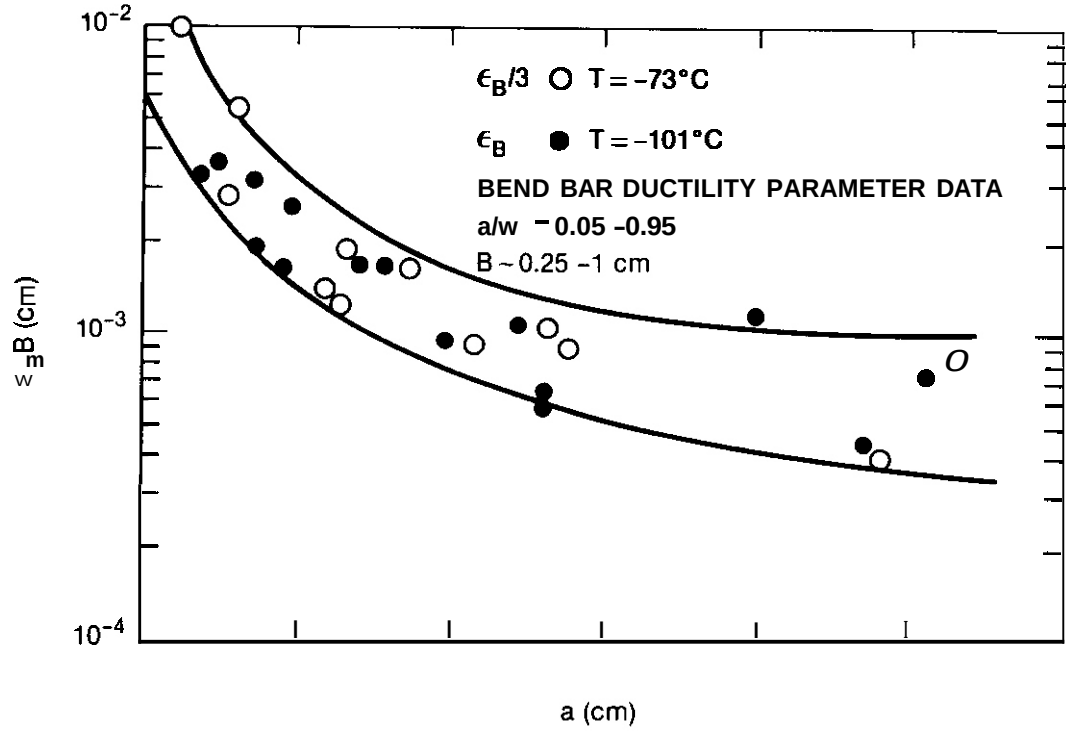

Fig. 11. Variation of the product of bend ductility and specimen thickness with crack length.

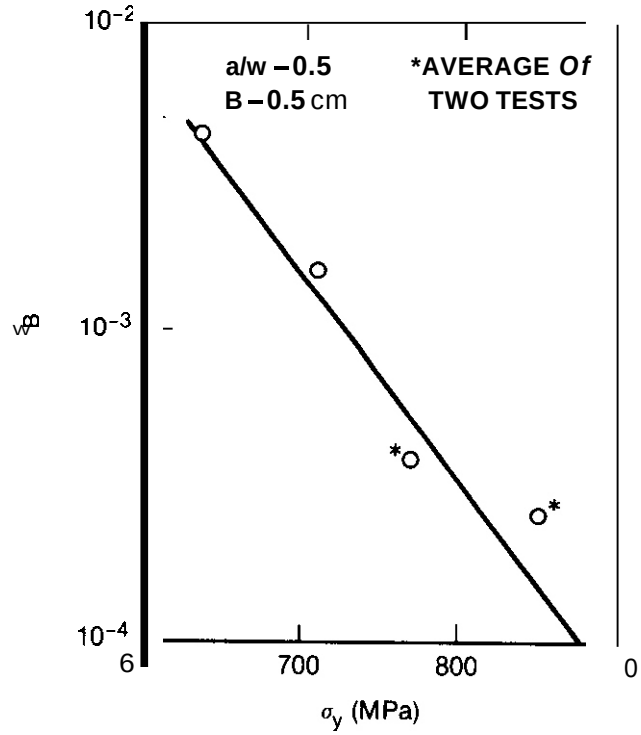

Fig. 12. Variation of bend ductility with yield stress for the B = 0.5 cm bend bar.

Table 7

Bend Ductilities for B ≈ 0.5 cm Bend Bars with a/w ≅ 0.5[f]

a/w	$\dot{\varepsilon}$ (s^{-1})	ε_B ($\times 10^{-3}$)
.536	$5\times10^{-3}/5\times10^{-2}$	1.6
.506	$5\times10^{-3}/5\times10^{-2}$	1.6
.515	$10^{-1}/10^{0}$	.5
.631	$10^{-1}/10^{0}$	.2
.515	$10^{1}/10^{2}$	.5
.557	$10^{1}/10^{2}$	~ 0 (<.1)

(f) T = -101°C

The high sensitivity of the bend ductility to temperature suggests a strong dependence on yield stress; e.g., an approximately 75 MPa increase in strength in going from -73° to -101°C leads to a reduction in ductility by about a factor of about 3. Table 7 shows the effect of strain rate for .5 cm thick bend bars tested at -101°C; clearly, higher strain rates lead to lower ductility limits. Figure 12 plots the bend ductility at a/w = .2 against the corresponding yield stress for B = .5 cm bend bars at the two temperatures and three strain rates. The high sensitivity is clearly evident. The micromechanical implications Of these results will be assessed in future research.

The effect of stress state variations due to side grooving can also be evaluated from the B = .4 cm bend bar tests reported earlier. The results are shown in Table 5 and can be briefly summarized as follows. At low a/w ratios (~ .1), side grooving reduced the ductility significantly; at side grooves of 12.5% and 25% the reduction was about a factor of 2 and at 37.5% about a factor of 4. At high a/w ratios (a/w ~ .75) the effect was reversed and the side notched specimens had somewhat more ductility with an increase of about 1.5 at side notches of 25% and 37.5% and about 2 for the 12.5% side notch. Thus there was no uniform trend with increasing notch depth. The effects were null at intermediate notch depths of a/w ~ 0.5. This behavior is Consistent with the argument that notching reduces stable crack growth at low a/w and with a ligament size effect at higher a/w. Overall, the differences are not large compared to the variability in the data.

it should be emphasized that the ductility discussed here is not a simple material property. The values depend on the specific test specimen loading geometry configuration . However, as noted above and discussed elsewhere, in the cleavage fracture regime the ductility is probably close to minimal in the "brittle" bend geometry. Based on this assumption cleavage fracture regime deflection limits on the order of 1-2 cm/m Of structural beam equivalent can be anticipated, for thin wall structures containing shallow fatigue cracks. Hence, this might be used by designers to evaluate the feasibility of operation in the cleavage fracture lower shelf toughness regime.

5.3 Micromechanics

5.3.1. Overview

The micromechanics of fracture in tempered martensitic HT-9 has been discussed previously.' Briefly it was shown that fracture is controlled by a critical cleavage fracture stress σ_f^*. Further, for sharp cracks the appiied tensiie stress must act over a critical microstructural distance l^*. Hence, quantitative micro-cechanical models are needed to relate the microstructure, including irradiation-induced changes to the σ_f^* and l^* parameters.

While relatively simple models have been successfully developed for ferritic alloys, the situation is more complex and less understood for bainitic and martensitic lath microstructures. For steels such as HT-9 with relatively larger carbides located on prior austenite grain boundaries, fracture initiation is believed to be controlled by propagation of a crack from a large cracked carbide. For a Griffith-type fracture and ignoring a small contribution from dislocation pile-ups, the microcleavage fracture stress σ_f^* can be written generally as

$$\sigma_f^* = \sqrt{\frac{1.5\ E\ \gamma_p}{Z}} \qquad (5)$$

where E is the elastic modulus, 2 characteristic size and γ_P a plastic work term

Data developed by Brozzo et al[7] and others[8,9] suggest an inverse square root relationship between lath packet size and fracture stress. The large value of the fracture stress at about 2500 MPa implies very high values of γ_p, approximately 120 J/m^2. Knott[10] proposes a model involving the internal necking and ductile fracturing of unfavorably oriented lath structures to rationalize this high value of γ_p. Other workers[11] propose a significant role of alternate microstructural features including fine-scale secondary hardening particles, dislocation structures and perhaps solution hardening elements. Curry[12] has recently reported results for a bainitic pressure vessel steel which are consistent with a critical stress criterion; in addition. he determined values for σ_f^* which were consistent with predictions based on propagation of stablf, lath-packet-sized microcracks, assuming high values of γ_p (~ 120 J/m^2). Alternately, he notes cleavage in these steels could proceed by a dislocation mechanism, in which case σ_f^* would depend on slip band length which can be influenced by factors such as packet size and lath width as proposed by Naylor.[13] In a study of martensitic steels, King et al.[14] suggest that interlath carbides control fracture and the magnitude of the microcleavage fracture stress; and further, that, as proposed by others for high strength 4340 steels[15], the reduction in the toughness associated with tempering at 350°C is a result of coarsening of the interlath carbides, thereby lowering σ_f^*.

The results reported previously for HT-9[2] are generally consistent with these previous observations: l* is observed to be on the order of the prior austenite grain size; and σ_f^* is consistent with an observed packet size on the order of 5-10 μm based on the relation $\sigma_f^* = 190 \pm 20$ MPa$\sqrt{m}/\sqrt{d}$ determined from the data in the literature, as noted above.

The model proposed by Knott to rationalize the high γ_p value appears to be the most promising approach. It derives from the following picture of the fracture process. Propagation of a crack from a carbide initiation site is controlled by stresses needed to link and propagate microcracks which form readily within lath packets. While such cracks propagate easily within a packet, they may arrest upon intersecting a high angle packet boundary. Since there is concurrent formation of packets within a grain, such high angle intersections and arrests may occur on the order of one to several packet widths. Because of misorientation of the cleavage fracture planes continued propagation of a crack past a high angle boundary requires plastic rupture of the intervening laths. By equating local internal necking strain displacement leading to 45° fracture of laths of thickness t with a critical crack displacement for stable crack growth δ_x ($\cong K_c^2/2\sigma_y E$), Knott obtains the following estimate of σ_f^*

$$\sigma_f^* = (4E\sigma_Y t/\pi(1 - \nu^2)\ d_p)^{1/2}, \qquad (6)$$

For E = 200 GPa, σ_Y = 800 MPa, t = .2 μm and d_P = 8 μm, the predicted value of σ_f^* is 2400 MPa.

While a number of criticisms can be aimed at this model (e.g., use of a mixture of elastic and elastic-plastic fracture concepts on a microscale where neither apply rigorously, and the predicted yield stress dependence which is not observed) the most significant question concerns the underlying description of the fracture process. Therefore, a microscopic investigation was carried out to determine if there is evidence of microcracking, microcrack arrest, and ductile deformation and fracture in association with cleavage microcrack propagation.

5.3.2 Fractography Studies

Extensive evaluation of fracture surfaces of specimens tested over the range of size, geometry, temperature and strain rate conditions discussed in Section 5.2 was carried out on an ETEC scanning electron microscope

(SEM). While there were differences in detail, a number of highly consistent observations were obtained which can be summarized as follows:

1. As noted above, the predominant mode of fracture was cleavage for all low temperature test conditions. Indeed, the fracture surface appearance was on a gross scale independent of strain rate, specimen size, a/w ratio and temperature below about -50°C. This basic fracture surface morphology is illustrated in Figure 13, which clearly demonstrates the correspondence of cleavage facets to the bainitic packet size scale.

2. However, on a more limited scale, there was also evidence of ductility for essentially all test conditions. Fi[illegible], as expected, small shear lips were observed near the edges of the specimens. However, the shear regions were in general a very small fraction (less than a few percent) of the total fracture surface area. Additional evidence of ductility randomly distributed on the interior of the fracture surface was also observed in the form of tear ridges which failed by microvoid coalescence. A typical example is shown in Figure 14a. These ductile regions usually exhibited a width dimension of the order of the packet size, although they tended to be strung out in ridge-like structures, as implied in the name and illustrated in Figure 14a. In other cases, more isolated packet size tearing regions were identified, as illustrated in Figure 14b and 14c. While the apparent frequency of these regions increased at lower strain rates and higher test temperatures, the differences were not large.

3. These observations were made on regions of the fracture surface corresponding to crack propagation, albeit close to the initiation site. Efforts to use river pattern techniques to identify the actual initiation sites were largely unsuccessful. This difficulty is due primarily to the extremely fine scale of the fracture surfaces. However, occasionally features that suggested an initiation site were observed as illustrated in Figure 15. Here a sizable spherical feature which may be a grain boundary carbide or inclusion is surrounded by a region of radiating cleavage facets mixed with light regions indicating ductility.

These observations support the postulate that cleavage fracture propagation is not uniform and is interrupted by small regions of ductile fracture. Observations of such regions in association with rapidly propagating cracks associated with high dynamic stress intensities suggests that such ductile fracture may be an even more important component of the cleavage fracture initiation event.

To better determine the possible role of crack formation, microcracking and microcrack arrest, a two-stage replication examination was carried out of the region near the initial crack tip and below the fracture surface (~ 1 mm). The procedure involves the following steps: electropolishing of a mechanically-prepared surface; negative replication of the surface using a plastic tape softened in acetone; negative replication of the tape by carbon deposition; shadowing the now-positive carbon replica of the surface using a high contrast element, in this case chromium; transmission electron microscopy (TEM) examination of the shadowed replica using a JEM-200CX.

Abundant evidence of subsurface microcracking and arrest was found as illustrated in Figure 16. The microcracks can be identified as regions of light alternating with black (the shadow) against a grey background. Figure 17 shows the morphology of an isolated microcrack. Here an interlath crack appears to have made a small-angle turn but arrested at high angle intersection with another lath packet.

Clearly, these observations support the general phenomenology of cleavage fracture in lath microstructures proposed by Brozzo[7] for low carbon martensites and Curry[9] for a bainitic low alloy steel (A533B). Hence, the general modeling approach of Knott appears reasonable, although a more rigorous approach to the mechanics of the microscopic deformation to fracture process may be required. The results do further suggest appropriate heat treatments which could improve fracture toughness by: maintaining fine carbides and packet structures; enhancing the ductility of and internal misorientations of packet structures; and increasing the spacing of carbides. As an illustration, one might consider starting with a refined microstructure, heating rapidly to high temperatures to promote rapid recrystallization and large austenite grains (large 1^*) and then rapidly quenching to promote fine packet structures. Subsequent intermediate temperature tempering could be used to attempt to optimize the formation of fine and stable carbides to moderately lower the yield stress. This and other alloy optimization approaches will be pursued in future research.

5.3.3 Hydrogen Effects on Fracture

Significant quantities of dissolved isotopic (D, T, H) hydrogen may exist in fusion structures. Hence the effects of this variable on low temperature fracture processes is of considerable interest. Further, the effect of hydrogen may provide additional clues to the micromechanisms of fracture. For example, if some

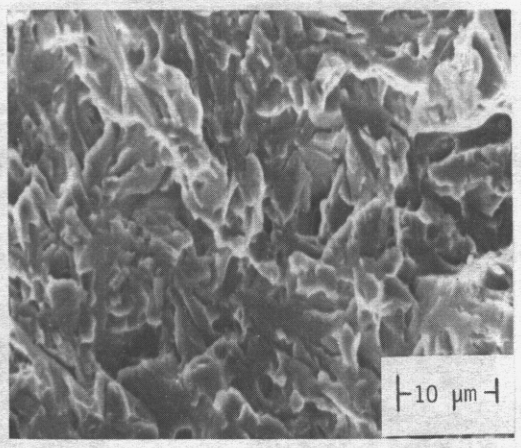

Fig. 13. Fractograph representative of cleavage fracture surface on bend specimen.

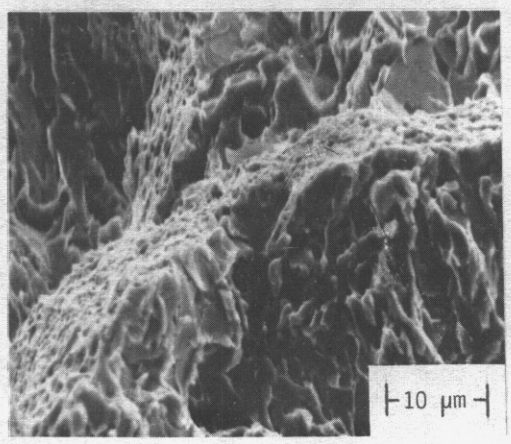

(a)

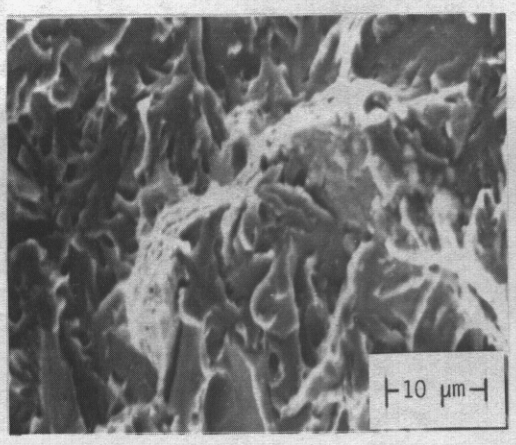

(b)

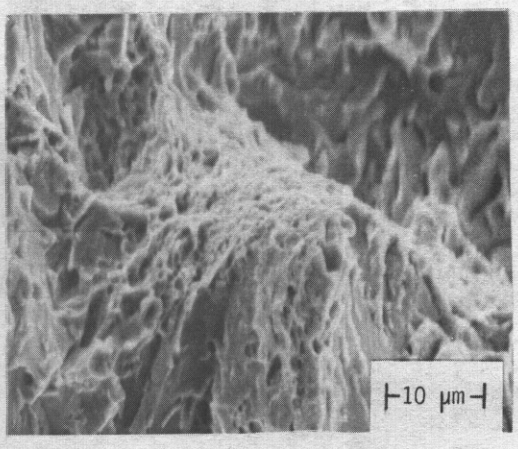

(c)

Fig. 14. Fractographs showing tearing ridges on cleavage fracture surfaces.

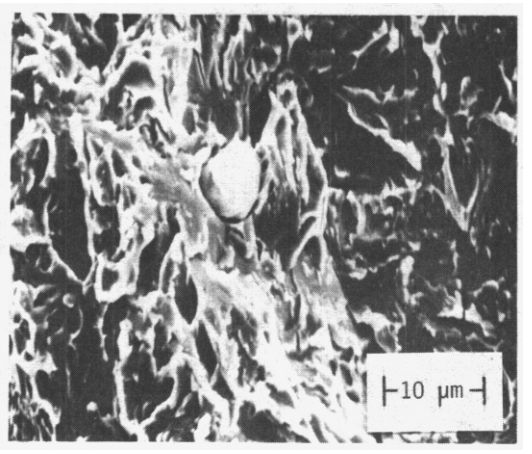

Fig. 15. Fractograph showing a possible crack initiation site associated with large three-dimensional defect.

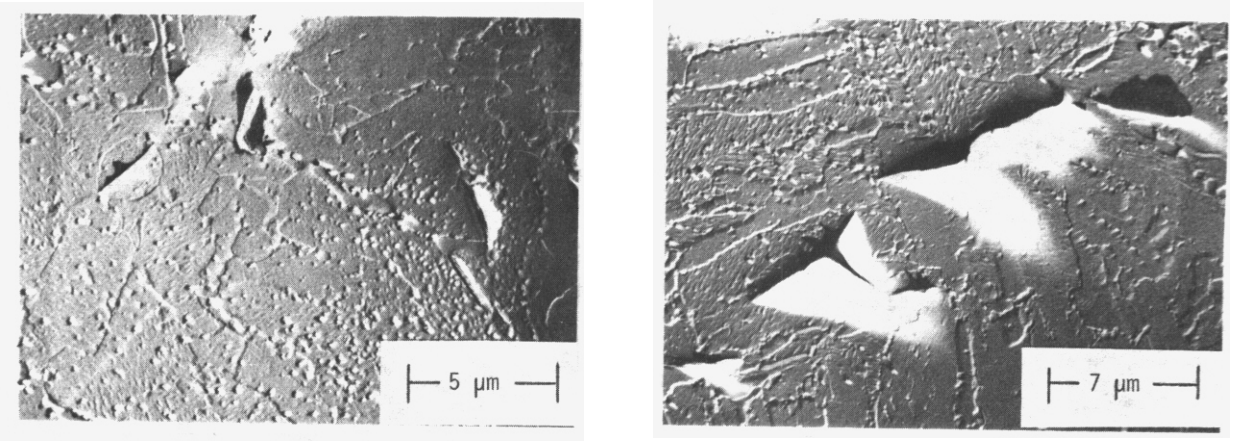

(a) (b)

Fig. 16. TEM micrographs of surface replicas showing microcrack locations with respect to microstructure.

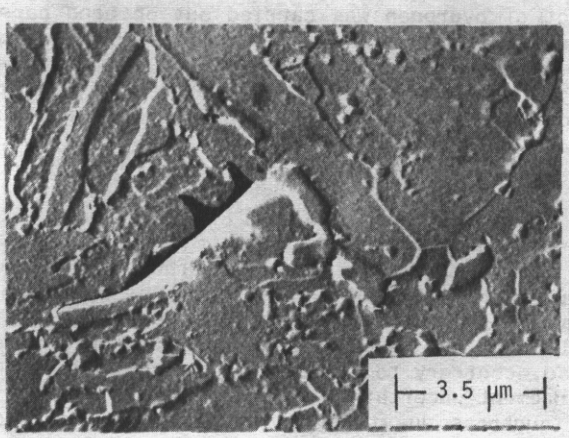

Fig. 17. TEM Micrograph of surface replica showing isolated microcrack. Microcrack appears to have arrested at a high angle boundary.

Table 8

Dissolved Hydrogen Effects on Fracture of Bend Bars(j)

B (cm)	Condition	a/w	T (°C)	σ_f (MPa)	σ_f/σ_c	K_Q (MPa$\sqrt{m}$)
.25	H-charged	.73	-73	1780	.98	29
	control	.74		1780	.96	36
.50	H-charged	.55	-73	1270	.69	40
	control	.52		1428	.77	51
.50	H-charged	.51	-101	1230	.62	45
	control	.54		1256	.63	49

(j) Strain rate $\dot{\varepsilon} \sim 5\text{x}10^{-3}/5\text{x}10^{-2}\text{s}^{-1}$

localized ductile fracture process controls the magnitude of the microcleavage fracture stress, as suggested above. then a relative insensitivity to hydrogen would be anticipated. This, of course, presumes that there is not a shift to an intergranular fracture mode/ path.

A preliminary study of the effect of hydrogen was carried out on bend bars with B = .25 cm and a/w of .75 and .5 at -73°C and -101°C tested at static strain rates. This represents a range of relatively ductile to moderately brittle fracture conditions (σ_f/σ_c ~ .95 to .65). The specimens were hydrogen charged in an autoclave at about 10 MPa hydrogen pressure at 500°C. They were then rapidly cooled at pressure (200°C in 0.5h) and subsequently discharged and tested. Based on equilibrium solubility estimates, the hydrogen content was about 10 ppm.

The fracture toughness results are summarized in Table 8. In general, there appears to be substantial reduction in the fracture resistance induced by hydrogen charging from about 9 to 23 percent with an average reduction of about 17 percent. The results for the deep crack a/w should be viewed with some suspicion since the differences reside largely in the high sensitivity of the compliance function to a/w in this range; notably, the maximum load for the hydrogen specinen is larger in this case, but the P_Q load is slightly smaller 20.5 versus 21.8 kg). Further, the apparent reduction at -101°C is less than for the nominally less brittle -73°C case, contrary to expectation. Thus some of the apparent hydrogen effects may be due to data scatter and measurement uncertainty in assessing invalid K_Q toughness indices; nevertheless, the trend to some reduction of toughness due to hydrogen charging is consistent and seems clear. However. the maximum load-based fracture-to-collapse stress ratio is clearly less sensitive with a maximum reduction of about 11% and an average decrease of about 5%.

As expected. fractography studies did not indicate a significant difference in fracture surface appearance. Further, evaluation of ductilities for charged and uncharged specimens showed relatively little effect. Additional studies of hydrogen will be carried out on larger specimens at lower test temperatures and higher strain rates. These studies will also include the effect of thermal aging to try to temper-embrittle the alloys. charging to higher hydrogen levels, and charging in flawed specimens under a maintained crack tip stress field.

5.3.4 Strain Rate Effects

As discussed elsewhere', simple theory suggests that l^* and σ_f^* are relatively insensitive to temperature and strain rate over a considerable range in the lower-shelf toughness regime. Stress-controlled cleavage fracture models further predict relatively constant lower shelf toughness for constant l^* and σ_f^* even though the yield stress increases with decreasing temperature and increasing strain rate.

Therefore, the reduction in lower shelf toughness with increasing strain rate and decreasing temperature reported in Section 5.2 suggests a change in either the micromechanism of fracture, variation in the fracture parameters, σ_f^* and l^*, or both. Indeed, data in the literature for mild and low alloy steel suggest that at very low temperatures there is a change in the basic cleavage fracture mechanisms. signaled by a large drop in σ_f^*. Therefore, a study of the strain rate sensitivity of the basic fracture parameters was undertaken. Further, dynamic yield strength measurements were extended to lower temperatures from the previous limit of about -129°C; the yield strength data are needed along with the toughness data given in Section 5.2 to clarify fracture mechanisms at high strength limits associated with low temperatures and high strain rates.

The temperature and strain rate sensitivity of σ_f^* was investigated with Griffiths-Owen (GO) type four point bend bars[16] using procedures discussed elsewhere.[2] Tests were conducted at nominal notch tip strain rates of $\dot{\varepsilon} = 50 s^{-1}$ at temperatures from -73 to -195°C. One GO test was conducted at a lower strain rate $\dot{\varepsilon} = 10^{-3}/10^{-2} s^{-1}$ at 195°C. Standard tensile tests were conducted at strain rates of 10^{-3} and 3 s^{-1} at temperature from -129°C to -195°C.

The tensile data are shown in Fig. 18. The yield strength measurements are correlated by a nominal temperature strain rate parameter $T \ln(10^8/\dot{\varepsilon})$. Several previously-reported instrumented C_v general yield data points are also shown in Fig. 18. These results can be reasonably represented by a relation

$$a_{ys} = 4.7 \times 10^4 [T \ln(10^8/\dot{\varepsilon})]^{-0.5} \qquad (7)$$

The $10^8/\dot{\varepsilon}$ strain rate parameter is equivalent to an activation enthalpy H for dislocation motion on the order of $H = Q^* - V^*\sigma = 24.0 kJ/mole$, where Q^* is the intrinsic activation energy for slip and V^* the

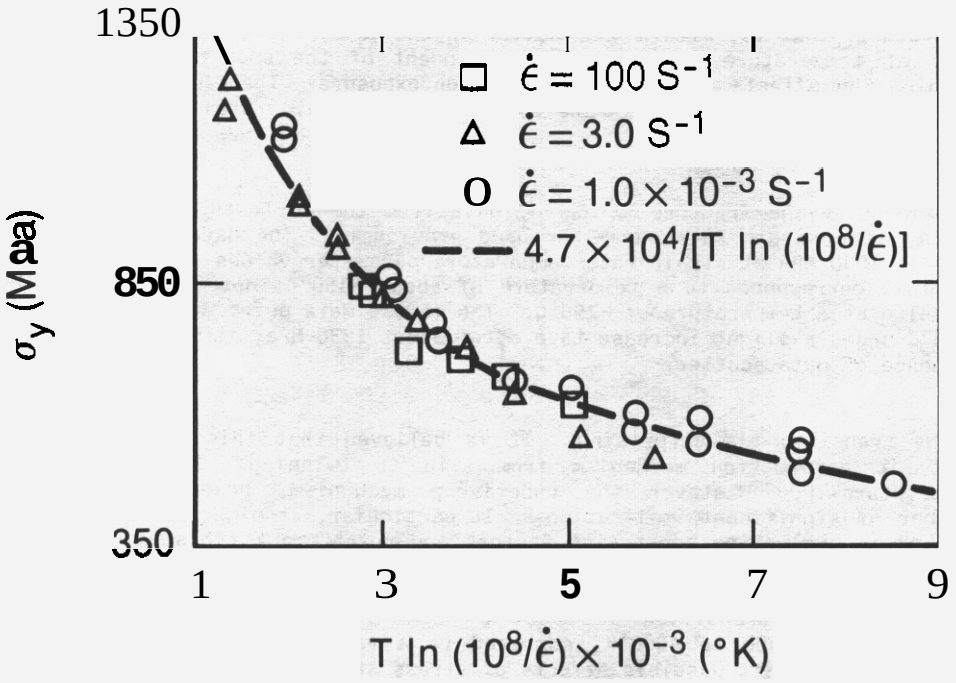

Fig. 18. Variation of yield stress with temperature/strain rate parameter.

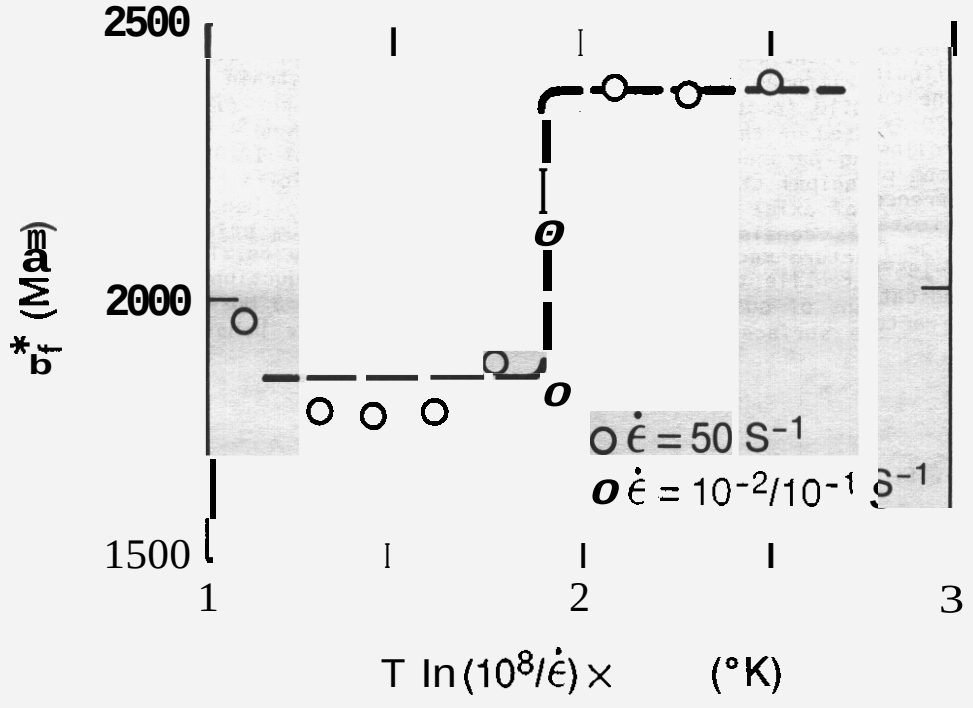

Fig. 19. Variation of σ_f^* with temperature/strain rate parameter.

activation volume. This value is consistent with a wide array of low temperature deformation studies in iron-based, body-centered cubic alloys. The temperature and strain rate dependence described by eqn. (7) is very similar to the behavior of a range of low-alloy pressure vessel steels. It has been shown recently[17] that there is a unique relation in this alloy class for the increase in the dynamic and static yield stress with decreasing temperature; that is, within the scatter in the data, the average absolute increase in yield stress per increment of temperature decrease is independent of the specific alloy type, condition and strength level including the effects of neutron irradiation exposure. Therefore, the applicability of this behavior to martensitic steels and more accurate evaluation of strain rates will be further evaluated in future research.

Figure 19 shows the microcleavage fracture stress σ_f^* data from the GO tests. Again, the data are plotted against the same temperature strain rate parameter used previously. The data show a rapid drop in σ_f^* from about 2400 MPa to about 1800 MPa at strain-rate-temperature parameter values of about 1750°K for the strain rate of $\dot{e} = 50s^{-1}$. This corresponds to a temperature of about -150°C; note the test at lover strain rate shows a similar low value at a temperature of -195°C. The lowest data point at the higher strain rate and a a temperature of -195°C shows a slight increase to a σ_f^* of about 1930 MPa; it is not known if this is a real effect or the consequence of data scatter.

The abruptness of the transition is surprising. It is believed that this may be the consequence of a transition in the basic deformation mechanism from slip to twinning. However, this remains to be demonstrated microstructurally. Whatever the underlying mechanism, however, the abruptness of the transition has a number of significant implications. In particular, it might be used as a second reference point for purposes such as evaluating constraint factors and notch/crack tip strain rates. Indeed, if the transition were only dependent on the uniaxial yield strength (~ 1100 MPa for the specimens at -150°C and $\dot{\varepsilon}$ = 150s^{-1}) it could serve as an absolute reference point.. However, this does not appear to be the case. The dynamic toughness data show a transition at about $\dot{\varepsilon} = 10^{2}/10^{1}$ and -101°C. This corresponds to a $T\ln(10^8/\dot{\varepsilon})$ parameter of about 3600 to 4000°K, compared to a value of about 1700 to 2100 for the GO-bar determined σ_f^* values. This suggests possible effects of stress state on the transition. The maximum principal to yield stress ratio R^{max}_{YY} for a loaded, initially-sharp crack is about 3.6 for an alloy with a work hardening exponent of about _ ■ _This is calculated using Crack tip field fits to finite element calculations.* The maximum ratio in GO specimens is about 2.7[16] (it is lower due to the blunt notch). It is assumed that the geometrically-sensitive stress state behavior is represented by these maximum ratios and that equivalent behavior is observed at equal values of $R^{max}_{YY}\sigma_y$. This suggests that equivalency in going from an initially-sharp crack fracture specimen to a GO specimen would require about a factor of 1.3 increase in yield stress. As shown in Fig. 18, this closely corresponds to the increase in the yield strength over the strain rate parameter range of 3400 (~ MPa) to 1900 (~ 1070 MPa). Hence, there is a strong indication that the transition is controlled by stress-state-dictated constraint factors; viz., maximum principal stresses on the order of 2900 MPa are required. Further evidence is found in the results of tensile tests at liquid nitrogen temperature (-195°C) and at high strain rates(3s^{-1}) which indicates a classical cup and cone ductile fracture mode. Representative micrographs of the ductile fracture surface are shown in Figure 20. Based on the measured reduction in area (44%) and a Bridgman analysis at the Point of fracture,[18] the following parameters are obtained: yield stress of 1220 MPa; true fracture stress of about 1400 MPa; maximum principal stress of about 1800 MPa. Evidence of a highly triaxial stress state is observed in the occurrence of axial cracks also visible in Figure 20. Hence, the observation of ductile fracture in tensile tests is consistent with the value of the maximum principal stress insufficient to trigger either cleavage fracture mechanism. Finally, we note one very puzzling observation; namely, that the low strain rate -195°C tensile tests showed a lower ductility (reduction in area of ~ 22% in a highly diffuse neck) and indications of quasi cleavage fracture, albeit with a more three-dimensional morphology than for bend bar fracture surfaces. Possible explanations for this behavior are under investigation.

6.0 References

1. G.R. Odette and G.E. Lucas, J. Nucl. Mat., 117 (1983) 214.
2. G.R. Odette. G.E. Lucas, R. Maiti, J.W. Sheckherd, J. Nucl. Mat.. 122/123 (1984) 442.
3. R.O. Ritchie, J.F. Knott, J.R. Rice, J. Mech. Phys. Sol., 21 (1973) 39.
4. G.R. Odette and G.E. Lucas, J. Nucl. Mat., 117 (1983) 276.
5. B.A. Bilby, A.H. Cottrell, K.H. Swinden, Proc. Roy. Soc. (London), A272 (1963) 304.
6. G.G. Chell. Met. Technol., March (1977) 136.
7. P. Brozzo, G. Buzzichelli, A. Mascanzoni, M. Mirabile, Met. Sci., 11 (1977) 123.

8. G. Green, Ph.D. Thesis, Cambridge University (1975).

9. D.A. Curry, Met. Sci., 16 (1982) 435.

10. J.F. Knott, Conf. on Fracture Mechanisms in Design and Service: Living with Defects, Roy. Soc. London, London (1979).

11. G.G. Sanders, Ph.D. Thesis, Cambridge University (1975).

12. D.A. Curry; Met. Sci., 16 (1982) 435.

13. J.P. Naylor, Met. Trans., 10A (1979) 861.

14. J.E. King, R.F. Smith, J.F. Knott, Proc. 4th Int'l Conf. on Fracture, Waterloo (1977) 57.

15. R.O. Ritchie and R.M. Horn, Met. Trans., 9A (1978) 331.

16. J.R. Griffiths and D.R.J. Owen, J. Mech. Phys. Solids, 19 (1971) 419.

17. G.R. Odette, P.M. Lombrozo, R.A. Wullaert, "The Relation Between Irradiation Hardening and Embrittlement of Pressure Vessel Steels", Proc. 12th Symp. on Rad. Effects on Matls.", ASTM, Williamsburg, VA (June, 1984).

18. P.W. Bridgman, Studies in Large Plastic Flow and Fracture, Harvard University Press (1969).

19. W.L. Server, J. Test. Eval., 6, 1 (1978) 29.

20. S. Timoshenko, Strength of Materials, D. Van Nostrand, NY, 1930.

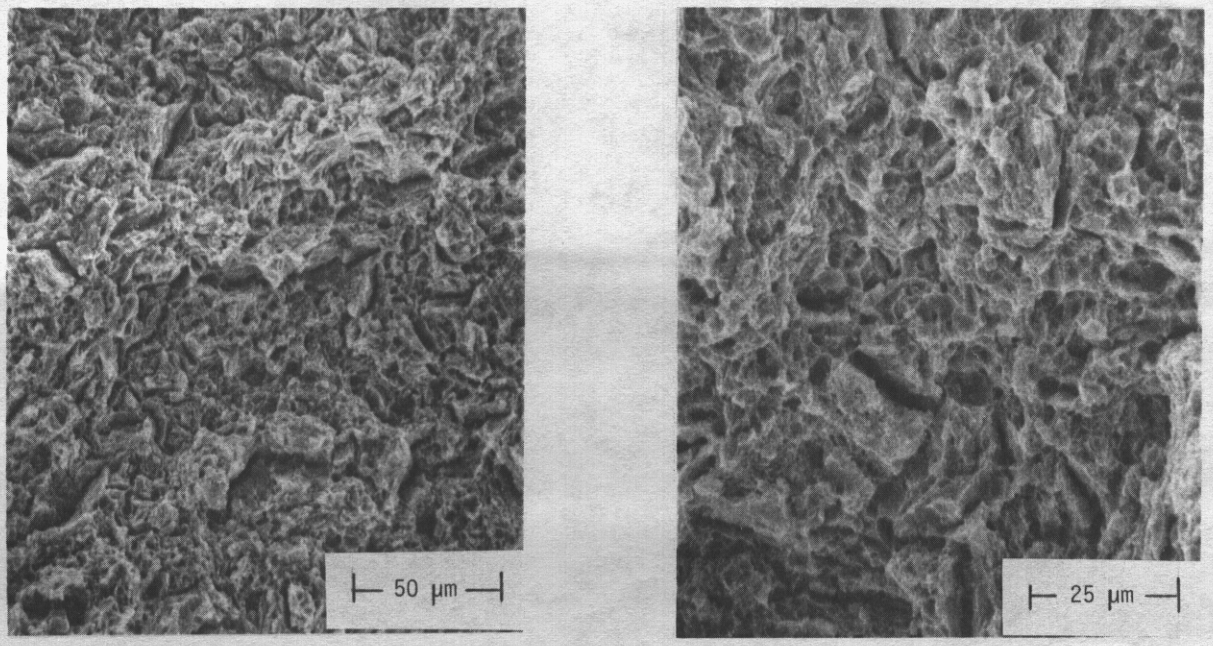

Fig. 20. Fractographs showing ductile fracture of a dynamic tensile specimen tested at -195°C.

7.0 Future Work

As indicated throughout Section 5, a variety of tests are planned and ongoing. We plan to further address the effects of side grooving by investigating larger samples and maintaining B constant while varying B_o. Studies will be performed to address the observation of systematic deviation in predicted and measured values of a_f/σ at small values of a/w in both side-grooved and plain specimens. The micromechanical model for cleavage fracture will be further tested against a matrix of heat treatments including 5 reaustenizations, 3 cooling rates and 5 tempering conditions. In addition, some simulated heat-affected zone material will be studied. Hydrogen charging studies will continue with emphasis on larger specimens, on hydrogen charging stressed specimens and on higher strain rate, lower temperature test conditions. In addition, we will attempt to examine the potential role of temper embrittlement. The temperature and strain rate dependence of the yield stress will be compared to a master curve successfully developed for a variety of ferritic steels, and implications will be assessed. The microstructural studies will be continued. Emphasis will be on characterizing microstructures developed in the heat treating matrix described above, and on microcrack evolution as a function of test temperature, constraint and strain rate. Finally, we plan to evaluate the TPP by performing tests on specimens other than bend bars, for instance, with center-cracked panels. In addition, the issue of variation in stress and deformation fields around part-through cracks will be addressed.

SOME CONSIDERATIONS OF RADIATION EFFECTS ON STRESS CORROSION CRACKING OF FUSION REACTOR MATERIALS

R. H. Jones (Pacific Northwest Laboratory)

1.0 Objective

The purpose of this evaluation was to identify potential synergisms between irradiation phenomena and stress corrosion processes. There have been few studies on the stress corrosion behavior of irradiated material and no reported studies of in-situ stress corrosion. Therefore, an assessment of potential irradiation and stress corrosion synergisms was undertaken to identify possible concerns for fusion reactor materials.

2.0 Summary

Published research on radiation enhanced corrosion was reviewed and it was concluded that radiolysis is not expected to increase the corrosion rate of fusion reactor materials by more than a factor of 3; however, hydrogen uptake could increase significantly in ferritic, refractory and reactive alloys. The effect of irradiation enhanced creep on intergranular stress corrosion cracking, IGSCC, was modeled and it was concluded that irradiation creep could significantly increase the crack growth rate at stresses below the yield strength. A phosphorus segregation induced IGSCC process was also evaluated and shown that radiation induced phosphorus segregation could dominate all other IGSCC effects. Calculated K_{IC} and K_{TH} results for HT-9 were reviewed and compared with published K_{IC} results fran the ADIP program. This comparison suggests that the model used to calculate the effects of increasing yield strength and grain boundary segregation on K_{IC} gives calculated values significantly less than the experimental results.

3.0 Program

Title:. Mechanical Properties
Principal Investigator: R. H. Jones
Affiliation: Pacific Northwest Laboratory

4.0 Relevant DAFS Program Plan Task/Sub-Task

Subtask II.C.8 Effects of Helium and Displacements on Fracture
Subtask II.C.9 Effects of Hydrogen on Fracture
Subtask II.C.12 Effects of Cycling on Flow and Fracture

5.0 Accomplishments and Status

5.1 Background

5.1.1 Radiation-Enhanced Corrosion

Radiation may alter the corrosion behavior of materials by causing chemical changes in the environment, by altering the protective properties of the passive film or by chemical or phase changes in the alloy. Radiation induced chemical changes in the environment are called radiolysis and occur by excitation and ionization of the atoms and molecules in the environment. Changes in chemical composition produce a change in chemical activity of the environment or the kinetics of the cathodic or anodic electrochemical processes. In a fusion reactor system, radiolytic effects will occur primarily fran the interaction of gamma rays and beta particles from the activated structure or from radionuclides in the coolant. In a water cooled system, the dominant radionuclide is expected to be ^{16}N formed by (n,p) reactions which decays into 6.1 MeV gamma

rays and 10.4 MeV and 4.3 MeV beta particles. The gamma and beta spectrum emanating from the activated structure will depend on the chemical composition of the blanket structure. Radiolytic processes are not expected in liquid metal cooled systems although chemical or phase changes in the material contacting the liquid metal coolant could affect the corrosion rate.

Most corrosion resistant materials form a thin protective film on their surface when exposed to aqueous environments. This film is generally about 100 Å thick and is thought to be a hydrated oxide which reduces cation and anion diffusion sufficiently to reduce the corrosion rate by several orders of magnitude. Radiation can degrade the protective properties of a passive film by atomic displacements which increase the cation or anion diffusivity through the film or from a photo-radiation effect which alters the semiconducting properties of the film.

Byalobzhesky[1] has reviewed the radiolytic, damage and photoconductive effects of irradiation on corrosion and for most materials an increase of only 1.5 to 3 times is noted. For some selected cases however the increase was several orders of magnitude. Stobbs and Swallow2 also reviewed the effects of radiation on metallic corrosion although most of their examples are for zirconium and uranium alloys. In summarizing the results of many investigations, Stobbs and Swallow2 state that the corrosion behavior of stainless steel in high purity water at temperatures up to 300°C and a pH of 10 is affected very little by a neutron flux of 10^{13} to 10^{14} cm^{-2} s^{-1} (thermal). Similarly, corrosion studies of stainless steel irradiated with electrons and deuterons showed little effect of these irradiations. The results on carbon steels in reactor loops at 300°C are conflicting showing both an increase and a decrease in corrosion rate[2]; however, with increasing chromium content and therefore with increasing passivity the effect of radiation diminishes.

Van Konynenberg and McCright[3] recently reviewed the effect of radiation on corrosion in steam generators. In this case, radiation resulted fran decay of ^{16}N into gamma rays and beta particles and no neutrons were present. The chemical changes occurring in pure water can be represented by the following overall reaction:

$$5.08\ H_2O \rightarrow 2.63\ e^-_{aq} + 0.55\ H + 2.72\ OH + 0.68\ H_2O_2 + 0.45\ H_2 + 3.63\ H^+ + 1.00\ \bar{O}H.$$

In a closed container there is no net chemical change because the reverse reaction of free radicals to form water is very fast. In an open system with gas bubbling through solution, the H_2 gas goes off and the H_2O_2 concentration increases and reaches a steady state concentration. In reviewing the effects of radiation on corrosion of carbon steels, Van Konynenberg and McCright[3] concluded that in temperature and pH regimes at which a passive film is not stable radiation increased the corrosion rate while in temperature and pH regimes in which a passive film is stable, radiation assists in film formation and reduces the corrosion rate. Under conditions in which radiation increased the corrosion rate, the increase was only about a factor of 2 although one study reported an increase of 12.7 for electron irradiation.

Nelson, Westerman, and Gerber[4] recently reported corrosion tests conducted on several ferritic steels and titanium alloys in a cobalt-60 facility. Tests were conducted at 250°C in Grande Ronde Basalt groundwater with a gamma ray dose rate of 2×10^6 rad/hr. The ferritic alloys were a ductile cast iron, a cast 1025 steel, a cast 2 112 Cr-1%Mo steel and a wrought 1020 steel while the titanium alloys were titanium grade 2 and grade 12. While the materials, water chemistries, and gama spectrum and fluxes are not directly applicable to fusion reactors, it is encouraging to note that Nelson, Westerman, and Gerber[4] observed at most a factor of 2 increase in the corrosion rate of ferritic steels. The most corrosion resistant ferritic steel tested, 2 1/2 Cr-1 Mo steel, showed little if any increase in the corrosion rate which is consistent with the results reported by others[2,3]. Perhaps of greater concern was the hydrogen uptake observed for the titanium alloys which reached 100 wt. ppm after a 10 month exposure.

In summary, it would appear that alloys such as 316 SS and HT-9 which form passive layers in high temperature water would not experience an increased corrosion rate from the gama and beta radiation emanating from the blanket region of a fusion reactor. The effect of neutron induced damage to the passive film is not included in this assessment. If an increase is observed it would be small and of the order of 2-3 times. Low alloy steels such as 1 1/4 Cr-1 Mo would also not likely experience corrosion rates more than 2-3 times faster in the blanket structure. A closer evaluation for the gamma spectrum expected in a fusion reactor blanket structure combined with fusion energy neutron reactions is needed before the possibility of enhanced corrosion in a fusion reactor blanket structure can be dismissed. Since both ferritic and austenitic stainless steels can be embrittled by hydrogen, the possibility of enhanced hydrogen absorption in fusion reactor structural materials is of greater concern than the possibility of enhanced corrosion rates. It would appear that a hydrogen embrittlement study of fusion reactor materials exposed to radiation while in contact with water is warranted.

5.1.2 Stress Corrosion Cracking of Irradiated Materials

Unlike the subject of radiation effects on corrosion, there have been relatively few studies on the effect of radiation on stress corrosion cracking. The notable exception to this is zircaloy although the main failure mechanisms in zircaloy cladding is a combination of stress rupture and embrittlement by iodine or liquid metal. There are a number of radiation damage processes which may effect the stress corrosion behavior of materials including:

- Hydrogen embrittlement from radiolytic hydrogen uptake coupled with radiation hardening,
- Radiation induced segregation as discussed by Jones and Wolfer,[5]
- Radiation induced precipitation which increases the corrosion rate or causes a faster crack growth rate due to embrittlement,
- Radiation effect on the corrosion rate,
- Helium embrittlement causing a faster stress corrosion crack growth rate,
- Irradiation creep enhanced stress corrosion cracking as discussed below.

Of these processes, hydrogen embrittlement of ferritic steels is the greatest concern because it appears that radiation will increase the yield strength, induce impurity segregation to grain boundaries, and enhance hydrogen absorption. All three effects will reduce the lifetime of fusion reactor materials. The effects of radiation induced precipitation and helium embrittlement are unknown hut should not be ignored while irradiation enhanced corrosion will affect stress corrosion but the effect should he small. It was estimated by Jones and Wolfer[5] that radiation induced grain boundary segregation of phosphorus in 316 SS could increase the stress corrosion crack growth rate by a factor of 8 while in the evaluation given in Section 5.2 it was estimated that irradiation creep could increase the crack growth rate by 10^3 times at a stress of 10 MPa and a factor of 4 at 100 MPa. Therefore, both of these processes should not be overlooked in reactor design.

Fujita et al.[6] evaluated the stress corrosion cracking behavior of 304 SS in high temperature water (250°C) during a gamma ray radiation of 4.5 x 10^4 rad/hr. They found that the fracture strain at strain rates of 5 x 10^{-7} to 5 x 10^{-6} s^{-1} was unaffected in water with less than 20 ppb oxygen but was decreased about 50% in water with 8 ppm oxygen. Fujita et al.[6] suggested that the increased hydrogen concentration in the water from radiolysis caused the breakdown of the passive film and thereby caused intergranular stress corrosion, IGSCC, of sensitized material. Kuribayashi and Okabayashi[7] also observed increased IGSCC of 304 SS from γ radiation in oxygenated high purity water and in a boiling 12% NaCl solution with a pH of 3. In the low pH experiment, Kuribayashi and Okabayashi[7] concluded that the gamma radiation caused a radiolytic reaction of $Fe^{2+} \xrightarrow{\gamma} Fe^{3+}$ and that the strong oxidizing ferric ions accelerated the corrosion rate and hence affected the IGSCC.

Votinov et a1.8 evaluated the susceptibility of stainless steel irradiated at 70°C to a fluence of 3 x 10^{20} cm^{-2} to intergranular corrosion (IGC). Samples were irradiated in the austenitized condition *and* subsequently heat treated to produce sensitization. Irradiation caused IGC to occur at shorter times and at lower temperatures and to persist to longer times at higher temperatures than for unirradiated samples. IGC of irradiated 18/8 stainless steel occurred after 1.5 hr at 350°C while 100 hr at 400°C was needed to produce IGC in unirradiated material. The reason for the enhanced sensitization was not identified but at 70°C it is not expected that grain boundary carbide precipitation or impurity Segregation occurred during irradiation. The most likely cause is a change in the dislocation structure and perhaps point defect concentration produced accelerated diffusion during the post-irradiation annealing. The significance of these results to fusion reactor materials is not clear but it does suggest that enhanced sensitization could occur for components subjected to neutron irradiation at temperatures of 350 to 400°C.

5.2 Assessment of Irradiation Creep Enhanced Stress Corrosion Cracking

Stress corrosion cracking of materials which form protective, passive films in aqueous solutions has been described by a passive film rupture model by Vermilyea[9] and extended by Ford[10] to account for the effect of crack tip strain rate on the film rupture rate. In Ford's analysis, the crack growth rate for times less than the passive film incubation time, t_o, is given by a simple Faradaic dependence:

$$da/dt = \frac{M}{n\rho F} i_o \qquad (1)$$

wnere

M = atomic weight of the alloy
n = valence change in the total oxidation reaction
ρ = density of the alloy
F = Faraday's constant
i_o = bare surface dissolution rate.

For times exceeding the passive film incubation time, Ford expressed the crack growth rate as follows:

$$da/dt = \frac{M}{n\rho F} \frac{i_o t_o^{1/2} \dot{\varepsilon}^{1/2}}{\varepsilon_f^{1/2}} \quad (2)$$

where

t_o = passive film incubation time,
$\dot{\varepsilon}$ = crack tip strain rate,
ε_f = passive film fracture strain.

For strongly passivating materials, t_o is about 10^{-3} s; therefore, the stress corrosion crack growth rate should be controlled by Equation 2 for 316 SS and HT-9. This assumption does not consider the possibility of a mechanical fracture component to stress corrosion as proposed by Jones et al.[11] but only considers the Faradaic component to stress corrosion. A boundary condition on Equation 2 is that $t_o^{1/2} \dot{\varepsilon}^{1/2} / \varepsilon_f^{1/2} < 1$ since a system in which a passive film covers the crack tip for some fraction of time will have less charge transfer than one in which no passive film is present.

For 304 SS in water containing 0.2 ppm oxygen at 288°C, Ford[10] derived the following relationship between the stress corrosion crack growth rate and the crack tip strain rate:

$$da/dt = 1.5 \times 10^{-4} \dot{\varepsilon}^{1/2} \quad (3)$$

which is shown plotted in Figure 1. This data indicates that a crack tip strain rate of 10^{-6} s^{-1}, which is commonly used in laboratory stress corrosion tests, would give a crack growth rate of about 10^{-7} cmls. Under these conditions, a stress corrosion crack would penetrate a 2 mm thick wall in about 500 hr. At crack tip strain rates exceeding about 10^{-3} s^{-1}, ductile fracture processes occur in preference to stress corrosion cracking. The stress corrosion crack growth rate at this strain rate would be about 10^{-5} cm/s resulting in penetration of a 2 mn thick first wall in 5 hr. However, crack blunting and ductile fracture would be more likely to occur at high strain rates with crack propagation dependent on the tearing modulus of the first wall structure.

In the model presented by Ford[10] in Equation 3, the crack tip strain rate results from thermally activated creep processes; however, a material in a neutron flux environment will also undergo irradiation enhanced creep. The contribution of irradiation enhanced creep to stress corrosion cracking has been estimated by assuming that the thermally activated creep rate, $\dot{\varepsilon}_t$, and irradiation enhanced creep rate, $\dot{\varepsilon}_I$, are additive such that the crack tip strain rate given in Equation 3 is the sum of $\dot{\varepsilon}_t + \dot{\varepsilon}_I$ and that the stress corrosion crack growth rate is given by the following relationship:

$$da/dt = 1.5 \times 10^{-4} (\dot{\varepsilon}_t + \dot{\varepsilon}_I)^{1/2}. \quad (4)$$

Since thermally activated creep is expected to dominate at high stresses and irradiation enhanced creep is expected to dominate at low stresses, the crack growth rate give by Equation 4 was expressed in terms of stress using the following relationships[10,12] between strain rate and stress:

$$\dot{\varepsilon}_t = B \sigma^6 t^{-1} \quad (5)$$

where $B = 3 \times 10^{-20}$ $MPa^{-6} - s^{-1}$

and

$$\dot{\varepsilon}_I = B \sigma \quad (6)$$

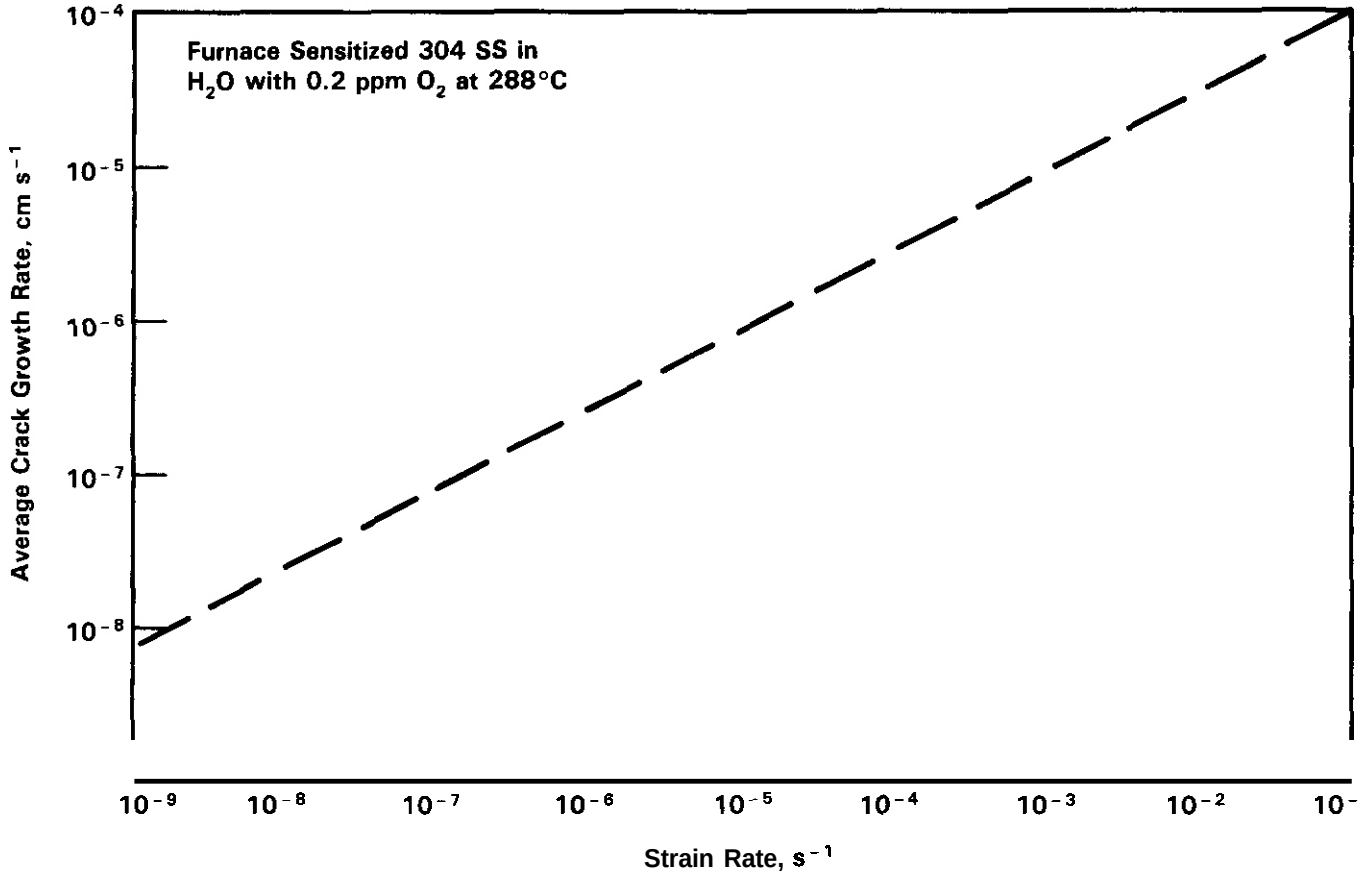

FIGURE 1. Calculated Crack Growth Rate Versus Strain Rate for 304SS Based on Equation 3 by Ford.[9]

where $B = B_O + B_S = 3 \times 10^{-3}$ MPa^{-1}-dpa^{-1}. For a displacement rate of 10^{-6} dpa/s the crack growth rate is as follows:

$$da/dt = 1.5 \times 10^{-4} (3 \times 10^{-9} \sigma + 3 \times 10^{-20} \sigma^6)^{1/2}. \quad (7)$$

The stress dependence of the crack growth rate is given in Figure 2 where it can be seen that irradiation enhanced creep makes a significant contribution to stress corrosion cracking at stresses below the yield strength (~200 MPa) of annealed 304 SS. The results shown in Figure 2 indicate that stresses exceeding 10 MPa will produce stress corrosion crack growth rates exceeding 2×10^{-8} cm/s. Since it is unlikely that the sum of applied and residual stresses will be less than 10 MPa, a crack growth rate of 2×10^{-8} cm/s appears to be the minimum value for a structure in a neutron flux induced displacement rate of 10^{-6} dpa/s. This minimum stress corrosion crack growth rate will cause a crack to penetrate a 2 mm thick wall in about 2500 hr which is a short time in the life of a fusion reactor blanket structure. Therefore, it appears that stress corrosion and irradiation enhanced stress corrosion need to be considered in the design of water cooled fusion reactor blanket structures. Water chemistry and material chemistry are two very important factors in the stress corrosion cracking of materials and since lowering the stress does not appear to eliminate stress corrosion in the presence of irradiation creep, it would appear that reduced stress corrosion crack growth rates will only come about by proper control of these chemistries.

5.3 Assessment of Irradiation-Induced Impurity Segregation

5.3.1 Intergranular Stress Corrosion Cracking

The most common cause of intergranular stress corrosion cracking (IGSCC) in austenitic stainless steels is chromium depletion adjacent to the grain boundaries because of chromium carbide precipitation at grain boundaries as described by the stress corrosion model by Ford[10] given in Equation 2.

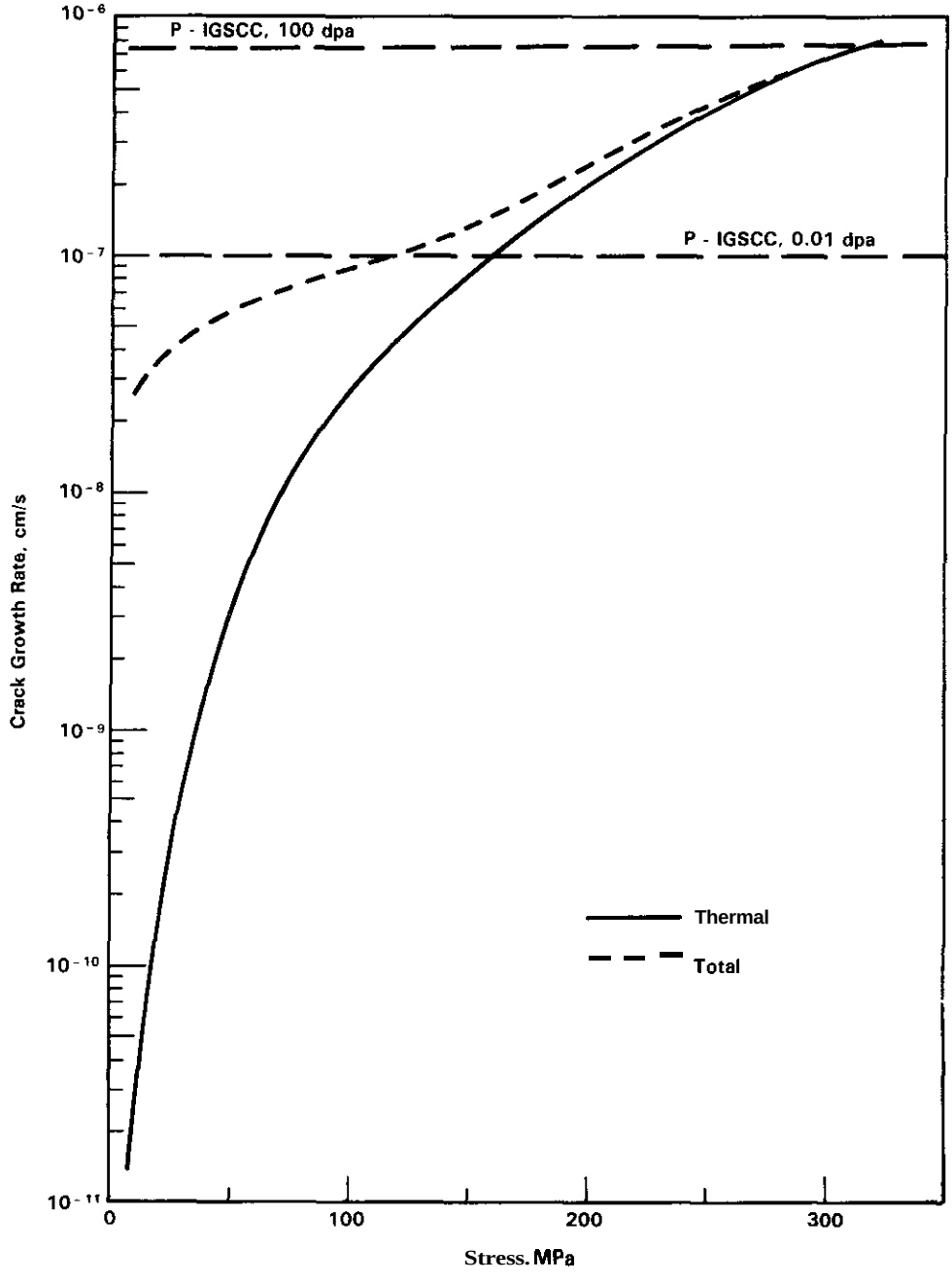

FIGURE 2. Calculated Crack Growth Rate Versus Stress for 304SS During Irradiation Based on Equation 7 and as a Result of Radiation Induced Phosphorus Segregation Based on Equation 8.

A second and less studied cause of IGSCC is that of impurity segregation (phosphorus, sulfur, etc.) to grain boundaries. In most applications, impurity segregation occurs during fabrication and only moderately during service; however, Brimhall, Baer, and Jones[13] have shown that irradiation can greatly enhance the segregation of phosphorus in austenitic steels and nickel based alloys. Also, there is evidence that phosphorus enhances the intergranular corrosion and stress corrosion of austenitic steel,[14] nickel,[11] and nickel based alloys.[15] Marcus, Oudar, and Olefjord[16] have shown that sulfur enrichment at the surface of nickel can completely eliminate passive film formation and it has also been shown" that phosphorus behaves similarly. A significant difference between sulfur and phosphorus however, is in their behavior on the surface of an anode. Phosphorus is oxidized and dissolved in the electrolyte while sulfur remains on the anode surface. Therefore, an intergranular crack propagating along a phosphorus enriched grain boundary would have a very active crack tip and relatively inactive crack walls while a crack along a sulfur enriched grain boundary would have an active tip and walls. Jones et al.[11] have shown for nickel that these two circumstances lead to rapid stress corrosion crack growth rates for phosphorus enriched grain boundaries and blunted nonpropagating cracks for sulfur enriched grain boundaries. Therefore, radiation induced phosphorus segregation is a concern for the stress corrosion behavior of 316 SS.

In an effort to estimate the effect of irradiation induced phosphorus segregation on the stress corrosion cracking of 316 SS, Jones and Wolfer[5] used the irradiation induced phosphorus segregation data of Brimhall et al.,[13] the corrosion rate versus phosphorus concentration data of Gulyaev and Chulkova[17] and Equation 1 to derive the following crack growth rate versus fluence relationship:

$$da/dt = 4.4 \times 10^{-7} + 16.1 \times 10^{-7} \log (\phi t/\phi t_o) \text{ mm/s} \quad (8)$$

where $(\phi t_o) = 0.004$.

Equation 8 is shown plotted in Figure 3 where it can be seen that a crack growth rate of 10^{-7} cmls is predicted for a fluence of 0.01 dpa and 7.5 x 10^{-7} cmls for a fluence of 100 dpa. These crack growth rates are equal to those predicted by the Ford model for chromium depletion induced IGSCC for stresses of 150 MPa and 300 MPa for the 0.01 dpa and 100 dpa fluences, respectively. The phosphorus induced stress corrosion processes are expected to be fairly independent of stress since the phosphorus enriched in the grain boundary is thought to eliminate the passive film in this vicinity and therefore the crack tip strain rate-film rupture rate relationship expressed by Equation 2 should not be a factor. The phosphorus induced stress corrosion crack growth rates are shown in Figure 2 as stress independent and suggest that at low fluences the minimum crack growth rate is 10^{-7} cmls and is dominated by phosphorus segregation up to a stress of about 100 MPa while at a high fluence the stress corrosion crack growth rate is dominated by phosphorus segregation up to a stress of 300 MPa. Both the phosphorus and chromium depletion induced intergranular stress corrosion can be significantly reduced by control of the bulk phosphorus and carbon concentrations. While the results shown in Figure 2 are calculated estimates which need experimental verification, the need to minimize the phosphorus and carbon concentrations is fairly evident.

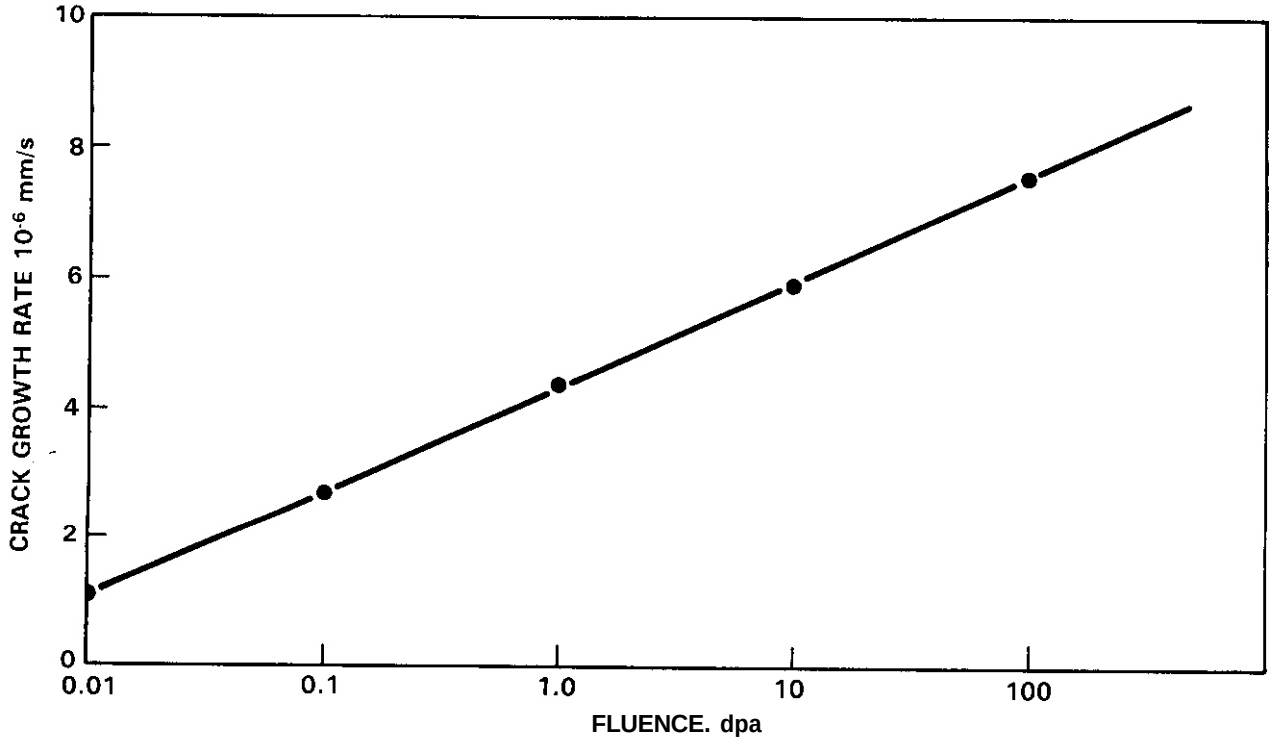

FIGURE 3. Calculated Crack Growth Rate Versus Fluence for Radiation Induced Phosphorus Segregation Based on Equation 8.

5.3.2 Hydrogen Embrittlement of HT-9

Radiation may affect the hydrogen embrittlement of ferritic steels in several ways:

- hydrogen production from (n,p) reactions, corrosion, radiolysis, and injection from the plasma,
- yield strength increase from displacement damage,
- a einbrittlement reactions fran radiation induced precipitation and segregation.

Stoltz et al.[18] calculated the steady state hydrogen concentration expected in HT-9 from (n,p) reactions and injection from the plasma and concluded that the maximum steady state concentration of hydrogen will not exceed 0.5 appm. Since this is less than the concentration present in most steels (1-5 appm), they concluded that hydrogen embrittlement would not be a concern for HT-9 during fusion reactor service. However, for a water cooled system, corrosion and radiolysis are two sources of hydrogen not considered by Stoltz et al.[18] which could produce a higher steady state hydrogen concentration. This potential for a hydrogen concentration exceeding 0.5 appm coupled with radiation induced strength increases and embrittling reactions suggests that hydrogen embrittlement of HT-9 in water cooled reactors is a possibility that should not be ignored.

Jones and Wolfer[5] have modeled the effect of phosphorus segregation to the grain boundaries of HT-9 on K_{IC} and K_{TH} with the results shown in Figures 4 and 5. These results indicate the potential sensitivity of HT-9 to radiation hardening and impurity segregation where a strength increase to 1000 MPa coupled with a grain boundary phosphorus concentration of 0.5 could reduce K_{IC} and K_{TH} to values approaching zero. The minimum toughness for a severely embrittled material is greater than zero and probably defined by the Griffith crack criterion in which the fracture energy is determined by the energy needed to create new surfaces. Brimhall et al.[13] observed 0.05 monolayers of phosphorus segregation to the free surface of HT-9 at a fluence of 0.8 dpa. Assuming the free surface segregation data is applicable to grain boundary segregation and that the segregation rate of 5%/dpa extends to higher displacements, a grain boundary phosphorus concentration of 50% could be reached in only 10 dpa. Recent data by Klueh and Vitek[19] shows that the yield strength of HT-9 at 22°C and 400°C was 1017 MPa and 872 MPa after irradiation in ERR II at 390°C to a fluence of 11 dpa. Therefore, the conditions depicted by the K_{IC} and K_{TH} curves for simultaneous increases *in* σ_y and X_p are a possibility. The ductility observed by Klueh and Vitek of 5.2% total elongation at 22°C and 3.4% at 400°C would suggest that the calculated values are extreme and that the K_{IC} would exceed that given by the lower curve in Figure 4. Huang and Gelles[20] measured the fracture toughness of irradiated HT-9 weld metal and

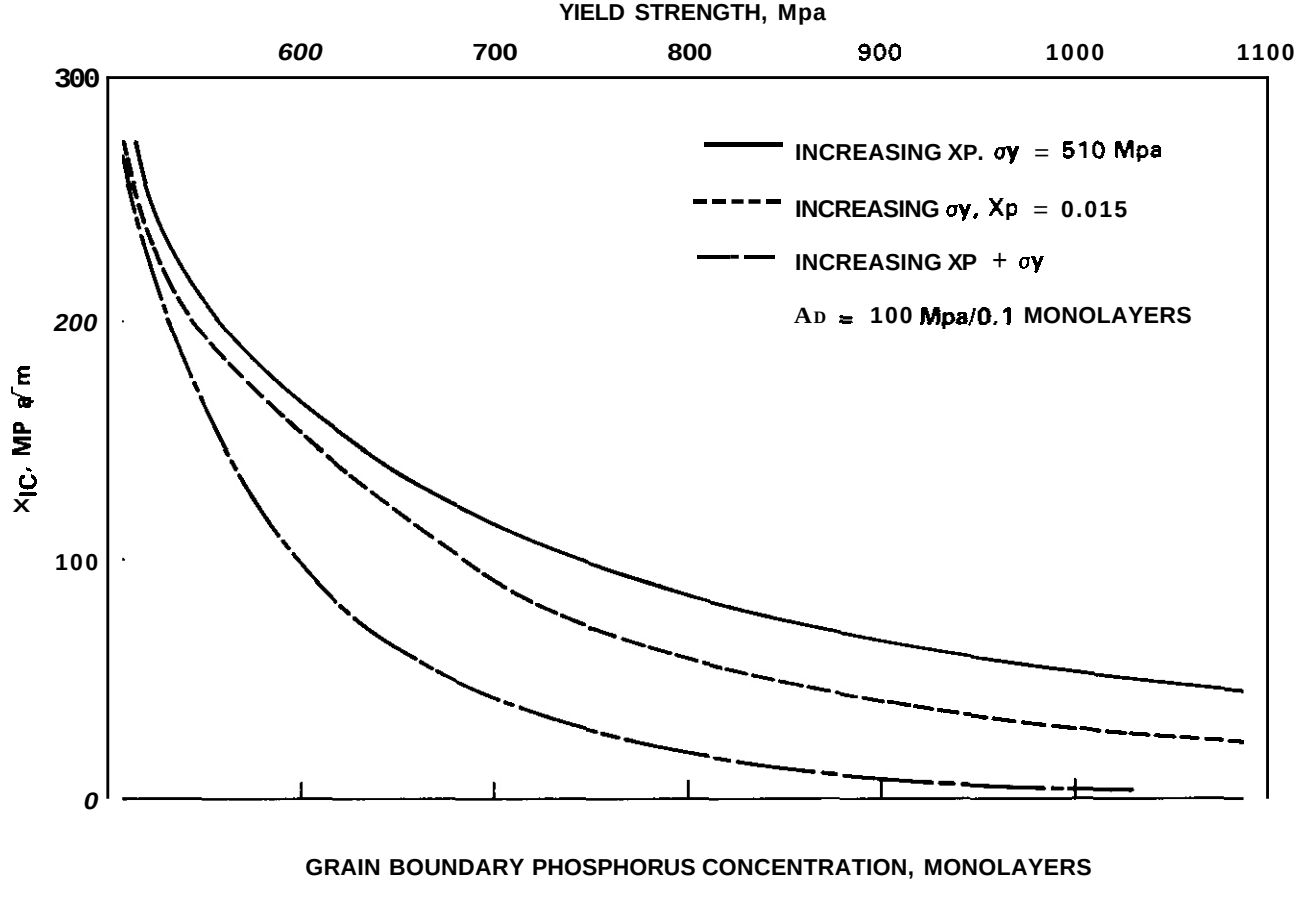

FIGURE 4. Calculated Fracture Toughness of HT-9 with Varying Grain Boundary Phosphorus Concentration and Yield Strength.

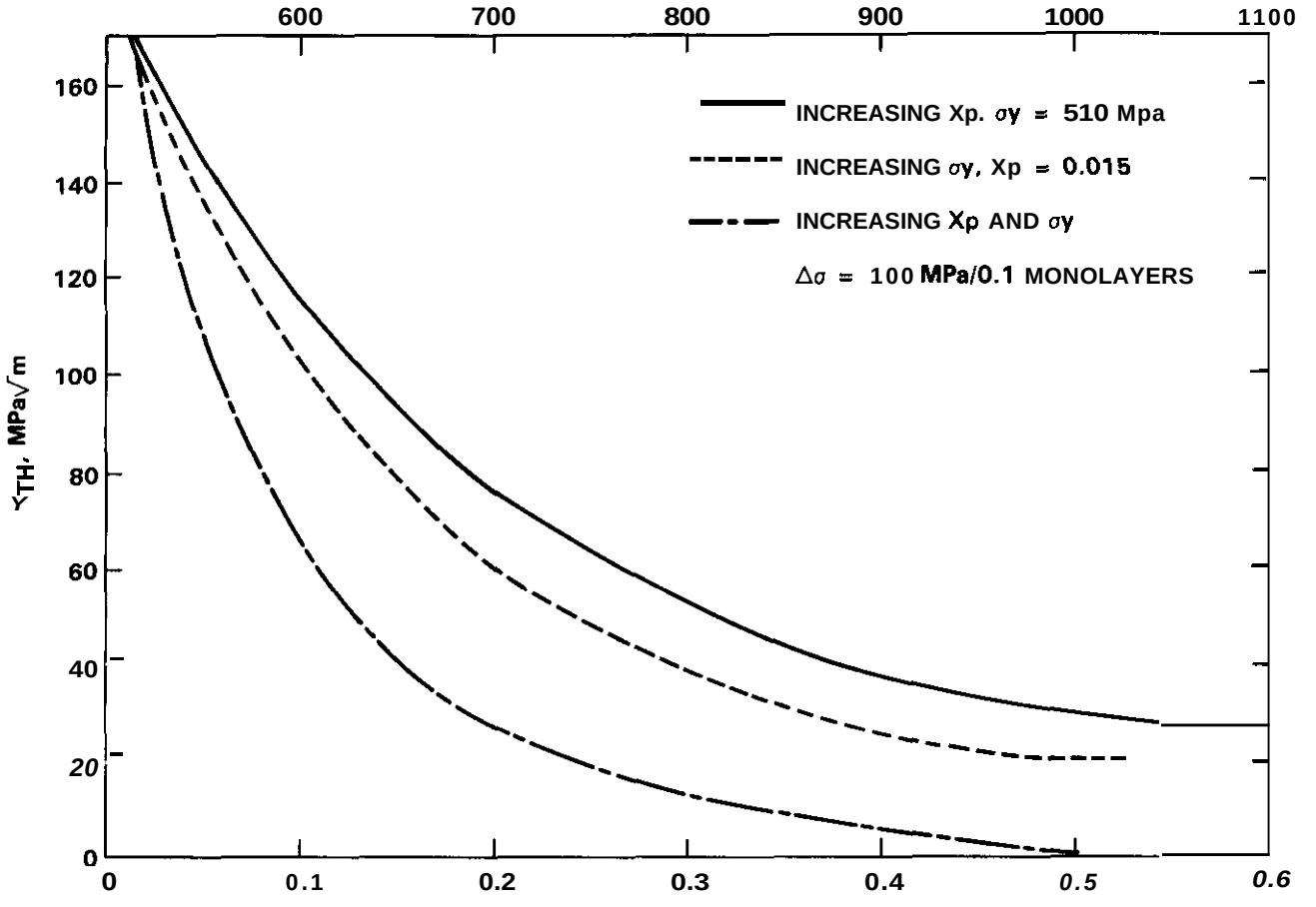

FIGURE

found that the J_{IC} of irradiated material was equal to or greater than the unirradiated. Since the calculated K_{IC} results given in Figure 4 are for plane strain conditions and the results of Huang and Gelles[20] are for plane stress conditions the results are not directly applicable; however, the calculated results suggest that a decrease in K_{IC} from 273 MPa $\sqrt{m}$ should result from a strength increase to 900 MPa. Clearly, the calculated results are qualitatively if not quantitatively inconsistent with the experimental results. The cause of this inconsistency is not presently known but will be the subject of further evaluation as more fracture toughness data for irradiated material becomes available.

6.0 References

1. A. V. Byalobzhesky, 3rd International Congress on Metallic Corrosion, Swets and Zeitlinger, Amsterdam, p. 287, 1966.

2. J. J. Stobbs and A. J. Swallow, Met. Rev. 1962 7(25), p. 95.

3. R. A Van Konynenberg and R. D. McCright, 'Radiation Effects on Tube Denting in the Steam Generators of Pressurized Water Reactors," Feb. 1980, UCRL-52892, Lawrence Livermore Laboratory, Livermore, CA, 31 pages.

4. J. L. Nelson, R. E. Westerman, and F. S. Gerber, "Irradiation-Corrosion Evaluation of Metals in Grande Ronde Basalt Groundwater for Nuclear Waste Package Applications" RHO-BW-SA-316A P, Presented at Materials Research Society Symposium - Scientific Basis for Nuclear Waste Management, Boston, MA, Nov. 14-17, 1983.

5. R. H Jones and W. G. Wolfer, "Modeling Crack Growth Processes in Fusion Reactor Materials," Third Fusion Reactor Materials Meeting, Albuquerque, NM, Sept. 1983.

6. N. Fujita, M Akiyama, and T. Tamura, Corrosion 37(6), p. 335, 1981.

7. M. Kuribayashi and H. Okabayashi, J. Jpn. Inst. of Metals 46, p. 170, 1982.

8. S. N. Votinov, Y. I. Kazemov, V. L. Rogoyavlenski, V. S. Belokopytov, E. A. Krylov, L, M. Klestova, and L. 1. Reviznikou, Translated from Atornnaya Energiya 41(6), p. 405, Dec. 1976.

9. O. A Vermilyea, Stress Corrosion Cracking and Hydrogen Embrittlement of Iron Base Alloys, eds. R. W. Staehle, J. Hochmann, R. D. McCright, and J. E. Slater, NACE-5, p. 208, 1973.

10. F. P. Ford, "Mechanisms of Environmental Cracking in Systems Peculiar to the Power Generation Industry," EPRI NP-2589, Electric Power Research Institute, Palo Alto, CA, 1982.

11. R. H. Jones, M. J. Danielson, S. M. Bruemmer, D. R. Baer, and M. T. Thomas, "Contributions of Segregated Phosphorus to the Intergranular Stress Corrosion Cracking of Nickel," In proceedings of a TMS-AIME symposium on "Localized Crack Chemistry and Mechanics in Environment Assisted Cracking," R. P. Gangloff, ed., October 1983.

12. J. L. Straalsund. "Irradiation Creep in Breeder Reactor Structural Materials" in Radiation Effects in Breeder Reactor Structural Materials, p. 191. M L. Bleiberg and J. W. Bennett, eds, American Institute of Mining, Metallurgical and Petroleum Engineers, N.Y., NY, June 1977.

13, J. L. Brimhall, D. R. Baer, and R. H. Jones, J. of Nucl. Mater. 17, p. 218, 1983.

14. C. L. Briant, Corrosion 36, p. 497, 1980.

15. M. Guttmann, Ph. Dumoulin, N. Tan-Tai and P. Fontaine, Corrosion 37, p. 417, 1981.

16. P. Marcus, J. Oudar, and I. Olefjord, Matl. Sci. and Engr. 42 p. 191, 1980.

17. A. P. Gulyaev and V. M Chulkova, Prot. Met. USSR 12, p. 259, 1970.

18. R. E. Stoltz, M. I. Baskes, and G. W. Look, "Calculations of Hydrogen Isotope Loading in HT-9 First Wall Structures," ADIP Quarterly Report, DOE/ER-0045/14, pp. 151-159, September 30, 1980.

19. R. L. Klueh and J. M. Vitek, Alloy Development for Irradiation Performance Semi-Annual Progress Report for Period Ending March 31, 1983, DOE/ER-0045/10, p. 104, 1983.

20. F. H. Huang and D. S. Gelles. ibid, p. 125.

7.0 Future Work

The effects of phosphorus segregation to the grain boundaries of 316 SS on intergranular stress corrosion cracking will be evaluated experimentally. The grain boundary chemistry will be established by thermal treatments and measured by Auger electron spectroscopy. Measurements of hydrogen uptake and embrittlement of HT-9 and 316 SS in a ^{60}Co γ source are being considered. Further modeling of hydrogen effects on crack growth behavior in HT-9 will be done to improve the correlation between calculated and experimental K_{IC}, to include temperature effects and dynamic crack growth.

STRENGTH AND MICROSTRUCTURE IN VANADIUM IRRADIATED HITH T(d,n) NEUTRONS AT 300K, 475K, and 675K

E. R. Bradley (Pacific Northwest Laboratory)

1.0 Objective

The purpose of this work is to determine the effects of 14-MeV neutron irradiation on the strength and microstructure in materials whose properties are sensitive to interstitial impurities. The ultimate application of this work is to identify potential impurity limits for the successful operation of fusion reactors.

2.0 Summary

Tensile tests and microstructural examinations have been conducted on vanadium wires and foils containing 1300 wt-ppm interstitial impurities following T(d,n) neutron irradiation at 300K, 475K, and 675K. Tensile results from wire samples show similar increases in yield strength for samples irradiated at 300K and 475K but strengthening decreased significantly following irradiation at 675K. SEM examination of the fracture surfaces showed all samples failed by ductile rupture after attaining more than 95%reduction in area. A reasonable correlation hetween microstructures and strengtheninp was obtained using a simple dispersed barrier strengthening model. A high density of extremely small (<7 nm diam.) defect clusters was responsible for the observed strengthening after irradiation at 300K. Following irradiation at 475K, interstitial loops with a<100> Burgers vectors were the predominant Strengthening defect with a smaller contribution from a/?<111> type loops. A heterogeneous distribution of dislocation loops and planar precipitates prevented definite correlations hetween strength and microstructure in samples irradiated at 675K from being made.

3.0 Program

Title: Mechanical Properties
Principal Investigator: R. H. Jones
Affiliation: Pacific Northwest Laboratory

4.0 Relevant DAFS Program Plan Task/Subtask

Subtask II.c.6 Effects of Damage Rate and Cascades on Microstructures
Subtask II.c.11 Effects of Cascades and Flux on Flow
Subtask II.c.18 Relating Low- and Migh-Exposure Microstructures

5.0 Accomplishments and Status

5.1 Introduction

Interstitial impurities are known to have a strong effect on the microstructures and mechanical properties neutron irradiated metals[1,2,3,4]. Structural materials for fusion reactors will contain interstitial impurities from fabrication, processing, and reactor operation; hence, it is important to study the effects nf these impurities on microstructure and properties in materials irradiated with high-energy neutrons.

Interstitial impurities affect radiation strenathening by interacting with point defects and changing the distribution and/or effectiveness of irradiation produced obstacles to dislocation motion. Bajaj and Wechsler[2] reported the defect cluster density increased and the average cluster size decreased with

increasing oxygen content in vanadium irradiated with fission neutrons at 375K. The differerce in microstructures was attributed to nucleation of defect clusters at oxygen atoms or oxygen-point defect complexes. A similar effect of oxygen on defect cluster density and size was also found in irradiated niobium by Loomis and Gerber[3]. In both studies, changes in the cluster distributions were the prinary cause of differences in radiation strengthening as measured by yield strength increases. Evidence for interstitial impurities increasing the barrier strength of defect clusters comes primarily from radiation-anneal hardening (RAH) studies in vanadium[2,5] and niobium[6]. Additional strenqthening is often observed in these metals followinu post-irradiation annealing at the temperatures hetween 450K and 700K. Gold and Harrod[5] reviewed RAH in vanadium and concluded the most probable mechanism was the migration of interstitial impurities to defect clusters, thereby increasing their effectiveness as barriers to dislocation motion.

The present work examines the strength and microstructures in vanadium containing 1300 wt-ppm interstitial impurities following T(d,n) neutron irradiation at temperatures where the interstitial impurities become mobile. Emphasis is place on the temperature dependence since the fluence dependence was discussed previously for the ambient temperature irradiations'. Future reports will examine the temperature dependence in niobium containing two levels of oxygen.

5.2 Experimental Procedures

VP grade vanadium wire, 0.5 mm diameter, was ohtained from Materials Research Corporation and foil material was prepared from the wire stock by cross-rolling to about 0.1 mm. Wire samples for tensile testing were annealed in vacuum (10^{-4} Pa) for 1 hour, straightened by a small amount of plastic deformation and, annealed for an additional hour prior to irradiation. Annealing temperature was 1225K which produced equiaxed grains of 25 μm diameter in the wire samples. The same annealing treatment was used an the foil materials. Chemical analysis of the wire materials indicated a total interstitial impurity content. of 1300 wt-ppm with oxygen heing the primary impurity, 920 wt-ppm.

Wire and foil samples were irradiated as part of the Japanese/PNL elevated temperature irradiation experiment conducted at the RTNS II facility at Lawrence Livermore National Laboratory (LLNL). The experiment used the dual-temperature vacuum-insulated furnace system that was desianed and fabricated at Hanford Engineering Development Laboratory (HEDL). Temperatures of the two furnace zones were maintained at 475K and 675K during the irradiation. The vacuum measured at the ion pump was less than $5x10^{-5}$ Pa although somewhat higher pressures would be expected in the sample chambers.

Two niobium foil capsules, 13x6x1 mm^3, containing the wire and foil samples were irradiated in each temperature zone. The capsules were positioned 1 nn and 6 mm from the front surface of stainless steel samples holders which enabled two fluence levels to be obtained at each temperature. Neutron fluence was determined from iron dosimeter foils which were counted and reported by personnel at LLNL. The results indicate fluence levels of 3 and $10x10^{21}m^{-2}$ for samples irradiated at 475K, while at 675K, the corresponding fluence levels were 3 and $6x10^{21}m^{-2}$. The difference in fluence levels indicates the neutron beam was offset slightly from the furnace centerline. Irradiation conditions for the 300K irradiation have been presented previously'.

Gage sections (0.25 by 3mm) were produced at the center of 12 mm long wire samples by electropolishing. The minimum diameter along the gage sections was measured with an optical microscope equipped with a calibrated eyepiece. The average of five measurements around the sample circumference was used to calculate tensile properties. The same procedures were used for preparing and measuring the 0.25 by 5 mm gage sections in 35 mm long wire samples from the 300K irradiations. Flow stress determinations were made by uniaxially straining the wire samples at room temperature in an Instron tensile testing machine. The average strain rate was about $6x10^{-4}$, hut local variation would exist because of the tapered nature of the electropolished gage sections. The samples were held in split grips and grip displacement was measured by a linear variable differention transformer (LVDT). The average tensile properties for a given material and fluence were determined from five to ten samples.

Thin foils for transmission electron microscopy were prepared by electropolishing and examined in a Phillips EM 400T electron microscope. Defect Cluster/loop diameters were measured from TEM photomicrographs using a calibrated 10x eyepiece. Stereomicrographs were used to measure foil thicknesses for estimating defect densities. The accuracy of the size and density measurements were estimated to be ±15 and ±30 percent respectively.

5.3 Results

5.3.1 Microstructures

Microstructures of the irradiated vanadium were strongly dependent on irradiation temperature as shown by Figure 1 and the data in Table 1. Irradiation at 300K produced a high density of very small defect clusters or loops. The type and nature of the defects were not identified because of their small size and high density. However, it is reasonable to assume a/2<111> type loops based on previous studies of fission neutron irradiated vanadium. The measured sizes and densities of the defects are in reasonable agreement with fission neutron irradiated vanadium when consideration is given to differences in impurity concentrations and the greater efficiency of 14-MeV neutrons in producing microstructural damage.

TABLE 1

MICROSTRUCTURAL DATA FROM T(d,n) NEUTRON IRRADIATED VANADIUM

Irradiation Temperature K	Neutron Fluence m^{-2}	a<100> Loop Diameter nm	a<100> Loop Density m^{-3}	a/2<111> Loops Diameter nm	a/2<111> Loops Density m^{-3}
300	$8x10^{21}$	-	-	2.5	$5x10^{22}$
	$2x10^{22}$			3.5	$\sim 1x10^{23}$
473	$3x10^{21}$	21	$2.1x10^{21}$	3.5	$6.0x10^{21}$
	$1x10^{22}$	15	$8.0x10^{21}$	4.5	$3.9x10^{21}$

The predominant feature of the microstructures following irradiation at 475K was the appearance of interstitial loops with a<100> type Burgers vectors lying on (100) planes. These loops were uniformly distributed throughout the grains except for denuded regions at grain boundaries. Loop density increased with neutron fluence but, surprisingly, loop diameter decrease at the higher fluence level. This decrease in loop size could be attributed to either a difference in neutron flux or temperature between the two sample positions. Neutron flux was a factor of three higher at the high fluence position which could have affected loop nucleation and growth. Alternatively, heat losses from the furnace front could have reduced the irradiation temperature for samples irradiated to the higher fluence level and thereby decreased their size. Since the furnace was designed to minimize axial temperature gradients, differences in neutron flux are most likely responsible for the differences in measured loop diameters.

In addition to the a<100> type loops, smaller diameter a/2<111> loops were identified in samples irradiated at 475K. These small loops were distributed throughout the grains, but were most evident along grain boundaries where the larger a<100> loops were not present, Figure 2. The lack of a grain boundary denuded zone for the a/2<111> loops suggests they are vacancy loops; however, positive identification was not made. No large differences in size or density of the small loops was observed between the two fluence levels examined. The measured diameters show a small increase, 1 nm, while the density decreased somewhat at the higher fluence level. These differences are generally within the experimental uncertainty for analyzing small defects.

Increasing the irradiation temperature to 675K produced a heterogeneous distribution of dislocation loops and planar precipitates, Figure 1 c and d. Loop size and density varied locally within a given grain and also from one grain to another. Loop diameters ranged from 5 to 70 nm with densities below $2x10^{20}m^{-3}$. Precipitates were observed at grain boundaries, along existing dislocations, and within the matrix. Similar precipitate distributions were also observed in unirradiated samples vacuum annealed for 300 hours at 675K. This indicates that precipitation was thermally activated although irradiation may have enhanced the precipitation process. Isolated precipitates were also observed following the lower temperature irradiations which tends to support irradiation enhanced precipitation in agreement with previous studies of fission neutron irradiated vanadium[8,9].

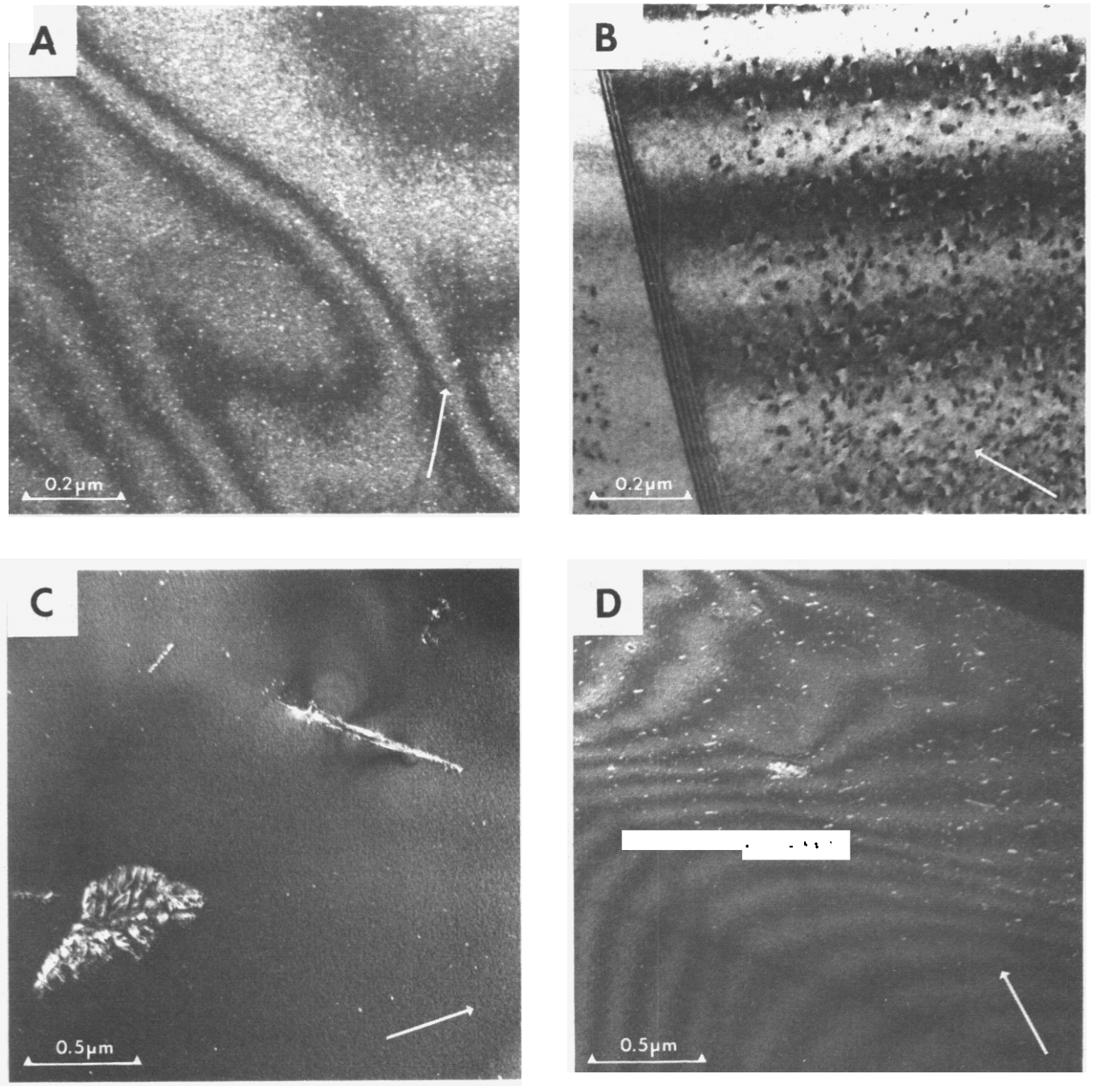

FIGURE 1 **Effect rf Irradiation Temperature on Microstructure in T(d,n) Neutron irradiated Vanadium:** a) T = 300K Øt = $8x10^{21}m^{-3}$, g/3g g = [110]; b) T = 475K Øt = $1x10^{22}m^{-2}$, g = [110]; c and d) T = 675K Øt = $6x10^{21}m^{-2}$, g/3g g = [110]. **(Arrows Indicate Direction of g)**

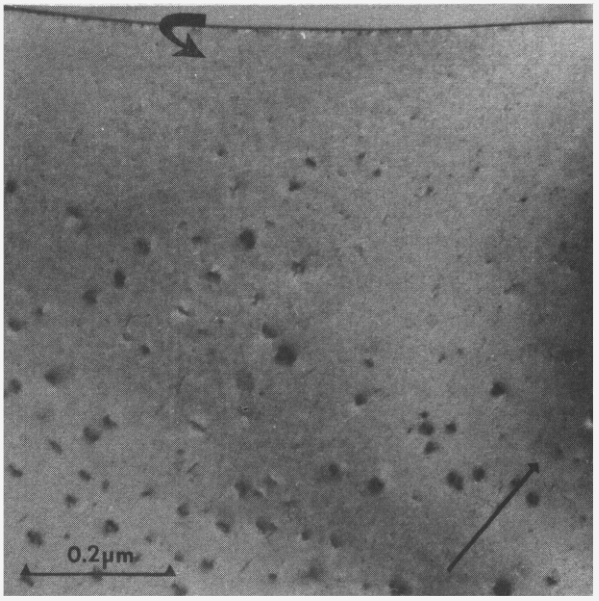

FIGURE 2. Dislocation Loops in Vanadium Irradiated at 475K, $\phi t = 3x10^{21}m^{-2}$. Note Small a/2<111> Type Loops Within Grain Boundary Denuded Region of the Larger a<100> Type Loops. $\underline{g} = [200]$

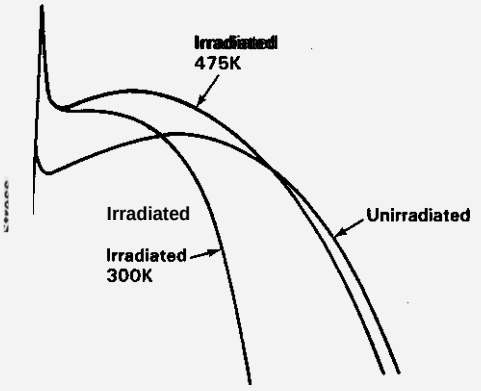

FIGURE 3. Effect nf Irradiation Temperature on Stress-strain Behavior of Vanadium Wires.

5.3.2 Tensile Properties

Results from tensile tests of the irradiated and unirradiated vanadium wire samples are summarized in Table 2. The average tensile properties and standard deviations that were obtained from five to ten individual samples are given. Standard deviations in the strength properties were generally less than 10% of the average. The lower yield strength data were more reproducible and were used to evaluate radiation strengthening. Uniform and total elongation data represent the average elongation along the tapered gage sections as measured at the ultimate tensile strength and failure, respectively. Since strain varies locally along a tapered gage section, the primary value of these data is determining the relative changes produced by irradiation in samples of similar geometry.

The effect of irradiation temperature on the stress-strain behavior of the wire samples is shown schematically in Figure 3. Stress-strain curves for the unirrradiated wires can be described by upper and lower yield points followed by a region where the stress increased to the ultimate tensile strength wherein plastic instability led to failure. Irradiation reduced the strain-hardening portion of the flow curves and its effect increased with decreasing irradiation temperature. Plastic instability occurred immediately after yielding and the ultimate tensile strength (UTS) equaled the lower yield strength (LYS) for samples irradiated at 300K to fluence levels above $3x10^{21}m^{-3}$. Irradiation at 475K reduced the difference between the UTS and LYS by about 50% and slightly decreased the uniform elongation, Table 2. Little change in the stress-strain behavior was observed following irradiation at 675K.

Although differences were observed in the stress-strain behavior, tensile fracture was quite independent of irradiation or irradiation temperature. Examination of fractured tensile samples by scanning electron microscopy (SEM) showed failure occurred by ductile rupture after extensive plastic deformation. No significant differences in the fracture surfaces between unirradiated or irradiated samples were observed; all samples examined showed more than 95% reduction in area at fracture. Typical electron micrographs are shown in Figure 4.

TABLE 2

SUMMARY of VANADIUM WIRE TENSILE DATA

Irradiation Temperature	Neutron Fluence m^{-2}	UYS MPa	LYS MPa	UTS MPa	Uniform* Elongation %	Total* Elongation %
300K	0	470±30	393±30	493±30	8	19
	$1x10^{21}$	495±15	350±30	392±20	7	14
	3x1021	565	402	410±30	-	11
	6x1021	555±110	430±15	480±15	-	11
	$8x10^{21}$	590±90	445±30	445±30	-	11
473	0	425±30	371±14	452±20	9	23
	3x1021	528±49	425±20	463±22	8	25
	$1x10^{22}$	509	470±12	498±15	6	21
673	0	392±21	348±12	475±15	10	23
	$3x10^{21}$	396±17	360±12	429±9	11	27
	6x1021	419±12	385±17	452±14	11	26

* Average Elongation over gage section.
Local Elongation would be greater.

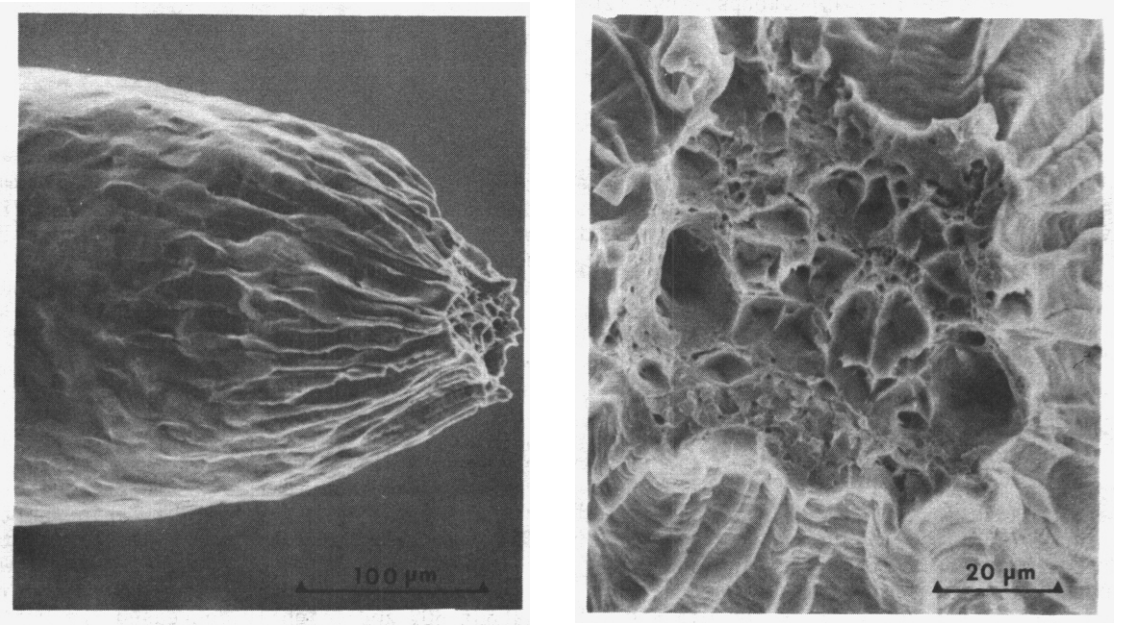

FIGURE 4. Scanning Electron Micrographs Showing Fracture Characteristics of Vanadium Wire Tensile Samples.

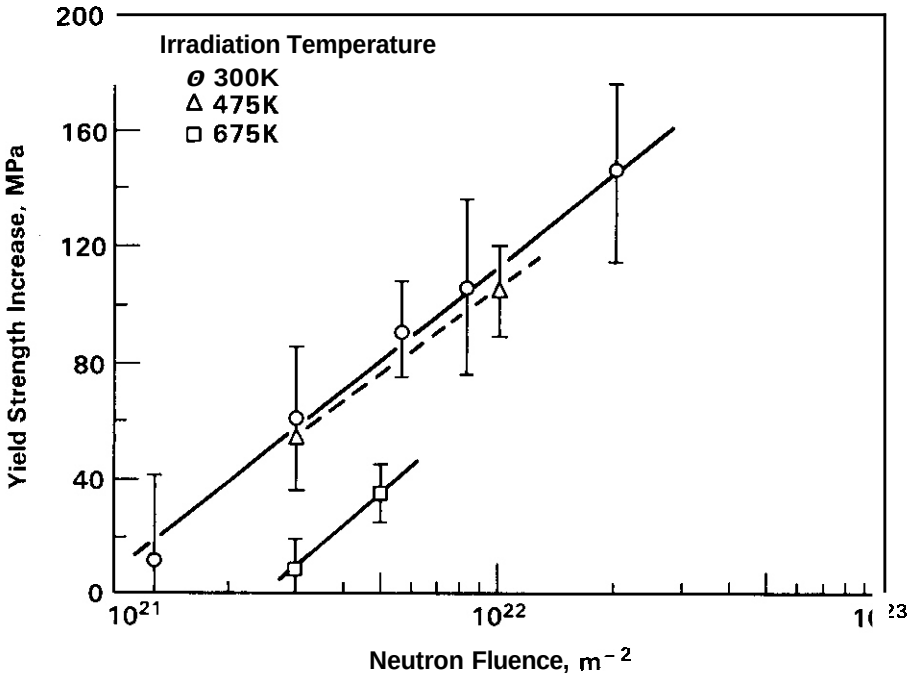

FIGURE 5. Yield Strength Increase Versus Fluence For T(d,n) Neutron Irradiated Vanadium.

Radiation strengthening was independent of irradiation temperature from 300K to 475K, but decreased following irradiation at 675K. This is shown in Figure 5 where the increases in lower yield strength as a function of neutron fluence are compared. Measurable strengthening began at a fluence of about $1x10^{21}m^{-2}$ and increased to 140 MPa at $2x10^{22}m^{-2}$ for samples irradiated at 300K. These data approximately follow a $(\emptyset t)^{\frac{1}{2}}$ fluence dependence which is consistent with Thompson's analysis of radiation induced defect strengthening[10]. The small defect clusters provide the obstacles to dislocation movement. Yield strength increases following irradiation at 475K were within 10% of the values from the 300K irradiated sariples although large differences in microstructure were observed. The similar size and density for the small a/2<111> type loops at the two fluence levels suggests the larger a<100> loops are the primary cause of the observed strengthening. Smaller defect production at 675K shifted the strengthening response in these samples to higher fluence levels. The measured yield strength increase at a fluence of $6x10^{21}m^{-2}$ was about 50% lower than for irradiation at 300K or 475K.

5.4 Discussion

5.4.1 Microstructures

Microstructures of the T(d,n) neutron irradiated vanadium agree reasonably well with previous studies of fission neutron irradiation except for the a<100> type dislocation loops observed following irradiation at 475K. Precipitates are commonly observed in vanadium irradiated at elevated temperatures and attributed to interstitial impurities[8,9]. The present results suggest precipitation was thermally activated since sinilar precipitates were observed following vacuum annealing for 300 hours at 675K. Irradiation may have enhanced the precipitation process, but sufficient data are not available to establish the contribution from irradiation. In accordance with the present results, high densities of small defect clusters have been reported in vanadium following fission neutron irradiation at ambient reactor temperatures, i.e., < 375K. Interstitial impurities affect the defect distributions as demonstrated Bajaj and Wechsler[2,11] where the defect cluster size decreased and density increased with increasing oxygen concentrations. A similar effect of oxyaen on defect distribution was also observed in niobium by Loomis and Gerber[3]. The changes in defect distributions were attributed to increased cluster nucleation at oxygen atoms or oxypon-defect complexes. Direct quantitative comparisons of cluster size and density between fission and T(d,n) neutron irradiations is not possible because of differences in material purity, fluence levels, irradiation temperature, and neutron energy. However, the present results indicate higher densities of smaller clusters than generally observed after fission neutron irradiation[11] which is consistent with the high level of interstitial impurities in the T(d,n) neutron irradiated vanadium.

Although a<100> loops have not previously been reported in irradiated vanadium, their formation was not totally unexpected since they have been observed in iron and ferritic alloys following irradiation with neutrons[12-14], 1 MeV electrons[15], and heavy ions[16]. Little et al. proposed a model to account for the experimental observations in ferritics and suggested a<100> loops should also form in vanadium and niobium[14]. The model is based on Eyre and Bullough's model for loop nucleation in bcc metals[17] and assumes a small probability for forming a<100> interstitial loops relative to the more common a/2<111> type interstitial loops. The a<100> loops grow by preferential interstitial capture while the more numerous a/2<111> interstitial loops shrink and eventually disappear by a net influx of vacancies. The experimental data for the a/2<111> type loops in Table 1 agree qualitatively with this model if both interstitial and vacancy loops are assumed present at the lower fluence level. Growth of the vacancy loops would provide the observed increase in loop size while the total loop density would decrease by elimination of small interstitial loops. However, the density of the larger a<100> is much greater thar predicted by the model. Calculations, using 5.5×10^{-5} as the relative probahility for forming a<100> loops in vanadium[14] and the measured cluster density following T(d,n) neutron irradiation at 300K, i.e., $1 \times 10^{23} m^{-3}$, indicate an a<100> loop density of $5.5 \times 10^{18} m^{-3}$ compared to $8 \times 10^{21} m^{-3}$ measured experimentally in the high fluence sample. This large difference in density suggests other factors may contribute to the formation of a<100> type dislocation loops.

The reason a<100> have not previously been found in irradiated vanadium may be related to the interstitial impurity concentration. Shiraishi et al.[18], and Horton and Farrell[8] examined the microstructures of vanadium irradiated near 475K and reported only a/2<111> dislocation loops. In both studies, the total interstitial impurity concentrations were less than 350 wt-ppm compared to 1300 wt-ppm for the vanadium used in the present study. Oxygen and carbon atoms become mobile at about 340K and it seem reasonable that interaction between these mobile impurities and vanadium interstitial atoms could promote nucleation of the a<100> loops. However, a specific mechanism for this interaction is not known. Neutron energy is not considered a viable explanation for the difference in loop structure because a<100> loops formed in mild steel during 1 MeV electron irradiation's where Frenkel pair defects are created. Future experiments using niobium with two oxygen impurity levels may clarify the role of interstitial impurities in nucleating the a<100> type loops.

5.4.2 Strength-Microstructure Correlations

The strengthening produced hy T(d,n) neutron irradiation in vanadium, Figure 5, can be predicted from the microstructural data in Table 1 using a simple dispersed barrier model. Small defect clusterslloops provide the barriers to dislocation motion in samples irradiated at 300K while both a<100> and a/2<111> type dislocation loops contribute to strengthening the 475K irradiated samples. The contribution to the strength increase for each microstructural component was estimated from the relation

$$\Delta\sigma = \frac{2\,\mu\,b}{\beta\,\bar{\ell}}$$

where $\Delta\sigma$ = yield strength increase,
$\bar{a}$ = average interbarrier distance which is equal to $(Nd)^{-\frac{1}{2}}$,
N = barrier density,
d = barrier diameter,
μ = shear modulus (4.63×10^4 MPa),
b = Burgers vector of slip dislocation (0.263 nm),
β = a constant which is related to the barrier strength.

The increase in yield strength was calculated with a relation such as proposed by Koppenaal and Kuhlmann-Wilsdorf[19]

$$\Delta\sigma_{total} = (\Delta\sigma_1^2 + \Delta\sigma_2^2)^{\frac{1}{2}}$$

where $\Delta\sigma_1$, and $\Delta\sigma_2$ are the contributions from the a/2<111> and a<100> type dislocation loops, respectively.

The best correlation with the experimental data from each irradiation temperature was obtained by varying β_1 and β_2 incrementally between 2 and 6. For samples irradiated at 300K, only one microstructural component was considered and the best correlation was nbtained using a value of 3 for β_1. The calculated yield strength increases were 90 and 151 MPa compared to 105 and 145 MPa increases measured experimentally. Previous studies of radiation strengthening from small defect clusters in a variety of materials have found β values ranging from 2 to 4[6,20-23] which is consistent with the present results. The best correlation with the experimental data from samples irradiated at 475K was obtained using $\beta_1 = 6$ for the a/2<111> loops and $\beta_2 = 2.6$ for the a<100> loops. The corresponding calculated and experimental yield

strength increases were 64 and 60 MPa, respectively, for the low fluence data and 103 MPa compared to 105 MPa at the higher fluence. The large differences in β indicates the a/2<111> loops are weak barriers compared to the a<100> loops. This is consistent with the larger displacement vector and stress field associated with a<100> type loops. However, the correlation was based on limited data using a simplified model and quantitative comparisons ere not considered reliable. Reasonable correspondence between calculated and measured yield strength increases could also be obtained using other combinations for β_1 and β_2.

5.5 Conclusions

Radiation strengthening in T(d,n) neutron irradiated vanadium containing 1300 wt-ppm interstitial impurities was independent of irradiation temperature at 300K and 475K but decreased at higher temperatures. Small diameter defect clustersIloops were the radiation-produced obstacles to dislocation motion in samples irradiated at 300K. Dislocation loops with a<100> type Burgers vectors provided most of the strengthening in 475K irradiated samples with a smaller contribution from a/2<111> type loops. A dispersed barrier model shows good agreement with the experimental data from samples irradiated at 300K and 475K, but heterogeneous distributions of dislocation and precipitate structures did not allow the strenghtening mechanism to be identified in samples irradiated at 675K.

6.0 References

1. D. F. Hasson and R. J. Arsenault, Rad. effects 21, p.203, 1974.
2. R. Bajaj and M. S. Wechsler, in Fundamental Aspects of Radiation Damage in Metals, CONF-751006-P2, p.1010, 1975.
3. B. A. Loomis and S. B. Gerber, Acta Met. 21, p.165, 1973.
4. E. R. Bradley and R. H. Jones, in Proceedinas of the Third Fusion Reactor Materials Meetinq, Albuquerque, NM, September 1983.
5. R. E. Gold and D. L. Harrod, Inter. Met. Rev. 5&6, p.232, 1980.
6. S. M. Ohr, R. P. Tucker, and M. S. Wechsler, Phys. Stat.Sol.(a) 2, p.559, 1970.
7. E. R. Bradley and R. H. Jones, J. Nuclear Matl. 103 & 104, p.901, 1981.
8. L. L. Horton and K. Farrell, in Proceedings of the Third Fusion Reactor Materials Meetinq, Albuquerque, NM, September 1983.
9. F. W. Wiffen and J. O. Stiegler, Trans. Am. Nucl. Soc. 53, p.119, 1969.
10. M. W. Thompson, Defects and Radiation Damage in Metals, Cambridge Univ. Press, p.344, 1969.
11. R. Bajaj and M. S. Wechsler, Met. Trans. 7A, p.351, 1976.
12. L. L. Horton, "A Transmission Electron Microscope Study of Fusion Environment Radiation Damage in Iron and Iron-Chromium Alloys", ORNL/TM-8803, 1982.
13. D. S. Gelles, J. Nucl. Mnter. 108 & 109, p.515, 1982.
14. E. A. Little, R. Rullough, and M.H. Wood, Proc. Roy. Soc. London) A372, p.565, 1980.
15. E. A. Little and R. L. Eyre, Met. Sci. J. 71, p.100, 1973.
16. B. C. Masters, Phil. Mag. 11, p.881, 1965.
17. R. L. Eyre and R. Bullough, Phil. Mag. 12, p.31, 1965.
18. K. Shiraishi, K. Fukaya, and Y. Yatano, J. Hucl. Mater. 44, p.59, 1972.
19. T. J. Koppenaal and D. Kuhlmann-Wilsdorf, Applied Physics Letters 4, p.59, 1964.
20. F. Kroupa and P. B. Hirsch, Disc. Faraday Soc. 38, p.49, 1964.

21. A. J. E. Foreman, Phil. Mag. 17, p.353, 1968.

22. R. L. Fleischer, Acta Metall. 10, p.385, 1962.

7.0 Future Work

Tensile tests and transmission electron microscopy will be used to determine the strength and microstructures in niobium samples containing two levels of oxygen following irradiation at 475K and 675K. These samples were irradiated with the vanadium and are currently heing prepared for ***testing.*** The results will be compared to those from 300K irradiated samples to determine the dependence of irradiation temperature on strength and microstructures in these materials.

CHAPTER 5

CORRELATION METHODOLOGY

CORRELATION OF IRKADIATEO 20% CW 316 STAINLESS STEEL FRACTURE TOUGHNESS WITH TEST TEMPERATURE

R. L. Simons and M. L. Hamilton (Hanford Engineering Development Laboratory)

1.0 Objective

The objective *of* this effort is to develop correlation equations for the fracture toughness of irradiated 70% CW 316 SS as a function of test temperature.

2.0

A three parameter function was developed to correlate fracture toughness (J_{Ic}) in 20% CW 316 SS as a function *of* test temperature. The equation is applicable for the exposure range 40 to 60 dpa, irradiation temperature range 643 to 680°K, and test temperature range 293 to 923°K.

3.0

Title: Irradiation Effects Analysis (AKJ)
Principal Investigator: 0. G. Ooran
Affiliation: Hanford Engineering Development Laboratory

4.0 Relevant DAFS Plan Task/Subtask

Subtask II.C.I Effects *of* Materials Parameters on Microstructure

Subtask II.C.8 Effects of Helium and Displacements on iracture

Subtask II.C.14 Model of Flow and Fracture Under Irradiation

5.0 Accomplishments and Status

5.1 Introduction

In order to determine the lifetime of first-wall or structural components of fusion devices exposed to high neutron damage exposures, it will be necessary to evaluate the elastic-plastic fracture behavior of the component. The fracture toughness (J_{Ic}) is a material parameter needed in the analysis. An empirical equation was developed describing the J_{Ic} behavior in 20% CW 316 SS as a function of test temperature and applicable to damage exposures ranging from 40 to 60 dpa and irradiation temperatures ranging from 643 to 688°C. The results will be submitted for inclusion in the Materials Handbook for Fusion Energy Systems[1] (MHFES).

5.2 Data Source

The compact tension specimens used for fracture toughness tests were fabricated from sections of Duct X231 (Heat 81594) of 20% CW 316 SS following irradiation in the P14A experiment in EBRII[2]. Since austenitic stainless steels generally exhibit elastic-plastic oehavior, the J-integral approach was used to measure the ductile fracture toughness of First Core steel. The J values determined for irradiated and unirradiated specimens, and their corresponding yield and ultimate tensile strengths are listed in Table 1. Tnr 0.040 inch thick specimens satisfied the thickness reauirement for a valid J_{Ic} determination.

TABLE 1

FRACTURE TOUGHNESS DATA FOR 20% CW AISI 316 STAINLESS STEEL

	Test Temperature (°K)	Irradiation Temperature (°K)	dpa	J_{Ic} (kJ/m^2)	σ_{ys} (MPa)	σ_{uts} (MPa)
Irradiated Specimens						
	505	650	56	39.7	894	94Y
	700	673	57	27.0	775	831
	811	661	56	31.5	716	760
	923	655	55	5.8	501	527
	866	648-688	39	23.4	707	738
Unirradiated Specimens						
	505	---	--	67.9	579	730
	700	...	..	59.8	524	669
	Ell	--	--	52.5	496	627
	923	---	..	24.7	386	448

An additional datum point was obtained from Reference 3 for an irradiation temperature of 648 to 688°K and an exposure of ~39 dpa. The test temperature was 688°K. It was noted in Reference 2 that this J_{Ic} value was obtained from specimens having only marginally satisfactory thickness.

5.3 Discussion

The J-integral approach was used to evaluate the effect of irradiation on the toughness of First Core steel. The J_{Ic} values are listed in Table 1 for specimens irradiated to approximately 40-60 dpa and 20-30 appm helium at temperatures ranging from 648 to 688°K. The tests were conducted on specimens of the same thickness as the actual subassembly ducts of interest (0.040 inches or 0.10 cm). Saturation in toughness appears to have occurred by approximately 40 dpa. There are no low dpa exposure data availaole to determine the transient behavior. Since the data are available for only a limited range of irradiation temperature, no dependence on irradiation temperature has been included. A linear recovery factor was applied to the J_{Ic} values to account for testing above the irradiation temperature. A linear recovery factor is justifiable on the grounds that the Hahn and Rosenfield model4 and a modified Krafft model[5] both show that J_{Ic} should be proportional to the yield strength when the work hardening coefficient is small. Irradiated 20% CW 316 stainless steel satisfies this reouirement.

The following equation was developed to describe the dependence of fracture toughness (in units of kJ/m^2) on test temperature:

$$J_{Ic} = [38 - 1.18 \times 10^{-4}(T-525)^2]\, Z \qquad (1)$$

where:

T = Test temperature in units of °C for the range $293 < T < 923$°K.
Z = The recovery effect produced by testing at a temperature above the irradiation temperature

Due to the limited data, Equation 1 has the following limitations imposed on it:

$$643°K < T_{IRRAD} < 688°K$$
$$40 < dpa < 60$$
$$20 < \left(\frac{appm}{helium}\right) < 30$$

The recovery effect produced by testing at a temperature above the irradiation temperature is given by[1,6]:

$$Z = 1 - b\left[\sigma^*/(E/E_0) + \frac{1}{\alpha}\ln\left(\frac{1 + \exp[\alpha\{\sigma_0 - \sigma^*/(E/E_0)\}]}{1 + \exp(\alpha\sigma_0)}\right)\right], \quad (2)$$

where:

$\sigma_0 = 951.5 - 0.676\ (T-273)$,

$b = 2.03 \times 10^{-4}\left[0.931 + \tanh\left(\frac{T-823}{130}\right)\right]^3$,

T = Test temperature, °K, $(T > T_{irrad})$

$\alpha = 0.0145$,

$\sigma^*/(E/E_0) = 648 + (648 - C_R)\ (e^{-t\ A_1\ \phi/\phi_0} - 1)$

$+ \Delta\sigma\ \{\pi^{-1}\ \arctan\ f0.007\ (t - t_2)\] + 0.51\ (MPa)$,

where:

$t_2 = \exp\left(\frac{61131}{T_i} - 51.517\right)$ (hr),

T_i = Temperature of irradiation (°K),

t = Irradiation time (hr),

$C_R = 1034 - 605.77\ \{\pi^{-1}\ \arctan\ [0.036551\ (Ti - 273) - 17.01641 + 0.51$,

$\Delta\sigma = -305.047\ \{\pi^{-1}\ \arctan\ [0.15669\ (T_i - 273) - 116.47161 + 0.51$,

$A_1 = 0.0330261\ \{\pi^{-1}\ \arctan\ [0.068773\ (Ti - 273) - 51.1211 + 0.5\}F$,

$F = 1/[0.001 + 7.86 \times 10^8\ \exp(-12533/T_i)]$, $T_i < 612$ °K

$F = 1.0$, $T_i \geq 612$°K

x = dpa/sec

$\phi = x$ for $T_i < 753$ °K,

$x_0 = 7.5 \times 10^{-7}$ dpa/sec

$\phi = \frac{(T_i - 863)x - (T_i - 753)x_0}{-110}$ for $753 \leq T_i \leq 863$ °K,

$\phi = x_0$ for $T_i > 863$ °K,

The modulus ratio, E/E_0 is given by

(a) For $T < 1043$°K,

$$E/E_0 = \{\exp[\exp(0.8706 - 1928.23/T)]^{-1}\},$$

(b) For $T > 1043$°K,

$$E/E_0 = \{\exp[\exp(3.2399 - 4400.3/T)]\}^{-1}$$

A comparison of measured J_{Ic} values and predicted J_{Ic} values based on Equation 1 is shown in Figure 1. The uncertainty in J_{Ic} is ± 7 kJ/m^2 and this includes the variation in irradiation temperature.

The J_{Ic} values for unirradiated material are 1.79 times the values from Equation 1. Figure 2 shows the test temperature dependence of the unirradiated and irradiated J_{Ic} values normalized by the recovery term (Z).

6.0 References

1. Materials Handbook for Fusion Energy Systems, DOE/TIC-10122.

2. F. H. Huang, "The Fracture Characterization of Highly Irradiated Type 316 Stainless Steel," International Journal of Fracture 25, No. 3, July 1984.

3. F. H. Huang and R. L. Fish, "Effects of Fast Neutron Irradiation on the Fracture Behavior of Stainless Steel," Effects of Radiation on Materials: Eleventh Conference, ASTM STP 782, H. R. Brager ana J. S. Perrin Eds., 1982, pp. 701-719.

4. G. T. Hahn and A. R. Rosenfield, "Sources of Fracture Toughness: The Relation Betwen K_{Ic} and the Ordinary Tensile Properties of Metals," ASTM STP 432 (1967) pp. 5-32.

5. M. L. Hamilton, F. A. Garner and W. G. Wolfer, "Correlation of Fracture Toughness with Tensile Properties for Irradiated 20% Cold-Worked 316 Stainless Steel," Journal of Nuclear Materials, 122 & 123 (1984) 106.

6. R. L. Fish, N. S. Cannon and G. L. Wire, "Tensile Property Correlations for Highly Irradiated 20 Percent Cold-Worked Type 316 Stainless Steel," ASTM STP 683 (1979) pp. 450-465.

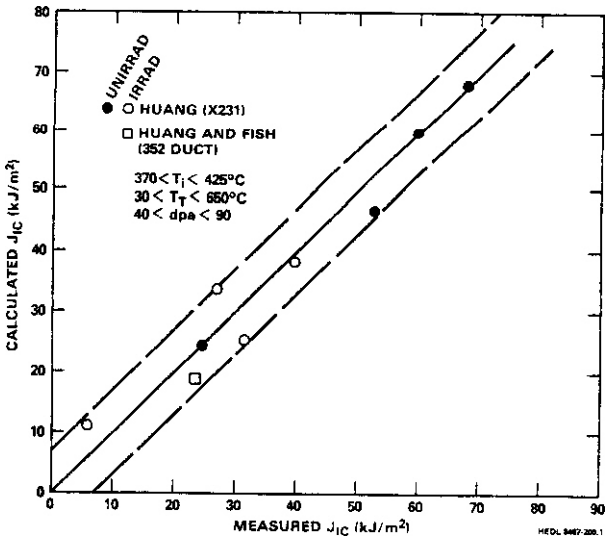

FIGURE 1. Comparison of Measured J_{Ic} and Predicted J_{Ic} Values.

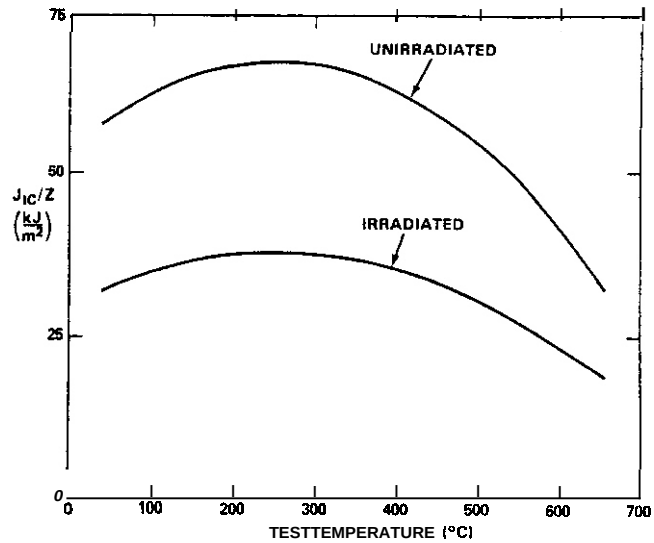

FIGURE 2. Fracture Toughness of 20% CW 316 SS

A COMPARISON OF DEPTH-DEPENDENT MICROSTRUCTURES OF ION-IRRADIATED 316-TYPE STAINLESS STEELS

R.L. Sindelar, R.A. Dodd and G.L. Kulcinski (University of Wisconsin)

1.0 Objective

The goal of this program is to characterize the effects of heavy-ion irradiation on the microstructural/microcompositional evolution of 316-type stainless steels.

2.0 *Summary*

The microstructural response of P7, a high-swelling, "pure" 316-type stainless steel and the MFE heat of 316 stainless steel were investigated after 14-MeV Ni-ion irradiation. Specimens of the P7 alloy were irradiated to fluences of 3.3 x 10^{16} 14-MeV Ni ions/cm^2. Irradiation temperatures ranged from 500°C to 650°C (0.45 - 0.6 T_m). In addition, a sample of 316 SS was irradiated at 650°C (0.6 T_m) to a fluence of 3.3 x 10^{16} 14-MeV Ni ions/cm^2. The irradiated specimens were examined in cross-section by electron microscopy. The 500°C irradiation of the P7 alloy produced a depth-dependent void distribution influenced by the excess interstitial effect of the bombarding ions. The 650°C irradiations of the P7 alloy produced a bi-modal void distribution at the damage peak. The 650°C irradiation of 316 SS produced needle-like precipitation in the entire damage region.

3.0 Programs

Title: Radiation Damage Studies
Principal Investigators: G.L. Kulcinski and R.A. Dodd
Affiliation: University of Wisconsin-Madison

4.0 Relevant DAFS Program Task/Subtask

Subtask II.C.1.1: Phase Stability Mechanics
Subtask II.C.6.1: Effect of Damage Rate on Microstructural Evolution

5.0 Accomplishments and Status

5.1 Introduction

Materials to be used in the construction of near-term fusion reactors will be tailored to meet various criteria. These criteria include the maintenance of mechanical stability and the resistance to cavity-induced swelling during exposure to intense radiation environments. Even minimal variations in the composition of a promising alloy may lead to different microstructural/microchemical evolutions under irradiation which cause the alloy to not satisfy the design requirements.[1,2]

Slight compositional alterations of major alloying elements and even "impurity" elements in 316-type stainless steels have produced varied irradiation responses. This behavior has been observed after fast reactor,[3,4] high-energy electron,[5] and heavy-ion[6,7] radiation exposure. In addition, reactive (e.g. hydrogen and oxygen) gases dissolved in a metal seem likely to assist in cavity nucleation and growth

TABLE 1. COMPOSITION OF MFE HEAT # 15893 316 SS AND THE "PURE" 316 SS, P-7 ALLOY

	Composition (wt.%)					
Material	Cr	Ni	Mo	Mn	Si	C
316 SS	17.4	12.6	2.2	1.81	0.65	0.05
P7 alloy	17	16.7	2.5	0.03	0.1	0.005

Material	P	S	Ti	O	W	Fe
316 SS	0.030	0.020	< 0.001	0.005	-	Bal.
P7 alloy	-	-	0.01	0.03	0.068	Bal.

processes.[8-10] Therefore, actual large scale fabrication of reactor components may have to be monitored carefully to assure the "proper" composition of the finished product.

One type of 316 stainless steel with reduced impurity levels has been recently studied in dual-ion and fast reactor experiments.[11-17] This alloy, P7, was fabricated as a "pure" 316 stainless steel alloy in order to provide an alloy resistant to phase instabilities. This alloy was found to swell readily with essentially no incubation dose. This paper investigates the different response of this "pure" 316 stainless steel alloy, P7, compared to the MFE heat of 316 stainless steel after 14-MeV Ni-ion irradiation.

5.2 Experimental

The compositions of the alloys irradiated in this study are shown in Table 1. Note that the MFE heat #15893 of 316 SS contains higher levels of most impurity elements than does P7. Also note that the P7 alloy stock contains a high matrix oxygen content. The pre-irradiation treatment of the P7 alloy stock involved rolling to a thickness of 500 μm followed by a solution quench after a 1 hour anneal in air at 1000°C. Oxygen was present in the anneal furnace as evidenced by a surface oxide coating on the P7 alloy, and this had to be removed prior to irradiation. A simple calculation using oxygen solubility data[18,19] estimates that the resultant matrix is saturated with oxygen at or near the value shown in Table 1. Pre-irradiation preparation consisted simply of successive mechanical polishing operations using abrasives down to 0.3 μm alumina powder. The samples were not electropolished prior to irradiation in order to preclude the introduction of hydrogen into the specimen.[20] Irradiations were performed at the University of Wisconsin Heavy-Ion Irradiation Facility using 14 MeV Ni^{3+} ions.

Figure 1 shows the displacement damage as a function of depth for 14 MeV Ni ions on 316-type stainless steel targets. Recent studies[22] have found that the displacement efficiency (K) varies as a function of PKA energy, in contrast to the standard value of K = 0.8 as proposed by Torrens and Robinson.[23] At high energies the value of K has been found to be about 0.3, independent of energy. Therefore, we have used K = 0.3 in all of our dpa calculations in this paper.

The samples were irradiated at temperatures between 500°C and 650°C 10.45 - 0.55 T_m) to peak damage levels of 20 dpa (K = 0.3). Table 2 lists the irradiation parameters used in this study. Post-irradiation preparation for TEM analysis involved a cross-section technique described in detail elsewhere.[24] This procedure allows the entire damage range shown in Fig. 1 to be analyzed for a single irradiated sample. The microscopy analysis was performed using a JEOL TEMSCAN-200 CX electron microscope.

Voids densities were determined in 0.25 μm intervals along the ion range with the data points plotted in the middle of the interval. Error bars reflect the uncertainty in foil thickness determination (~ 10%) and the statistical counting uncertainty ($\sqrt{n}/n$) where n is the total number of voids in a 0.25 μm interval.

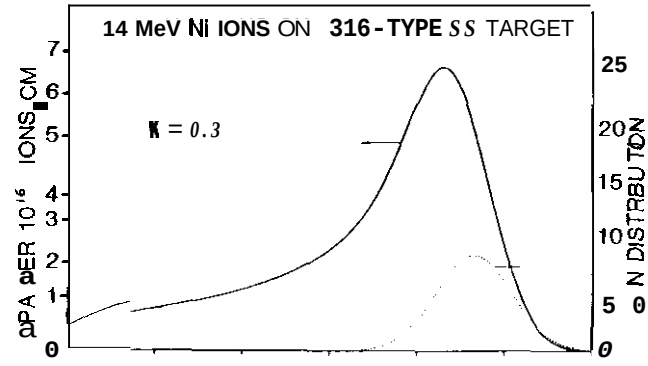

FIGURE 1. Damage (dpa) vs. distance from the irradiated surface calculated using the Brice code.[21] The damage efficiency (K) used is 0.3. E_d = 32 eV.

TABLE 2. 14 MeV Ni-ION IRRADIATION PARAMETERS

Samples irradiated at a flux of 3 x 10^{11} ions/cm^2/s.

Material	dpa at 1 μm*	peak dpa*	Fluence (ions/cm^2)	Irradiation Temp. (°C)
P7 alloy	1	5	0.8 x 10^{16}	500
P7 alloy	4	20	3.3 x 10^{16}	500
P7 alloy	1	5	0.8 x 10^{16}	650
P7 alloy	4	20	3.3 x 10^{16}	650
316 SS	4	20	3.3 x 10^{16}	650

*displacement efficiency K = 0.3

5.3 Results

Figure 2 shows the TEM micrographs which span the entire damage range of the low (5 dpa peak, K = 0.3) and high fluence (20 dpa peak, K = 0.3) 500°C irradiation of the P7 alloy. Figure 3 shows the average cavity diameter, cavity density, and cavity-induced swelling as a function of distance from the sample surface for these two irradiation conditions. It is evident from Fig. 3 that there is a suppression in the average cavity diameter and number density of the high fluence specimen in a region approximately 2.0 to 2.6 μm from the sample surface. This region is coincident with the range of the bombarding Ni ions. The suppression of cavity growth[25] and cavity nucleation[26,27] is thought to be caused by these injected ions providing interstitials in excess of the Frenkel defects produced during the irradiation.

Figure 4 contains the through-range microstructures of the low (5 dpa peak, K = 0.3) and high fluence (20 dpa peak, K = 0.3) 650°C irradiation of the P7 alloy. Figure 5 shows the average cavity diameter, cavity density, and cavity-induced swelling as a function of distance from the sample surface for these two irradiation conditions. It is apparent that there is bi-modal void distribution in the peak damage region (see Fig. 1) at 650°C. To aid in distinguishing the two distributions, cavities > 100 nm were classified as "large voids" whereas those < 100 nm were labeled "small voids." The diameters of the "large voids" in the high fluence specimen approach the value of the TEM specimen thickness in this region (~ 200 nm). Hence, many of these voids intersect the foil surface. Stereo microscopy analysis in thicker regions of the foil revealed that these features are not artifacts but are completely contained within the specimen. Figure 4

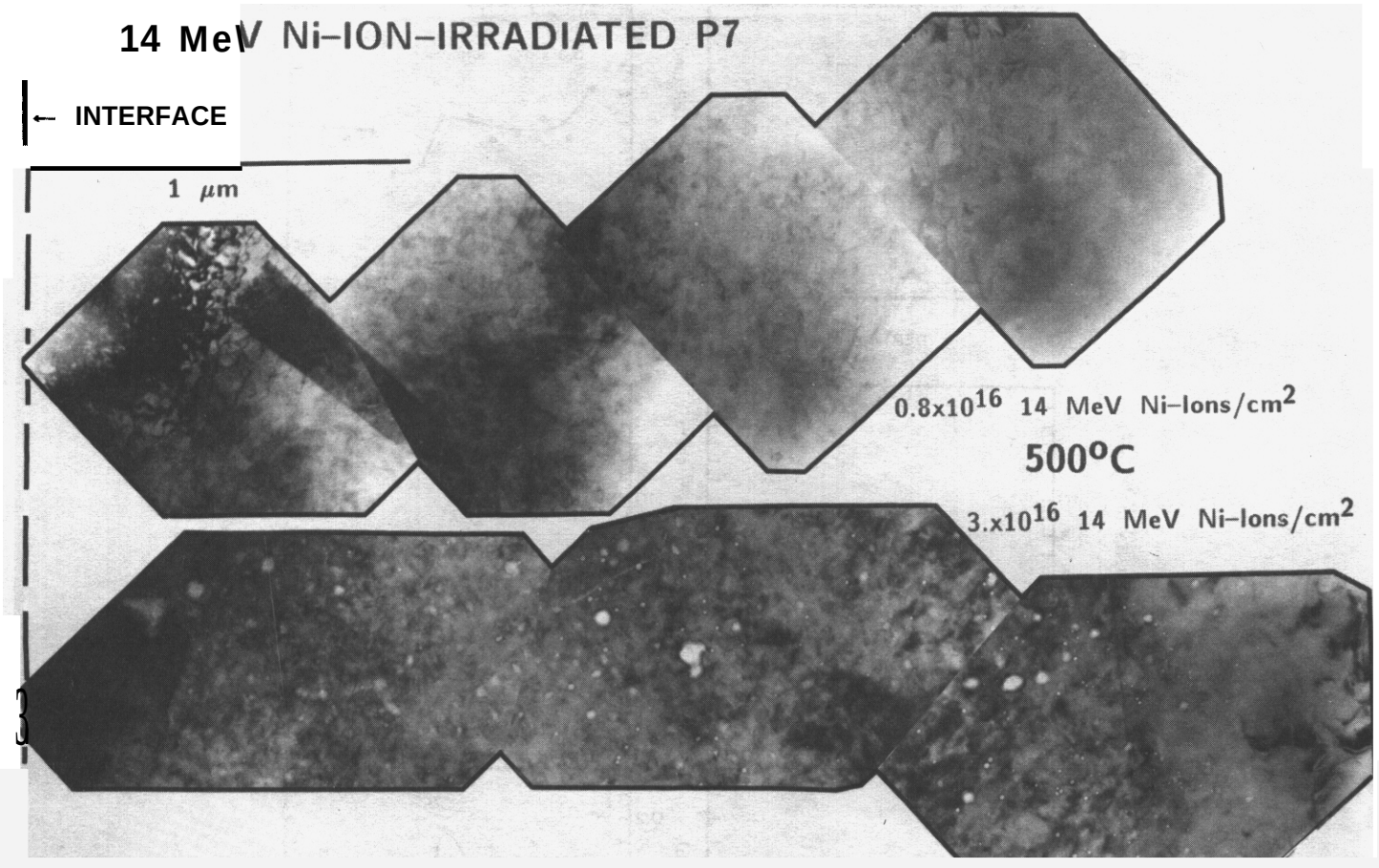

FIGURE 2. TEM micrographs spanning the entire damage region for the low and high fluence 500°C irradiations of P7. Note the suppression in cavity density and average diameter at the ~ 2.5 μm depth in the high fluence sample.

and 5 suggest that the voids present at the low fluence are the precursor distribution of the "large void" distribution in the high fluence sample. A denuded zone of ~ 0.6 μm from the foil surface is present in the high fluence 650°C sample. The absence of voids in this region is attributed to the diffusion of defects to the free surface. Garner and Thomas[28] have shown in HVEM studies that a 0.6 μm void free zone also exists at a dose of 6 dpa (K = 0.8) in 316 SS at 650°C.

Figure 6 shows the precipitation response of the entire ion-damage region for the 316 SS sample. It is evident that there is an absence of cavities throughout the entire damage region. In addition, the irradiation produced a network dislocation structure whose density is ~ 10^{10} cm^{-2} throughout the damage region.

The precipitation response of this sample to irradiation can be seen in the optical micrographs of Fig. 7. The ~ 3 μm of enhanced precipitation at the interface corresponds to the depth of the damage region characteristic of 14 MeV Ni ions. The precipitation response in the damage region was predominantly needle-shaped precipitates. These precipitates had a uniform distribution over the depth of ~ 0.75 μm to ~ 3.0 μm with an average length of 150 nm and density ~ 1 x 10^{14} cm^{-3}. Figure 7d displays a micrograph of the damage region which shows these precipitates at a depth of 1.5 μm from the foil surface. Needle-shaped precipitates of this approximate size and density have previously been observed in dual-iron irradiation studies[29] where they were determined to be an iron phosphide phase, Fe_2P. The typical composition of the needles given was (wt.%) 16Si-5P-4S-19Cr-29Fe-27Ni.

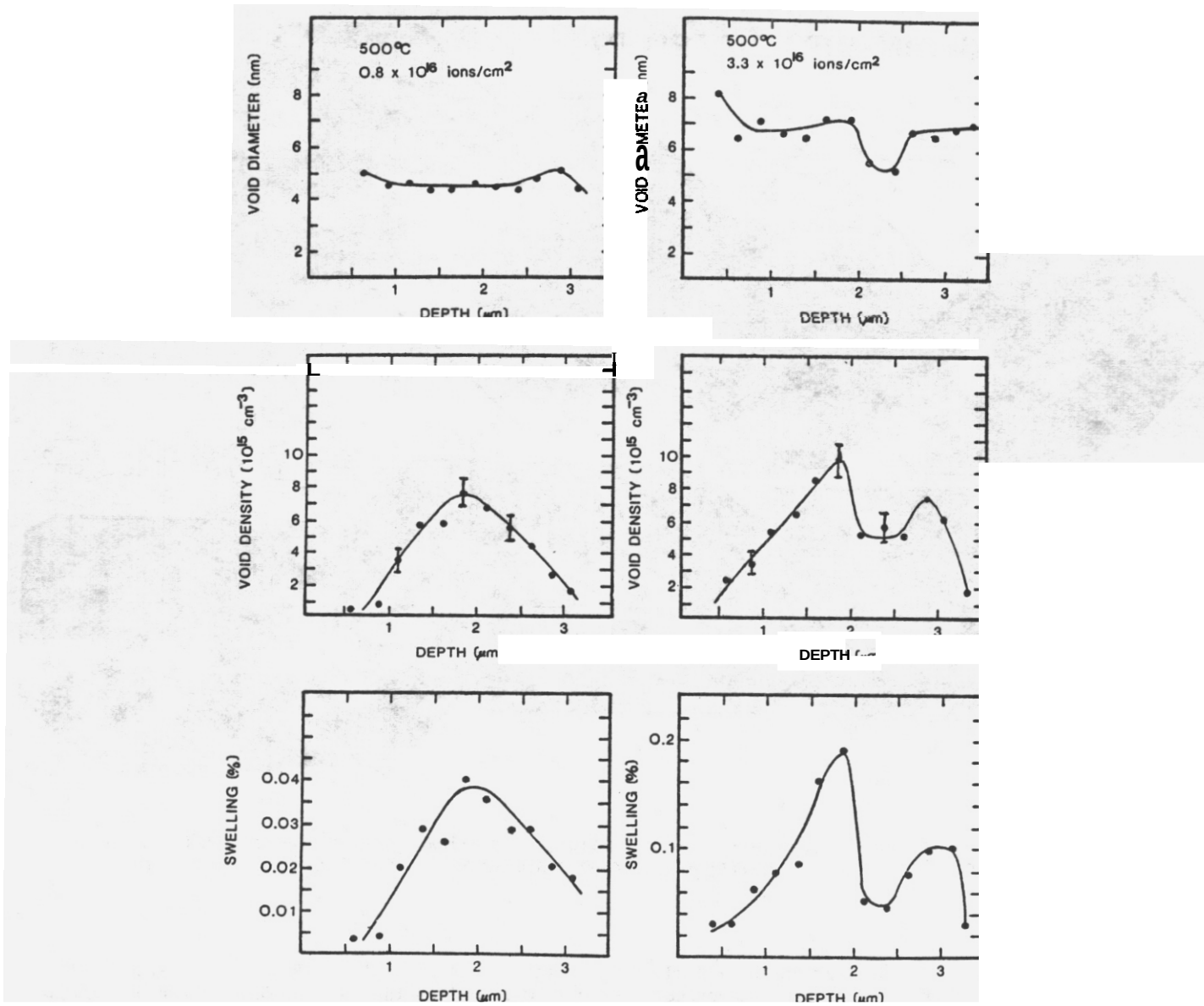

FIGURE 3. Cavity mean size, density, and swelling results for the low and high fluence 500°C irradiation of P7.

Optical micrographs of the cross-sectioned sample (Figs. 7a,7b) reveal extensive grain boundary precipitation throughout the unirradiated region. TEM analysis shows that these regions contain blocky $M_{23}C_6$ precipitates (see Fig. 7c) along the grain boundaries. Figure 7b also includes a feature in the boundary region where two austenite grains have intersected at the nickel plate - 316 SS foil interface. This is an artifact of the plating process. Corrosion at this location occurred when the irradiated foil was anodic in the strike cell.[24] When the current was reversed this corrosion pit was filled with the nickel plate.

5.4 Discussion

The above results show a varied response to 14-MeV Ni-ion irradiation for i) identical samples irradiated at different temperatures and for ii) samples with different impurity and reactive gas levels irradiated at the

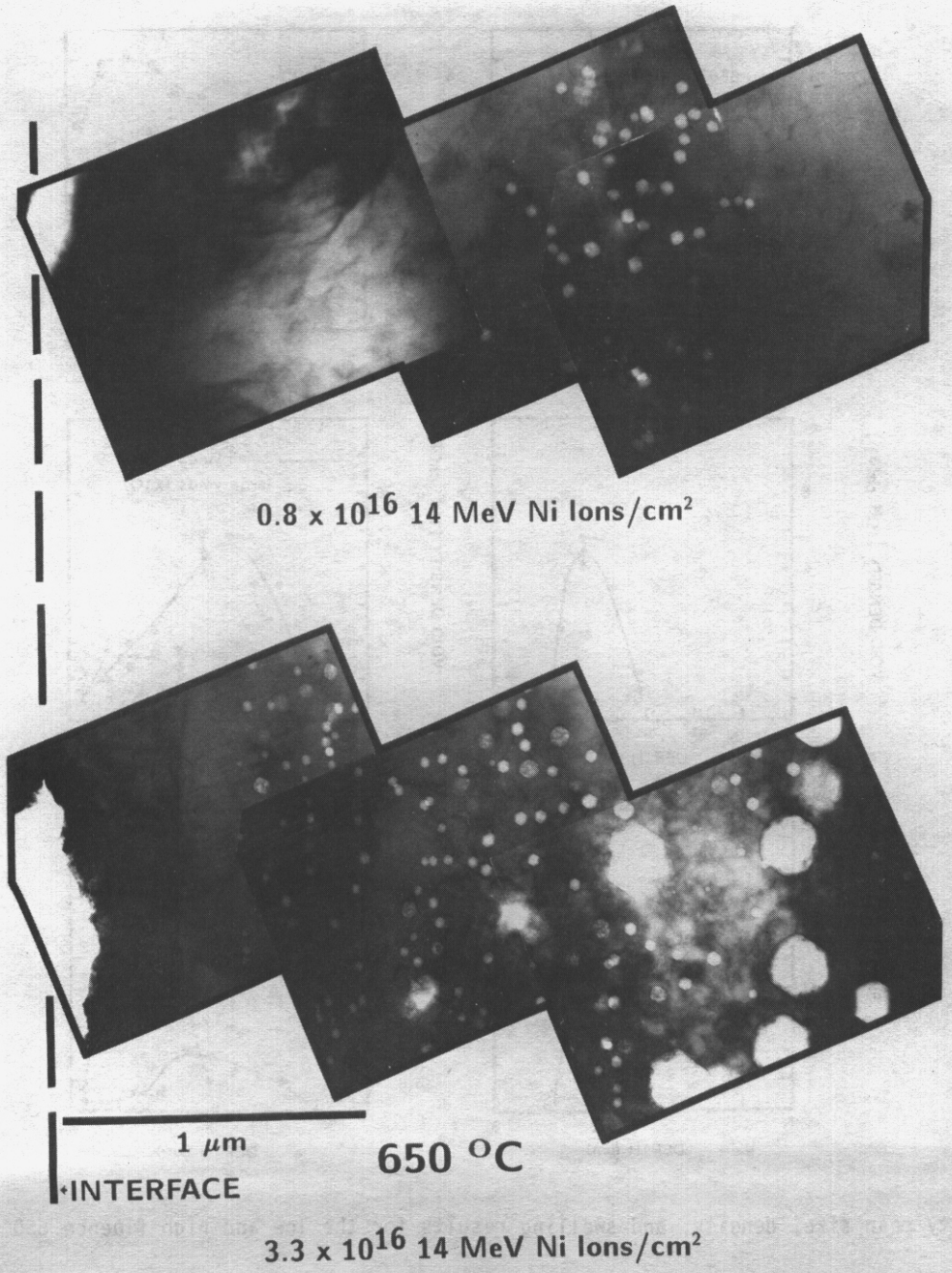

FIGURE 4. TEM micrographs spanning the entire damage region for the low and high fluence 650°C irradiations of P7. Note the evolution of a bi-modal void distribution near the damage peak at ~ 2.5 μm.

same temperature. The response of each set of samples to heavy-ion irradiation showed interesting microstructural features.

First, a suppression in cavity number density and average diameter was noted at the region that coincides with the range of the incident ion species in the high fluence 500°C P7 sample. A retardation of cavity growth from these injected interstitials has been previously postulated by Brailsford and Mansur.[25] The suppressed cavity density is attributed to a decreased cavity nucleation rate in this region where the bombarding ions come to rest. This effect is important at temperatures where recombination is the dominant loss mechanism for point defects, and is well modelled elsewhere.[27] A discrepancy does exist, however, in

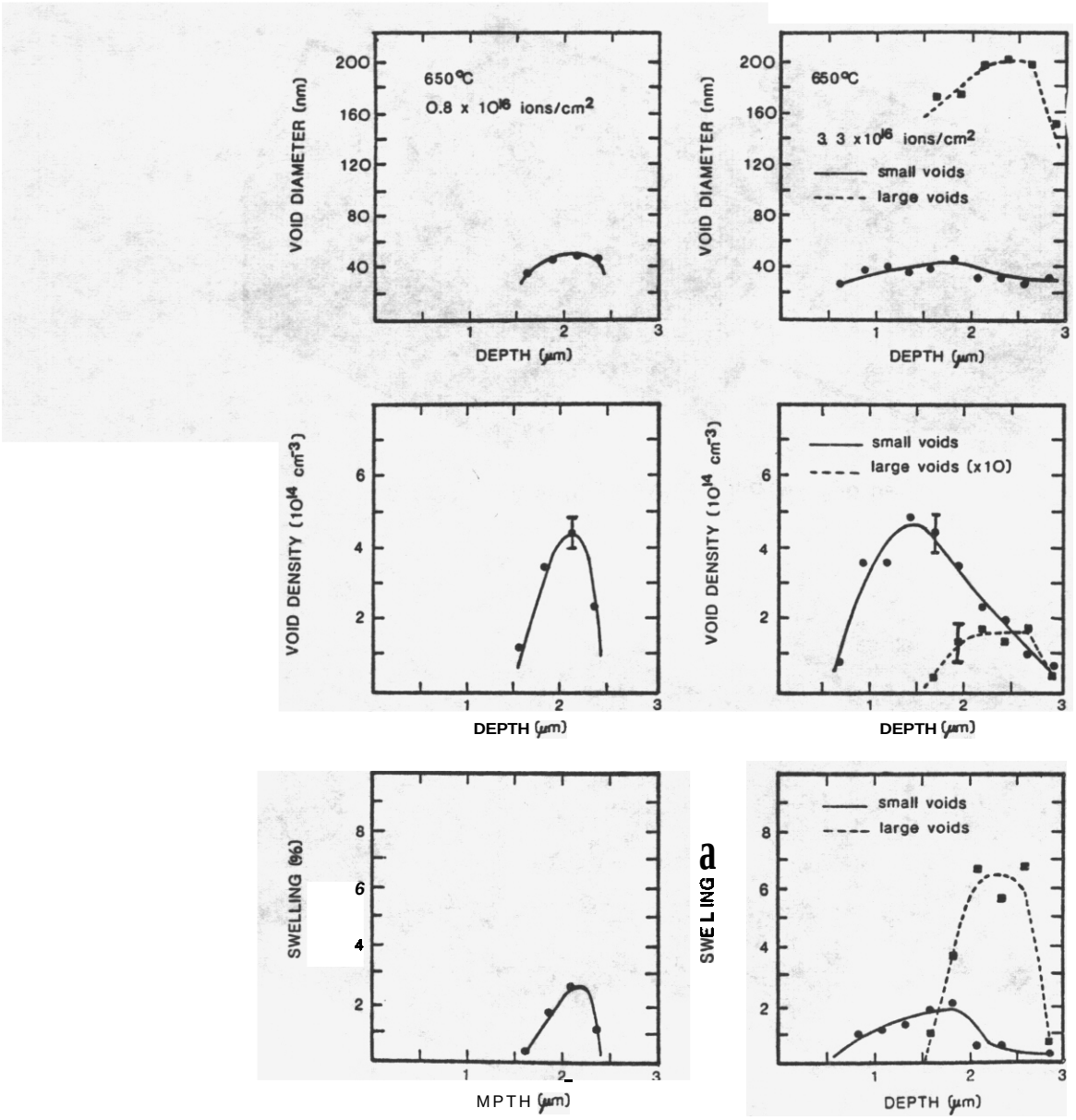

FIGURE 5. Cavity mean size, density, and swelling results for the low and high fluence 650°C irradiation of Pl.

the low fluence 500°C P7 sample where no dip in the cavity density is noted at the peak damage region. In addition, the dpa level at 1 μm in the high fluence sample was approximately the same as the peak dpa value of the low fluence sample (5 dpa), yet the cavity number density was slightly greater in the peak damage tinguishing small cavities (1 nm - 2 nm) from artifacts in a TEM foil - 100 nm thick and therefore the discrepancy lies within the error estimation of the cavity number density.

In the 650% irradiations of the P7 alloy, a bi-modal void distribution was observed to evolve. A bi-modal void distribution has only been previously observed in a heavy-ion irradiated single phase material when it contained injected or transmuted gas. The presence of a high matrix oxygen level, which is assumed to be highly mobile in the P7 matrix at this 650°C irradiation temperature, is believed to be responsible for this bi-modal void development. Calculations using oxygen solubility data from From and Gebhardt,[18] the heat of chemisorption equations of Tanaka and Tamaru,[30] and the heat of oxide formation from Robie et al.,[31]

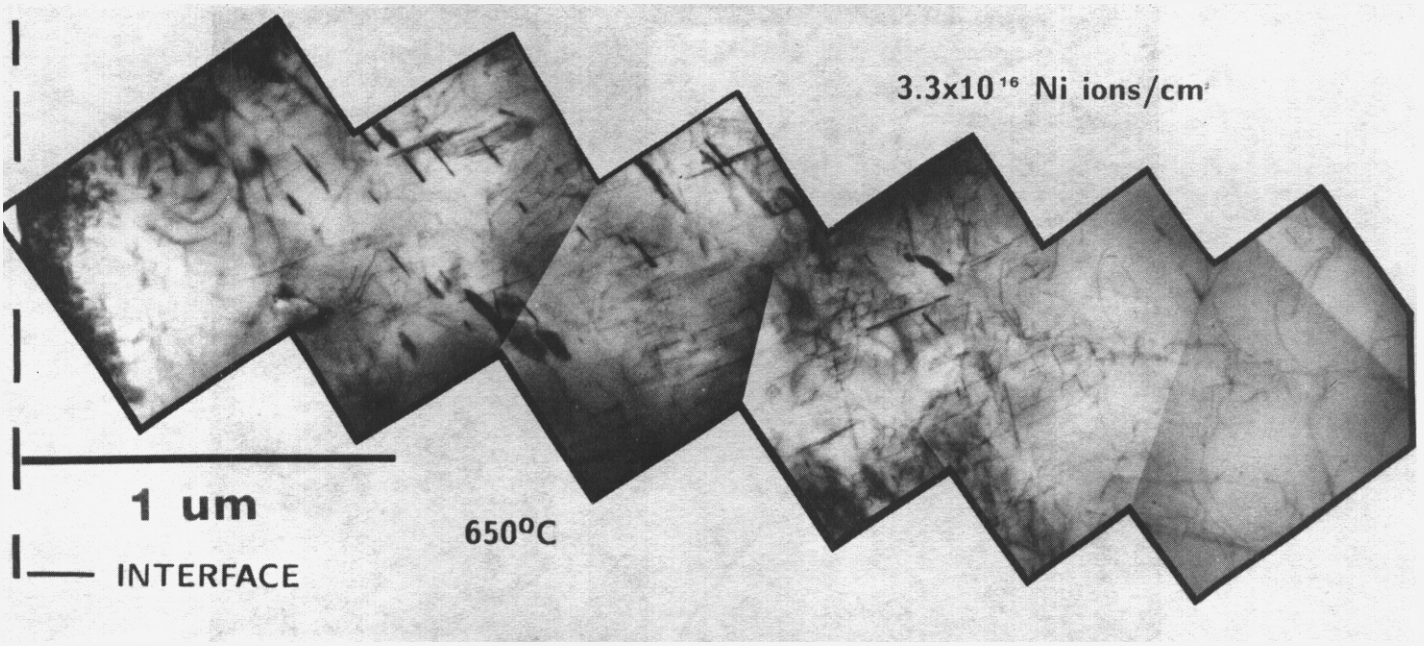

FIGURE 6. TEM micrographs spanning the entire damage region for the 316 SS sample. Note the absence of voids and the residual absorption contract of the needle-like phase in the low contrast micrographs.

predict that the heat of chemisorption of oxygen on γ-Fe (-272 kJ/mole oxygen at 650°C) is greater than the heat of solution of oxygen in γ-Fe (-93 kJ/mole oxygen at 650°C). This large difference provides the driving force for oxygen to come out of solution and collect on a clean, free surface. Oxygen should therefore be attracted to the surface of a void nucleus, and thus affect the surface energy of the cavity. According to Bernard and Lupis,[32] the surface energy γ is determined by

$$\gamma = \gamma_o + \frac{kT}{A} \ln (1-\theta)$$

where θ is the degree of coverage of the surface, γ_o is the energy of the clean metal surface (θ = 0) and A is the area effectively occupied by a chemisorbed oxygen atom. Jones and Wolfer[33] recently performed a similar analysis of hydrogen in a-iron with a resultant substantial reduction in surface energy. When surface energy is reduced, void nuclei are more readily stabilized and accelerated cavity growth can take place.

The Void nucleation rate in P7 should be the greatest in the peak displacement rate region (2.3 μm depth) as shown by another study.[27] Using a diffusion equation given for oxygen in γ-iron given in,[38]

$$D = 5.75 \exp\left(\frac{-40,300}{1.98\ T}\right) \text{ cm}^2/\text{s}$$

it can be shown that D = 1.5 x 10^{-9} cm^2/s at 650°C. Thus, oxygen should be highly mobile and may freely migrate towards the void embryos forming in the peak damage region. This process appears to be efficient in reducing the surrounding matrix oxygen level since the low fluence 650°C P7 sample contains voids in the peak damage region only. Later in the irradiation, additional cavities can nucleate and grow throughout the damage region. Those cavities in the peak region have a lower number density and average diameter which could be due to the effect of the "large voids." Note, however, the difference in the cavity number density of the low fluence sample and the "large void" density in the high fluence sample. A calculation of the maximum possible density of 200 nm spheres is ~ 1 x $10^{14}/cm^3$ when considering a simple cubic dense packing arrangement. A more realistic estimate would take a simple cubic arrangement of spheres with spacing equal to one diameter. This would yield a density ~ 2 x 10^{13} $spheres/cm^3$. Therefore, since the measured void density is ~ 4 x 10^{14} $cavities/cm^3$ in the low fluence sample, an interactive process must take place between

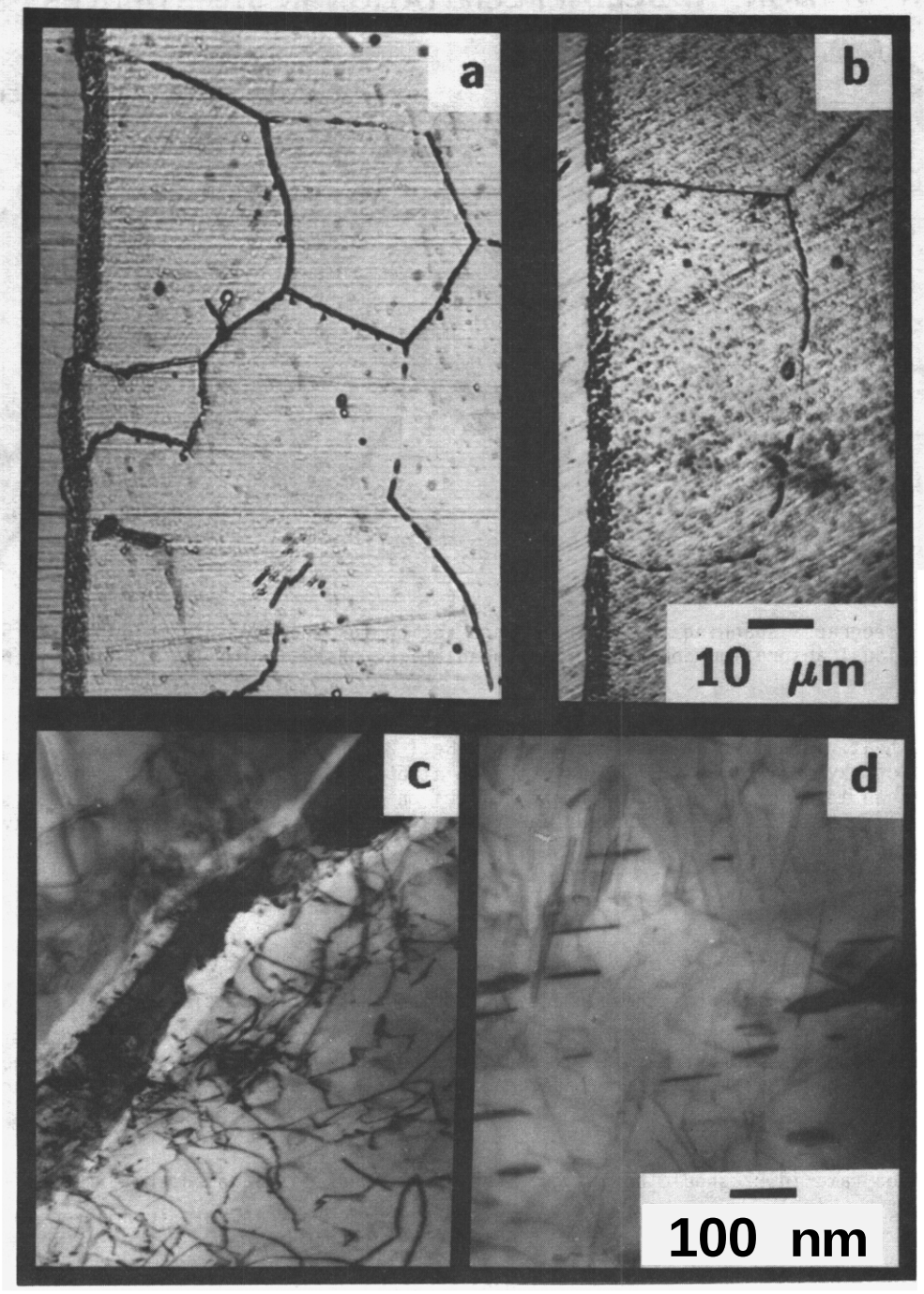

FIGURE 7. a), b) Optical micrographs for the 650°C 316 SS sample. The highly etched region on the nickel plate - 316 SS foil interface (vertical band on left hand side of micrograph) is clearly visible. This ~ 3.0 μm width region corresponds with TEM observations of needle-like precipitates which are found up to ~ 3.0 μm from the foil surface.

c) TEM micrograph of $M_{23}C_6$ precipitates on a grain boundary in the unirradiated region. This precipitation is evident in Fig. 7a.

d) TEM micrograph of the needle-like precipitates in a region ~ 1.5 μm from the foil surface.

the cavities during their growth stage in order to reduce their number density to the ~ 2 x 10^{13} cavities/cm3 observed for the large size class in the high fluence sample. One possible process to reduce void number density in this manner would be the actual coalescence of voids. Mansur[34] describes such a process and cites experimental evidence for its occurrence.

Lastly, the needle-shaped precipitation which occurred in the damage region only for the 650°C 316 SS sample in this study is similar to that observed in dual ion-irradiation studies.[29,35,36] This phase appeared early in these irradiations only to dissolve upon further irradiation. Recently, Lee et al., discovered these needles after dual-ion irradiation of an alloy similar to 316 SS and identified them as the Fe_2P phase.

No thermal aging studies of 316 SS have shown the Fe_2P phase to form. However, such a phase has formed in 321 SS.[37] In the Lee et al. study,[29] a post-irradiation thermal aging at the irradiation temperature of 675°C for 16 hours was seen to cause a partial dissolution of the Fe_2P phase. In the present study, a TEM foil having the needle precipitates was ion-milled without specimen cooling. Subsequent TEM analysis of this post-milled sample revealed that no needles were present. The tentative conclusions of these experimental observations suggest that the needle-shaped Fe_2P phase is radiation-induced and will dissolve at high temperatures in the absence of irradiation. Further work is necessary to confirm this hypothesis.

6.0 Conclusions

The cross-section technique has been applied to heavy-ion irradiated 316-type stainless steels to allow the complete damage region to be analyzed. Several interesting effects of the ion damage were noted:

1. Suppression in void nucleation and growth was observed in a region near the end of range of the incident ions in the low temperature (500°C) irradiation of the P7 alloy. This suppression is attributed to the "excess interstitial" effect of the bombarding ions.

2. A bi-modal void distribution was observed to evolve in the peak damage region of the high temperature (650°C) irradiation of the P7 alloy. Oxygen initially present in the matrix is believed to be responsible for this development.

3. Needle-like precipitates were found in the damage region of heavy-ion irradiated 316 SS. This phase has been observed before as a transitory phase in dual-ion irradiation studies where it was identified as an Fe_2P phase.

7.0 Acknowledgements

The authors wish to express thanks to L.E. Seitzman for his assistance in this project. This research was sponsored by the Department of Energy.

8.0 References

1. Kulcinski, G.L.. "Materials Problems and Possible Solutions for Near Term Tokamak Fusion Reactors," Proceedings of the International School of Fusion Reactor Technology, Meeting on Tokamak Reactors for Breakeven - A Critical Study of the Near-Term Fusion Reactor Programme, held at Erice, Sicily, Sept. 20 - Oct. 1, 1976.

2. Abdou, M.A. and El-Derini, Z., J. Nucl. Mat. 85 & 86 (1979) 57-64.

3. Bates, J.F. and Johnston, "Effects of Alloy Composition on Void Swelling," International Conference: Radiation Effects in Breeder Reactor Structural Materials, AIME (1977) pp. 625-644.

4. Weiner, R.A. and Boltax, A., "Comparison of High-Fluence Swelling Behavior of Austenitic Stainless Steels," Effects of Radiation on Materials: Tenth Conference, ASTM STP 725, 1981 pp. 484-499.

5. Nakata, K., et al., "Effects of Nitrogen and Carbon on Void Swelling in Electron-Irradiated Austenitic Stainless Steel," Third Topical Meeting on Fusion Reactor Materials, Albuquerque, NM, Sept. 19-23, 1983.

6. Williams, T.M., J. Nucl. Mat. 88 (1980) 217.

7. Bates, J.F., et al., "Radiation of Irradiation-Induced Creep and Swelling in AISI 316 by Compositional Modifications," Effects of Radiation on Materials, ASTM STP 725 (1981) p. 73.

8. Farrell, K., Rad. Effects Vol. 53 (1980) 175–194.

9. Glowinski, L.D. and Fiche, C., J. Nucl. Mat. 61 (1976) 22; 61 (1976) 29.

10. Wolfer, W.G., "Advances in Void Swelling and Helium Bubble Physics," Third Topical Meeting on Fusion Reactor Materials, Albuquerque, NM, Sept. 19–23, 1983.

11. Farrell, K. and Packan, N.H., J. Nucl. Mat. 85 & 86 (1979) 683-687.

12. Packan. N.H. and Farrell, K., J. Nucl. Mat. 85 & 86 (1979) 677-681.

13. Miyahara, K., et al., Effects of Radiation on Materials: Eleventh Conference, ASTM STP 782 (1982) 941-952.

14. Packan, N.H., J. Nucl. Mat. 103 & 104 (1981) 1029.

15. Johnston, W.G., et al., "The Effect of Metallurgical Variables on Void Swelling," General Electric Report 76CRD010, Jan. 1976.

16. Leitnaker, J.M., et al.. J. Nucl. Mat. 49 (1973) 57–66.

17. Brager, H.R. and Garner, F.A., Effects of Radiation on Materials: Eleventh Conference, ASTM STP 782 (1982) 152–165.

18. Fromm, E. and Gebhardt, E., "Gase and Kohlenstoff in Metallen," Reine und angewandte Metallkunde in Einseldarstellungen, Band 26, Springer-Verlag, 1976.

19. Coplan, D. and Burr, A.A. Trans. AIME 203 (1955) 1052.

20. Whitley, J.B., Ph.D Thesis, University of Wisconsin, 1978.

21. Brice, D.K., "Ion Implantation Range and Energy Deposition Codes COREL, RASE4, and DAMG2," SAND 77–0622 (1977).

22. Kinney, J.H., et al., Presented at the Third Topical Meeting on Fusion Reactor Materials, Albuquerque, NM, Sept. 19–23, 1983.

23. Torrens, I.M. and Robinson, M.T., Radiation Induced Voids in Metals, J.W. Corbett and I.C. Ianniello, eds. (1972) 739.

24. Sindelar, R.L., et al., Presented at the Third Topical Meeting on Fusion Reactor Materials, Albuquerque, NM, Sept. 19–23, 1983.

25. Brailsford, A.D. and Mansur, L.K., J. Nucl. Mat. 71 (1977) 110.

26. Plumton, D.L. and Wolfer, W.G., J. Nucl. Mat. 120 (1984)

27. B. Badger Jr., et al., "Experimental Investigation of the Effect of Injected Interstitials on Void Formation," 12th International Symposium on the Effects of Radiation on Materials, 18–20 June 1984, Williamsburg, VA.

28. Garner, F.A. and Thomas, L.E., Effects of Radiation on Substructure and Mechanical Properties of Metals and Alloys, ASTM STP 529 (1973) 303-325.

29. Lee, E.H. et al., "The Effect of Phosphorus on the Swelling and Precipitation Behavior of Austenitic Stainless Steels During Irradiation," Third Topical Meeting on Fusion Reactor Materials, Albuquerque, NM, Sept. 19–23, 1983.

30. Tanaka, K. and Tamaru, K., J. of Catalysis 2 (1963) 366.

31. Robie, R.A., et al., Thermodynamic Properties of Minerals and Related Substances at 298.15 K and 1 Bar (10^5 Pascals) Pressure and at Higher Temperatures, U.S. Government Printing Office, Washington, 1978.

32. Bernard, G. and Lupis, C.M.P., Surface Science 42 (1974) 61–85.

33. Jones, R. H. and Wolfer, W.G., Third Topical Meeting on Fusion Reactor Materials, Albuquerque, NM, Sept. 19–23, 1983.

34. Mansur, L.K., Nuclear Technology 40 (1978) pp. 5–34.

35. Packan, N.H. and Farrell, K.. Effects of Radiation on Materials: Eleventh Conference, ASTM STP 782, (1982) pp. 885-894.

36. Wood, S., et al., Effects of Radiation on Materials: Tenth Conference, ASTM STP 725 (1981) pp. 455-469.

37. Bentley, J. and Leitnaker, J.M., The Metal Science of Stainless Steels, Proceedings of Symposium on the 107th AIME Annual Meeting (1978), Eds. E.W. Collings and H.W. King, The Metallurgical Society of AIME, pp. 70–91.

38. Swisher, J.H. and Turkdogan, E.T., Trans. Met. Soc. AIME 239 (1967) 426–431.

MICROSEGREGATION OBSERVED IN Fe-35.5Ni-7.5Cr IRRADIATED IN EBR-II

H. R. Brager and F. A. Garner (Hanford Engineering Development Laboratory)

1.0 Objective

The object of this study is to determine the microstructural and microchemical origins of radiation-induced property changes in structural alloys.

2.0 *Summary*

At 593°C one alloy, Fe-35.5Ni-7.5Cr, which was particularly resistant to swelling in EBR-II, increased in density 0.9% at 7.6 x 10^{22} n/cm^2 (E > 0.1 Mev). Examination by energy dispersive x-ray analysis revealed that substantial oscillations occur in the nickel content of the alloy, varying from 25 to 53% about the nominal level of 35.5%. These oscillations exhibit a period of ~200 nm. Regions enriched in nickel are depleted in chromium and iron, and the reverse is true in regions of low nickel content. This spinodal-like process produces a net densification and also appears to eventually destroy the swelling resistance of the alloy. Once voids form in the nickel-poor chromium-rich regions, further segregatlon of nickel to void surfaces is expected to accelerate the loss of swelling resistance.

3.0 Program

Title: Irradiation Effects Analysis (AKJ)
Principal Investigator: D. G. Ooran
Affiliation: Hanford Engineering Development Laboratory

4.0 Relevant DAFS Program Plan Task/Subtask

II.C.1 Effects of Material Parameters on Microstructure
II.C.16 Composite Correlation Models and Experiments

5.0 Accomplishments and Status

5.1 Introduction

Charged particle simulation studies of neutron-induced void growth have often been used to forecast the compositional dependence of swelling. There is near universal agreement from such studies that the swelling of Fe-Cr-Ni austenitic alloys can be minimized if the nickel is increased to 35-45 wt% and the chromium is reduced to 10% or less.[1,2] Recent neutron irradiation studies in the EBR-II fast reactor confirm the validity of this prediction.[3-5]

In Figure 1 we can compare the swelling behavior of a cold-worked, solute-bearing commercial alloy, AISI 316, with the much lower swelling of annealed, essentially solute-free Fe-35.5Ni-7.5Cr. Not only does this simple ternary alloy resist swelling but it actually densifies prior to and during the onset of swelling. One specimen irradiated at 593°C to 7.6 x 10^{22} n cm^{-2} (E > 0.1 MeV) or ~38 dpa increased its density 0.9%. The thermal equilibrium diagram for the Fe-Ni-Cr system at 600°C does not display any miscibility gaps or phases which form under these conditions, however, and the observed densification was therefore rather surprising.

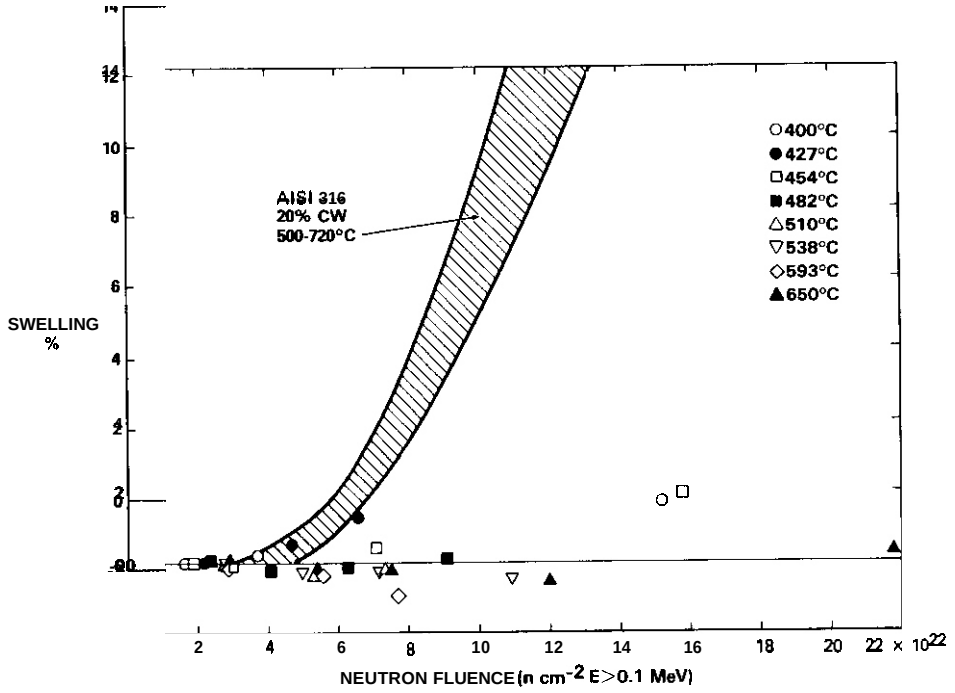

FIGURE 1. Comparison of the swelling behavior in EBR-II of 20% cold-worked AISI 316 and that of annealed Fe-35.5Ni-7.5Cr.

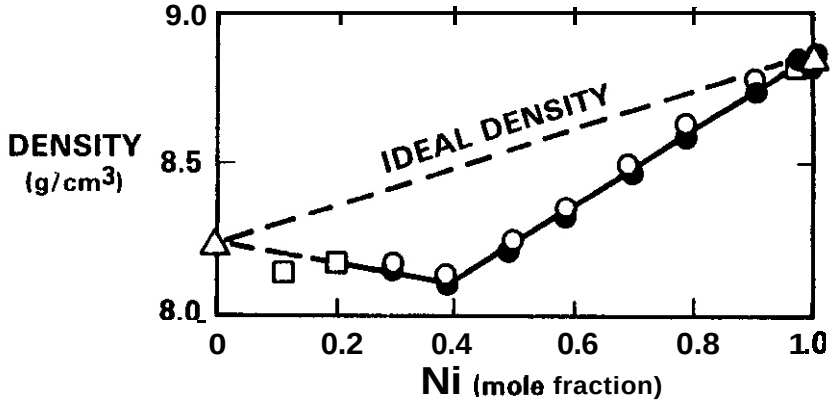

FIGURE 2. Density of Fe-Ni Alloys at 25°C, as reported by Tomlinson and Andrews.(6)

It was noted, however, that a minimum in density exists at Fe-40Ni-OCr at room temperature,[6] as shown in Figure 2. Thus the Fe-35.5Ni-7.5Cr alloy lies very close to a density minimum and radiation-enhanced segregation might lead to an increase in the average density of the alloy.[2] Transmission electron microscopy and energy-dispersive x-ray analysis were therefore performed on the (593°C, 38 dpa) specimen to check this hypothesis.

5.2 Results

Figures 3 and 4 are micrographs of this alloy. A very low density of dislocations was observed, consistent with that usually found at this high irradiation temperature. A very small ($\leq 10^{12}$ cm^{-3}) number of voids were also found and these were usually attached to a likewise small number of precipitates. There was, however, a relatively high density (1×10^{16} cm^{-3}) of small (≤ 5 nm) cavities that appear to be bubbles incorporating the ~30 appm helium generated by transmutation. There were no nickel-rich precipitates observed which could account for the densification, however.

When x-ray analysis was performed, however, it appeared that substantial segregation was occurring in the matrix of this alloy. Figure 5 shows ~100 compositional measurements of small areas in four separate grains, using an electron beam ~30 nm in diameter. There is a persistent tendency of the alloy to exhibit enhanced nickel levels at the expense of chromium in some areas and to do the opposite in other areas. The iron concentration follows the same trend as that of the chromium. Variations in the nickel level between 25 and 53% were found which could easily lead to some densification, as shown in Figure 6.

It is important to note, however, that these measurements are averaged over a finite volume of foil so the actual range of nickel variation probably extends both above and below the 25-53% range.

It was therefore decided to measure the spatial variation of the matrix composition at fixed intervals along traverses across thin (60 nm) sections of foil. Figure 7 shows the results of a typical traverse for both the irradiated foil and an unirradiated specimen, using 50 nm sampling intervals and a beam width of 40-40 nm. While no large compositional variations are seen in the unirradiated soecimen, rather large and periodic variations are seen in the nickel concentration in the irradiated specimen. Note also that whenever the nickel level was above that of the bulk average concentration, the iron level tended to be below its bulk-averaged concentration. Both the iron and chromium profiles appear to be mirror images of the nickel profile. The traverses shown in Figure 7 used dislocations as starting points.

When a rare precipitate or void surface was used as a marker (Figure 8), one observed a perturbation related to the surface of the marker and then the development of the compositional micro-oscillations far from the marker surface. These oscillations exhibit a periodicity on the order of several hundred nm. The micro-oscillations could not be correlated with any components of the microstructure which currently existed in the foil. To verify that the microscillations were reproducible, measurements on many of the traces were taken on more than one occasion, as illustrated using different symbols in Figures 7 and 8.

5.3 Discussion

The oscillations can arise from three possible sources. Two of these are perturbations due to microstructural sinks either outside the foil volume or formed earlier within the foil volume but which no longer exist. The first of these is exemplified by voids and grain-boundaries, both of which are known to segregate nickel at the expense of iron and chromium. The concentrations of these are too low to create the oscillations. The second type of perturbation might arise from dislocation loops which are also known to segregate nickel. Perhaps the resulting nickel enhancement persists after the loop unfaults and the resultant dislocation moves away. The highest density of loops found at these temperatures is much too small to yield the observed scale of oscillations, however.

The third candidate mechanism does not require either pre-existing or radiation-induced sinks. Assume for the moment that spontaneous spinodal-type oscillations occur that are created or perhaps merely accelerated by irradiation. Although no actual miscibility gap has been observed in this compositional regime in thermally-aged Fe-Ni or Fe-Ni-Cr alloys, the existence of concentration inhomogeneities on a small scale has frequently been suggested in the literature. It has even been suggested that the true equilibrium diagram for the Fe-Ni system contains a number of miscibility gaps and comprises the γ-disordered phase, γ' - Fe Ni ordered phase, γ'' - $FeNi_3$ ordered phase and γ''' - Fe_3Ni ordered phase.[7] This assumption seems to be partially confirmed by the observation of an Fe-Ni ordered phase in meteorites formed billions of years ago.[8] If this assumption is correct then alloys in the composition range occupied by the Fe-35.5NI-7.5Cr alloy do not exist in the true eauilibrium state, but the kinetics of transformation to the ordered state are too slow to be observable in human experience.

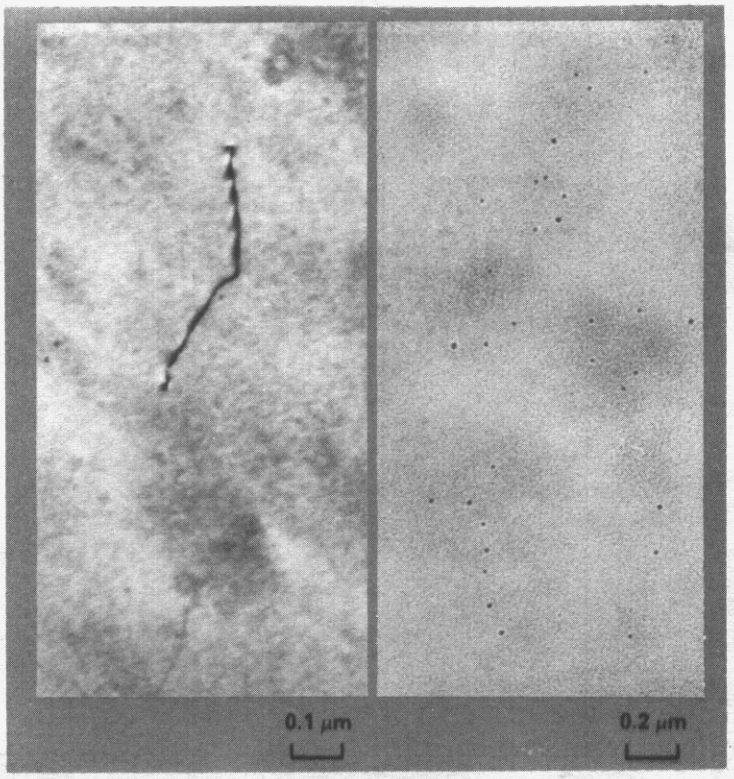

FIGURE 3. Micrographs of Fe-35.5Ni-7.5Cr after irradiation to 7.6 x 10^{22} n cm^{-2} (E > 0.1 MeV) at 593°C, showing a very low density of dislocations, an absence of Frank dislocation loops and a high density ($\sim 10^{16}$ cm^{-3}) of small cavities assumed to be helium bubbles.

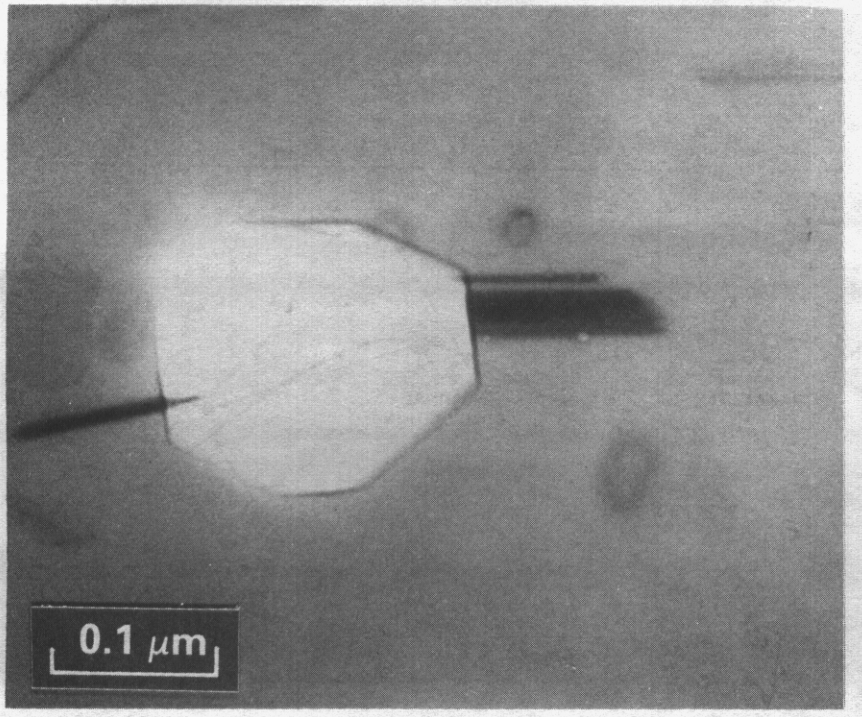

FIGURE 4. Representative example of one of the small number of voids found in Fe-35.5Ni-7.5Cr at 593°C and 38 dpa.

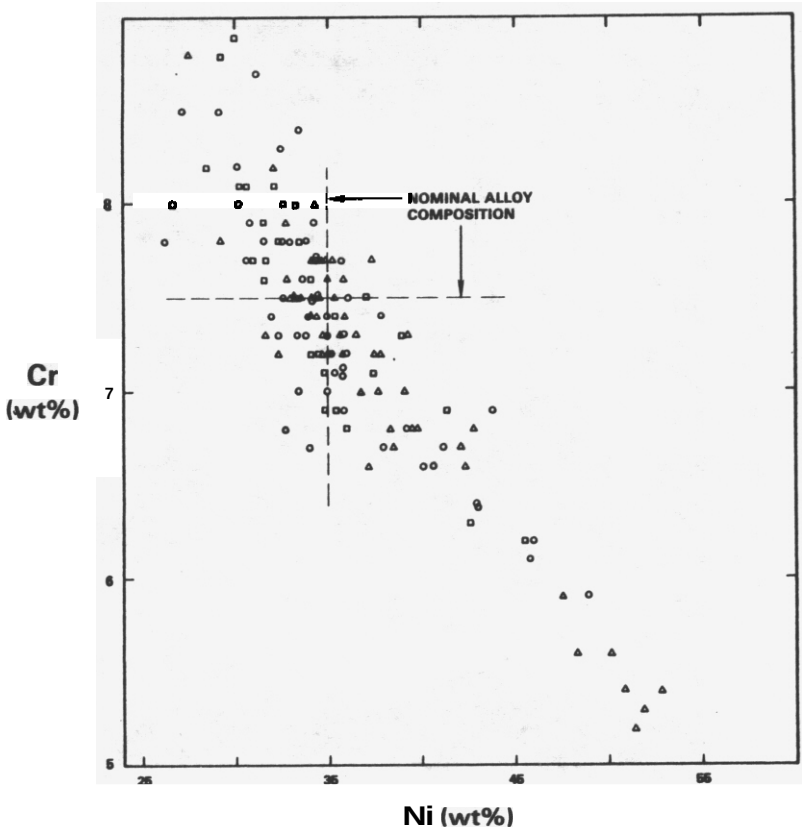

FIGURE 5. Relationship between local nickel and chromium levels, as measured in random small areas 30 nm in size. The three types of symbols denote separate measurements on three different days.

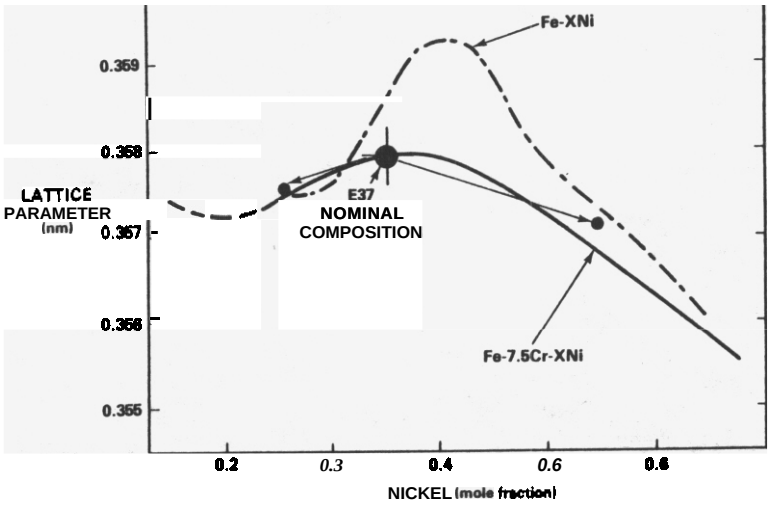

FIGURE 6. Lattice parameters of Fe-Ni and Fe-7.5Cr-XNi austenitic alloys at 25°C. Also shown is the range of average nickel levels observed in Figure 5 to illustrate the origin of the densification.

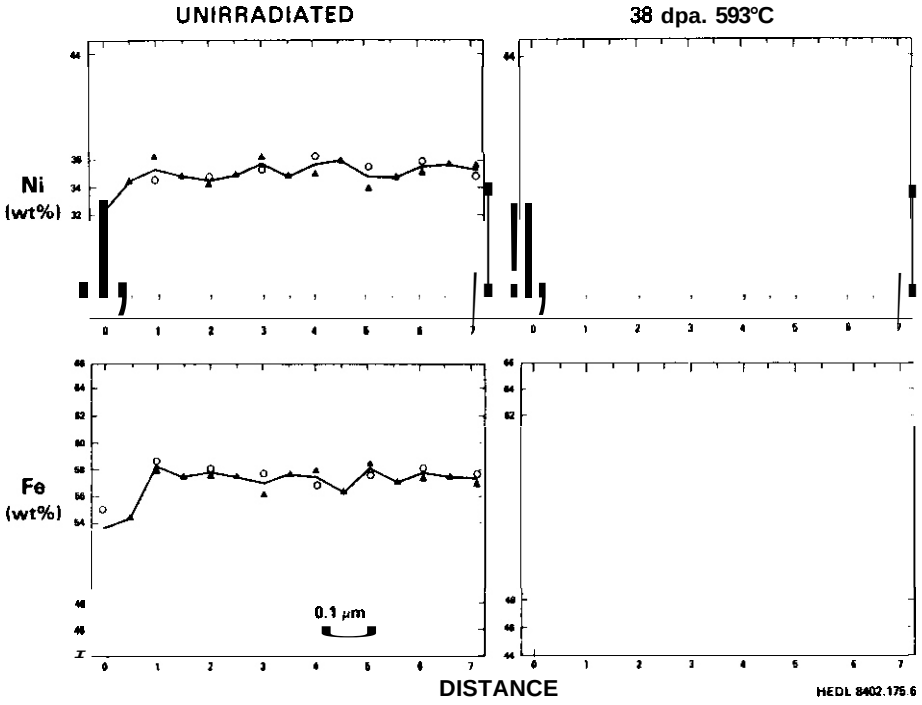

FIGURE 7. Typical compositional traverses across thin foil sections using a dislocation as a starting point. The different symbols represent separate measurements on different days to demonstrate the reproducibility of the measurements.

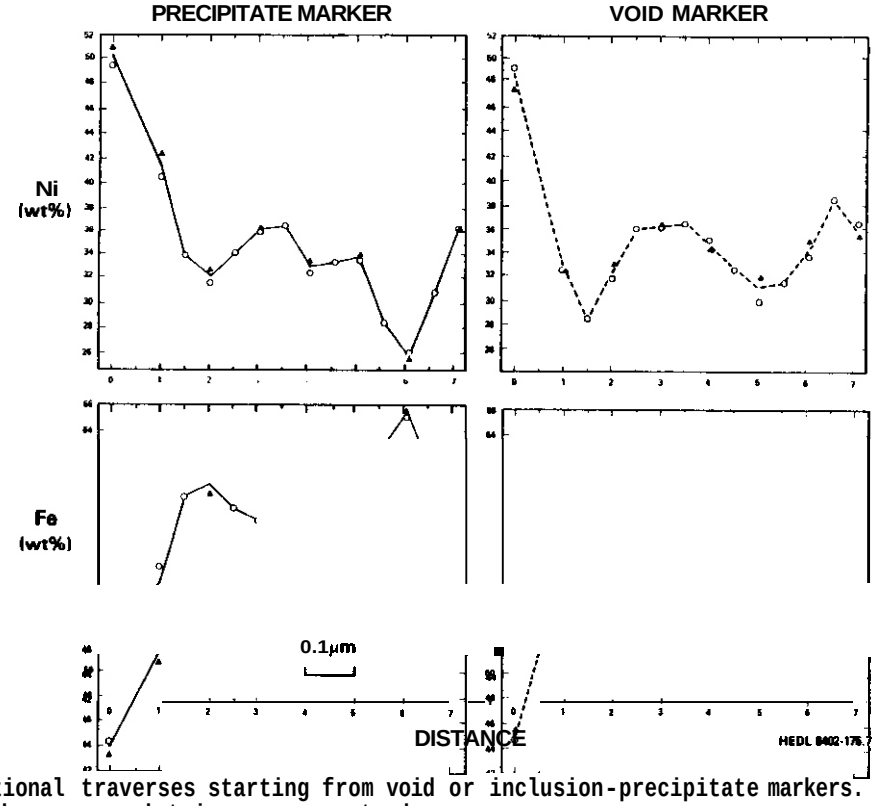

FIGURE 8. Compositional traverses starting from void or inclusion-precipitate markers. Note the reproducibility when measured twice on separate days.

This compositional regime has received a large amount of scientific attention since the low-swelling regime happens to coincide with the compositional range referred to as Invar alloys. It is well known that many physical properties, such as thermal expansion, magnetic properties, elastic moduli, lattice parameter and excess free energy, exhibit rather marked variations with relatively small changes in composition. The Invar regime is frequently referred to as the anomalous property regime.

Many researchers have therefore used charged particle or neutron irradiation to speed up the kinetics of transformation and test the stability of Invar alloys. The earliest of these studies are summarized in Reference 9. Their major conclusions were that the order-disorder transformation is accelerated by irradiation and is a vacancy-dominated Process, although interstitials produced by irradiation can also participate. The anomalous Invar properties usually disappear after irradiation and both short-range and long range ordering occurs. The degree of ordering *is* sensitive *to* the composition, temperature and displacement rate. Most evidence of ordering has been inferred from indirect observational techniques (Mossbauer, induced magnetic anisotropy, resistivity, nuclear gamma resonance, neutron scattering, lattice parameter measurements, etc.) and comparison with similar studies on easily ordered systems such as Cu-Au. There has been one other direct observation of compositional oscillations induced by irradiation. Penisson and Bourret irradiated Fe-50Ni with 1.0 MeV electrons and observed high densities of ordered micro-domains $\lesssim$50 nm in size using dark field electron microscopy.[10] The micro-domains formed only when the irradiation was conducted below the critical ordering temperature, which is $\sim$320°C for Fe-50Ni.

It is not unreasonable to assume that the ordering process requires first a segregation process and that this precursor segregation process does not cease abruptly above the critical ordering temperature. In the disordered state, however, one cannot observe with electrons the existence of compositional oscillations since the structure factors of the three solvent atoms (Fe,Ni,Cr) are quite similar. Therefore the presence of micro-oscillations at reactor-relevant temperatures can only be inferred by x-ray measurements or by the use of indirect techniques which measure the radiation-induced modification of various anomalous Invar properties.

It has been shown by Pauleve and *coworkers*[11] that two overlapping types of ordering ($FeNi$, $FeNi_3$) develop in irradiated Fe-Ni alloys in the range of 37-70% nickel, as shown in Figure 9. If we ignore the chromium in our alloy for a moment we can see from Figure 9 that, for Fe-35.5Ni our entire range of irradiation temperature (400-650°C) lies above the critical ordering temperatures of both phases. The addition of chromium has been shown to reduce the tendency toward short-range order[12,13] but not suppress it totally. Chromium additions also tend to reduce the degree of anomaly in some properties such as Young's modulus,[14] The addition of chromium also introduces the possibility of ordered phases involving chromium,[15-17] such as Ni_2Cr which forms thermally. Wahi recently reported that precipitates of $Cr_{38}Fe_{11}Ni$ are formed in thin foils of Fe-40Ni-13Cr which were thermally-annealed in vacuum at 700-900°C, although such Precipitates did not form in hulk samples.[18]

The effects of chromium, then, is such that one would expect to see similar compositional micro-oscillations even more easily in Fe-35.5Ni than in Fe-35.5Ni-7.5Cr. There has been one indirect measurement that supports this conclusion. Chamberod and coworkers[7] irradiated with electrons a series of alloys with compositions between Fe-28Ni and Fe-50Ni at temperatures of 80, 250 and 400°C. The last temperature lies above the critical ordering temperature for this composition range. As shown in Figure 10, the anomalous peak in lattice parameter in the Invar range disappears at the lower two irradiation temperatures. In effect, the Invar alloys densify just as did the Fe-35.5Ni-7.5Cr alloy of this study. One can see, however, that at 400°C the anomaly is also beginning to disappear, even though the irradiation was conducted above the critical ordering temperature. This supports our hypothesis that the precursor segregation process continues well above the critical order-disorder temperature. It is not unreasonable to expect that, not only will the rate of segregation he temperature-dependent, hut also that the period of the micro-oscillations will be strongly sensitive to temperature.

In another study it was shown that simultaneously decreasing the nickel and increasing the chromium level will strongly reduce the incubation period of swelling in neutron-irradiated alloys.[5] The spinodal decomposition of our alloy is creating relatively large zones of crystal with such lowered swelling resistance, and it is reasonable to expect that voids will nucleate first in these regions. Once voids nucleate and grow to reasonably large sizes they begin to segregate nickel at their surfaces and reject chromium back into the matrix, as seen in Figures 8 and 11. Each void, once formed, then alters the surrounding (matrix in a manner which makes the nucleation of the next void easier. This sets into motion a positive feedback urocess *oi* enhanced void nucleation. While nickel-rich precipitates do not form in these alloys the voids themselves become the reservoir for nickel removal. Note in Figure 11 that the matrix at a distance 100 to 150 mm from a void in a Fe-35.1Ni-21.7Cr alloy has been depleted to $\sim$30% nickel. The swelling Produced in this specimen at 538°C by 36 dpa neutron irradiation is 7.7% and the transient regime is essentially over.

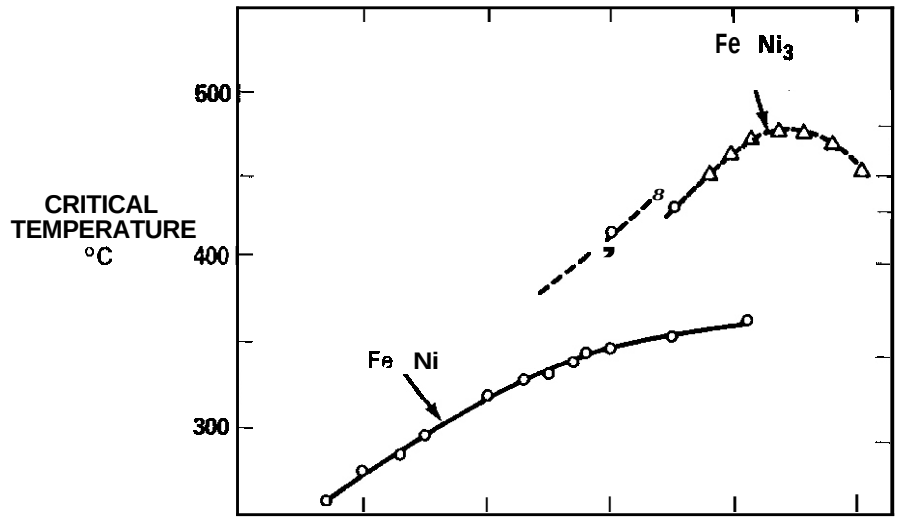

FIGURE 9. Critical temperatures for the order-disorder transitions of the NiFe and Ni_3Fe types in Fe-XNi alloys.(11)

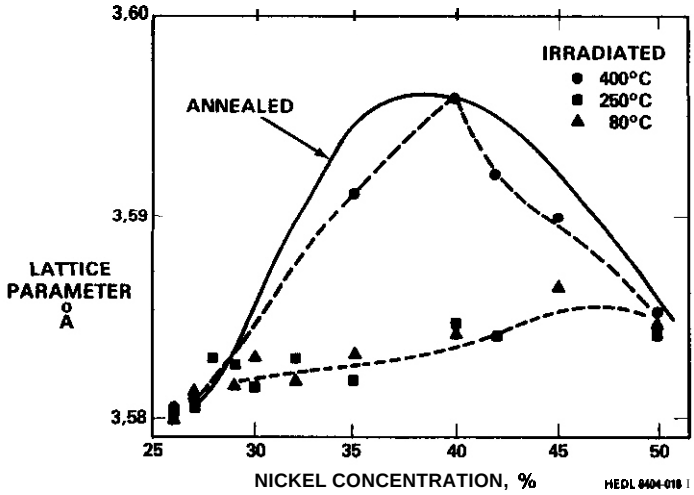

FIGURE 10. Lattice Parameters of Fe-XNi Alloys Measured at Room Temperature Before and After Electron Irradiation. (7)

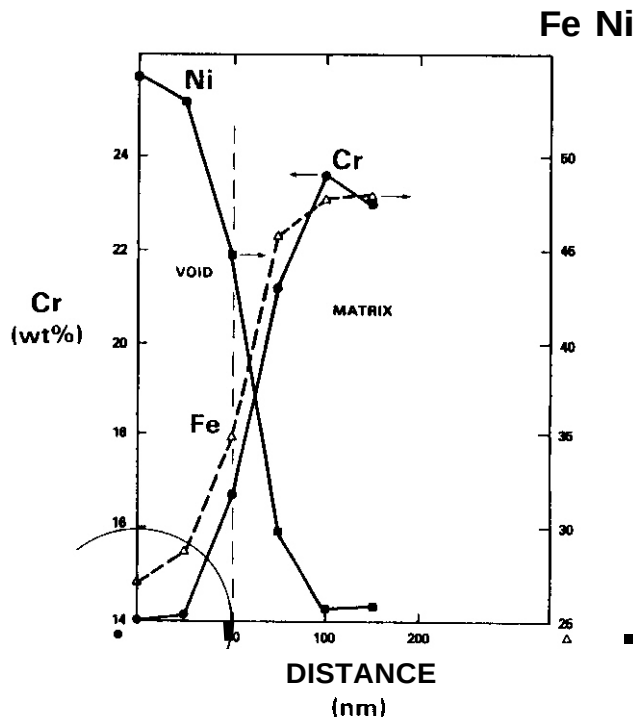

FIGURE 11. Concentration Profiles Observed in the Vicinity of a Void Surface in Fe35.1Ni-21.7Cr Alloy Irradiated to 7.2 x 10^{22} n/cm^2 (E>0.1 MeV) at 538°C. (19) The reduction in matrix Ni content due to segregation at the void surfaces.

5.4 Conclusion

The simple homogeneous austenite region shown on phase diagrams for Fe-Ni-Cr alloys near the Invar compositional range appears not to be the true equilibrium state. Radiation seems to accelerate the evolution toward true stability particularly if the irradiation occurs below the critical order-disorder temperature. Even above the critical temperature a spinodal-like decomposition occurs during irradiation. This produces comuositional micro-oscillations with periods on the order of hundreds of nanometers. This process leads to the earlier nucleation of voids in the nickel-poor chromium-rich zones, shortening the duration of the transient regime of swelling. It also leads to the elimination of the anomalous Invar properties. Another consequence is a net densification of the alloy.

6.0 References

1. W. G. Johnston, J. H. Rosolowski, A. M. Turkalo and T. Lauritzen, J. Nucl. Mater. 54 (1974) 24.

2. D. Gulden and K. Ehrlich, Dimensional Stability and Mechanical Behavior of Irradiated Metals and Alloys, British Nuclear Energy Society, London, 1983, Vol. 1, 13-16.

3. F. A. Garner, Damage Analysis and Fundamental Studies Quarterly Progress Report, DOE/ER-0046/14 (Aug. 1983) 133.

4. H. R. Brager and F. A. Garner, ibid, P. 152.

5. F. A. Garner and H. R. Brager, Damage Analysis and Fundamental Studies Quarterly Progress Report, DOE/ER-0046/16 (April 1984) 38.

6. W. J. Tomlinson and A. J. Andrews, Metal Science, 12 (5) (1978) 263-264.

7. A. Chamberod, J. Laugier and J. M. Penisson, J. Magnetism and Maqnetic Materials, 10 (1979) 139-144.

8. J. F. Petersen, A. Aydin and J. M. Knudsen, Phys. Lett. 62A (1977) 192.

9. D. Dautrebbe, "Radiation Effects in Magnetic Materials" in Studies In Radiation Effects in Solids, Vol. 3, Gorden and Breach, G. J. Dienes, id. 1966.

10. J. M. Penisson and A. Bourret, B.I.S.T, 207 (Oct. 1975) 59-63.

11. J. Pauleve, A. Chamberod, K. Krebs and A. Marchand, IEEE Trans. Magnetics, Vol. MAG-2, No. 3 (Sept. 1966) 475-478.

12. K. N. Binnatov, A. A. Katsnel'son and Yu. L. Rodionov, Fiz. Met. Metalloved., 39, No. 5(1975) 1021-1025.

13. V. I. Goman'Kov, I. M. Puzei, and E. I. Mal'tsev, Soviet Physics-Doklady, 15, No. 9 (1971) 874-876.

14. V. M. Kalinin and V. A. Kornyakov, Fiz. Met. Metalloved., 51, No. 5, (1981) 1110-1113.

15. H. Heidsiek, R. Scheffel and K. Lucke, J. De Physique, Colloque C7, Suppl. No. 12, 38, (1977) C7-174.

16. V. I. Goman'kov and N. I. Nogin, Fiz. Met. Metalloved., 52, No. 3 (1981) 665-667.

17. E. Z. Vintaikin and G. G. Urushadze, Soviet Physics-Doklady, 14, No. 1 (1969) 84-87.

18. R. P. Wahi, Scripta Met., 14, No. 11, (1980) 1229-1232.

19. H. R. Brager and F. A. Garner, Damage Analysis and Fundamental Studies Quarterly Progress Report DOE/ER-0046/12, (Feb. 1983) 170-177.

7.0 Future Work

Additional examination of other neutron-irradiated ternary alloys will continue. The ion-irradiated specimens described in Reference 1 will also be examined for evidence of spinodal-like behavior.

8.0 Publications

This report will be published in ASTM STP 870, Proceedings of 12th International Symposium on Effects of Radiation on Materials, edited by F. A. Garner and J. S. Perrin.

EXPERIMENTAL INVESTIGATION OF THE EFFECT OF INJECTED INTERSTITIALS ON VOID FORMATION

B. Badger, Jr., D.L. Plumton, S.J. Zinkle, R.L. Sindelar, G.L. Kulcinski, R.A. Dodd, and W.G. Wolfer (University of Wisconsin)

1.0 Objective

The objective of this study is to assess the influence of injected ions on void nucleation in different metallic systems. The effect of temperature on the suppression of void formation in the peak damage region is examined. The experimental results are compared to a theoretical void nucleation model. The ultimate goal of this investigation is to obtain a better correlation between neutron displacement damage and ion-induced damage.

2.0 Summary

Pure nickel, a "pure" 316-type stainless steel (P7) and two high strength copper alloys have been irradiated with either 14-MeV nickel or copper ions to a peak damage level of 50 dpa (K = 0.8) at homologous temperatures ranging from 0.4 to 0.6 Tm. The irradiated foils have been examined in cross section in an electron microscope. The injected interstitial effect on the suppression of the measured void densities in Ni and P7 was found to increase with decreasing temperature. The comparison of these results with nucleation theory shows good qualitative agreement. Quantitative discrepancies are attributed to diffusional spreading of point defects and to the presence of impurity atoms in the matrix. A copper alloy irradiated at 300°C showed a small heterogeneous void density characteristic of the high temperature end of the void swelling regime, while no voids formed in the alloys irradiated > 400°C. This result is in excellent agreement with nucleation theory which indicates the void swelling regime in ion-irradiated, low impurity copper should be less than 300°C (0.42 Tm).

3.0 Programs

Title: Radiation Damage Studies
Principal Investigators: G.L. Kulcinski and R.A. Oodd
Affiliation: University of Wisconsin-Madison

Title: Effect of Radiation and High Flux on the Performance of First Wall Components
Principal Investigator: W.G. Wolfer
Affiliation: University of Wisconsin

4.0 Relevant DAFS Program Task/Subtask

DAFS Subtask II.B.2.3
Subtask C. Correlation Methodology

5.0 Accomplishment and Status

5.1 Introduction

During the past decade many radiation effects studies have utilized heavy ions to produce displacement damage in metals. Heavy ion irradiation offers the advantage of rapid accumulation of displacement damage as compared to neutron irradiation. However, differences in the displacement cascade structure and dis-

placement rates between ion and neutron irradiations, along with the absence of transmutation products in ion irradiations, make it difficult to establish correlations between the damage resulting from the two types of irradiations. An additional factor which has received somewhat less attention is that heavy ion irradiation deposits the irradiating ion in the matrix in the form of an excess interstitial. This injected ion effect was originally assumed to be minimal, but has subsequently been found to significantly reduce void formation and growth under the appropriate conditions.

Where point defect recombination is dominant, the injected interstitials can reduce the void growth rate. This effect was predicted by Brailsford and Mansur[1] and experimentally verified by Lee et al.[2] The reauction is significant when the bias is small, i.e. when the current of vacancies is almost equal to tne current of interstitials into the void. Obviously this is the case for voids of the critical size. Therefore, it may be expected that the injected interstitials will affect void nucleation to a greater extent than void growth. Plumton and Wolfer[3] have recently shown that void nucleation can be suppressed by the presence of the injected ions.

An injected ion comes to rest in the matrix as an interstitial without a vacancy partner. Therefore, there exists an excess number of interstitials in the region where the ions are deposited. In a heavy ion irradiation the peak in the damage profile overlaps the ion deposition profile, meaning that there is an excess of interstitials in the damage peak. These excess interstitials may perturb the balance between the vacancy and interstitial flux to the void nuclei, causing suppression of void nucleation. Since the excess interstitials are a small fraction of the total interstitial concentration. they are only important when most of the point defects produced by displacements are recombining. The effect of the injected ions on void nucleation should therefore become increasingly important at lower temperatures. Garner[4] recently reevaluated previous work in light of this suppression effect and found that in various metals injected interstitials may have a pronounced effect on experimental void swelling results.

For high energy ions, in contrast to low energy ions,[3,5] there exists a region midway along the range that is not affected by either the front surface or by the injected ions. The development of the cross section procedure for post-irradiation examination allows void swelling data for different displacement rates and fluences to be obtained from one sample.[6-9] Transmission electron microscopy (TEM) observations over the entire damage range allows a determination to be made of the effect of injected interstitials on void formation. The cross section technique is now well-established for nickel,[6] copper,[7] and stainless steel.[8,9]

Pure nickel, a "pure" 316-type stainless steel (P7), and 2 high strength copper alloys have been irradiated with either 14-MeV nickel or copper ions. These samples have been electroplated with nickel or copper and thinned to observe the damage region in cross section. The use of 3 different metallic systems allows an assessment to be made of the general influence of injected ions on void nucleation. The irradiations were conducted at homologous temperatures ranging from 0.4 Tm to 0.6 Tm in order to determine the effect of temperature on the suppression of void formation in the peak damage region.

5.2 Experimental Procedure

The composition and impurity content of the "pure" 316-type stainless steel alloy P7, nominally Fe-17Cr-16.7Ni-2.5Mo,[9,10] and AMZIRC (Cu-0.15Zr) and AMAX-MZC (Cu-0.6Cr-0.15Zr-0.05Mg) copper alloys[11] are given elsewhere. The purity of the nickel used in this investigation was 0.99995. The pre-irradiation preparation of all three materials involved successive mechanical polishing operations down to an abrasive of 0.3 μm alumina powder. In addition, the copper alloys and pure nickel samples were electropolished to remove any cold work from the mechanical polish.

The materials were irradiated at the University of Wisconsin Heavy-Ion irradiation Facility using 14-MeV Ni^{3+} ions for the P7 alloy and pure nickel samples and 14-MeV Cu^{3+} ions for the copper alloys. Table 3 lists the irradiation parameters used in this study.

Post-irradiation preparation for TEM analysis involved a cross-section technique described e sewhere for the pure nickel,[6] the copper alloys[7] and P7 alloy.[9] These procedures allow the entire damage region of

the heavy ions to be analyzed for a single irradiated sample. TEM was performed using a JEOL TEMSCAN-POOCX electron microscope.

5.3 Theoretical Parameters and Procedures

Comparisons between materials with varying amounts of irradiation-induced displacement damage are usually done in terms of displacements per atom, DPA. This value is obtained by use of a modified Kinchen and Pease model[12] so that the number of displacements (R_D) is given by

$$R_D = \frac{\phi K S_D(x)}{2 \rho E_D}$$

where ϕ is the fluence, P is the atomic density, E_D is the effective displacement energy and $S_D(x)$ is the energy available for displacements at a depth x (damage energy). The last parameter, K, is the displacement efficiency which Torrens and Robinson took to be 0.8, which has been used as a standard value over the years for DPA calculations. Recent experimental and theoretical studies on the displacement efficiency have revealed that it is strongly dependent on energy, with K decreasing for increasing recoil energy (see Ref. 13 for a review). These results indicate that for high energy ($\gtrsim$ 1 MeV) neutron or heavy ion irradiations of fcc metals the efficiency is $\sim$ 0.3, which reduces many previously cited damage values by a factor of ***318.*** The defect production efficiency used in this paper for the determination of DPA rate and excess interstitial fraction (ϵ_i) is K = 0.3.

The Brice code[14] has been used to calculate the damage rates and excess interstitial fractions for 14-MeV Cu or Ni ions incident on copper, nickel or stainless steel. The excess interstitial fraction, ϵ_i, taken as the ratio of deposited ions to the interstitials produced by damage that survive cascade recombination is also affected by the efficiency. ϵ_i is taken as

$$\epsilon_i = \frac{f(x)\,\phi}{E_{ff}\,\rho\,R_D}$$

where f(x) is the deposited ion distribution function at a depth x and E_{ff} is the fraction of defects that escape in-cascade recombination. Therefore, while previous damage rates scale by ***318,*** previous excess interstitial fractions scale by ***813.*** The effective displacement energies used for the Cu, Ni and P7 stainless steel damage calculations are 29, 40 and 32 eV respectively.

The steady State void nucleation theory for heavy ion irradiations presented by Plumton and Wolfer[3] is used here along with the modification of a vacancy surface sink term previously included[5] in the nucleation computer code. The materials parameters, Table 1, used in the nucleation calculations are experimentally determined values taken from the literature. An attempt has been made to qualitatively match the theoretical output with the experimental results. The matching is accomplished by slightly modifying some of the input materials parameters listed in Table 1. The materials values that have been used to adjust the theoretical nucleation profiles are the energies and entropies of vacancy migration and formation (E_v^m, E_v^f, S_v^m, S_v^f), the surface energy of the metal (γ) and the void bias factors (Z_i^o, Z_v^o) for interstitial and vacancy capture. The adjustment consists of matching the theoretical nucleation rate with the experimentally determined void density. The experimental void density is assumed to be the density that is reached after nucleation has stopped so that the nucleation period must be less than the total irradiation time. A nucleation rate of $\sim 10^{18}$-10^{19} voids/m^3/s was obtained from measured void densities of 10^{20}-10^{22} voids/m^3 and total irradiation times of $\sim 10^3$ s.

The vacancy diffusivity (D_v) and thermal equilibrium concentration (C_v^{eq}) were determined in accordance with the formalism of Seeger and Mehrer[15] for the self-diffusion coefficient (D_{SD}):

$$D_{SD} = (D_v)(C_v^{eq}) = a^2 \upsilon_o e^{\frac{S_v^m + S_v^f}{k}} e^{-\left(\frac{E_v^m + E_v^f}{kT}\right)} \qquad (1)$$

TABLE 1. MATERIALS PARAMETERS

Parameter	Ni	cu	P7	Reference
Lattice parameter, a_o (nm)	0.352	0.361	0.356	38
Surface energy. γ_o (J/m^2)	0.8	0.8	0.8	
Shear modulus, μ (MPa)	9.47×10^4	4.1×10^4	6.55×10^4	39.40
Poisson's ratio, ν	0.28	0.33	0.28	39.40
Vacancy formation energy[a], E_v^f	1.84	1.29	1.82	see text
Vacancy migration energy[a], E_v^m	1.04	0.77	1.29 (Ni) 1.38 (Cr) 1.39 (Fe)	see text
Pre-exponential factor, (m^2/s) $D_{vo} = a_o^2 \nu_o e^{\tilde{}v}$				
	4×10^{-6}	1.3×10^{-6}	---	
Mass of diffusing atom, M (amu)	58.1	63.5	56	
vacancy formation entropy[b], S_v^f	3.0	2.4	2.5	see text
Vacancy migration entropyb, S_v^M	2.3	1.2	3.1 (Ni) 4.3 (Cr) 4.8 (Fe)	see text
Interstitial relaxation volume[c], v_I	1.8	1.55	1.8	41
vacancy relaxation volume[c], v_v	-0.2	-0.1	-0.1	30
Interstitial polarizability', α_I^G	72	34	52	42
Vacancy polarizability[a], α_V^G	39	18	28	42
Modulus variation, $\Delta\mu/\mu$	2×10^{-5}	3×10^{-4}	4×10^{-5}	
Lattice parameter variation, $\Delta a_o/a_o$	2×10^{-5}	3×10^{-4}	4×10^{-5}	
Cascade survival fraction, n	0.15	0.15	0.15	43
Sink strength, S (m^{-2})	5×10^{13}	10^{14}	10^{14}	
Bias factor ratio, $\bar{Z}_I/\bar{Z}_V$	1.4	1.4	1.4	see text
Thickness of segregation shell, h/r	0.1	0.1	0.1	

[a] In units of eV

[b] In units of the Boltzmann constant k

[c] In units of the atomic volume $\Omega = a_o^3/4$

where the jump frequency for FCC crystals ν_o is $\frac{1}{a}\sqrt{E_v^m/M}$, a is the lattice parameter and M is the average mass of the atoms making up the lattice. Experimental self-diffusion data only allows the sums $S_v^m + S_v^f$ and $E_v^m + E_v^f$ to be determined. Therefore a decrease in S_v^f or E_v^m implies an increase in S_v^m or E_v^f. A complete parametric study of varying the energies and entropies of vacancy migration and formation and determining the impact on void nucleation is beyond the scope of this paper. However, several trends have been noticed as these input parameters are modified. Raising E_v^f or lowering S_v^f increases the nucleation rate, most noticeably at high temperatures, while the effect of the injected interstitials on void nucleation suppression is decreased.

The vacancy energies and entropies for copper and nickel have been extensively examined in the literature. For copper the self-diffusion data is well determined. Using an energy for self-diffusion of Q_{SD} = 2.06 eV,[16] and a vacancy formation energy of E_v^f = 1.29 eV[17] leads to a vacancy migration energy of 0.17 eV. The low temperature self-diffusivity data[18,19] and Q_{SD} are then used in Eq. (1) to determine the entropy for self-diffusion, $S_v^m + S_v^f$ = 3.63 k. This entropy can then be broken into the migration and formation components by using a vacancy concentration of C_v = 190 ppm at 1075°C[20] and C_v^{eq} in Eq. (1). This results

in S_v^m = 1.2 k and S_v^f = 2.4 k. For nickel, the self-diffusivity data are also fairly well known. The self-diffusion energy has been found to be 2.88 eV[21] which corresponds well with independent measurements of E_v^f = 1.8[22] and E_v^m = 1.04 eV.[23] However, values for the entropies are uncertain. Using the formalism of Eq. (1) for the data of Maier et al.[21] yields $S_v^m + S_v^f$ = 5.27 k, but the division between the two entropies is unknown.

Reliable self-diffusion data for stainless steel are scarce. Rothman et al.[24] have used tracer diffusion techniques to examine the diffusivity of the major elements Fe, Ni and Cr in an alloy of approximately the same composition as the P7 examined here. Appreciable differences were found by Rothman et al. in the diffusivities of the alloy components for a given composition as well as variations with composition between the same components in different alloying systems. Care must therefore be exercised in using diffusivity data from one steel alloy System and applying it to another. Making use of Eq. (1) again and Rothman et al.'s data give the results listed in Table 2. The division of these sums into their individual components is again unknown. For the nucleation calculations, the division is made by assuming constant values of E_v^f and S_v^f for all components, but different values of E_v^m and S_v^m for each alloy component. The vacancy diffusivity is then determined as an average

$$D_V = \overline{D}_V = \sum_X C_X D_V^X \tag{2}$$

where C_X is the fraction of X in the alloy and

$$D_V^X = a^2 \upsilon_o \exp\left(\frac{S_V^m(X)}{k}\right) \exp\left(\frac{-E_V^m(X)}{kT}\right) \tag{3}$$

with $\upsilon_o = \frac{1}{a}\sqrt{\overline{E_V^m}/M}$; $\overline{E_V^m} = \sum_X C_X E_V^m(X)$.

The surface energies used in this study are less then the values tabulated by Murr[25] by a factor of 2-3. This must be done because steady state void nucleation rates are too low when surface energy values for clean surfaces are employed.[26] This implies that either some unknown impurity segregation occurs to the void embryo surface which reduces its surface energy, or that there exists gas such as hydrogen or helium in the metal that can pressurize the void embryo. Both affect the vacancy concentration in equilibrium with a void[27] containing x vacancies, i.e.

$$C_v^o(x) = C_v^{eq} \frac{r(x-1)}{r(x)} \frac{Z_v^o(x-1)}{Z_v^o(x)} \exp\left[\frac{\gamma^o(x) - \gamma^o(x-1) - P\Omega}{kT}\right] \tag{4}$$

by changing the surface energy $\gamma^o(x)$ and the gas pressure P. Here, the surface energy $\gamma^o(x)$ has been corrected for temperature and curvature, $\gamma \Rightarrow \gamma^o(r(x),T)$, according to Si-Ahmed and Wolfer.[28] The other factors in Eq. (4) are the void radius, r(x), and the void bias for vacancies, $Z_v^o(x)$. As the surface energy, γ, is decreased, the void nucleation rate increases dramatically, in particular at high temperatures. The reduction In the vacancy concentration in equilibrium with a void embryo as given by Eq. (4) leads to a slower vacancy re-emmission rate. Similarily if the embryo is pressurized, the nucleation rate also increases.

The void bias factors Z_i^o and Z_v^o are obtained from a shell model presented previously.[4,28,29] The shell model also implies that a segregation region exists around the void which has a different shear modulus and lattice parameter than the matrix. This difference need only be on the order of 0.002-0.03% for void nucleation to occur at the desired rate. The effect of increasing the difference in shear modulus or lattice parameter is to increase the void bias for vacancies and decrease the bias for interstitials. The sink averaged bias factor ratio, $\overline{Z_I}/\overline{Z_V}$, for void nucleation is taken to be 1.4 which is about halfway to the large void steady state swelling value calculated by Sniegowski and Wolfer.[30]

TABLE 2. SELF-DIFFUSION *DATA* IN A STEEL ALLOY

Component	$S_v^m + S_v^f$	$E_v^m + E_v^f$
17% Ni	*5.58* k	3.11 eV
17% Cr	6.85 k	3.2 eV
66% Fe	7.3 k	3.21 eV

5.4 Results

The experimental results from the copper alloy, nickel, and P7 stainless steel irradiations can be grouped into three broad categories based on the observed effect of excess interstitials on the void density. The three categories are (a) voids observed, with the magnitude of the injected ion effect quantitatively determined, (b) voids observed, but no observed suppression in void density, and (c) no voids observed. Table 3 summarizes these results for the various conditions that were investigated. The lower homologous irradiation temperatures generally give rise to a greater void density suppression, in agreement with theory.

5.4.1 Copper Alloys

NO void formation was observed in cold-worked plus aged copper alloys that were irradiated up to peak damage levels of 15 dpa (K = 0.3) at homologous temperatures of 0.5–0.6 Tm (400–550°C). Irradiation of an annealed (500°C, 1 hr) AMZIRC (Cu–Zr) alloy to the same fluence at 300°C resulted in a sparse distribution of large (~ 250–500 nm diameter) voids. The void density was estimated to be on the order of $10^{17}/m^3$. The few voids which were observed were preferentially found in the vicinity of large zirconium particles present in the damage region of the alloy. Figure 1 shows two voids observed in cross-section in the irradiated AMZIRC alloy.

The calculated void nucleation rate versus irradiation temperature for pure copper is shown in Fig. 2. The void nucleation rate without excess interstitials ($\varepsilon_i = 0$) is compared to the nucleation rate with an excess interstitial fraction corresponding to the peak damage region ($\varepsilon_i = 10^{-3}$). The displacement rate was taken as 3×10^{-3} dpa/s (K = 0.3), which corresponds to the peak damage rate during the copper alloy irradiations. It can be seen that the steady-state nucleation theory predicts an absence of homogeneous void nucleation in copper for irradiation temperatures $\gtrsim$ 300°C, in agreement with tine experimental observations. The effect of the injected interstitials on void nucleation is predicted to be negligible for temperatures $\gtrsim$ 150°C.

5.4.2 Nickel

The 14-MeV Ni ion irrddiations of nickel at 425°C and 450°C (0.40–0.42 Tm) both show a suppression in the void number density in the peak damage region. Figure 3 shows the observed TEM depth-dependent void distribution for a nickel sample irradiated to a peak damage level of 2 dpa (K = 0.3) at 450°C. The reduction in void density in the injected ion region is clearly visible in this figure. The void number density versus depth for both the 425°C and the 450°C nickel samples is shown in Fig. 4. The maximum suppression occurs at a depth of 1.6 and 2.1 μm for the 425 and 450°C irradiation temperatures, respectively. The extent of the suppression region for the 425°C sample, 0.5–2.8 μm, is larger than that for the 450°C sample (1.0–2.6 μm). The void number density for the 425°C sample is less than the 450°C sample density in the suppression region.

The calculated void nucleation rate as a function of depth for a 14-MeV Ni ion irradiation of nickel is Shown in Fig. 5. The 450°C sample is seen to have a lower nucleation rate than the 425°C sample except in the region of suppression. This result agrees with the experimentally observed void density (Fig. 4). The maximum suppression of void nucleation is predicted to occur at 2.2 μm. The widths of the calculated suppression regions for the 425°C and 450°C cases are 1.6 to 2.5 μm and 1.6 to 2.4 μm, respectively.

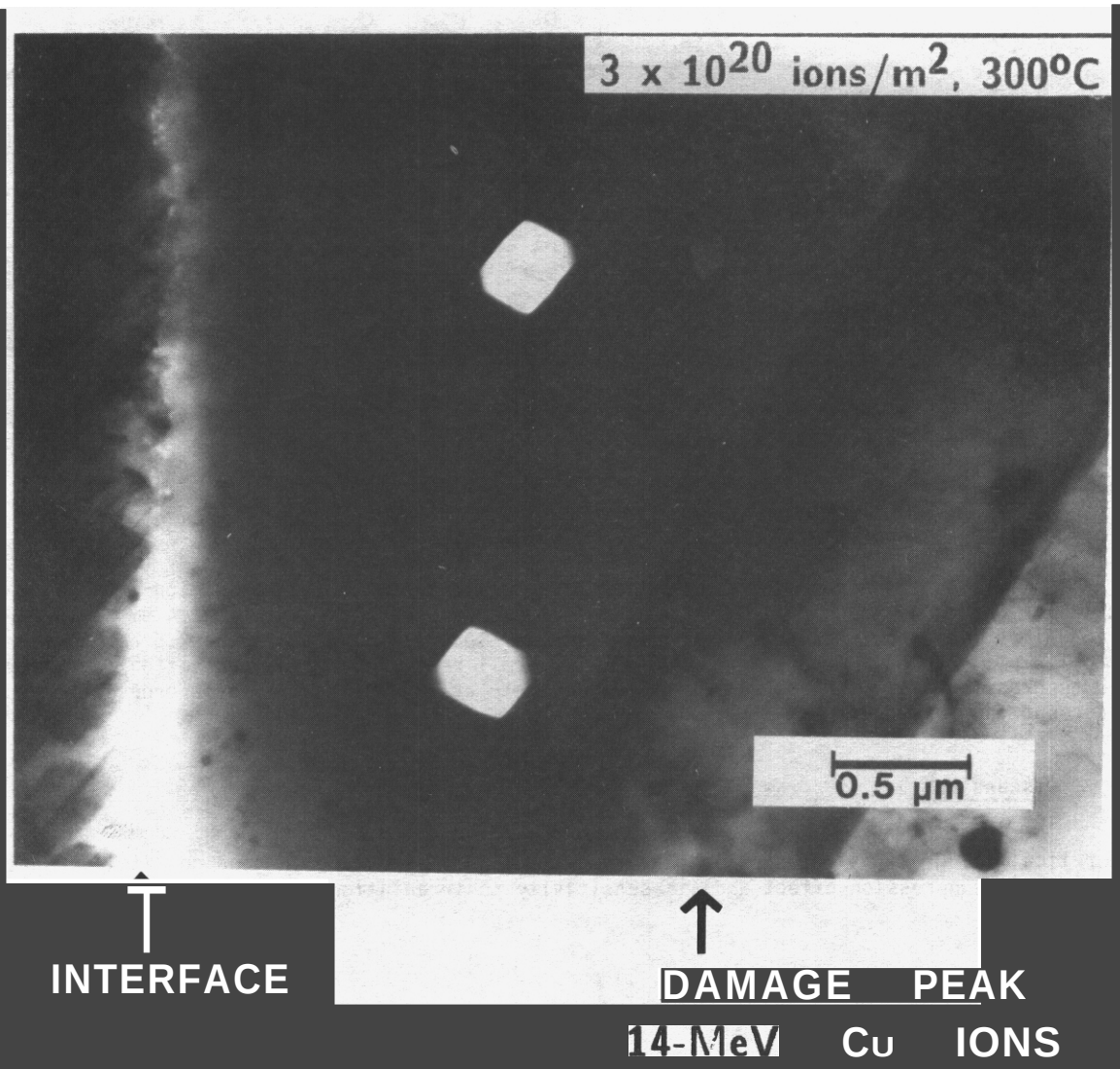

FIGURE 1. Cross-section TEM micrograph showing voids in annealed AMZIRC irradiated with 14-MeV Cu ions to a peak damage level of 15 dpa (K = 0.3) at 300°C.

5.4.3 P7 Stainless Steel

The P7 stainless steel samples were irradiated at 400°, 500' and 650°C up to a peak damage level of 20 dpa (K = 0.3). Small voids (diameter $\lesssim$ 2 nm) were observed at the end of range in the 400°C sample. However, inconclusive results were obtained for the depth-dependent void density due to the small void size. A suppression effect on void number density was observed in the high fluence 500°C sample [20 dpa (K = 0.3) at the peak damage region] whereas the low fluence 500°C sample (4 dpa peak damage) and the high fluence 650°C sample (20 dpa peak damage) showed no suppression effect. The low fluence 500°C sample had voids 1-2 nm in diameter which are difficult to detect due to their small size. This gives a large measurement error which is believed to be the reason no suppression effect was observed. Figure 6 shows TEM micrographs spanning the damage region in the 500°C high fluence P7 sample. A small decrease in the void number density in the peak region is evident. The void number density versus depth for the high fluence 500°C and 650°C samples are shown in Fig. 7. For the 650°C data the decreasing void number density in the peak damage region results from the large voids (~ 200 nm diameter) in the bimodal distribution reducing the number of voids through coalescence. The two size classes found in the 650°C sample are believed to be the result of an oxygen effect as discussed elsewhere.[9,10] Experimentally. the maximum suppression at 500°C is centered at 2.4 μm, where the amount of suppression results in a void number density decrease by a factor of ~ 3. The width of the suppressed region is. from 1.9 μm to 2.9 μm. There is no apparent suppression in the 650°C sample.

TABLE 3. EXPERIMENTAL RESULTS

Material	Temperature	T/T_m	Peak (dpa)	Suppression Results
Cu Alloys	300°C	0.42	15	Inconclusive
	400°C	0.50	15	No voids
	500°C	0.57	15	No voids
	550°C	0.61	15	No voids
Ni	425°C	0.40	2	Suppression
	450°C	0.42	2	Suppression
P7	400°C	0.40	20	Inconclusive
	500°C	0.45	4,20	Suppression
	650°C	0.54	20	No suppression

*Displacement efficiency K = 0.3

Figure 8 is a plot of the theoretical nucleation rate versus depth for 14-MeV Ni ion-irradiated P7. The 400°C calculations show a significant suppression effect centered at a depth of 2.4 μm and extending from 1.7 μm to 3.1 μm. The 500°C calculation shows a smaller suppression centered at 2.5 μm and extending from 1.8 μm to 2.8 μm. At 650°C, there is only a small overall reduction of the nucleation rate with no characteristic suppression dip. The calculated nucleation rate at 650°C is about seven orders of magnitude too lcm to account for the experimental results.

5.5 Discussion

The theoretical calculations and experimental results of this study are in good qualitative agreement on the magnitude of the suppression effect and its sensitivity to irradiation temperature. A quantitative compari

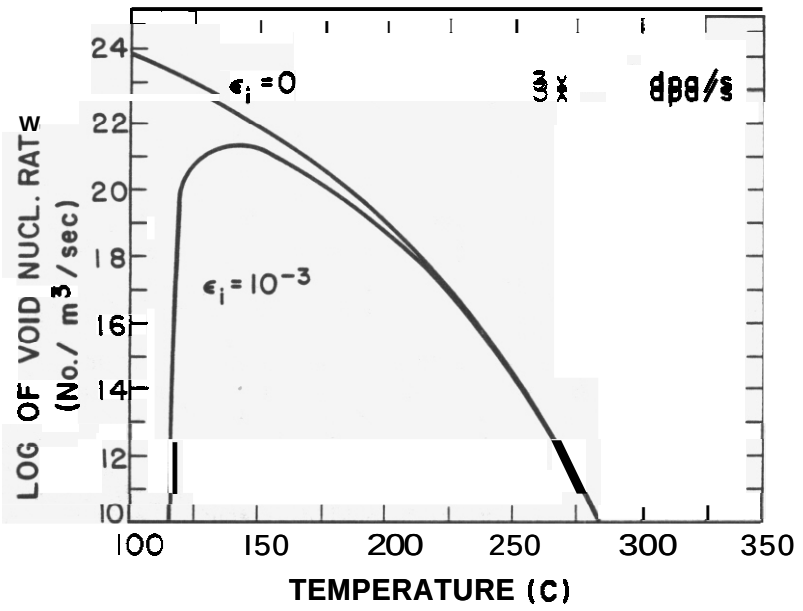

FIGURE 2. Theoretical void nucleation rate vs. temperature in Cu at a damage rate of 3×10^{-3} dpa/s with $E_v^m = 0.77$ eV.

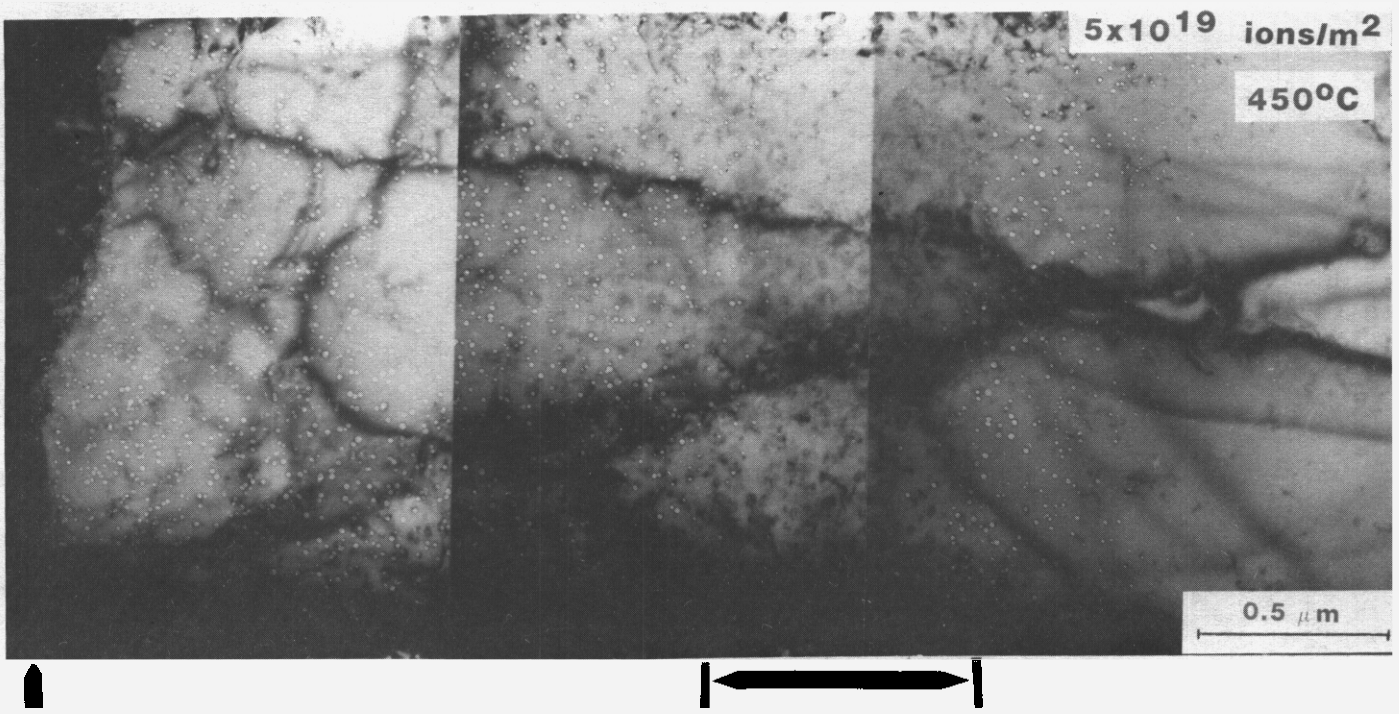

FIGURE 3. Depth-dependent void microstructure of nickel irradiated with 14-MeV Ni ions to a peak damage level of 2 dpa (K = 0.3) at 450°C. Note the absence of voids in the implanted ion region.

son between experiment ana theory shows differences which must be attributed to additional effects not yet incorporated in the theory, and to the complex interdependence of materials parameters in an irradiation environment. At "low" temperatures the discrepancies between theory and experiment concerning the amount and position of the-suppression of void nucleation may be attributed mainly to diffusional spreading. At "high" temperatures, where the excess interstitial effect is unimportant. the discrepancy between theoretical void nucleation rate and experimental observations may be attributed to the effect of impurities in the metal. Both of these effects are discussed below. Whether an irradiation is at a "high" or "low" temperature is unique to the metal being investigated and depends on the vacancy mobility and the impurity content.

For the "low" temperature irradiated Ni specimens, the observed suppression was larger and closer to the surface than the theoretical calculations would predict (Figs. 4. 5). The 425 and 450°C nickel samples gave a maximum suppression at depths of 1.6 and 2.1 μm with the suppression extending over a width of 2.3 and 1.6 μm, respectively. The theoretical results in Ni give a maximum suppression at 2.2 μm with widths of 1.0 and 0.8 μm. The increased width of the suppression zone with lower temperatures is probably due to recombination mechanisms becoming more dominant, which in turn enhance the effect of injected ions on void suppression. The differences in the maximum suppression position and in the width of the suppression region are more difficult to explain. One possible explanation for this difference is diffusional spreading. This is more apparent when the P7 results are examined. The P7-500°C sample has a maximum experimental suppression at 2.4 μm which extends over 1 μm in width and this agrees with the 2.5 and 1 μm from the theoretical results (Figs. 7, 8). The P7 experimental results are much closer to the theoretical predictions than in the case of nickel. From the materials parameters in Table 1 (e.g., E_v^m, S_v^m) it is apparent that the vacancy mobility in P7 will be lower than in the nickel. Diffusional spreading, which has recently been shown to be important,[31,32] will then be larger in nickel than in P7 due to the differences in the vacancy mobility. This results in a larger shift of the suppression maximum towards the front surface for Ni relative to P7. Another indication of the diffusional spreading differences between the two metals is seen by examining the end of range data. Comparing theoretical to experimental end of range for Ni and P7 gives 2.8 to 3.4 μm and 3.1 to 3.5 μm, respectively. The end of range diffusional spreading is larger for nickel, 0.6 μm, than for P7, 0.4 μm.

At "high" temperatures, when there is very little suppression, the lack of good correlation between theory and experiment could be due to the presence of impurities in the metal that are not properly accounted for in the nucleation model. The copper alloy, AMZIRC, at 300°C and the stainless steel P7 at 650°C are good examples of this point. For AMZIRC. the nucleation code is based on "pure" copper while the irradiated

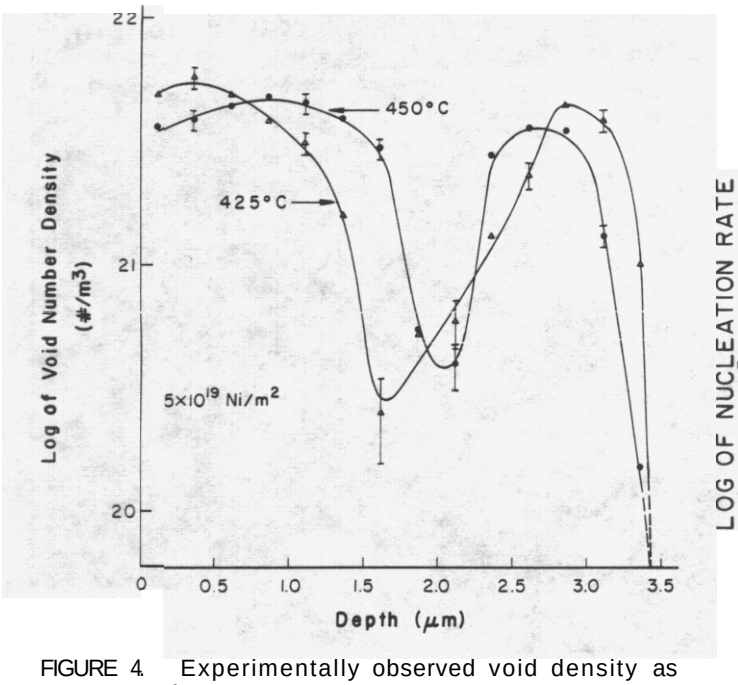

FIGURE 4. Experimentally observed void density as function of depth for nickel following 14-MeV Ni ion irradiation at 425°C and 450°C to peak damage levels of 2 dpa (K = 0.3).

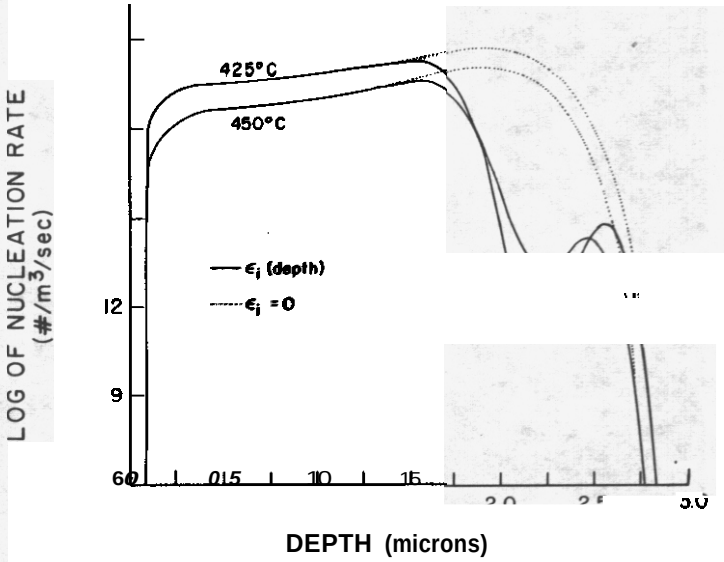

FIGURE 5. Theoretical void nucleation rate vs. a depth for 14-MeV Ni on Ni at 425°C and 450°C. Dashed line corresponds to no injected ions ($\epsilon_i = 0$). Solid line uses ϵ_i from Brice.[14]

specimen is a commercial copper alloy. If the solutes and impurities in the alloy act as trapping sites for vacancies, then the vacancy mobility is effectively decreased.[33] This decrease In the mobility can be accounted for in the nucleation code by raising the vacancy migration energy. Figure 9 is a plot of the void nucleation rate versus temperature in copper when $E_v^m = 0.87$ eV, implying an energy of 0.1 eV for trapping.[34] Comparison of Figs. 2 and 9 shows that the decrease in vacancy mobility will shift the "high" temperature nucleation rate by 30°C. The overall nucleation rate at 300°C has risen by.. 5 orders of magnitude to a value of $10^{11}/m^3$-s. The disparity between the theoretical rate of $10^{11}/m^3$-s and the experimental rate of $\sim 10^{14}/m^3$-s is not considered to be significant since it occurs at the upper temperature limit for void nucleation. Also evident from Fig. 9 is that a reduction in vacancy mobility increases the suppression. effect of the injected interstitials on void nucleation.

Many of the voids Observed in AMZIRC (Cu-Zr) were in the vicinity of large zirconium precipitates. The extreme heterogeneity of the voids in the copper alloy indicates that special circumstances are required for their formation. These circumstances are only approximated In the steady-state nucleation code because the sink density and segregation effects are time and space averages. An additional increase of 0.05 eV in the trapping energy. a small decrease of the surface energy (which would occur If impurities segregated to the void embryos), or a small decrease in the sink strength brings the calculated void nucleation into exact agreement with the AMZIRC experimental results.

The appropriate surface energy of voids is an unknown parameter, yet it has a pronounced effect on the nucleation rate. Oxygen in the P7 alloy could have migrated to a void embryo surface and reduced the surface energy, thereby increasing the nucleation rate dramatically.[9,10] Decreasing the surface energy or increasing the gas pressure has a similar effect on the void nucleation. Figure 10 shows the theoretical predictions of the void nucleation rate when the surface energy of P7 is reduced to 0.1 J/m^2. This change gives a nucleation rate at 650°C which is approximately equal to that observed. A surface energy of 0.1 J/m^2 is. however, unrealistically low. and some other effects such as vacancy trapping by impurities or gas stabilization of void embryos must also play a role.

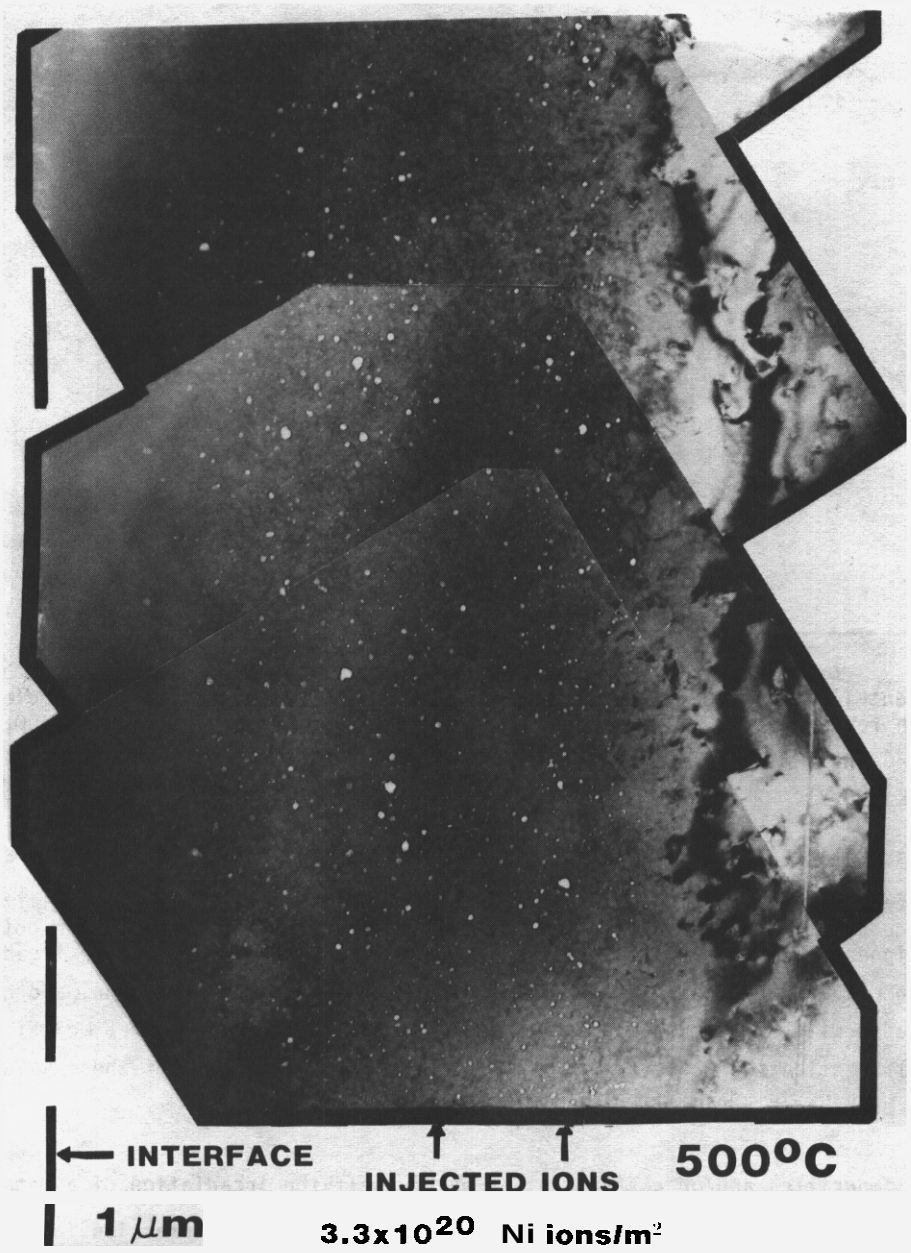

FIGURE 6. Depth-dependent void microstructure of P7 irradiated with 14-MeV Ni ions to a peak damage level of 20 dpa (K = 0.3) at 500°C.

At very high temperatures. the theoretical predictfans are in agreement with experimental results. The copper alloys that were ion irradiated ≳ 400°C did not produce any voids. which is in agreemnt with the theory (Figs. 2 and 9). One reason for this lack of void nucleation may be that the vacancy reemission rate from a void, which increases with temperature. is too high due to lack of gas stabilization of the voids. When combined with the high vacancy mobility. which lowers the vacancy supersaturation, it makes void nucleation very unlikely. These results then indicate that in the absence of impurities, the peak void swelling temperature for ion irradiation of copper alloys is probably below 300°C. In this context it is important to note that both AMZIRC and AMAX-MZC are manufactured under carefully controlled (oxygen-free) environments using OFHC copper, which mans a low content of gaseous impurities. Other experimental work on fon-irradiated copper by Glowinski[35] and Knoll[7] confirm that voids do not form in degassed copper. This contrasts with the published neutron irradiation data which show that voids form readily between 220 and 550°C (0.35-0.60 Tm).[36] Clearly, more research is required on the effect of gas on void nucleation in copper.

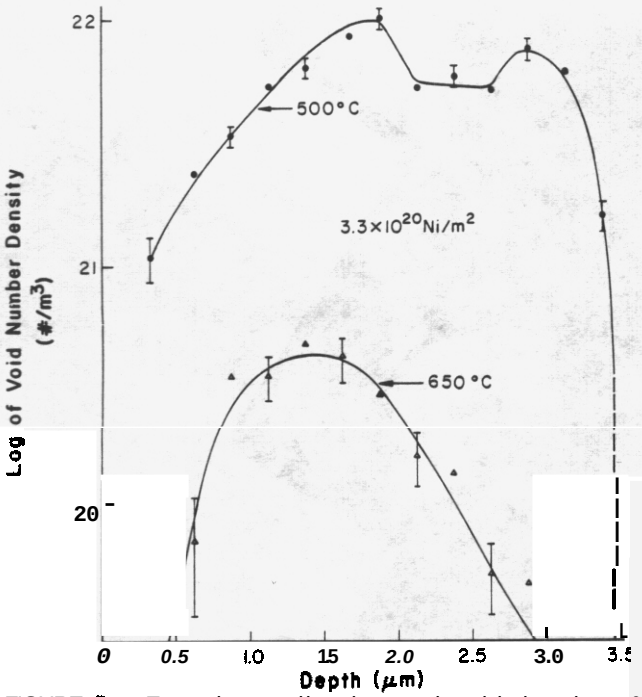

FIGURE 7. Experimentally observed void density as a function of depth for P7 following 14-MeV Ni ion irradiation at 500°C and 650°C to peak damage levels of 20 dpa (K = 0.3).

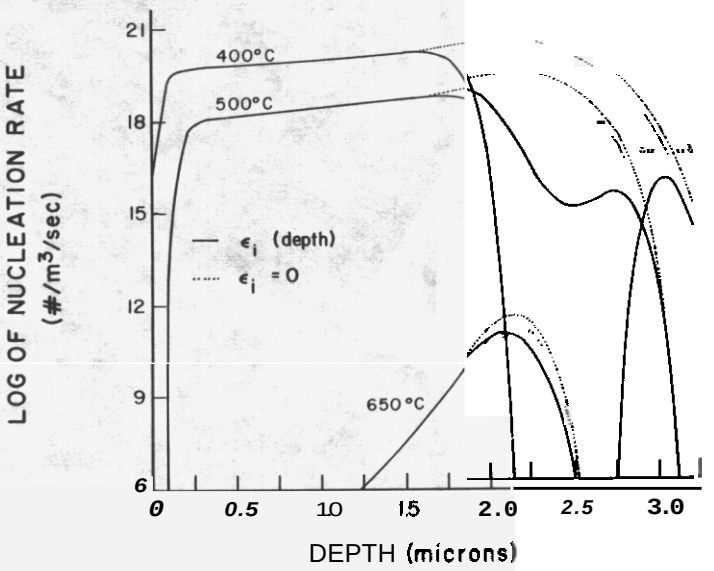

FIGURE 8. Theoretical void nucleation rate vs. depth for 14-MeV Ni on P7 at 400. 500 and 650°C assuming $\gamma = 0.8$ J/m^2. Dashed line is $\varepsilon_i = 0$, solid line is ε_i from Brice.[14]

The suppression effect of the injected interstitials on void nucleation need not be limited to low temperatures. The presence of impurities and or gas in the metal may shift the start of the point defect recombination regime to higher temperatures. The use of low energy ($\lesssim$ 5 MeV) self-ions to irradiate the metal would exacerbate such a temperature shift because the excess interstitial fraction, and hence the suppression effect, increases with decreasing ion energy.[3,5] For 14-MeV compared to 5-MeV Ni ions on nickel, the excess interstitial fraction increases from 3×10^{-3} to 6×10^{-3} where both of these values correspond to the ion deposition peak and K = 0.3.[3]

The combination of impurities and/or gas with a low energy self-ion irradiation of a metal is illustrated by the following cases. Johnston et al.[37] found an extensive mid-range suppression in the void density for 5-MeV Ni ion irradiated stainless steel at 625°C. Farrell et al.[32] observed a mid-range suppression in the void density of nickel dual-irradiated with helium and 4-MeV Ni ions at 600°C. These observed suppression effects occurred at temperatures much higher than expected from self-ion irradiation results presented here and elsewhere.[6] The impurities (or solutes) in the steel and the implanted gas (and/or impurities) in the nickel may have trapped the point defects in such a manner as to cause recombination to dominate the point defect loss mechanisms. This would make the excess interstitials a larger fraction of the point defects going to sinks (e.g. voids) and would result in reduced void nucleation. The above indicates that any void swelling results obtained from the peak damage region must be used with caution.

6.0 Conclusions

The following general conclusions may be drawn concerning void formation in ion-irradiated metals. These conclusions are currently valid only when applied to nickel. copper and stainless steel but may be more broadly applicable to all metals.

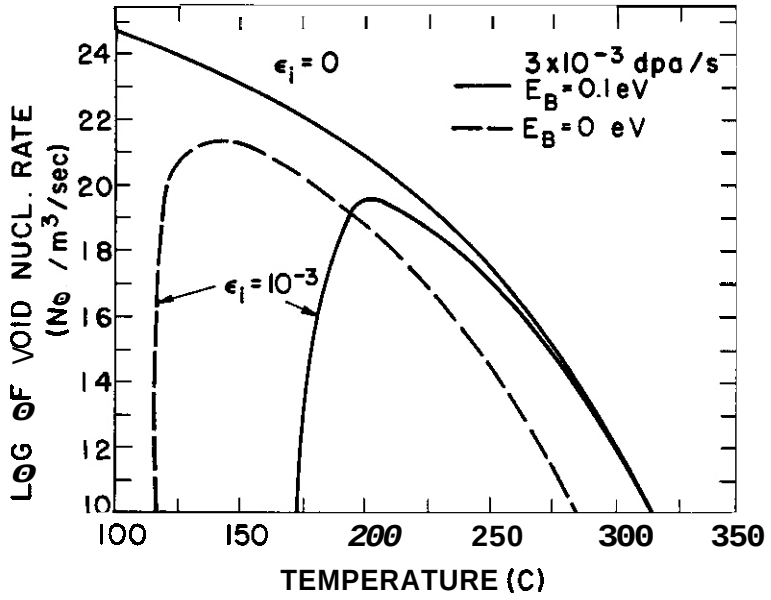

FIGURE 9. Comparison of the theoretical void nucleation rate vs. temperature in Cu at a damage rate of 3 x 10^{-3} dpa/s with and without a vacancy binding energy of 0.1 eV.

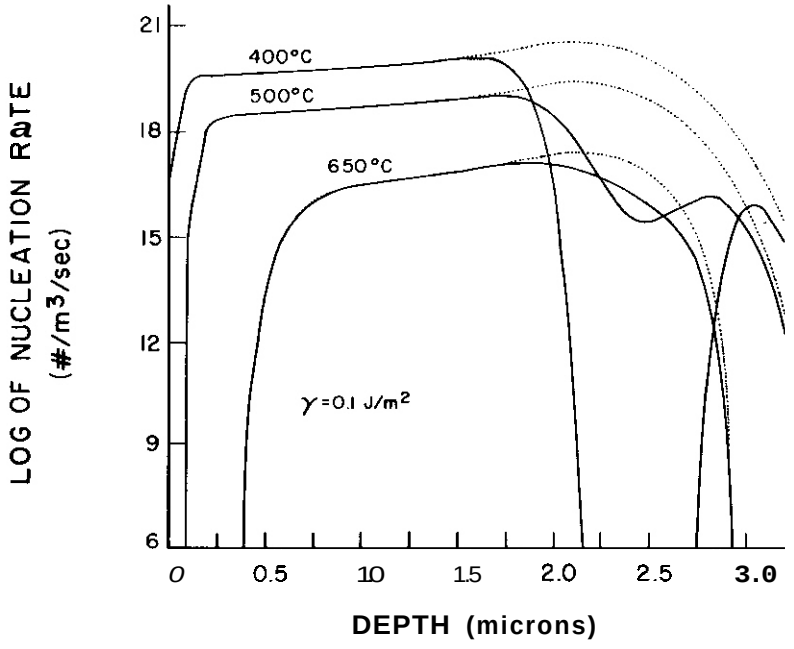

FIGURE 10. Theoretical void nucleation rate vs. depth for 14-MeV Ni on P7 at 400, 500 and 650°C assuming γ = 0.1 J/m^2. Dashed line is ε_i = 0, solid line is ε_i from Brice.[14]

1. Qualitative agreement between theory and experiment regarding void nucleation in the presence of injected ions is very good. The injected ion effect becomes important as the irradiation temperature is decreased. The actual temperature where the effect becomes significant depends on the metal being investigated and on the impurity and/or gas content of that metal.

2. Quantitative agreement between theory and experiment regarding the effect of injected ions on void nucleation is fair. It appears that the discrepancies are due to neglect of diffusional spreading and impurity effects in the nucleation theory.

3. The magnitude of void nucleation suppression can be very significant below certain temperatures. Void swelling data from ion irradiations should not be taken from the peak damage region when experimental conditions exist which make the injected ion effect important.

4. As is evident from ion irradiation studies on pure copper and copper alloys. the relative temperature regime for swelling is determined by the vacancy mobility, not by the mlting point of the metal, i.e. the void swelling regim is not necessarily 0.35-0.6 Tm.

Acknowledgements

The authors gratefully acknowledge the support of the Department of Energy, Office of Fusion Energy. We would also like to thank D.B. Sullen for preparation of the nickel samples used in this study.

7.0 References

1. A.D. Brailsford and L.K. Mansur, J. Nucl. Mat. 71 (1977) 110.

2. E.H. Lee, L.K. Mansur and M.H. Yoo, J. Nucl. Mat. 85 & 86 (1979) 577.

3. D.L. Plumton and W.G. Wolfer, J. Nucl. Mat. 120 (1984).

4. F.A. Garner, J. Nucl. Mat. 117 (1983) 177.

5. O.L. Plumton. H. Attaya and W.G. Wolfer, "Conditions for the Suppression of Void Formation During Ion-Bombardment," Third Topical Meeting on Fusion Reactor Materials, Albuquerque, NM, 19-23 Sept. 1983.

6. J.B. Whitley, G.L. Kulcinski, P. Wilkes and H.V. Smith Jr., J. Nucl. Mat. 7 (1979) 159.

7. R.W. Knoll, "Effects of Heavy Ion Irradiation on the Phase Stability of Several Copper-Base Alloys." Ph.D. Thesis, Nuclear Engineering Department, University of Wisconsin-Madison (UWFDM-436).

8. K. Shiraishi, M.P. Tanaka, T. Aruga and S. Hamada. ASTM STP 782 (1982) pp. 927-940.

9. R.L. Sindelar, G.L. Kulcinski and R.A. Dodd, "Depth Dependent Micrcstructure of Ion-Irradiated Type 316 Stainless Steel," Third Topical Meeting on Fusion Reactor Materials, Albuquerque, NM, Sept. 19-23, 1983.

10. R.L. Sindelar, R.A. Dodd and G.L. Kulcinski, "A Comparison of the Depth-Dependent Microstructure of Ion-Irradiated 316-Type Stainless Steels," Proc. of 12th International Symposium on the Effects of Radiation on Materials, 18-20 June 1984. Williamsburg. VA.

11. S.J. Zinkle, R.A. Dodd and G.L. Kulcinski, "Comparison of Thermal and Irradiated Behavior of High-Strength, High Conductivity Copper Alloys," Proc. of 12th International Symposium on the Effects Of Radiation on Materials, 18-20 June 1984, Williamsburg, VA.

12. I.M. Torrens and M.T. Robinson, Radiation Induced Voids in Metals, J.W. Corbett and I.C. Ianniello, Eds. (1972) 739.

13. J.H. Kinney, M.W. Guinan and Z.A. Munir, Presented at the Third Topical Meeting on Fusion Reactor Materials, Albuquerque, NM, Sept. (1983).

14. D.K. Brice. Sandia National Laboratory Report SAND 75-0622 (1977).

15. A. Seeger and H. Mehrer, Vacancies and Interstitials in Metals, ed. by A. Seeger, D. Schumacher, W. Schilling and J. Diehl, North Holland, Amsterdam, 1970, p. 1

16. R.R. Eourassa and B. Leugeler, J. Phys. F: Metal Phys. 6 (1976) 1405.

17. W. Triftshauser and J.D. McGervey, Appl. Phys. 6 (1975) 177.

18. K. Maier, C. Bassani and W. Schule, Phys. Lett. 44A (1973) 539.

19. N.Q. Lam, S.J. Rothman and L.J. Nowicki. Phys. Stat. Sol. (9) 23 (1974) K35.

20. R.O. Simmons and R. Balluffi. Phys. Rev. 129 (1963) 1533.

21. K. Maier, H. Mehrer, E. Lessmann and W. Schule, Phys. Stat. Sol. 78 (1976) 689.

22. L.C. Smedskjaer, M.J. Fluss, D.G. Legnini. M.K. Chason and R.W. Siegel, J. Phys. F: Metal Phys. 11 (1981) 2227.

23. S.K. Khana and K. Sonnenberg, Rad. Effects 59 (1981) 91.

24. S.J. Rothman, L.J. Noicki and G.E. Murch, J. Phys. F: Metal Phys. 10 (1980) 383.

25. L.E. Murr, Interfacial Phenomena in Metals and Alloys, Addison-Wesley, Reading, MA (1975).

26. W.G. Wolfer and M.H. Yoo, in "Radiation Effects and Tritium Technology for Fusion Reactors,' Gatlinburg, TN (1976), Yol. II, CONF-750989.

27. J.L. Katz and H. Wiedersich. J. Chem. Phys. 55 (1971) 1414.

28. A. Si-Ahmed and W.G. Wolfer, ASTM STP 783 (1982) 1008.

29. W.G. Wolfer and L.K. Mansur. J. Nucl. Mat. 91 (1980) 265.

30. J.J. Sniegowski and W.G. Wolfer. "On the Physical Basis for the Swelling Resistance of Ferritic Steels," Topical Conf. on Ferritic Alloys for Use in Nuclear Energy Technologies, Snowbird, UT, USA, 19-23 June 1983.

31. L.K. Mansur and M.H. Yoo, J. Nucl. Mat. 85 & 86 (1979) 523.

32. K. iarrell, N.H. Packan and J.T. Houston, Rad. Effects 62 (1982) 39.

33. F.A. Garner and W.G. Wolfer, J. Nucl. Mat. 102 (1981) 143-150.

34. M. Doyama, J. Nucl. Mat. 69 & 70 (1978) 350.

35. L.D. Glowinski and C. Fiche, J. Nucl. Mat. 61 (1976) 22.

36. R.W. Knoll, "A Literature Review of Radiation Damage Data for Copper," University of Wisconsin Fusion Engineering Program Report UWFDM-384 (Oct. 1980).

37. W.G. Johnston, J.H. Rosolowski, A.M. Turkalo, T. Lauritzen, J. Nucl. Mat. 62 (1976) 167.

38. B.D. Cullity, "Elements of X-Ray Diffraction," 2nd Ed., Addision-Wesley, Reading, MA (1978) pp. 506-508.

39, J.P. Hirth and J. Lothe, "Theory of Dislocations." 2nd Ed., John Wiley & Sons, New York (1982) p. 837.

40. G.E. Dieter. "Mechanical Metallurgy," 2nd Ed., McGraw-Hill, New York (1976) p. 51.

41. P. Ehrhart. Conf. on Dimensional Stability and Mechanical Behavior of Irradiated Metals and Alloys, BNES, London, 1983. paper 17.

42. K.H. Robrock, Conf. on Dimensional Stability and Mechanical Behavior of Irradiated Metals and Alloys, BNES, London, 1983, paper 18.

43. U. Theis and H. Wollenberger, J. Nucl. Mat. 88 (1980) 121.

THE EFFECT OF VOID SURFACE MOTION ON THE VOID SINK STRENGTH FOR POINT DEFECTS

R. Bullough (Theoretical physics Division, AERE Harwell, UK), N.M. Ghoniem (UCLA)

1.0 Objective

At very high damage rates, or generally under conditions of substantial radial cavity growth rates, the fast motion of cavity boundary is envisioned to simultaneously influence the ability of the cavity for paint defect absorption. In this report, we derive analytical formulas for the cavity sink strength including such boundary motion.

2.0 *Summary*

By a generalization of an analysis due to Frank of the growing precipitate we derive an analytic sink strength for the growing void that takes account of the void surface motion in a self-consistent fashion. The lower mobility of the vacancies compared to the interstitials ensures that a growing Void captures more vacancies than the usual quasi-static void. The various consequences of this void bias for vacancies are discussed in relation to the swelling of reactor materials.

3.0

Title: Radiation Effects on Structural Materials (This work has been performed at the Theoretical Physics Division of Harwell during Professor Ghoniem's sabbatical leave.)
Principal Investigator: N.M. Ghoniem
Affiliation: University of California, at Los Angeles

4.0 Relevant DAFS Program Plan *Task/Subtask*

Correlation Methodology/Microstructure

5.0 Accomplishments and Status

5.1 Introduction

Void growth in irradiated materials leads to a net volume increase, or swelling, of such mterials and has been the subject of much experimental and theoretical investigation since Cawthorne and Fulton[1] first observed the phenomenon in stainless steel fast reactor fuel cladding. Such voids are usually considered to be relatively neutral sinks for mobile point-defects and their growth, in such materials, occurs because interstitials are lost preferentially at the dislocations so that, in a steady-state irradiation environment. there must be a consequent excess vacancy flux into relatively neutral sinks such as voids. The dependence of the kinetics of void swelling on the physical and irradiation parameters and on the overall microstructural state of materials has been extensively studied using the rate theory model of the total evolving microstructure[2,3,4,5,6]. A description of the microstructure is thus provided by replacing the crystalline material, with its spatially varying local point-defect concentrations in the neighborhood of each sink. by an effective medium in which the point-defect concentrations are homogeneous and the actual sinks are replaced by effective sinks. The effective medium is thus a lossy continuum in which the variouse sink types, that together define the total microstructure. each have an associated sink strength. The sink strengths for many of the important sink types have now been obtained using the consistent embedding

procedure, the fundamental basis of which has been reviewed by Brailsford and Bullough[7]. In most of these sink strength calculations a quasi-static approximation is adopted in which the motion or transient morphological changes of the sink caused by the net flux of point-defects absorbed by it are assumed to have negligible effect upon the flux itself. Rauh and Bullough[8] have recently studied the effect of dropping this restriction for the edge dislocation sink; they have shown that the climb motion of the dislocations can have a significant effect upon their strength at high damage rates. In particular the climb motion increases the vacancy flux into a dislocation and thereby reduces its effective preference (or bias) for the interstitials which, in turn, reduces the actual climb rate.

The purpose of the present paper is to present an analogous, albeit simpler, analysis for the growing void in which the actual motion of the void surface is included in a self-consistent fashion. In section 2 we present the calculation of the self-consistent growing void sink strength using an embedding model valid for low sink densities. In addition. some limiting analytic features of the solution are discussed and related to the usual quasi-static results for void swelling in the presence of a second sink. A range of numerical evaluations of the general solution are described in section 3 using physical parameters appropriate for stainless steel. Finally in section 4, we discuss the practical relevance of the present growing void sink strength, together with its physical limitations and suggest how its significance could be investigated in the future.

5.2 The Sink Strength for the Growing Void

If the effective medium[7], which represents the real material, has total sink strength k_α^2, where henceforth the subscript α can be i (for interstitial) or v (for vacancy) to distinguish the two point-defects, we have

$$k_a^2 = k_{\alpha D}^2 + k_{\alpha C}^2 \ , \qquad (1)$$

where $k_{\alpha D}^2$ is the dislocation sink strength and $k_{\alpha C}^2$ is the void (cavity) sink strength we seek; for simplicity the only sink types deemed to be present in the microstructure will be dislocations and voids. In the usual notation we write

$$k_{\alpha D}^2 = Z_\alpha \rho_D \qquad (2)$$

Where $Z_\alpha (Z_i > Z_v)$ are the dislocation bias parameters defining the dislocation preference for interstitials compared to vacancies and ρ_D is the edge dislocation density. For such a homogeneous medium the steady state point-defect concentration is

$$c = K/D_\alpha k_\alpha^2 \qquad (3)$$

where K is the point-defect production (damage) rate, assumed to be equal for vacancies and interstitials, D_α is the diffusion coefficient of the point-defect a and thermal emission of point-defects from the sinks together with loss of point-defect8 due to bulk recombination are neglected.

To obtain the exact consistent sink strength of the growing voids for interstitials and vacancies we must attempt to follow the embedding prescription[7] and identify at time t one of the voids embedded in the effective medium of (unknown) radius $r_C(t)$. The point defect concentration around such a void satisfies the conservation equation:

$$\frac{D_\alpha}{r^2}\frac{6}{6r}\left(r^2 \frac{\delta c_a}{6r}\right) + K - D_\alpha k_\alpha^2 c_\alpha = \frac{\delta c_a}{6t} \qquad (4)$$

where the center of the void is located at the origin. r=o of a spherical coordinate system. In the effective medium. away from the vicinity of the identified void the spatial and explicit transient variation of c_α must vanish and, from (3)

$$c_a = c_a^\infty = K/D_\alpha k_\alpha^2 \quad \text{as } r \to \infty. \qquad (5)$$

For simplicity we may treat the void as an ideal sink for either point-defect and thus

$$c_\alpha = o \quad at \quad r = r_C(t) \ . \tag{6}$$

We can specify a small value (or zero) for the radius of the void at t=0:

$$r_C(t) = r_C^o \ at \ t=o \tag{7}$$

Finally the consistent velocity of the void surface is given by the net vacancy flux into the void:

$$\dot{r}_C(t) = [D_v \frac{\delta c_v}{\delta r} - D_i \frac{\delta c_i}{\delta r}]_{r=r_C(t)} \tag{8}$$

By equating the point defect loss rate to the identified void

$$4\pi r_C^2(t) D_\alpha \frac{\delta c_\alpha}{\delta r}]_{r_C(t)} \tag{9}$$

to the corresponding loss rate in the effective medium

$$k_{\alpha C}^2 \ D_\alpha c_\alpha^\infty / C_C \ , \tag{10}$$

where C_C is the volume concentration of voids, we obtain the implicit equation for the required growing void sink strength[4,7]

$$k_{\alpha C} = \frac{4\pi r_C^2(t) C_C}{c_\alpha^\infty} [\frac{\delta c_\alpha}{\delta r}]_{r_C(t)} \ . \tag{11}$$

It is clear that to solve (4) when the boundary condition (6) is specified on a surface $r = r_C(t)$ whose value has to be consistently deduced by integrating (8) is a mathematically formidable problem; this is particularly true also when the $k_{\alpha C}^2$ component of k_α^2 in (4) is the quantity we seek from (11). To obtain a solution of these equations we can simplify the conservation equation (4) by removing the explicit source and sink terms ($K - D_\alpha k_\alpha^2 c_\alpha$) with the knowledge that this approximation will yield a sink strength result that is correct to lowest order in the sink density[7]. When the void growth is neglected, as in the usual quasi-static approximation, equation (4) becomes

$$\frac{1}{2} \frac{d}{dr} (r^2 \frac{dc_\alpha}{dr}) = 0 \tag{12}$$

which, from (5), (6) and (11) yields the first-order neutral sink strength:

$$k_{\alpha C}^2 = k_C^2 = 4\pi r_C C_C \tag{13}$$

The adoption of this approximation thus ensures that our final result will yield the correction to the lowest order void sink strength due to its growth and its use must therefore be restricted with this in mind. As discussed by Brailsford and Bullough[7] the approximation is only valid when the sink-sink interactive correction terms are negligible; that is when

$$k_\alpha r_C \ll 1. \tag{14}$$

Replacing equation (4) by the dilute sink density form:

$$\frac{D_\alpha}{r^2} \frac{\delta}{\delta r} (r^2 \frac{\delta c_\alpha}{\delta r}) = \frac{\delta c_\alpha}{\delta t} \tag{15}$$

and considering the growth of the voids from zero radius ($r_C^o = 0$ in (7)) we can then proceed to obtain a consistent solution of (15) that satisfies (5), (6), (7) and (8). To do so we follow a previous analysis of the growing spherical precipitate due to Frank[9] and assume a trial function for $r_C(t)$ of the explicit form

$$r_C(t) = A\sqrt{t}. \tag{16}$$

We now seek a constant value for A such that the solution of (15) satisfies the boundary condition (5), (6) and (7) together with the growth velocity condition (8). If A is constant then (16) automatically satisfies the initial condition (7), with r_C^o set to zero. The required solution of (15) for the point-defect concentration c_α around the growing void may be obtained by replacing the variables (r,t) by the single variable s. such that

$$s = r/\sqrt{t} \ . \tag{17}$$

With this transformation equation (15) is replaced by the ordinary differential equation

$$\frac{d^2 c_\alpha}{ds^2} + \left(\frac{s}{2D_\alpha} + \frac{2}{s}\right)\frac{dc_\alpha}{ds} = 0 \tag{18}$$

The solution of this equation and hence of the original equation (15), that satisfies both (5) and (6) is, in terms of the r and t variables

$$c_\alpha = c_\alpha^\infty \left\{1 - \frac{F(r/\sqrt{t}, D_\alpha)}{F(A, D_\alpha)}\right\} \ , \tag{19}$$

where

$$F(x,y) = \frac{\exp(-x^2/4y)}{x} - \frac{1}{2}\sqrt{\pi/y}\ \mathrm{erfc}(x/2\sqrt{y}) \tag{20}$$

The value of A must now be both constant and consistant with the growth velocity equation (8); substitution of (19) into (8) yields the required relation for A

$$\frac{A}{2} = c_v^\infty \sqrt{D_v}\ \phi(A/\sqrt{D_v}) - c_i^\infty \sqrt{D_i}\ \phi(A/\sqrt{D_i}) \tag{21}$$

where

$$\phi(\gamma) = \frac{\exp(-\gamma^2/4)}{\gamma} \Big/ \left\{\exp(-\gamma^2/4) - \frac{\gamma\sqrt{\pi}}{2}\ \mathrm{erfc}(\gamma/2)\right\} \ . \tag{22}$$

The existence of the relation (21) for A confirms the validity of the trial solution (16) and that (19) is the required solution for the point-defect concentration around the growing void.

The required growing void sink strengths now follow from (11) and (19) and may be written in the form

$$k_{\alpha C}^2 = k_C^2\ \xi_\alpha \tag{23}$$

where

$$\xi_\alpha = (A/\sqrt{D_\alpha})\phi(A/\sqrt{D_\alpha}) \tag{24}$$

are the growth correction factors on the first order neutral void sink strength k_C^2, given by (13). The explicit relation for A now follows by substituting the c_α^∞ concentrations given, from (1), (2), (5) and (23), by

$$c_\alpha^\infty = K/D_\alpha(Z_\alpha\rho_D + k_C^2\xi_\alpha) \quad , \tag{25}$$

into the relation (21) to yield

$$A[Z_v\rho_D + k_C^2(A/\sqrt{D_v})\,][Z_i\rho_D + k_C^2(A/\sqrt{D_i})\phi(A/\sqrt{D_i})\,] = 2K\rho_D[(Z_i/\sqrt{D_v})\phi(A/\sqrt{D_v}) - (Z_v/\sqrt{D_i})\phi(A/\sqrt{D_i})\,] \quad . \tag{26}$$

Before presenting results obtained by solving equation (26) numerically it is instructive to replace (26) by an approximate form valid when the argument of the function ϕ, defined by (22), is small. It is then easily shown that

$$\phi(\gamma) = \frac{3}{\gamma}/[1 - \sqrt{\gamma}\gamma + \frac{\gamma^2}{2}\,1 \text{ when } \gamma < 2/\sqrt{\pi} \tag{27}$$

which, when substituted into (26) yields the quadratic equation for A:

$$(Z_v\rho_D + k_C^2)(Z_i\rho_D + k_C^2)A^2 - K\rho_D\sqrt{\pi}(Z_v/\sqrt{D_v} - Z_i/\sqrt{D_i})A - 2K\rho_D(Z_i - Z_v) = 0 \quad . \tag{28}$$

Since $D_i \gg D_v$, the required positive real root of (28) is accurately given by:

$$A = \frac{K\rho_D\sqrt{\frac{\pi}{D_v}}\,Z + \left[\frac{K^2\rho_D^2\pi Z^2}{D_v} + 8k_o^4K\rho_D(Z_i - Z_v)\right]^{1/2}}{2k_o^4} \tag{29}$$

where Z_i and Z_v have teen replaced by Z when the small difference between them is unimportant and

$$k^2 = Z\rho_D + k_C^2 \tag{30}$$

Two extremes can be identified from (29):

i) If the vacancies are very mobile (D_v large) then the growth of the voids will have a negligible effect on their sink strength and (24) yields

$$A = A_b = [2K\rho_D(Z_i - Z_v)/k_o^4]^{1/2} \quad , \tag{31}$$

where the subscript b indicates 'bias' dominated value.

ii) Conversely when the vacancies are not very mobile (D_v small) the void growth will lead to extra vacancy

capture and the value of A will increase towards

$$A = A_g = K\rho_D \sqrt{\frac{\pi}{D_v}}\ Z/k_o^4 , \qquad (32)$$

where the subscript g indicates 'growth' dominated value.

When the volume concentration of voids is C_C the expected void swelling rate must he

$$\frac{d}{dt}\left(\frac{\Delta v}{v}\right) = 4\pi r_C^2\, r_C\, C_C \qquad (33)$$

and thus, from (16)

$$\frac{d}{dt}\left(\frac{\Delta v}{v}\right) = 2\pi A^3 t^{1/2} . \qquad (34)$$

It is easily seen that (34), with A given by (31) is indeed the usual quasi-static swelling rate[4] when the effects of void growth are neglected together with the thermal emission and bulk recombination of the point-defects. In the other extreme, when void growth effects dominate over the bias growth *(34)* and (32) also lead to a "on-zero swelling rate. We thus conclude that once void growth begins it will continue in the presence of a second sink even if that second sink is completely neutral! This conclusion and its possible physical relevance will he further discussed in the final section.

5.3 Numerical Results

To explore the consequences of the present sink strengths for the growing voids we have solved the exact equation (26) for A by an accurate numerical iteration procedure using the physical parameters, reasonably appropriate to stainless steel[10], given in table *1*. In all the calculations we have assumed a small void radius of 1 n.m. and a fixed void concentration of 10^{21} m^{-3} and varied the dislocation density, temperature and damage rate. Figure 1 shows the variation of A^2 with dislocation density at a damage rate of 10^{-6} dpals for the temperatures *300°C* and 500°C. It is clear from (16) that the quantity A^2 is a measure of the mobility of the surface of a growing void and because its value is much less than that of the vacancy diffusion coefficient in this temperature range (D_v = 2.9 x 10^{-17} m^2 s^{-1} at 300°C and D_v = *4.5* x 10^{-14} m^2 s^{-1} at *500°C)* the motion of the void surface can have only a small effect at this low damage rate. This almost quasi-static behavior results in the near temperature independence of the curves and the position of the maximum in A^2 at about $\rho_D \simeq 10^{13}$ m^{-2}, when the sink strengths of the voids ($4\pi r_C C_C \simeq 1.2 \times 10^{13}$ m^{-2}) and dislocations are equal[4]. Figure 2 shows the same results far the higher damage rate of 10^{-3} dpals; it is immediately noticeable that the magnitude of A^2 is now much larger and that as it approaches the value of D_v the curves both change shape and exhibit a marked temperature dependence. To further clarify this behavior figures 3 and *4* show the varations of the ratio A^2/A_b^2 for the low (10^{-6} dpa/s) and high (10^{-3} dpa/s) damage rates respectively. This ratio is a measure of the 'self enhancement' of the void surface mobility and we see the enhancement is considerable at the higher damage rate in figure *4* with a strong temperature dependence especially at low dislocation densities.

The consequent variations of the growth correction factors ξ_α for the growing void sink strengths, as given by (23) and (24), are dipicted in figures 5, 6 and 7 by presenting the percentage increase of the void sink strength due to growth, $(\xi_\alpha - 1) \times 100$, again for the two temperatures 300°C and 500°C. We see, from figure 5, that for typical reactor conditions (K = 10^{-6} dpa/s) the increases for the vacancies are always small. typically small fractions of a percent. On the other hand, from figure 6. it is clear that for accelerator conditions (K = 10^{-3} dpa/s) increases of a few percent or greater can occur. For comparison with these sink strength increases for vacancies we show the corresponding sink strength increase, $(\xi_i - 1) \times 100$, for the interstitials in figure 7 for the high damage rate (10^{-3} dpals); even for this high damage rate the interstitial mobility is sufficiently high to ensure that the increase is always quite negligible compared with that for the vacancies. We conclude that void surface motion does not significantly affect the interstitial flux into the voids.

Finally, in figures 8 and 9 we present thc variation of the percentage fraction of the total swelling rate $\frac{d}{dt}\left(\frac{\Delta v}{v}\right)$, given by (34), due to the void surface motion, $(1 - (A_b/A)^3) \times 100$, for the respective low and

high damage rates used previously. Again results for the two temperatures 300°C and 500°C are given. At the lower, reactor, damage rate in figure 8 the swelling enhancement due to the void surface motion is restricted to a few percent whereas at the higher, accelerator, damage rate in figure 9 very large swelling enhancements obtain, particularly at the lower temperature. The practical relevance and validity of these swelling results will be discussed in the next section; it will suffice here to emphasize that these swelling curves are presented only for their interest as accurate evaluations of the simple theoretical expressions. such as (26), in the present paper and are not intended to have validity to any physical system over the complete range of ρ_D and T used here.

5.4 Discussion

In this paper we have used an embedding procedure to obtain a simple expression for the sink strength of a growing void. The essential feature of the study is probably the realization that such a self-consistent solution for the growing spherical sink exists when its growth is determined by the fluxes of more than one point-defect type. In this sense it represents a generalization of the original analysis due to Frank[9] of the growing spherical precipitate when only one point-defect type was involved in the precipitation process. Of course, the present calculation could be further generalized to invlove growth arising from the collective segregation of more than two point-defect types. It is, however, important to identify the inadequacies of the present analysis in relation to void processes in real irradiated materials. We have stated in the text that the embedding model used is only valid when sink-sink interactive effects are negligible, that is when the inequality (14) is satisfied, and thus any results we obtain can only by valid as corrections to the 'dilute' quasi-static void sink strength (13). It is to satisfy (14) that we deliberately present results for small voids of radius 1 n.m.; for this radius the condition (14) is satisfied for the complete range of ρ_D employed. For larger voids the upper limit of ρ_D would have to be lowered to comply with (14). However this tendency for the model to be inaccurate at high ρ_D is somewhat alleviated by the fact that the growth effects we are examining are in any case minimal when ρ_D is large.

In addition to the restriction (14) on the valididty of the results it is important to emphasize that point-defect loss due to bulk recombination has been neglected both in the derivation of the growing void dink strength in section 2 and in the subsequent evaluation of the swelling increase due to the void growth in figures 8 and 9. The error in the sink strength calculation is difficult to estimate but it arises because its value depends on the actual net flux of vacancies arriving at the void through equation (8); thus, in contrast to the usual quasi-static embedding calculations of sink strengths, the simultaneous presence of both point-defect types is implicitly understood and recombination loss should be included. The only mitigation we can claim stems from the fact that when such non-linear recombination loss has been included in quasi-static sink strength calculations its effect is small[10]. In addition the present sink strengths are probably satisfactory if their use is restricted to swelling situations when the point-defect loss occures predominantly at the sinks rather than by bulk recombination. Thus using a recombination parameter given by[11] $\alpha = 10^{20} D_i s^{-1}$ we can estimate the value of ρ_D, for each temperature and damage rate in figures 8 and 9, above which the curves are valid. Since no recombination has been included in the evaluations of these curves they can only he valid when $2K > \alpha c_i^{\infty} c_v^{\infty}$ where c_i^{∞} and c_v^{∞} are given in terms of A and the other parameters by (25). This comparison of total point-defect lass to the sinks with potential recombination loss yields the following conclusions: For the damage rate of 10^{-6} dpals, ρ_D must exceed 5×10^{14} m^{-2} at 300°C and 10^{13} m^{-2} at 500°C; at the higher damage rate of 10^{-3} dpa/s, ρ_D must exceed 10^{16} m^{-2} at 300°C and 5×10^{14} m^{-2} at 500°C. It follows that the results in figures 8 and 9 have limited validity and the percentage increase of swelling due to the motion of the void surface is probably always less than 5%.

Although we have presented results showing the temperature sensitivity of the void growth on the swelling our basic rate theory model for the swelling used here is extremely primitive. Thus not only have we neglected bulk recombination but we have also omitted any temperature variations of the sink densities themselves. The curves in figures 8 and 9 are thus not, in an sense, intended to represent predictions for stainless steel but are presented merely to provide insight into the kind of modifications the motion of the growing void surface could have an the total swelling of irradiated materials. It is interesting to speculate on the effect of including both the void surface motion as discussed here and the climb motion of the dislocations as discussed by Rauh and Bullough[8] in the same swelling analysis. The motion of void surface increases the growth rate of the void because the void surface captures more relatively sluggish vacancies, on the other hand the climb motion of the dislocation reduces the net interstitial flux to the dislocations and hence retards the void growth rate. Presumably if the two effects are simultaneously present the overall effect of such motions could be minimal and strong support for the accuracy of the quasi-static approach might be forthcoming.

Finally we have noted that the void surface motion provides a net vacancy bias for the growing void and thus we see that, even if the second sink is neutral. once void growth has commenced it should be self-driven by its own vacancy bias arising solely from the differences in point-defect mobility. Such an effect could well give significant assistanct to the growth of the vacancy clusters during the initial nucleation and growth stage.

References

1. C. Cawthorne and E.J. Fulton, Nature 216 (1966) 575.

2. H. Wiedersich, Conf. Proc. Vol. 2, Second Intern. Conf. on the Strength of Metals and Alloys (Amer. Sac. for Metals, 1970), p142.

3. S.D. Harknes and Li Che-Yu, Met. Trans. 2 (1971) 1457.

4. A.D. Brailsford and R. Bullough, J. Nucl. Mater. 44 (1972) 121.

5. L.K. Mansur, Nuc. Technol. 40 (1978) 5.

6. R. Bullough and M.H. woad, Harwell Res. Rep. TP.982 (1983); to be published in "Physics of Radiation Effects in Crystals" Ed. by R.A. Johnson (North-Holland Publishing Co.).

7. A.D. Brailsford and R. Bullough, Phil. Trans. R. Soc. 302 (1981) 81.

8. H. Rauh and R. Bullough, to he published.

9. F.C. Frank, Proc. R. Soc. 201A (1950) 586.

10. M.H. Wood, B. Jones and S.M. Pierce, Res. Mechanica 3 (1981) 283.

11. R. Bullough and T.M. Quigley, J. Nucl. Mater. 113 (1983) 179.

Table 1

Physical and irradiation parameters for 316 stainless steel used to obtain the results in figures 1–9

Interstitial diffusion coefficient, $D_i = D_i^o \exp(-E_i^m/k_B T)$

$D_i^o = 10^{-7} m^2 s^{-1}$

$E_i^m = 0.2$ eV

Vacancy diffusion coefficient, $D_v = D_v^o \exp(-E_v^m/k_B T)$

$D^o = 6 \times 10^{-5} m^2 s^{-1}$

$D_v^m = 1.4$ eV

Average cavity radius $r_C = 1$ n.m.

Cavity number density $C_C = 10^{21} m^{-3}$

Range of dislocation densities $\rho_D = 10^{13} - 10^{16} m^{-2}$

Range of temperatures T = 300 - 500°C

Range of damage rates $K = 10^{-3} - 10^{-6}$ dpa/s

Dislocation bias parameters $Z_i = 1.10$, $Z_v = 1.00$

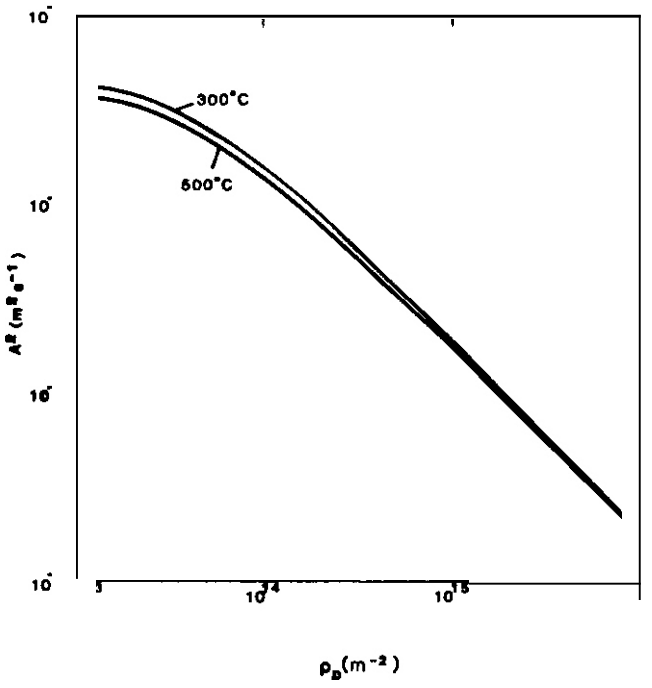

Figure 1 The variation of A^2, given by solving (26) with dislocation density ρ_D for the two temperatures specified. The damage rate $K = 10^{-6}$ dpa/s and the physical parameters in table 1 have been used for all the figures.

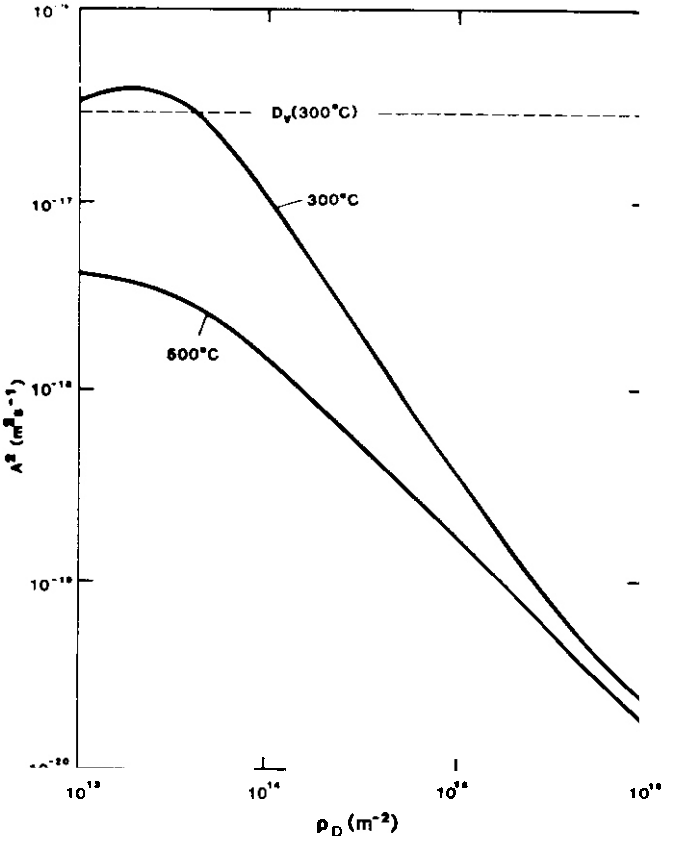

Figure 2 As for figure 1 but for a damage rate $K = 10^{-3}$ dpa/s; the value of the vacancy diffusion coefficient D_v at 300°C is indicated.

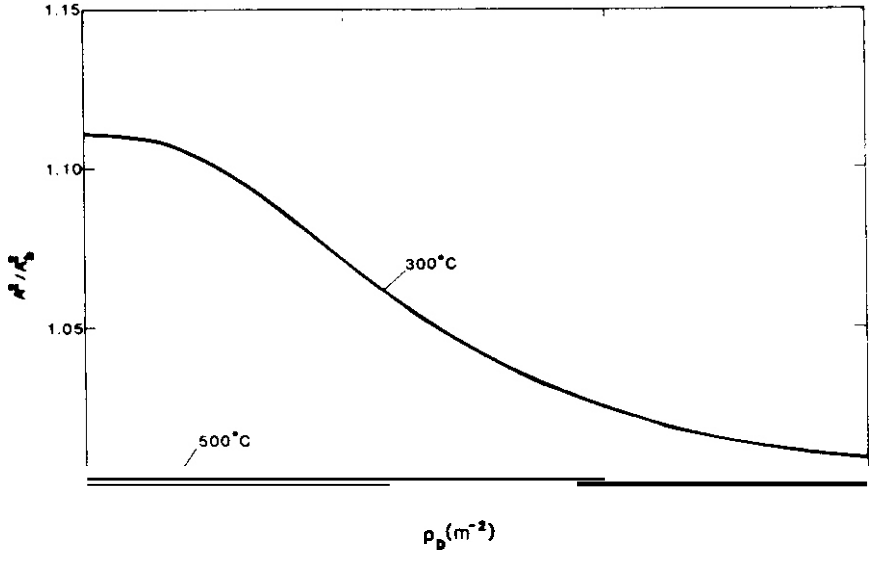

Figure 3 The variation of the ratio $(A/A_b)^2$, where A_b is given by (31), with dislocation density ρ_D for the two temperatures specified. The damage rate $K = 10^{-6}$ dpa/s.

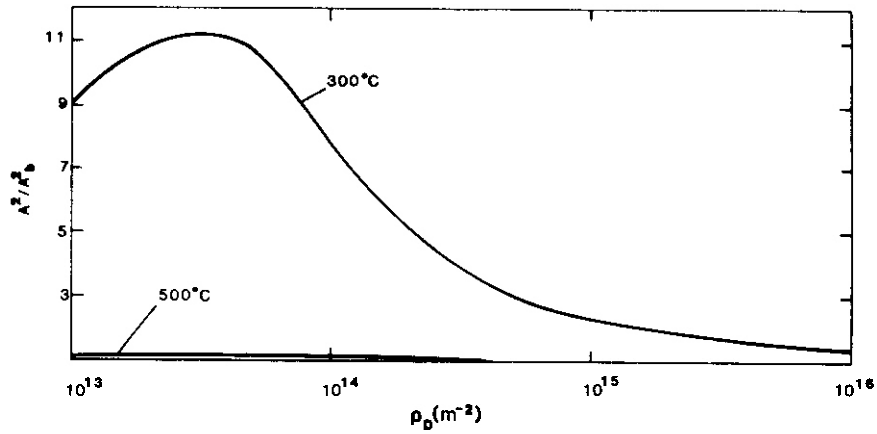

Figure 4 As for figure 3 but for a damage rate K = 10^{-3} dpals.

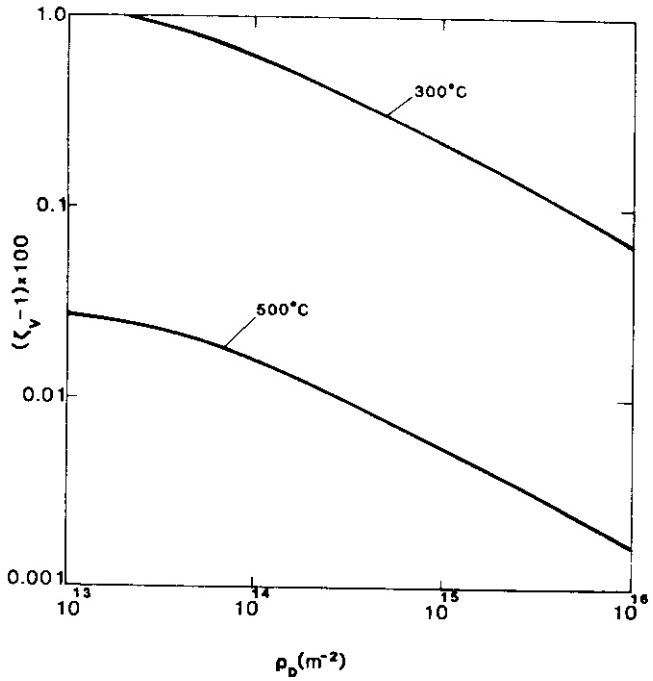

Figure 5 The variation with ρ_D of the percentage increase of the void sink strength for vacancies, $(\xi_v - 1) \times 100$, due *to* the motion of the void surface for the two temperatures specified. The damage rate K = 10^{-6} dpa/s.

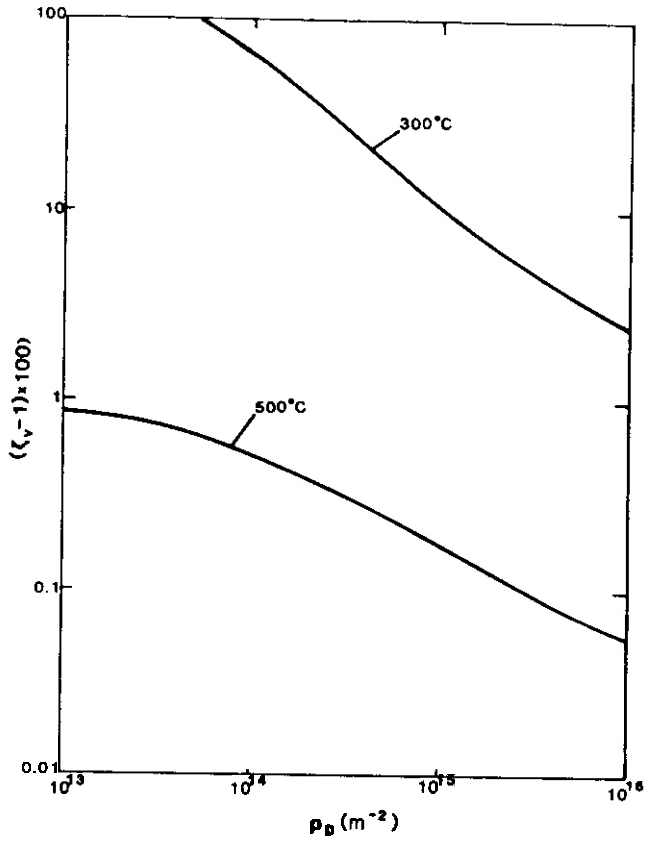

Figure 6 As for figure 5 but for a damage rate K = 10^{-3} dpa/s.

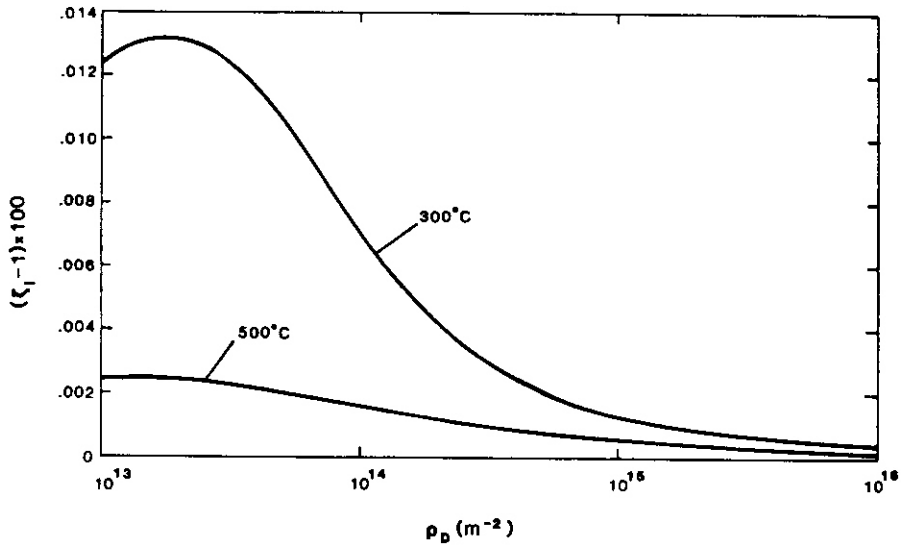

Figure 7 The variation with ρ_D of the percentage increase of the void sink strength for interstitials, $(\xi_i-1)\times100$, due to the motion of the void surface for the two temperatures specified. The damage rate K = 10^{-3} dpals.

Figure 8 The variation with ρ_D of the percentage of total swelling due to the motion of the void surface, $(1 - (A_b/A)^3) \times 100$, for the two temperatures specified. The damage rate K = 10^{-6} dpals.

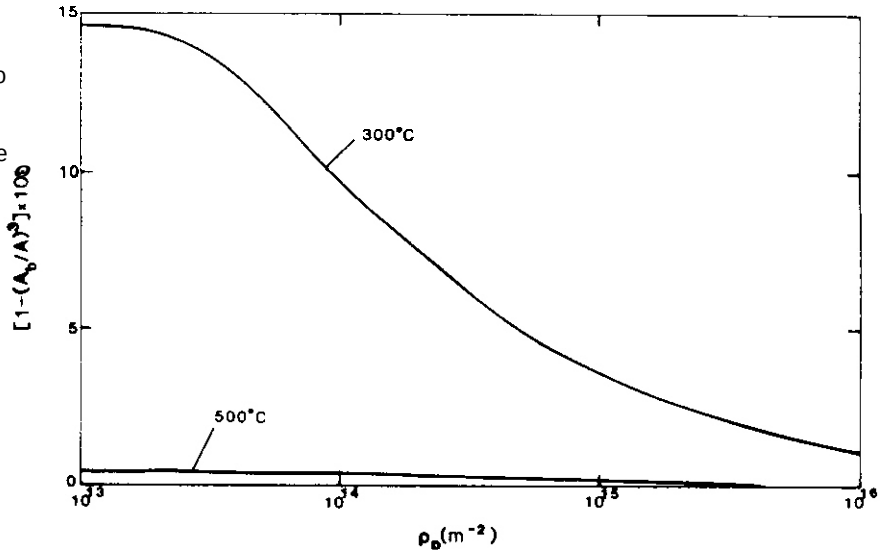

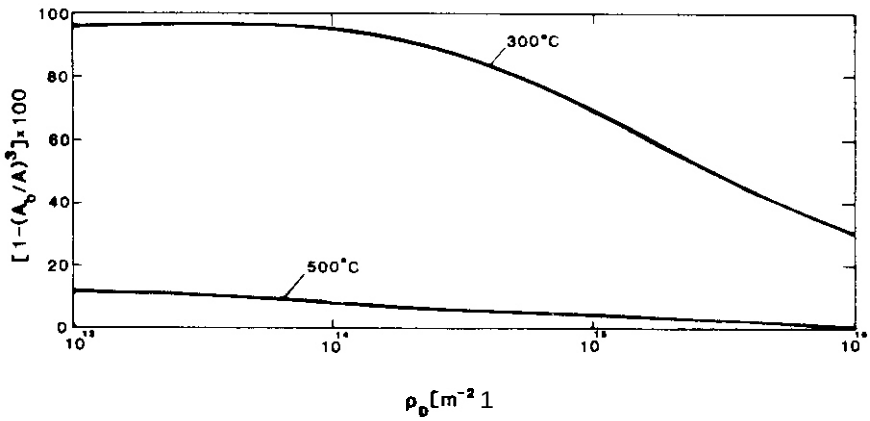

Figure 9 As for figure 8 but for a damage rate K = 10^{-3} dpa/s

PREPARATION OF ION-IRRADIATED FOILS FOR CROSS-SECTION ANALYSIS

S.J. Zinkle and R.L. Sindelar (University of Wisconsin-Madison)

1.0 Objectives

The objective of this report is to outline the experimental procedures used at the University of Wisconsin for obtaining foils suitable for cross-sectional analysis.

2.0 *Summary*

A simple, routine method has been developed which allows ion-irradiated foils to be examined in cross-section. The method has been successfully demonstrated on three alloy systems: stainless steel, a low-chromium steel, and some high-strength copper alloys. The technique is generally applicable to practically all metals.

3.0 Program

Title: Radiation Effects to Reactor Materials
Principal Investigators: G.L. Kulcinski and R.A. Dodd
Affiliation: University of Wisconsin-Madison

4.0 Relevant OAFS Program Task/Subtask

Subtask II.C.1.1: Phase Stability Mechanics
Subtask II.C.6.1: Effect of Damage Rate on Microstructural Evolution

5.0 Accomplishments and Status

5.1 Introduction

Ion irradiation experiments have been shown to be very useful as a radiation damage tool in scoping studies.(1) The high displacement damage rates associated with heavy ion irradiations allows high damage levels to be achieved in a very short time. Ion irradiation therefore enables one to quickly probe many interesting experimental conditions. The results from these ion irradiation studies may then be used as a basis for determining the appropriate experimental conditions for later neutron irradiations. Two major uses of ion irradiation studies are readily evident: First, for scoping studies on new alloy systems to determine what sort of radiation damage effects occur for a given set of experimental conditions. If the alloy looks promising, then a full-scale neutron irradiation program may follow. Otherwise, only limited neutron studies may be necessary merely to confirm the trends established by the ion irradiation. A second use of ion irradiation studies is for detailed investigation of the effect of changing various experimental parameters (temperature, alloy composition, etc.). These studies allow a single variable to be isolated, which is important for theoretical modeling of radiation damage.

Most ion irradiation studies to date have used conventional "back-thinning" methods for examining the irradiated region. A potentially more powerful technique is the cross-section method.(2) The cross-section procedure allows the entire ion damage region to be viewed at once. This is an important advantage since

the damage rate (and therefore the final damage level) vary with depth for ion irradiation. Separate control samples are eliminated when using the cross-section technique -- one merely cuts a cross-sectioned specimen from the non-irradiated portion of the sample. This results in the very desirable effect that the control specimens are from the same sample as the irradiated specimens.

A final potential advantage of the cross-section technique which has only recently been achieved in practice is multiplicity of irradiated specimens. Proper use of the cross-section method allows up to eight identical irradiated specimens to be obtained from a single sample. Therefore, favorable counting statistics may be obtained from the cross-section technique as compared to the back-thinning method.

Spurling and Rhodes[3] were the first researchers to apply the cross-section method to an ion-irradiated material. They successfully thinned proton-irradiated 316 stainless steel in cross-section by utilizing a nickel plating procedure. Unfortunately, their technique required a high-temperature (500°C) heat treatment in order to ensure an adequate bond at the foil-plate interface. A subsequent modification of their plating procedure by Whitley et al.[4] circumvented the high-temperature diffusion bond step, and therefore allowed lower irradiation temperatures to be investigated in cross-section. Whitley's method was only applied to ion-irradiated nickel which was electroplated with nickel. The cross-section procedure was extended to copper and copper alloys by Narayan et al.[5] and Knoll et al.[6] Recently, Shiraishi et al.[7] and Sindelar et al.[8] have demonstrated a cross-section technique for ion-irradiated 316 stainless Steel which uses a low-temperature Ni plating.

The purpose of this report is to outline the procedure presently used at the University of Wisconsin for obtaining cross-section specimens. Details of the experimental procedures followed for the cross-section technique have previously been available only in the form of unpublished documents.[9,10] We have recently expanded upon the techniques originally developed by Whitley[9] and Knoll,[10] and have developed a procedure which may be routinely applied to several alloy systems.

5.2 Experimental Procedures

5.2.1 The Cross-Section Technique

The basic steps followed to obtain a cross-sectioned TEM specimen from an ion-irradiated foil are outlined in Fig. 1. The critical points in the procedure are steps 2 and 4, where the irradiated foil is electroplated and thinned, respectively. Care during the electroplating step is required in order to provide a uniform, thick deposit layer with good adhesion to the foil surface. Different plating procedures are followed depending on the particular metal that is being investiaged. The cross-section technique described below has been successfully applied to pure nickel, pure copper and copper-based alloys, several austenitic stainless steel alloys, and some low chrome iron-based alloys. The plating conditions for each alloy class is given in Table 1.

Special pre-plating procedures are required in order to ensure a good plating bond. All foils are thoroughly degreased using acetone after removal from the irradiation facility. The irradiated nickel foils are given an activation treatment in a solution of Wood's nickel[11] (60 g $NiCl_2$, 31 ml HCl, 250 ml H_2O) by making the sample anodic for 3 seconds at a current density of 200 mA/cm^2. The purpose of this Step is to remove the metal oxide layer, which is necessary in order to obtain a good bond. Less than 0.1 μm of material is estimated to be removed from the irradiated surface as determined by inteference microscopy. After activation, the current is reversed in this same solution and a thin nickel strike applied for 5 minutes. In a similar procedure, the oxide layer on the austenitic stainless steels is removed in a solution of 60 g $NiCl_2$, 40 ml HCl, 250 ml H_2O at a current density of 250 mA/cm^2 for 2 seconds. The polarity on the sample is then reversed and the sample is plated in this solution for 5 minutes. The sample is then transferred into the plate bath where it is made anodic for 10 seconds with a current density of 200 mA/cm^2. The polarity is then reversed and the foil is plated until a 2 mm layer has been deposited.

The pre-plating treatment for pure copper and copper alloys involves electropolishing for 2 seconds in a solution of 33% HNO_3/67% CH_3OH cooled to -40°C at an applied potential of 5 V. This process is intended to

TABLE 1. ELECTROPLATING CONDITIONS FOR VARIOUS METALS

Metal	Electroplating Solutions	Experimental Conditions
Nickel	150 g $NiSO_4$ 150 g $NiCl_2$ 50 g boric acid 1000 ml H_2O	200 mA/cm^2 50°C
Stainless Steel	150 g $NiSO_4$ 150 g $NiCl_2$ 70 g boric acid 1000 ml H_2O	200 mA/cm^3 70°C
Copper/Cu Alloys	180 g $CuSO_4$ 30 ml H_2SO_4 950 ml H_2O	150 mA/cm^2 20°C
Iron Alloys	250 g $FeCl_2$ 100 g NaCl 750 ml H_2O	100 mA/cm^2 100°C

remove the oxide layer and any carbon contaminants which may be present on the foil surface. The irradiated foil is then transferred to the plating solution (180 g $CuSO_4$, 30 ml H_2SO_4, 950 ml H_2O), where it is made anodic for 1 to 2 seconds using a current density of 100 mA/cm^2. Interferometer measurements indicate that the total depth removed during the above electropolish and strike treatment is less than 0.1 μm. Following the strike treatment, the polarity of the plating cell is reversed and the foil is electroplated at a current density of 103-150 mA/cm^2.

The low chrome iron-based alloys are susceptable to corrosion during the oxide layer removal step, in which the sample is made anodic in an electrochemical cell. Therefore a pickling solution which has an inhibitor added to it is used to remove any metal oxide layer while minimizing corrosion of the base metal. Samples of 2-1/4 Cr-1 Mo steel have been successfully electroplated after pickling in 50 ml HCl in H_2O to which 1 g of thiourea was added. The specimens are dipped in this pickling bath for 2 minutes followed by a thorough water rinse. At this point the foil is directly transferred to the plating bath where the sample is plated at a current density of 100 mA/cm^2.

A common plating apparatus which consists of a current-controlled power supply, a heater base, a gas bubbler device, and a foil holder is used to achieve smooth electro-deposited stratums on the 0.5 cm x 1 cm irradiated foils. Figure 2 is a photograph of the equipment used for electroplating. The key features to note in the figure are the sacrificial anodes and the plexiglas sample holder. The anodes are bagged during the plating process to prevent sludge from electrodepositing on the foil. The sample holder has been designed so as to optimize the plating rate of the irradiated foils. A detailed schematic of the sample holder is shown in Fig. 3. The small 1/2 cm x 1/2 cm "window" in the holder serves to minimize foil edge effects on the plate layer, thereby allowing uniform deposition to occur. A common aquarium air stone is used to create a fine stream of nitrogen gas bubbles. The gas bubbles are directed through the channel in the sample holder and allowed to flow over the foil surface. The purpose of the fine gas stream is twofold: First, it ensures that hydrogen bubbles formed from electrolysis on the foil surface are swept away. Failure to remove these H_2 bubbles while electroplating would result in a porous plating. A second. related advantage of creating a turbulent layer near the foil surface is that the critical electroplating current density is inversely proportional to the film thickness. Therefore, higher current densities (and hence shorter plating periods) can be achieved when the plating solution is well agitated. However, too high of an agitation rate will also cause a porous plating.

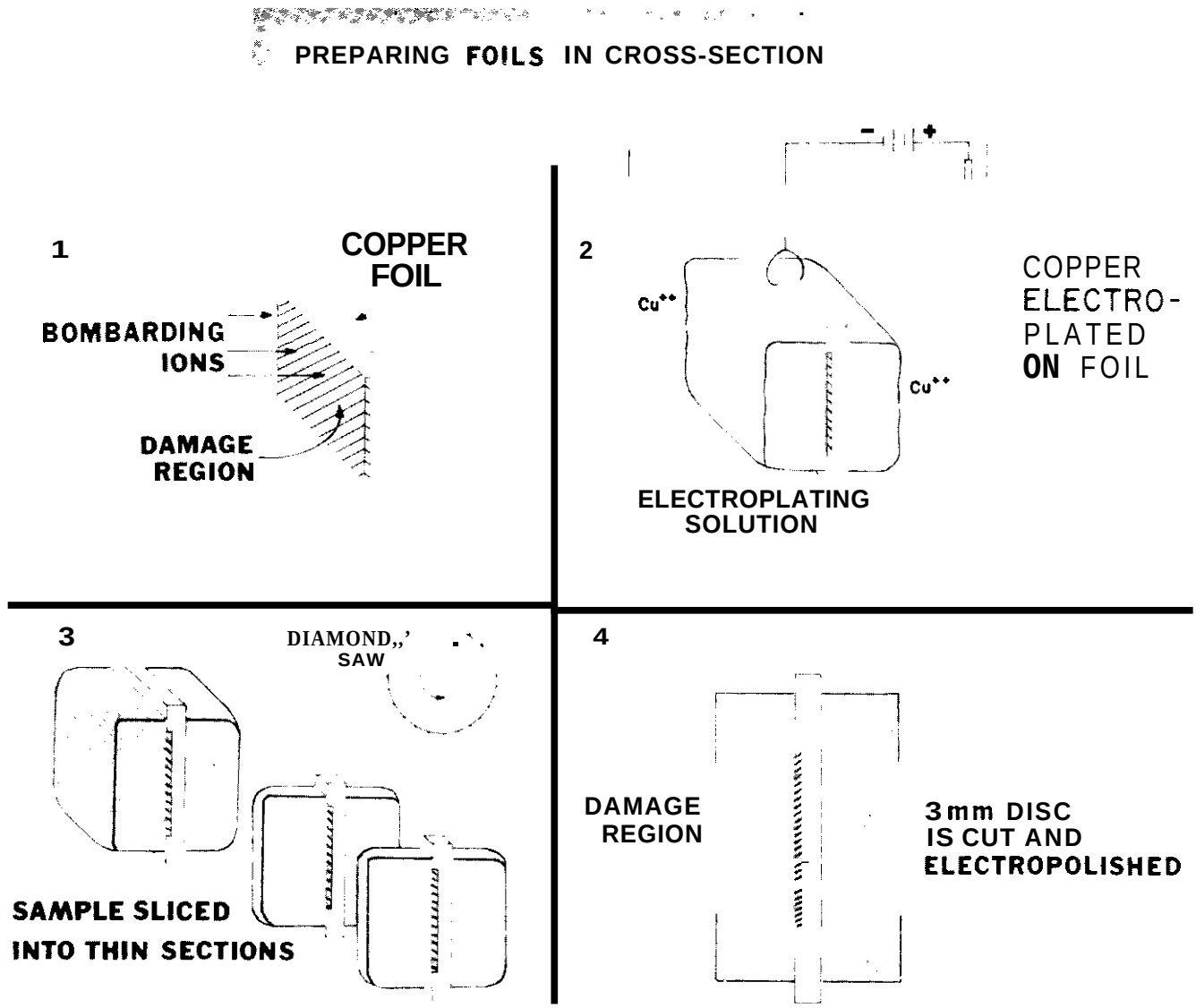

FIGURE 1. Procedure for preparing ion-irradiated foils in cross-section.

After a layer approximately 2 mm thick is deposited on each foil surface, the resultant sample is removed from the plate bath and mounted in epoxy. Figure 4 shows a plated copper foil as it appears prior to being mounted in epoxy. The 3 mm diameter disk defines the irradiated beam spot, and serves as an aid for determining whether a particular slice is from the irradiated or control region of the foil.

A diamond saw is used to slice specimens from the plated sample. With the use of a 150 μm-thick blade, it is possible to obtain as many as eight irradiated cross-section specimens from a single sample. A virtually unlimited number of control cross-section specimens may be obtained from the same sample. As described later, these multiple specimens allow several different experimental analyses to be performed (e.g., extraction replicas, TEM, etc.). Figure 5 shows the control and irradiated cross-section specimens for a stainless steel sample as they appear immediately after being sliced on a diamond saw.

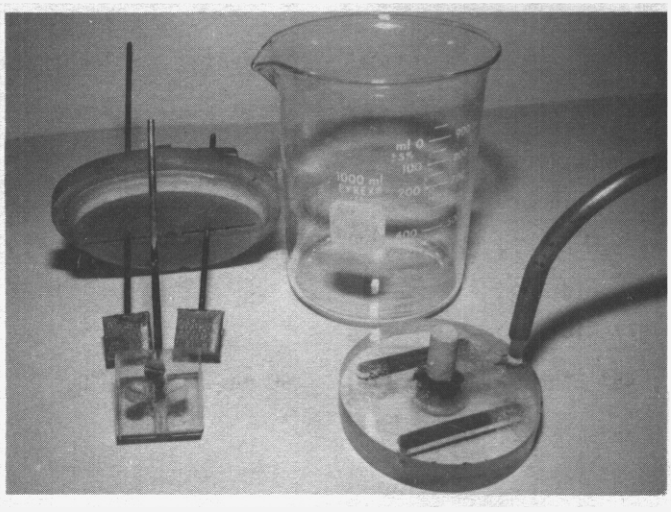

FIGURE 2. Apparatus used for electroplating ion-irradiated foils.

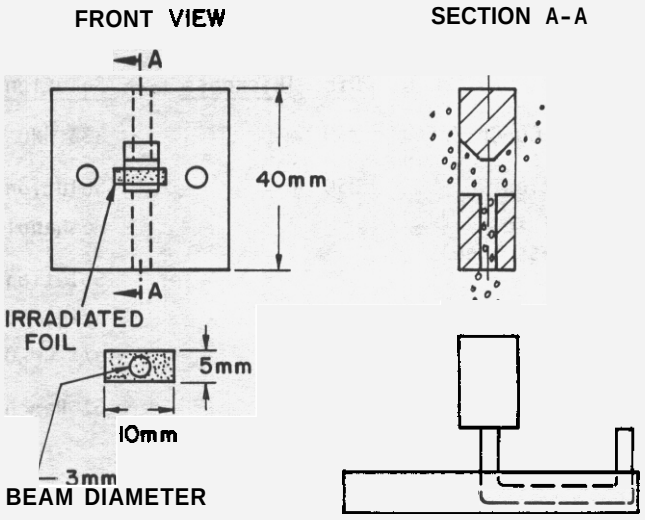

FIGURE 3. Schematic of sample holder and gas bubbler used for electroplating ion-irradiated foils.

5.2.2 Preparation of TEM Foils from Cross-Sectioned Specimens

Electropolishing techniques are generally used to prepare specimens for TEM analysis. Table 2 lists the solutions used for the jet-thinning of cross-sectioned samples for TEM specimens. Since the range of the incident ion is rather limited (~ 3 μm for 14-MeV Ni ions incident on nickel), it is essential to have the irradiated boundary region of the specimen transparent to electrons. One of the previous problems associated with the cross-section technique was the difficulty in obtaining adequate electron-transparent regions of the TEM foil at the irradiated boundary. Without utilizing special measures to force the thin area to occur at the irradiated boundary, a low success rate is obtained (typically $\lesssim$ 30%). This defeats the cross-section advantage of having multiple specimens. A further difficulty associated with many of the cross-sectioned alloy specimens is that the plating material thins at a different rate as compared to the alloy. In some cases, it is virtually impossible to obtain adequate thin area in the irradiated region of the cross-sectioned foil without a special experimental procedure. Two companion experimental methods have been developed to address this problem.

For most cross-sectioned materials. adequate thin area at the irradiated boundary may be obtained by simply using a protective lacquer to isolate the region of interest. The procedure is as follows: First both sides of the TEM disk are covered with a protective lacquer with the exception of a ~ 50 μm wide strip centered along the irradiated boundary. The specimen is then electropolished for a period of time ranging from 15 seconds to 2 minutes, depending on the foil thickness and the particular metal being investigated. Following this prepolish treatment, the lacquer is removed from the TEM disk and the specimen is electropolished until perforation occurs. Figure 6 is an optical micrograph which shows a typical result for an irradiated copper alloy following. the above procedure. The parallel, dark bands running horizontally across the micrograph outline the step height change from the prepolish treatment. Adequate thin area in the damage region has been obtained in about 80% of the cross-sectioned specimens which were prepared using the above technique. Since six to eight irradiated specimens are generally available from each plated sample, this high success rate allows multiple specimens to be analyzed.

A somewhat more complicated procedure is employed to electrochemically thin cross-sectioned stainless steel specimens. A two-step polishing technique which utilizes two different electropolishing solutions is used in conjunction with the above prepolish lacquer technique. The first step involves the application of the protective-lacquer covering which exposes the irradiated boundary only. The sample is then polished in solution 1 (see Table 2) which polishes the nickel plate at a slightly faster rate compared to the steel. After approximately two minutes. the lacquer is removed and the sample is polished to perforation in solution 2 which polishes the steel at a more rapid rate compared to the nickel plate.

TABLE 2. PARAMETERS USED FOR JET-ELECTROPOLISHING OF CROSS-SECTIONED SPECIMENS

Alloy	Initial TEM Disc Thickness	Solution	Volts	Current	Temperature
Cu-Zr, Cu-Cr-Zr	250 μm	33% HNO_3, 67% CH_3OH	15	90 mA	-20°C
300 Series Austenitic Stainless Steels	250 μm	Solution 1: 30% HNO_3, 70% Methanol, Time = 2 min	10 V	80-90 mA	0°C
		Solution 2: 10% Perchloric Acid, 40% Acetic Acid, 20 g/ℓ Cr_2O_3, 10 g/ℓ $NiCl_2$	45 V	80-90 mA	20-c
Low (< 4 wt.%) Cr Ferritic Steels	250 μm	5% Perchloric, 45% Ethanol	60 V	90 mA	0°C

5.3 Results

A variety of experimental techniques may be applied to the cross-sectioned specimen in order to obtain different pieces of information. A brief sampling of some typical results which may be obtained is presented below.

Optical microscopy may be performed on irradiated cross-section specimens in order to help characterize the effect of irradiation. Figure 7 is an optical metallograph of a 316 stainless steel specimen which has been

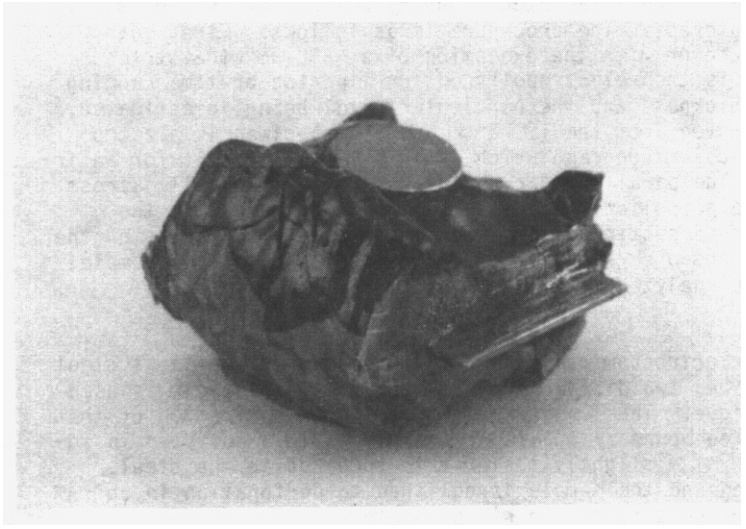

FIGURE 4. Photograph of an electroplated ion-irradiated copper foil.

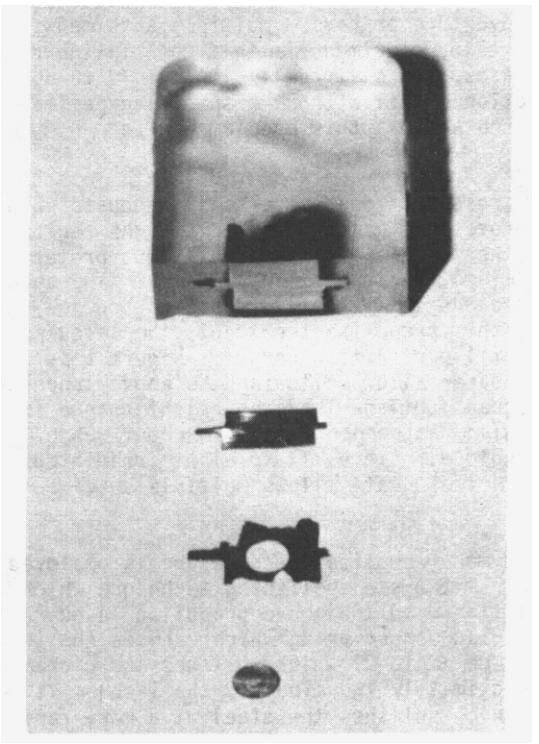

FIGURE 5. Control and irradiated cross-section specimens from a stainless steel sample.

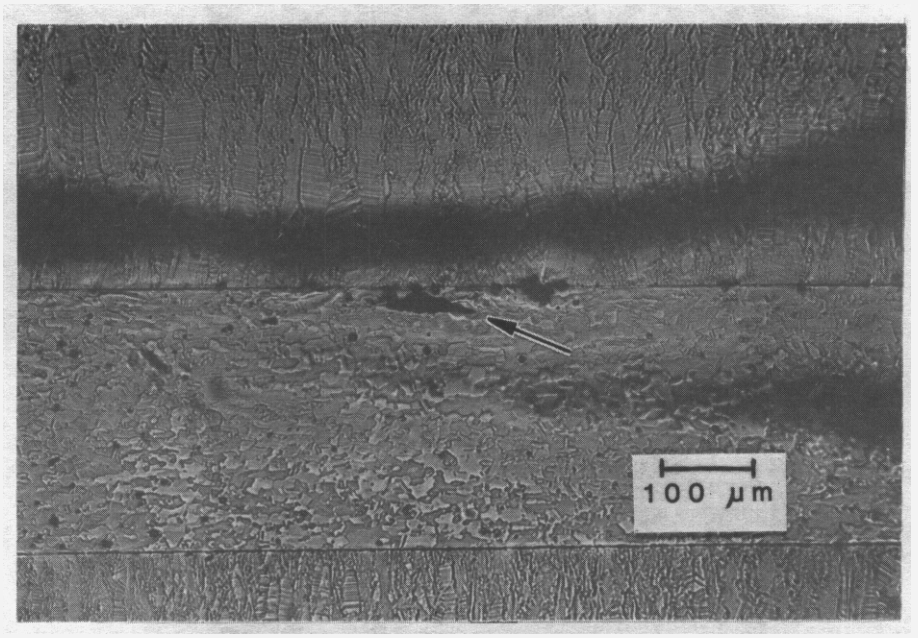

FIGURE 6. Optical micrograph of an electropolished copper alloy cross-section TEM specimen. The arrow points to the perforation in the foil next to the irradiated boundary.

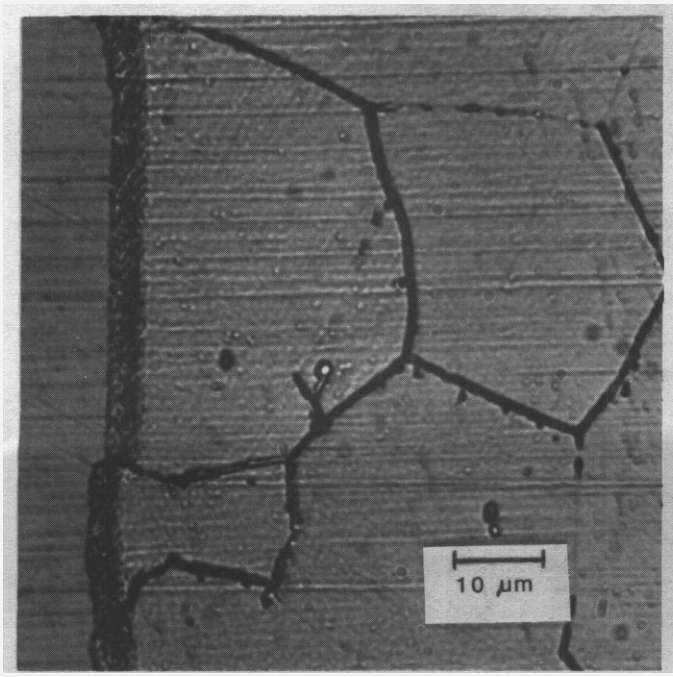

FIGURE 7. Optical micropraph of an irradiated stainless steel cross-section specimen. The 3 µm-wide band along the irradiated interface corresponds to the radiation damage region.

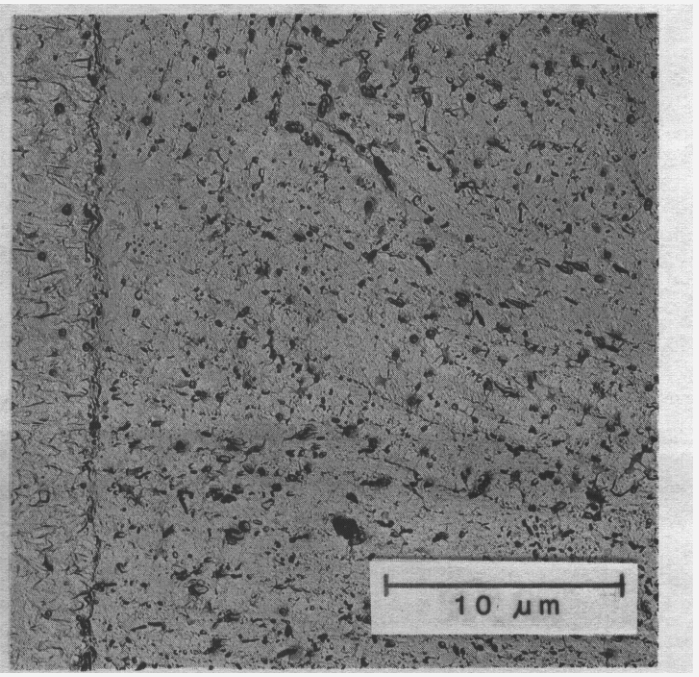

FIGURE 8. Extraction replica electron micrograph from a cross-sectional 2-1/4 Cr-1 Mo steel specimen.

irradiated with 14-MeV Ni ions at 650°C to a fluence of 3.3 x 10^{20} ions/m^2. The damage region is clearly visible in the micrograph as a ~ 3 µm wide band adjacent to the plated interface. The different etching behavior in the damage region was determined from TEM investigations to be due to iron phosphide precipitates. These precipitates were needle-shaped with an average length of 150 nm and density ~ 1 x 10^{20} m^{-3}.

FIGURE 9. TEM micrograph showing the extent of the electron-transparent region along the irradiated **boundary** of a cross-sectioned Cu-Zr specimen.

Extraction replica techniques are often utilized in alloys where irradiation can enhance *on* induce precipitation events. **It** is essential that the precipitates be extracted from the matrix in order for accurate quantitative microchemical analysis results to be **obtained.**[12] Figure 8 shows an extraction replica obtained **from** a cross-sectioned 2-1/4 Cr-1 Mo steel specinen. This micrograph **shows** extracted carbides from an unirradiated solution-quenched and aged foil that had been plated with iron.

Extensive thin area for TEM analysis at the irradiated boundary is achievable using the preparation techniques previously outlined. Electron-transparent regions which extend along the irradiated boundary for distances up to 100 μm have been obtained under favorable conditions. Figure 9 shows a portion of the thin area which was obtained along the irradiated boundary of a Cu-Zr specimen irradiated with 14-MeV Cu ions at 300°C to a fluence of 1×10^{20} ions/m^2. In this specimen, perforation during electropolishing occured on the interface and there was roughly equal amounts of thin area on either side of the hole.

5.4 Summary and Conclusions

A routine procedure has been developed which allows ion-irradiated metals to be examined in cross-section. The high success rate which is obtainable using this procedure allows multiple specimens to be examined. This implies that statistically significant void and precipitate distributions may be obtained from irradiated samples as a function of depth (damage level). The experimental procedure described in this report enables the cross-section procedure to operate at its full potential. The many potential advantages of the cross-section technique over conventional back-thinning methods may now be realized in practice.

6.0 Acknowledgments

This work was performed under appointment to a Magnetic Fusion Energy Technology Fellowship and with funds supplied by the Department of Energy.

7.0 References

1. "Critical Assessment of Dual-Ion and Charged Particle Research in the Fusion Materials Program," Report of the Ad Hoc Task Group on Charged Particle Research, G.R. Odette (Chairman). DAFS Quarterly Progress Report DOE/ER-0046/8, Vol. 1 (Feb. 1982) p. A-3.

2. J.B. Whitley, P. Wilkes and G.L. Kulcinski, "A Novel Method for Studying Damage Rate Effects in Ion-Bombarded Nickel," University of Wisconsin Fusion Engineering Program Report UWFDM-159 (June 1976).

3. R.A. Spurling and C.G. Rhodes. J. Nucl. Mater. 44 (1972) 341.

4. J.B. Whitley, G.L. Kulcinski, P. Wilkes and H.V. Smith, Jr.. J. Nucl. Mater. 79 (1979) 159-169.

5. J. Narayan, O.S. Oen and T.S. Noggle, J. Nucl. Mater. 71 (1977) 160-170.

6. R.W. Knoll, P.W. Wilkes and G.L. Kulcinski in Phase Stability During Irradiation, J.R. Holland, L.K Mansur. and D.I. Potter (Eds.), (1980) 123-137.

7. K. Shiraishi, M.P. Tanaka, T. Aruga and S. Hamada in "Effects of Radiation on Materials" (11th Conference), H.R. Brager and J.S. Perrin (Eds.), ASTM STP 782 (1982) 927.

8. R.L. Sindelar. G.L. Kulcinski and R.A. Dodd. "Depth Dependent Microstructure of Ion-Irradiated Type 316 Stainless Steels," 3rd Topical Meeting on Fusion Reactor Materials, Albuquerque, NM, (Sept. 1983), proceedings to be published in J. Nucl. Mater.

9. J.B. Whitley, 'Depth-Dependent Damage in Heavy-Ion Irradiated Nickel," Ph.D. Thesis, Nuclear Engineering Department, University of Wisconsin-Madison (August 1978).

10. R.W. Knoll, "Effects of Heavy-Ion Irradiation on the Phase Stability of Several Copper-Base Alloys," Ph.D. Thesis, Nuclear Engineering Dept., University of Wisconsin-Madison (August 1981).

11. T.M. Rodgers, Handbook of Practical Electroplating, MacMilland, New York (1959) 225.

12. N.J. Zaluzec in "Introduction to Analytical Electron Microscopy," J.H. Hren, J.I. Goldstein and D.C. Joy (Eds.), Plenum Press, New York (1979) 121-167.

CHAPTER 6

FUNDAMENTAL STUDIES OF SPECIAL PURPOSE MATERIALS

MICROSTRUCTURES AND PHYSICAL PROPERTIES OF Cu-Zr AND Cu-Cr-Zr-Mg ALLOYS

S.J. Zinkle, D.H. Plantz, G.L. Kulcinski and R.A. Dodd (University of Wisconsin)

1.0 Objectives

1) To investigate the physical properties and microstructures of two high-strength, high-conductivity copper alloys as a function of annealing conditions, and 2) to determine the source of the high strength of these two alloys. This will allow a better estimation to be made on the potential effects of irradiation on the mechanical properties of these alloys.

2.0 Summary

Electrical resistivity measurements have been made at 20°C on specimens of as-received AMZIRC and AMAX-MZC copper alloys as a function of annealing time and temperature. The electrical conductivity of both alloys steadily increases between 300 and 550°C. The maximum conductivity is about 90% IACS for MZC and ~ 100% IACS for AMZIRC. TEM observations indicate that AMZIRC contains incoherent Cu-Zr precipitates which are preferentially located at grain boundaries. The AMAX-MZC alloy contains the same Cu-Zr precipitates, and also coherent Cr precipitates which are uniformly distributed throughout the matrix.

3.0

Title: Radiation Effects to Reactor Materials
Principal Investigators: G.L. Kulcinski and R.A. Dodd
Affiliation: University of Uisconsin-Madison

4.0 Relevant DAFS Program Plan Task/Subtask

Subtask II.C.l.l: Phase Stability Mechanics
Subtask II.C.1.2: Modeling and Analysis of Effects of Materials Parameters on Microstructures

5.0 Accomplishments and Status

5.1 Introduction

High-strength. high-conductivity copper alloys are being considered for a variety of applications in proposed fusion reactors.(') This report summarizes some of the progress which has been made on determining the fundamental behavior during annealing of two candidate copper alloys, AMZIRC and AMAX-MZC. Previous reports have summarized the microhardness and preliminary resistivity measurements made on these alloys in their as-received[2] and annealed[3] states. It was determined that a large portion of the strength of these alloys is due to cold-working.

5.2 Experimental Procedure

The nominal alloy composition of AMZIRC and AMAX-MZC is given in Table 1. The heat treatment for the as-received alloys has been previously described.[3] Specimens for both alloys have also been obtained from

TABLE 1. NOMINAL COMPOSITION OF AMZIRC AND AMAX-MZC

Alloy	Cr (at %)	Zr (at %)	Mg	cu
AMZIRC	-	0.13-0.20	-	balance
AMAX-MZC	0.80	0.15	0.04	balance

AMAX Copper, Inc. in the solution annealed plus aged condition. The heat treatment for these alloys consisted of a solution anneal at 930°C for 45 minutes followed by aging for 1 hour at 450°C for the AMZIRC alloy and 500°C for the MZC alloy.

As-received foils (250 μm thickness) of both alloys were annealed for times ranging from 0.25 - 10 hours in a high vacuum furnace.[3] Resistivity specimens were cut from the annealed foil using a diamond saw[2] so as to give a square cross-sectional area (250 μm x 250 μm). Electrical resistivity measurements were made at room temperature on the as-received and annealed alloy specimens using standard 4-point probe techniques. One to two resistivity "wires" were measured for each thermal annealing condition. The measured resistivity values were converted to conductivity % IACS (International Annealed Copper Standard) units by assuming that pure copper has a resistivity of[4] 16.73 nΩ-m at 20°C with a temperature coefficient of 0.068 nΩ-m/°C. Selected specimens were examined in a JEOL TEMSCAN-200CX electron microscope.

5.3 Results

Figures 1 and 2 show the electrical conductivity of as-received AMZIRC and AMAX-MZC, respectively, as a function of annealing time and temperature. Typical experimental error bars are shown in both figures. The conductivity of AMZIRC is seen to steadily increase from 75% to 95-100% IACS as the annealing temperature goes from 300 to 550°C. The conductivity values of AMZIRC following a 0.25 hr anneal are consistently below that for a 1 hr and 10 hr anneal, which is an indication that the kinetics for microstructural changes is on the order of 0.25 hr in this temperature range. The electrical conductivity of MZC steadily increases from 55-60% to ~ 90% IACS over the temperature range of 300-550°C. The MZC conductivity values are also lowest for a 0.25 hr anneal, but the difference compared to the other annealing times is not nearly as great as for the AMZIRC alloy.

Vickers microhardness (VHN) measurements were made on solution annealed plus aged AMZIRC and AMAX-MZC foils obtained from AMAX Copper Inc. in order to determine the relative strength of these alloys due to precipitation hardening vs. cold working. The results of the VHN measurements are presented in Table 2 along with the as-received, solution-annealed (SA), and SA + aged (UW heat treatment) values which were previously given in Ref. 5. It can be seen that AMZIRC does not achieve any observable precipitation hardening, while MZC exhibits a fairly large amount of precipitation hardening. The strength of both of the aged alloys is significantly less than that of the as-received alloys, which indicates that much of the strength of the latter is due to cold-working.

The precipitate microstructures of the AMAX SA + aged alloys is shown in Fig. 3. Incoherent Cu-Zr precipitates were observed to preferentially nucleate at grain boundaries, in agreement with Ref. 6. The dominant microstructural feature of aged AMAX-MZC is the high density of homogeneously nucleated coherent Cr precipitates. Incoherent Cu-Zr precipitates have also been observed along grain boundaries in the aged AMAX-MZC alloy. An example of these grain boundary precipitates along with the matrix Cr precipitates is shown in Fig. 4.

5.4 Discussion

The observed dependence of the electrical conductivity of as-received AMZIRC and AMAX-MZC is in fairly good agreement with results found in the literature.[7-10] The conductivity vs. annealing temperature curve does not exhibit a well-defined "knee" such as was found in the previously reported microhardness

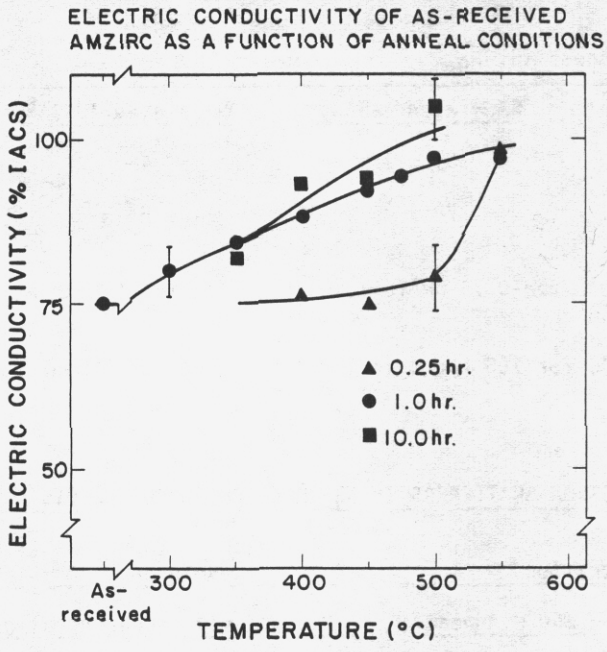

FIGURE 1. Electrical conductivity of as-received AMZIRC as a function of annealing time and temperature.

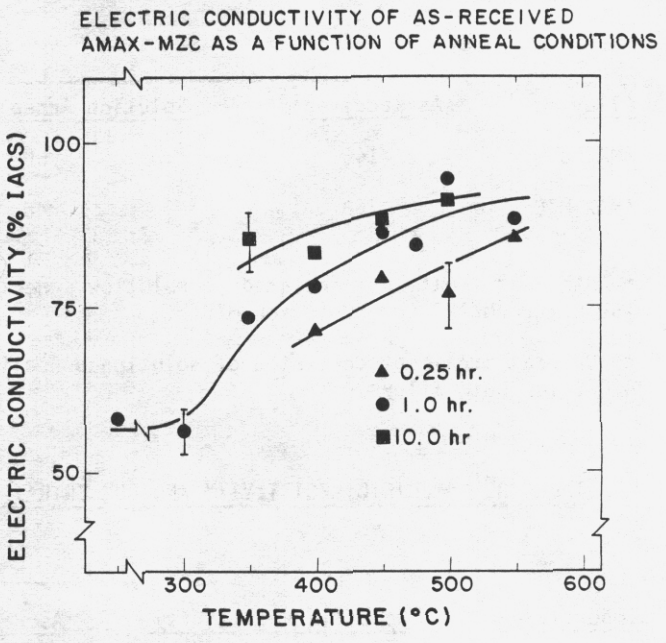

FIGURE 2. Electrical conductivity of as-received MZC as a function of annealing time and temperature.

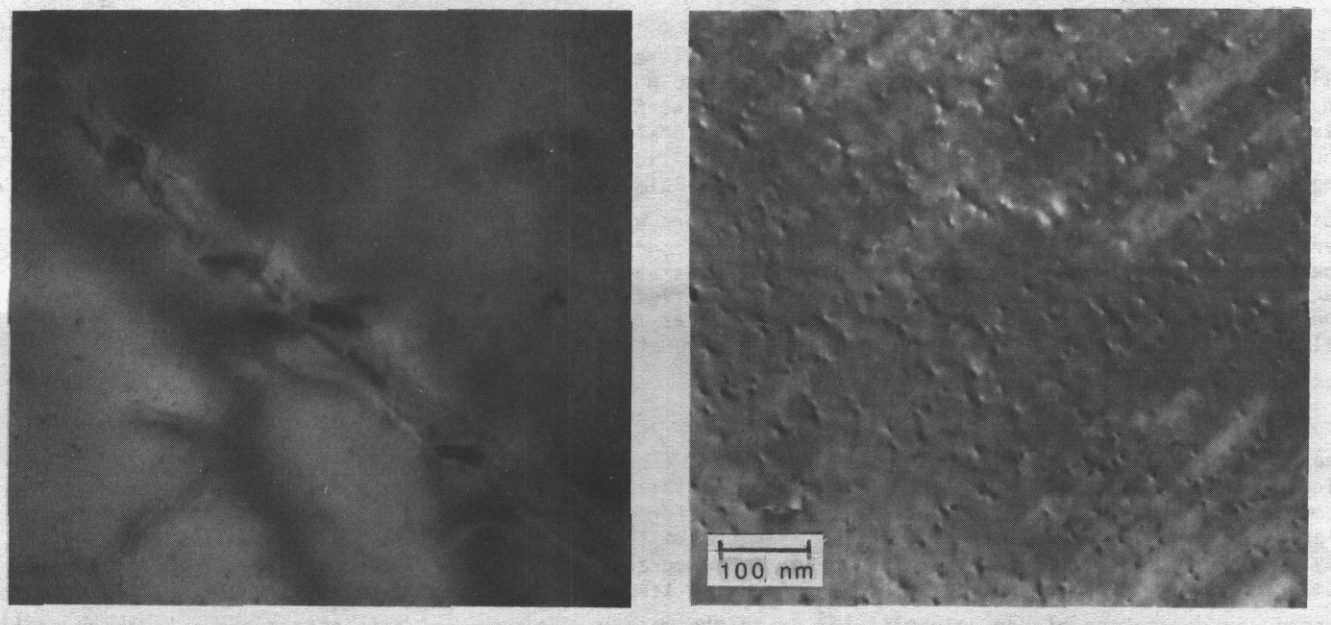

FIGURE 3. TEM microstructures for solution annealed plus aged AMZIRC (left) and AMAX-MZC (right), showing Cu-Zr precipitates on a grain boundary and coherent Cr precipitates in the matrix.

measurements.[3] This variance is due to the fact that the microhardness and resistivity measurements are sensitive to different microstructural features.[11]

TABLE 2 VICKERS MICROHARONESS OF HEAT-TREATED COPPER ALLOYS (200g load)

Alloy	Microhardness (HV_{200})			
	As-Received[5]	Solution Annealed (SA)[5]	SA + aged (AMAX)*	SA + aged (UW)[5]**
AMZIRC	146	50	51 ● 1	48
AMAX-MZC	168	46	78 ± 1	84

* AMAX heat treatment consisted of solution annealing at 930°C for 0.75 hr followed by aging for 1 hour at 450°C for AMZIRC and 500°C for MZC.

** UW heat treatment consisted of solution annealing at 950°C for 100 hours followed by aging for 1 hour at 470°C for both alloys.

TABLE 3 SPECIFIC RESISTIVITY AND CONCENTRATION OF ELECTRON SCATTERERS IN AS-RECEIVED COPPER ALLOYS

Impurity	Specific Resistivity	Concentration		Reference	
		As-Received	550°C Anneal	Resistivity	Concentration
Dislocations	1.3×10^{-13} μΩ-cm^3/n_d	~ 5 x 10^{12}/cm^2	≤ 1 x 10^9/cm^2	13	measured
Cr	4 μΩ-cm/at %	0.04 at %	0.06 at 4	14	16
Mg	0.8 μΩ-cm/at 4	0.04 at a	0.04 at %	14	16
Zr	0.8 μΩ-cm/at %	0.014 at %	0.02 at %	15	17

It is possible to compare the experimental electrical resistivity with the theoretical value for dilute alloys. This allows a determination to be made as to which microstructural feature has the dominant effect on the measured resistivity. For the present case, we have considered electron scattering to be due to dislocations and solute atoms, along with phonons. Grain boundary contributions to the resistivity were found to be insignificant for the conditions in this study. The effect of precipitates on scattering is neglected. We have also assumed that Matthiesson's Rule is obeyed at all temperatures. which is generally not true for copper.[12] Table 3 lists the parameters used to calculated the resistivity. Calculations were performed for both alloys in their as-received condition and also following a 550°C anneal for 1 hour. The dislocation density of the as-received alloys was estimated from TEM, but is rather uncertafn due to the very high strain present in the matrlx. The as-received solute concentrations were assumed to be the concentration present at equilibrium in pure copper at the aging temperature (400°C). Simple diffusion calculations indicate the the solute is mobile enough at these temperatures for this to be a resonable assumption. (18)

The results of the calculation are given in Table 4. The agreement between the measured and calculated electrical conductivity values is good. considering the assumptions which were used. Dislocations are the dominant contribution to the calculated resistivity for the as-received alloys (next to phonons). The electrical conductivity of annealed AMZIRC is close to that of pure copper due to the low specific resistivity of Zr. The high specific resistivity of Cr degrades the electrical conductivity of MZC by 10-15% compared to pure copper. Following higher annealing temperatures, the conductivity of MZC should become even lower due to the higher solubility of Cr in the matrix. Evidence of this effect has been observed.[19]

The microstructures observed in the SA t aged alloys serve to confirm the role of precipitates in determining the strength of AMZIRC and AMAX-MZC. Heterogeneous nucleation of Cu-Zr precipitates at grain boundaries and cell walls has been previously observed by several researchers.[6,19,20] The role of the Cu-Zr precipitates is to increase the alloy strength by impeding dislocation cell wall migration, and to prevent excessive grain growth by pinning grain boundaries. As is evident from Table 2, Cu-Zr precipitates have no strengthening effect in the absence of a well-developed dislocation structure.

FIGURE 4. TEM microstructure for solution annealed plus aged AMAX-MZC with both Cu-Zr grain boundary precipitates and Cr matrix precipitates visible.

TABLE 4. ELECTRICAL CONDUCTIVITY OF COPPER ALLOYS IN UNITS OF % IACS

	As-Received		550°C Anneal - 1 hr	
Alloy	Calc.	Meas.	Calc.	Meas.
AMZIRC	72%	75%	99%	98%
AMAX-MZC	66%	57%	85%	88%

The Cu-Zr precipitates also act to prevent grain growth in the MZC alloy. A considerable amount of strengthening in MZC can be attributed to Cr precipitation. Table 2 shows that aging for 1 hour at 470°C (UW treatment) results in a greater strength than aging for 1 hour at 500°C (AMAX treatment).

5.5 Conclusions

The electrical conductivity of as-received AMZIRC and AMAX-MZC increases steadily with annealing temperature over the range 300-550°C. Calculated resistivity values of the as-received and 550°C annealed alloys are in good agreement with experimental measurements. The as-recelved conductivity is mainly controlled by the dislocation density while the annealed conductivity is most affected by the Cr concentration. The precipitates in AMZIRC have a negligible effect on the alloy strength in the absence of a well-developed dislocation structure.

6.0 Acknowledgemnts

This work was performed under appointment to a Magnetic Fusion Energy Technology Fellowship and with funds supplied by the Department of Energy.

7.0 References

1. Copper and Copper Alloys for Fusion Reactor Applications: Proceedings of a DOE-OFE Workshop. F.W. Wiffen, T.C. Reuther, and R.E. Gold (Eds.), Oak Ridge National Laboratory. CONF-830466 (June 1984).

2. S.J. Zinkle. S.N. Farrens, G.L. Kulcinski and R.A. Dodd, DAFS Quarterly Progress Report DOE/ER-0046/15 (Nov. 1983) p. 127.

3. S.J. Zinkle. D.H. Plantz, R.A. Dodd and G.L. Kulcinski, DAFS Quarterly Progress Report DOE/ER-0046/17, p. 110.

4. CRC Handbook of Chemistry and Physics, R.C. Weast (Ed.) 59th Edition (1979).

5. S.J. Zinkle. R.A. Dodd and G.L. Kulcinski. 'Comparison of Thermal and Irradiated Behavior of High-Strength. High-Conductivity Copper Alloys", 12th Intern. Symp. on the Effects of Radiation on Materials (June 1984) Williamsburg, VA; to be publlshed by ASTM; also see DAFS Quarterly Progress Report DOE/ER-0046/17, p. 117.

6. T. Nai-Yong. 'High Temperature Deformation and Fracture of Cu-Cr Type Alloys." Ph.D. Thesis. Mechanical Engineering Dept.. University of Waterloo (1983).

7. T. Maruta. J. Japan Copper and Brass Res. Assn. 2, No. 1, (1963) 89-96.

8. H. Suzuki, I. Kawakatsu and H. Kitano, J. Japan Institute of Metals (NKG) 31 (1967) 342-346.

9. H. Suzuki, M. Kanno and I. Kawakatsu, J. Japan Institute of Metals (NKG) 33 (1969) 174-178.

10. T. Nagai. Z. Henmi, T. Sakamoto and S. Koda. Trans. Japan Inst. Metals E, No. 6, [1973) 462-469.

11. R.E. Reed-Hill, Physical Metallurgy Principles. 2nd Ed.. Brooks/Cole, Monterey. CA (1973) 267-325.

12. J. Bass, Adv. Physics 21 (1972) 431-604.

13. R.A. Brown. J. Phys F: Metal Physics 7 (1977) 1283.

14. F.J. Blatt, Physics of Electronic Conduction in Solids, McGraw-Hill, NY (1968) 196-202.

15. A.M. Korol'kov and E.V. Lysova In Structure and Properties of Light Alloys. ERDA. Natl. Sci. Foundation. ERDA-TR-75 (1980) 21-27 (transl. from Russian).

16. M. Hanson and K. Anderko. Constitutlon of Binary Alloys, McGraw-Hill, NY (1958).

17. V. Zwicker. Metall. 16, No. 5, (1962) 409.

18. D.B. Butrymowicr. J.R. Manning and M.E. Read, Olffusion Rate Data and Mass Transport Phenomena for Copper Systems, Monograph V in the INCRA Series on the Metallurgy of Copper (1977); also contained in a 5-part series in J. Physical and Chemical Reference Data, 2-6, (1973-1977).

19. H. Suzuki, M. Kanno and I. Kawakatsu. J. Japan Inst. Metals (NKG) 33 (1969) 628-633.

20. B.I. Boric. D.V. Mihailovic and M.L. Kostic, Glas Hem Drus. Beograd 35 No. 7-8 (1970) 405-414.

8.0 Future Work

Microhardness and resistivity measurements will be reported on specimens which have been annealed for 100 hours. Tensile tests will be performed on the as-received and annealed sheet specimens at HEDL. The yield strength results will be correlated with previously reported microhardness values.

MICROSTRUCTURE OF HIGH-STRENGTH, HIGH-CONDUCTIVITY COPPER ALLOYS IRRADIATED AT LOW TEMPERATURES

S.J. Zinkle, G.L. Kulcinski and R.A. Dodd (University of Wisconsin)

1.0 Objectives

The objective of this study is to determine the effect of ion irradiation on the microstructures of two commercial high-strength, high-conductivity copper alloys. From these microstructural observations, we hope to determine the suitability of the two alloys for fusion reactor applications.

2.0 Summary

Preliminary results have been obtained on the effects of ion irradiation on two high-strength copper alloys at temperatures 100-250°C. Both the AMZIRC and the AMAX-MZC alloy exhibit radiation-enhanced recovery and partial recrystallization at all temperatures following irradiation to a peak damage level of 15 dpa (K = 0.3). A high density of "black spots" have been observed for all irradiation conditions. There is no observable void formation in either of the as-received alloys following ion irradiation to 15 dpa (K = 0.3) at temperatures 100-550°C.

3.0 Program

Title: Radiation Effects to Reactor Materials
Principal Investigators: G.L. Kulcinski and R.A. Dodd
Affiliation: University of Wisconsin-Madison

4.0 Relevant DAFS Program Plan Task/Subtask

Subtask II.C.1.1: Phase Stability Mechanics
Subtask II.C.1.2: Modeling and Analysis of Effects of Materials Parameters on Microstructures

5.0 Accomplishments and Status

5.1 Introduction

A recent investigation of AMZIRC and AMAX-MZC copper alloys following high temperature ion irradiation determined that the main effect of irradiation was to cause an acceleration of the recrystallization process.[1] It was concluded that this irradiation effect might make AMZIRC and AMAX-MZC unsuitable for fusion reactor applications, since much of their strength is lost upon recrystallization. The previous study only investigated a limited temperature regime (400-550°C), which is at or above the upper limit for fusion reactor applications. To date, there is no known irradiation data on any high-strength, high-conductivity copper alloys at irradiation conditions similar to the environment that they will experience in a fusion reactor,[2] i.e., 50-400°C; 1-40 dpa (K = 0.3). The present study investigates the microstructures of AMZIRC and AMAX-MZC following heavy ion irradiation to peak damage levels of 15 dpa (K = 0.3) at 100-250°C.

TABLE 1. COMPOSITION AND OPTIMUM PHYSICAL PROPERTIES OF AMZIRC AND AMAX-MZC (FROM REF. 3)

Alloy	Cr (at %)	Zr (at %)	Mg	Electrical Conductivity @ 20° C	Yield Strength (0.2% Offset)
AMZIRC	-	0.13–0.20	-	93% IACS	410 MPa
MZC	0.80	0.15	0.04	80% IACS	517 MPa

TABLE 2. IRRADIATION PARAMETERS OF ION-IRRADIATED AMZIRC AND AMAX-MZC

Alloy	Irradiation Temperature	Calculated Damage (dpa)* 1 µm	Peak
AMZIRC, MZC	100°C	4	15
AMZIRC. MZC	150°C	4	15
AMZIRC. MZC	200°C	4	15
AMZIRC. MZC	250°C	4	15

*K = 0.3

5.2 Experimental Procedure

The composition and optimum physical properties of AMZIRC and AMAX-MZC are given in Table 1. As-received specimens of both alloys were irradiated with 14-MeV Cu^{3+} ions using the University of Wisconsin tandem Van de Graaf accelerator to a fluence of 3 x 10^{20} ions/m^2. Table 2 lists the irradiation conditions for these specimens. In keeping with recent displacement efficiency measurements,[4,5] we have used K = 0.3 in the modified Kinchin-Pease model for all of our dpa calculations (as opposed to the previous value of K = 0.8).

Following the irradiation, the samples were prepared for cross-section analysis using techniques which are described in detail elsewhere in this DAFS quarterly volume.[6] The cross-section specimens were jet-electropolished in a solution of 33% HNO_3/67% CH_3OH cooled to -20°C at an applied voltage of 15–20 V, and were examined in a JEOL TEMSCAN-200CX electron microscope.

5.3 Results

Radiation-enhanced recovery and partial recrystallization was observed in both AMZIRC and AMAX-MZC over the entire temperature range of 100-250°C. Figure 1 shows the effect of a 250°C irradiation on the microstructure of AMAX-MZC. The cross-section micrograph at the top allows the scale of the radiation damage region to be noted. with both the irradiated and nonirradiated portions of the foil observable. The bottom two micrographs present the irradiated and nonirradiated regions of the foil at higher magnification. Recovery of the cold-worked dislocation structure has occurred in the irradiated region of the foil, while the control microstructure remains similar to that of the as-received alloy. Subgrain development is observed to be more advanced in the damage region compared to the control. A third feature is the appearance of small "black spots" in irradiated regions of the foil. Similar results were obtained for AMZIRC irradiated at the same conditions.

Figure 2 shows the microstructures of AMZIRC and AMAX-MZC following irradiation at 100°C. Once again, the cold-worked dislocation structure has recovered during irradiation. Subgrain nucleation is visible in both micrographs. Both alloys contain a high density of small "black spots".

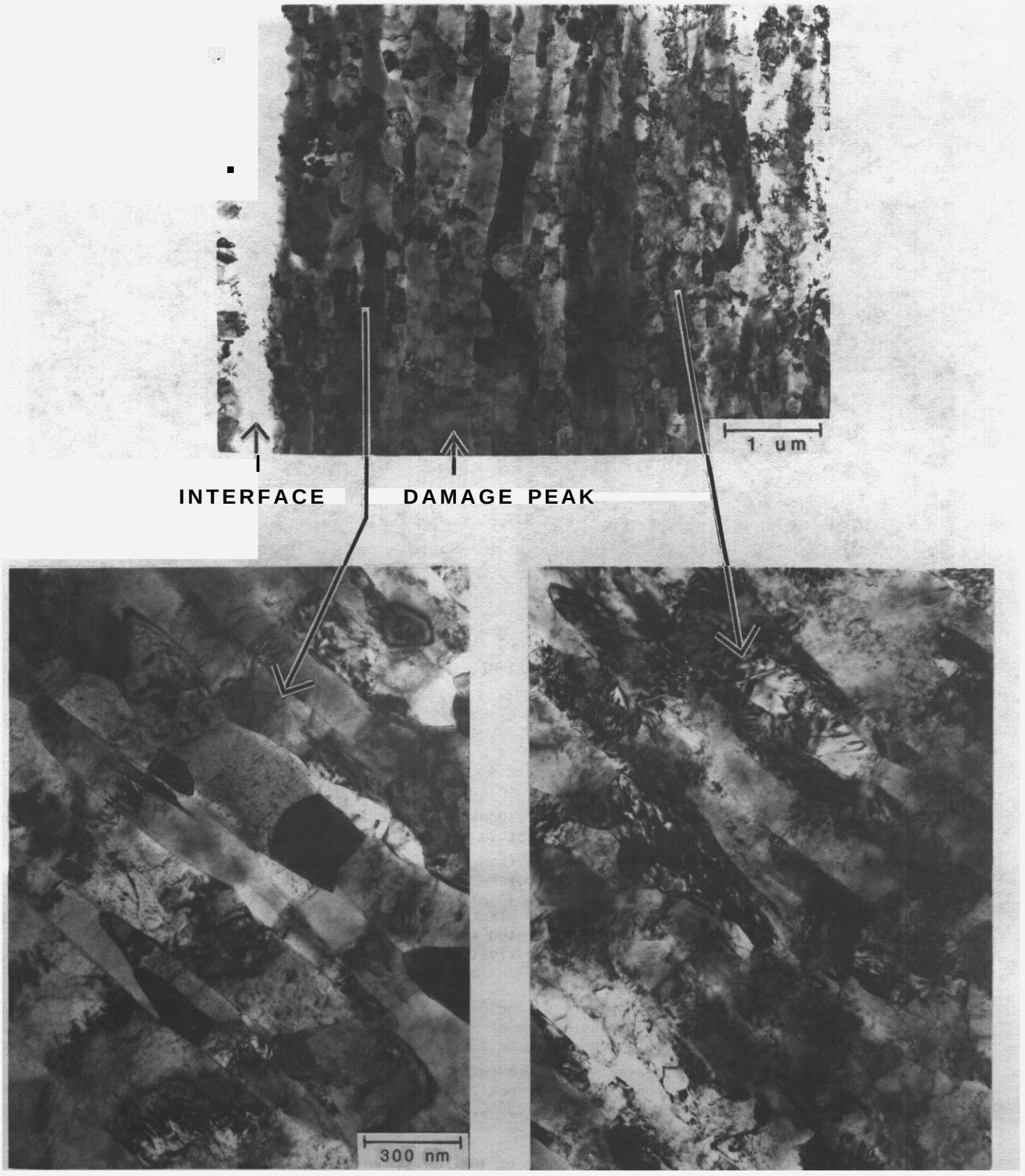

FIGURE 1. Radiation damage effects in as-received AMAX-MZC irradiated with 14-MeV Cu ions to a peak damage level of 15 dpa (K = 0.3) at 250°C. The top micrograph shows the irradiated and nonirradiated regions of the foil in cross section. The bottom two micrographs are higher magnifications of the damage (left) and control (right) regions.

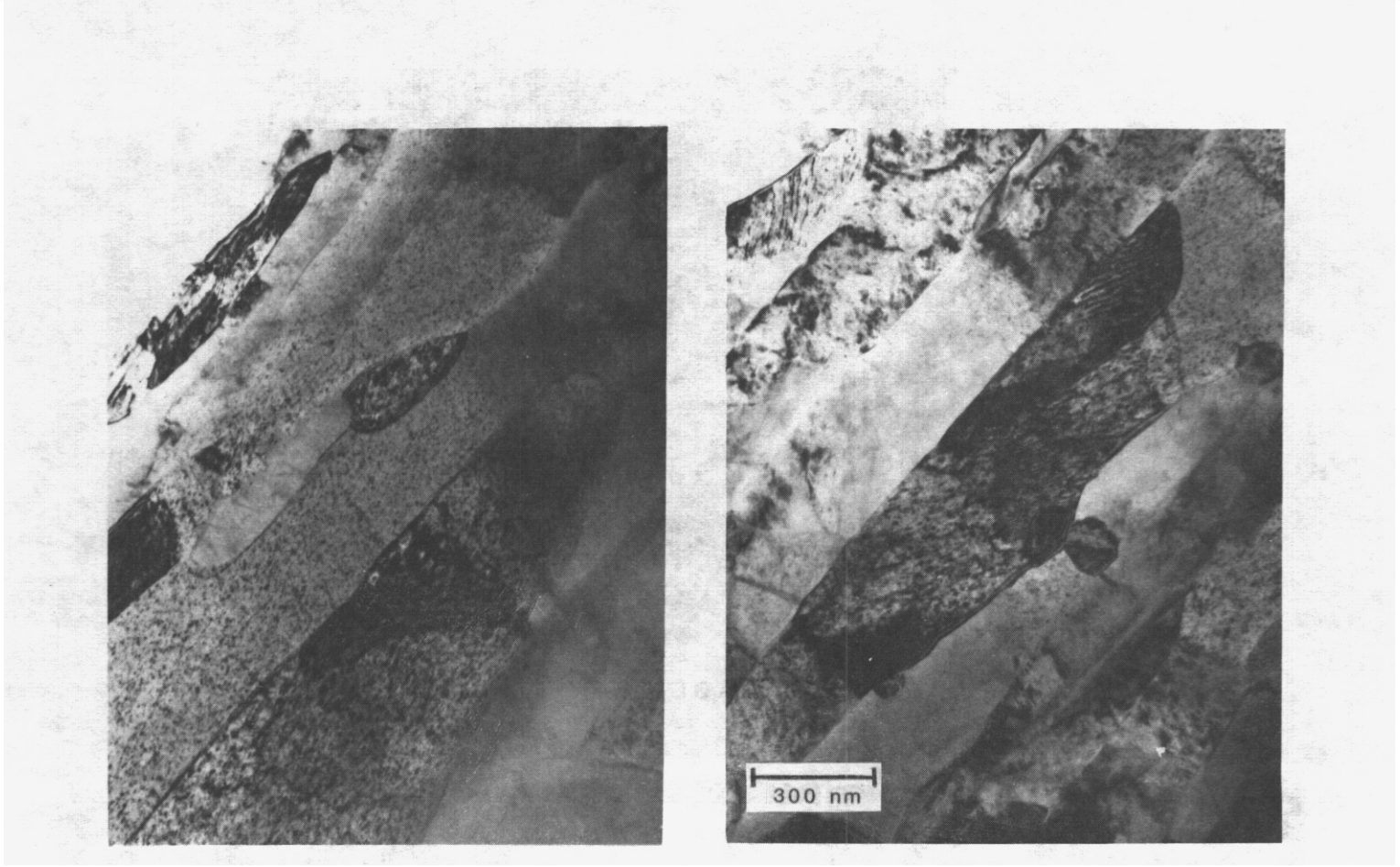

FIGURE 2. Microstructures of ANZIRC (left) and AMAX-MZC (right) following 14-MeV Cu ion irradiation to a peak damage level of 15 dpa (K = 0.3) at 100°C.

5.4 Discussion

AMZIRC and AMAX-MZC appear to have quite similar responses to moderately high ion Irradiation doses over the temperature range of 100-250°C. This is in contrast to their high temperature irradiation behavior. where AMAX-MZC exhibited more pronounced microstructural changes as compared to AMZIRC.[1] For irradiation temperatures of 100-250°C, both alloys undergo recovery of their cold-worked dislocation structure. Black spot formation and subgrain nucleation is observed at all temperatures. Qualitatively, it appears that the ANZIRC alloy may have a slightly higher density of black spots than MZC at the irradiation conditions investigated. The size of the subgrains in irradiated AMZIRC also appear to be somewhat larger on the average than the MZC subgrains. Quantitative investigation of these observations is in progress.

There is little or no influence of temperature on the damage microstructure of these alloys for irradiation temperatures of 100-250°C. Subgrain development is at most only slightly more advanced at 250°C as compared with 100°C. The density of black spots appears to be similar for all temperatures between 100 and 250°C for both alloys. This finding is in agreement with numerous[2] dislocation loop studies of copper using HVEM and ion irradiation, where it was found that loop density decreases very slowly (factor of two) as the irradiation temperature is increased from 50°C to 250°C.

Cross-section analysis allows the depth-dependence of the radiation damage to be determined. This is often important, since the peak damage level at 2 μm is about ffve times larger than the damage level at 0.5-1.0 μm. In the present case, however. we have not observed any significant depth-dependence of the radiation damage. Dislocation recovery was observed at all depths, and the subgrain size was similar throughout the damage region. Quantitative analysis of the depth-dependence of the black spot density was complicated by the presence of the numerous subgrains, which change the diffracting conditions. Qualitatively. the black spot density dld not vary greatly with depth.

A previous investigation of AMZIRC and MAX-MZC found that the strength of these alloys decreased dramatically upon recrystallization.[7] Therefore, it may be implied that the partial recrystallization which is observed in these alloys following irradiation could lead to a degradation in their strength, which would make them unsuitable for many fusion reactor applications. The high density of black spots (presumed to be small dislocation loops) should cause an increase in the strength of the alloys. The relative importance of these two competing effects could result in either a net increase or decrease in the alloy strength. Neutron irradiation of copper to a fraction of a dpa at 40°C has been found to increase the yield strength by more than 300 MPa, with saturation occurring at higher fluences.[8] This strength increase is about the same as the maximum loss of strength which could occur in AMZIRC or MZC if complete recrystallization occurs.[1] Since only partial recrystallization has been observed for the irradiation conditions in this study, it appears likely that the net effect of irradiation at temperatures of 100-250°C may be to produce a stronger alloy.

There was no observable void formation in either of the as-received copper alloys following ion irradiation at 100-250°C. A previous study[1] at higher temperatures did not detect void formation except in the case of annealed AMZIRC specimen at 300°C. Therefore, no voids have been observed in as-received MZIRC or MZC specimens following ion irradiation to 15 dpa (K = 0.3) over the wide temperature range of 100-550°C (0.28-0.61 T_m). One possible reason for the absence of void formation in the as-received alloys is the absence of gaseous nucleating agents (both alloys are fabricated from oxygen-free copper in a carefully controlled environment). A second explanation is that the high cold-work level in the as-received alloys may be delaying the onset of void formation. To investigate this possibility, we have irradiated foils of both alloys in a solution annealed plus aged condition at temperatures 100-400°C. This irradiation will also provide some insight whether point defect trapping on solute atoms or precipitates may be suppressing void swelling.

5.5 Conclusions

Ion irradiation of as-received AMZIRC and AMAX-MZC to 15 dpa (K = 0.3) at temperatures of 100-250°C results in the following microstructural changes: 1) recovery of the cold-worked dislocation structure, 2) possible enhancement of recrystallization processes, and 3) formation of a high density of black spots. Recovery and recrystallization tend to decrease the alloy strength, while radiation hardening due to black spot formation should increase the yield strength. The net effect of these competing processes may be an increase in the strength of these alloys following irradiation at 100-250°C. No void formation has been detected in the as-received alloys following irradition over a wide temperature range.

6.0 Acknowledgements

This work was performed under appointment to a Magnetic Fusion Energy Technology Fellowship and with funds supplied by the Department of Energy.

7.0 References

1. S.J. Zinkle, R.A. Dodd and G.L. Kulcinski, "Comparison of Thermal and Irradiated Behavior of High-Strength, High-Conductivity Copper Alloys", 12th International Symposium on the Effects of Radiation on Materials, (June 1984) Williamsburg, VA; to be published by ASTM; also see DAFS Quarterly Progress Report DOE/ER-0046/17, p. 117.

2. S.J. Zinkle and R.W. Knoll, "A Literature Review of Radiation Damage Data for Copper and Copper Alloys", University of Wisconsin Fusion Engineering Program Report UWFDM-578 (June 1984).

3. Interim Publications on AMZIRC and MAX-MZC Copper Alloys, MAX Copper, Inc., New York, NY (1982).

4. J.H. Kinney, M.W. Guinan and L.A. Munir, "Defect Production Efficiencies in Thermal Neutron Irradiated Copper", Third Topical Meeting on Fusion Reactor Materials, Albuquerque, NM (Sept. 1983); to be published in J. Nucl. Mater.

5. R.S. Averback, R. Benedek and K.L. Merkle, Phys. Rev. B 18, No. 8, (1978) 4156; also J. Nucl. Mater. 69/70 (1978) 786.

6. S.J. Zinkle and R.L. Sindelar, "Preparation of Ion-Irradiated Foils for Cross-Section Analysis", DAFS Quarterly Progress Report DOE/ER-0046/18 (this volume).

7. S.J. Zinkle, D.H. Plantz, R.A. Dodd and G.L. Kulcinski, DAFS Quarterly Progress Report DOE/ER-0046/17, p. 110.

8. M.G. Mohamed, A.M. Hammad and F.H. Hammad, Trans. Indian Inst. Metals, 36, No. 3 (June 1982) 258-262.

8.0 Future Work

Solution annealed plus aged specimens of AMZIRC and AMAX-MZC which have been irradiated with 14-MeV Cu ions will be analyzed in cross-section for void formation and precipitate stability during irradiation. Results will be presented in the next quarterly progress report.

9.0 Publications

None

EXTERNAL DISTRIBUTION

UC-20 (107), 20c (69)

DOE-HQ/Office of Breeder
Technology Projects
NE-53
Washington, DC 20545

PB Hemmig, Asst Director,
Reactor Physics Technology

DOE-HQ/Office of Fusion Energy (3)
Washington, DC 20545

JF Clark, ER-70
JF Decker, ER-54, G-256
S. Parket, ER-62, GTN

Argonne National Laboratory (5)
9700 South Cass Avenue
Argonne, IL 60439

LR Greenwood BA Loomis
A. Taylor H. Wiedersich
RE Nygren

Battelle
Pacific Northwest Laboratory (3)
P.O. Box 999
Richland, WA 99352

JL Brimhall
DA Dingee
TD Chikalla

Brookhaven National Laboratory
Associated Universities
Upton, Long Island, NY 11973

Chairman, Nuclear Energy Dept

Columbia University
Plasma Physics Laboratory
New York, NY 10027

RA Gross

Commission for the European Communities
200, Rue de la Loi
B-1049 Brussels, Belgium

J. Darvas

Energieonderzoek Centrum Nederland (2)
Netherlands Energy Research Foundation
Westinghouse 3, Postfach 1
NL-1755 ZG Petten, The Netherlands

B. vanderSchaaf
W. vanWitzenburg, Materials Dept

EURATOM
Joint Research Center Ispra
Materials Science Division
I-21020 Ispra, Varese, Italy

P. Schiller

General Atomic Company (2)
P.O. Box 81608
San Diego, CA 92138

GR Hopkins
JR Gilleland

General Electric
Advanced Nuclear Technology Operation (2)
310 DeGuigne Drive
Sunnyvale, CA 94088

ANTO Library, M/C S-02
S. Vaidyanathan, M/C S-53

Hahn-Meitner Institiit fur Kernforschung
Glienickerstrasse 100
D-1000 Berlin,
Federal Republic of Germany

H. Wollenberger

Hokkaido University (2)
Facility of Engineering
Kita-hu, Sapporo, 060 Japan

Mihio Kiritani, Precision Engineering
Taro Takeyama, Metals Research Institute

INESCO
11011 Torreyana Rd
San Diego, CA 92121

RD Stevenson

Japan Atomic Energy Research Institute (2)
Physical Metallurgy Laboratory
Tokai Research Establishment
Tokai-mura, Naka-gun, Ibaraki-ken, Japan

Shuichi Iwata, Physics
Kensuke Shiraishi, Nuclear Fuels Research

Kernforschungsanlage Jülich GmbH
Postfach 1913
D-517 Julich,
Federal Republic of Germany

P. Jung

EXTERNAL DISTRIBUTION (Cont'd)

Kernforschungszentrum Karlsruhe
Institut für Reaktorbauelemente
Postfach 3640
0-7500 Karlsruhe 1,
Federal Republic of Germany

K. Ehrlich

Kyushu University
Research Institute for Applied Mechanics
6-10-1 Hakozaki, Hiaashi-ku.
Fukuoka, 812 Japan

Kazunori Kitajima

Lawrence Livermore National Laboratory (4)
P.O. Box 808
Livermore, CA 94550

WL Barmore
DW Dorn
MW Guinan, L-396
CM Logan

Lawrence Livermore National Laboratory
P.O. Box 5511
Livermore, CA 94550

EC Oalder, L-643

Los Alamos National Laboratory (3)
P.O. Box 1663
Los Alamos, NM 87544

DJ Dudziak
CR high
J. Fowler, E-546

Massachusetts Institute of Technology (4)
77 Massachusetts Avenue
Cambridge, MA 02139

I-W Chen, 13-5118
NJ Grant, 8-305
L. Lidsky
JB vanderSande, 13-5025

Massachusetts Institute of Technology
Nuclear Reactor Laboratory
138 Albany St
Cambridge, MA 02139

OK Harling, NW12-204

McDonnell-Douglas Astronautics Co.
P.O. Box 516
St. Louis, MO 63166

D. Kummer

Mound Laboratory
P.O. Box 32
Miamisburg, OH 45342

Manager, Tech Applied & Development

National Bureau of Standards
Washington, DC 20234

JA Grundl

National Researcn Council
Montreal Road
Ottawa, Canada

EV Kornelson

National Research Institute for Metals
Nuclear Materials Division
1-2-1 Sengen, Sakura-mura,
Niihari-gun, Ibaraki, 305 Japan

Naoki Kishimoto

Naval Research Laboratory (3)
Washington, DC 20375

I. Manning, Code 6672
JA Sprague, Code 6395
LE Steele, Code 6390

North Carolina State University
Department of Nuclear Engineering
Raleigh, NC 26707

JR Beeler Jr

Oak Ridge National Laboratory (12)
P.O. Box X
Oak Ridge, TN 37830

Director
K. Farrell
ML Grossbeck
PJ Maziasz
LK Mansur
NH Packan
J. Sheffield
JO Stiegler
RE Stoller
C. Weisbin
FW Wiffen
M. Roberts

Osaka University (2)
2-1, Yamada-oka, Suita,
Osaka, Japan 565

Kenji Sumita, Dept of Nuclear Engineering
Toichi Okada, Institute of
Scientific & Industrial Research

Princeton University (4)
Plasma Physics Laboratory
Forrestal Campus
P.O. Box 451
Princeton, NJ 08544

H. Conrads
H. Furth
R. Little
K. Wakefield

Risø National Laboratory
Postfach 49
OK-4000 Roskilde, Denmark

B.N. Singh

EXTERNAL DISTRIBUTION (Cont'd)

Rockwell International
8900 DeSoto Ave
Canoga Park, CA 91304

DW Kneff

Sandia National Laboratories (2)
P.O. Box 5800
Albuquerque, NM 87185

FL Vook, Org 5100

Sandia National Laboratories (2)
Livermore, CA 94550

W. Garrison, Div 8314
WD Wilson

Science Applications Inc
1200 Prospect
LaJolla, CA 92037

H. Gurol

Science University of Tokyo
Engineering Dept
Kagurazaka, Shinjuku-ku,
Tokyo, 162 Japan

RR Hasiguti

Studiecentrum voor Kernenergie
Centre d'Etude de l'Energie Nucleaire
Boeretang 200
B-2400 Mol, Belgium

J. Nihoul

Swiss Federal Institute
for Reactor Research
CH-5303 Wuerenlingen, Switzerland

WV Green

Tokyo Institute of Technology
12-1. 2-Chome. O-Okavama
Meguro-ku, Tokyo, Japan

Kensutaka Kawamura

United Kingdom Atomic Energy Authority (2)
Atomic Energy Research Establishment
Oxfordshire, OX 11 ORA, UK

R. Eullough, Theoretical Physics Division

United Kingdom Atomic Energy Authority
Culham Laboratory
Applied Physics & Technology Oivision
Abingdon, Oxfordshire OX14 3DB, UK

GJ Butterworth

University of California (2)
Los Angeles, CA 90024

RW Conn
NM Ghoniem

University of Michigan
Nuclear Engineering
Ann Arbor, MI 48109

T. Kammash

University of Missouri
Mechanical & Aerospace Engineering
1006 Engineering Bldg
Columbia, MO 65211

M. Jolles

University of Missouri
Dept of Nuclear Engineering
Rolla, MO 65401

A. Kumar

University of Tokyo (3)
7-3-1 Hongo
Bunkyo-ku, Tokyo 113, Japan

Naohira Igata, Met & Material Science
Shiori Ishino, Nuclear Engineering
Taijiro Uchida

University of Virginia
Dept of Materials Science
Charlottesville, VA 22901

WA Jesser

University of Wisconsin
1500 W. Johnson Drive
Madison, WI 53706

WG Wolfer

Westinahouse
Advanced Energy Systems Division
Fuels Materials Technology
P.O. Box 158
Madison, PA 15663

A. Boltax, Manager

Westinghouse
Research and Development Center (2)
1310 Beulah Road
Pittsburgh, PA 15235

JA Spitznagel
S. Wood

INTERNAL DISTRIBUTION

DOE-RL/AMCW (2)
FMIT Facility Project Office
FED/642-F

GM Chenevert, Project Manager

HEOL (28)

SO Atkin	W/A-58
HR Brager	W/A-58
LL Carter	W/B-47
DG Ooran	W/A-57
EA Evans	W/C-23
FA Garner	W/A-58
DS Gelles	W/A-58
R. Gold	W/C-39
HL Heinisch	W/A-58
DL Johnson	W/A-4
GO Johnson	W/A-65
FM Mann	W/A-4
WN McElroy	W/C-39

DOE-RL/AME
Breeder Technology Division
Technology Development & Engineering Branches
FED/210

KR Absher, Chief

EK Opperman	W/A-58
NF Panayotou	W/A-65
RW Powell	W/A-58
RJ Puigh	W/A-58
FH Ruddy	W/C-39
FA Schmittroth	W/A-4
WF Sheely	W/C-62
RL Simons	W/A-57
JL Straalsund	W/A-61
HH Yoshikawa	W/C-44
Central Files (3)	W/C-110
Document Services	W/C-123
Microfilm Services	W/C-123